Thermodynamic properties of gases

from

measurements of the speed of sound.



A thesis submitted to the University of London
for the Degree of Doctor of Philosophy
and for the Diploma of Imperial College
by

Andrés Francisco Estrada Alexanders.

Department of Chemical Engineering and Chemical Technology
Imperial College of Science, Technology and Medicine.
Prince Consort Road, SW7 2BY
London, United Kingdom.

April 1996.

Acknowledgements.

I would like to thank to my supervisor, Dr. JPM Trusler, by all unconditional and patient help that I always found along any discussion taking place during this work. I also thank him by distinguishing me with his friendship which contributed to make my stay in this country more pleasurable and rich. I must recognise that working with Martin has been and, surely will it always be, an encouraging and quite stimulating experience from which I really think I enrich myself from a personal and professional point of view.

I could not forget to thank all people in the fluids group. They have provided a favourable **environment** for researching and ,of course, a superb friendly atmosphere. Special thanks not only to my labmates, Dr. M Costa Gomes, Dr. L Cusco, Dr. H Duriyabeleng, Mr. J Estela Uribe, Mr. P Stanley, but also to the rest of **postgraduate** students and postdoctoral researchers of the group Ms. J. Cebola, Mr S. Chawad, Dr. H. Messie-Brown, Mr. K Mongo, Dr. A. Padua, Dr. M Papadakis, Mr R Venable and Dr. (anticipated) T. Tsolakis.

I also like to thank to all my others friend which do not belong to the fluid group; I think a really ought to name them: Diana, Ali, Leon, Gary, Giota, Dave and of course all my **Mexican** friends of Imperial: Ruben and Clara, Rebeca and Rodi, Carlos and Margarita, Balder and Gliselda, Victor, Santiago, Jose Luis, Hector, Sandra, Sabino, Pedro and Francisco. Thanks to all of them.

And last but not least, I thank with all my heart the unfailing and **unconditional** support of all my family: my beloved parents, my dear brother and sisters and my nieces and nephew.

I acknowledge the financial support that I received during this work by CONACyT and Universidad Autónoma Metropolitana.

Abstract

In this work, measurements of the speed of sound in several gases have been made with a spherical acoustic resonator in very wide ranges of temperature and pressure. All measurements were taken along isotherms (fifty two in total) in the range from about $0.75 \cdot T^{c}$ to 450 K and the maximum pressure was estimated to reach half of the critical density at supercritical temperatures (reaching pressures as large as 19 MPa). The uncertainty of these determinations of the speed of sound was normally less than 0.004 per cent. This high accuracy has been exploited in determinations of thermodynamic properties from the speed of sound. Compression factors and heat capacities at constant volume and at constant pressure have been derived for argon and ethane from the speed of sound by means of a numerical integration at densities up to half the critical at supercritical temperatures and at up to eighty per cent of the saturated vapour density at subcritical temperatures.

A detailed description is given of the methods employed to carry out the integration. In addition, an extensive assessment of the uncertainty with which the compression factors and heat capacities may be derived by means of this numerical integration has been made. This was achieved through numerical simulations of the integration algorithm supported by an approximate analytical solution for the propagation of errors in the solution. The most demanding feature of the technique is the need for accurate initial conditions for the integration. Errors in the initial conditions can compromise the accuracy of the derived compression factor but likely errors in the speed of sound are small enough to have little effect. However, for the heat capacities, errors in both the initial conditions and the speed of sound become important.

The second acoustic virial coefficients have been utilised to determine a set of parameters in a site-site intermolecular potential model by means of a non-linear regression analysis applied to each of the following systems: ethane, carbon dioxide and the binary system (ethane plus carbon dioxide). A Maitland-Smith potential model was used to describe the interactions between a pair of sites on different molecules and, from these potentials, ordinary second virial coefficients were calculated and compared with values from the literature.

LIST OF CONTENTS.

Page

Acknowledgements 2

Abstract 3

List of contents 4

List of figures 8

List of tables 13

Chapter 1. Introduction. 15

1.1 Introduction. 15

References. 20

Chapter 2. Theory of acoustic resonators. 21

2.1 Introduction. 21

2.2 Theory of sound. 21

2.2.1 Hydrodynamic description of sound. 21

2.2.2 Propagational, thermal and shear modes. 25

2.2.3 Boundary layers. 29

2.3 Acoustic resonator theory 32

2.3.1 Ideal spherical resonator. 33

2.3.2 Driven cavity. 35

2.3.3 Real spherical cavity. 37

2.3.4 Boundary conditions. 39

2.3.5 Acoustic model. 40

2.3.6 Relaxation in gases. 45

References. 50

Chapter 3. Determination of thermodynamic properties of a fluid from its speed of sound. 51

3.1 Introduction. 51

3.2 The speed of sound and the equation of state. 51

3.2.1 Perfect gas limit. 52

3.2.2 The virial equation of state. 53

3.2.3 Relationship between the speed of sound and the compression factor. 55

3.3 Numerical techniques..... 60
3.3.1 Predictor-corrector method. 60
3.3.2 Initial conditions. 64
3.3.3 Interpolation of the speed of sound..... 69
3.4 Test of numerical method. 73
3.4.1 Simulation of the numerical method: size of steps. 73
3.4.2 Simulation of the numerical method: stability..... 76
3.5 Error propagation in numerical integration..... 79
3.5.1 Analytical solution. 80
3.5.2 Predictions and simulations of errors..... 86
3.5.3 Propagation of errors into the heat capacities. 89
References..... 93
Chapter 4. Intermolecular potential and virial coefficients..... 94
4.1 Introduction..... 94
4.2 Decomposition of the energy of interaction..... 95
4.3 Intermolecular potential model. 96
4.3.1 Maitland-Smith potential. 98
4.3.2 Site-site distances between like and unlike molecules..... 99
4.4 Second virial coefficient and the pair-wise intermolecular potential..... 100
4.4.1 Pure component..... 100
4.4.2 Binary mixture. 104
References..... 107
Chapter 5. Apparatus and experimental procedure. 108
5.1 Introduction..... 108
5.2 Description of the apparatus. 108
5.2.1 Spherical resonator..... 108
5.2.2 Temperature measurements. 112
5.2.3 Pressure measurements. 114
5.2.4 Electroacoustic transducers..... 118
5.2.5 Radius of resonator. 120
5.3 Experimental procedure. 121
5.3.1 Fit of radial modes. 121

5.3.2 Fit of non-radial mode (1, 1) 122
5.4 Substances. 126
5.4.1 Argon. 126
5.4.2 Ethane 126
5.4.3 Carbon dioxide. 127
5.4.4 Mixture of carbon dioxide and ethane. 127
References. 129
Chapter 6. Experimental results. 130
6.1 Introduction. 130
6.2 Analysis of uncertainties in speed of sound. 130
6.3 Argon. 133
6.3.1 Speed of sound. 133
6.3.2 Radius calibration. 140
6.3.3 Acoustic virial coefficients. 141
6.4 Ethane 148
6.4.1 Speed of sound in Ethane. 148
6.4.2 Heat capacities of perfect gas. 153
6.4.3 Acoustic virial coefficients. 157
6.5 Carbon Dioxide. 159
6.5.1 Non-radial mode (1, 1). 159
6.5.2 Speed of sound. 163
6.5.3 Heat capacities and second acoustic virial coefficient. 167
6.6 Binary mixture $(1\text{-}x)C_2H_6 + xCO_2$. 170
6.6.1 Speed of sound. 171
6.6.2 Composition of the mixture. 175
6.6.3 Acoustic virial coefficients. 181
References. 184
Chapter 7. Analysis of data. 186
7.1 Introduction. 186
7.2 Thermodynamic properties derived from the speed of sound 186
7.2.1 Argon. 186
7.2.2 Ethane 193

7.3 Intermolecular potential model. 197
7.3.1 Numerical calculations. 198
7.3.2 Ethane 198
7.3.3 Carbon Dioxide. 202
7.3.4 Mixture of ethane and carbon dioxide. 206
References. 210
Appendix. 211
Chapter 8. Conclusions. 231

List of figures.

Figure.	Caption	Page.
3.1	Lines at constant ϕ for argon. The function f(T) is obtained from an expression of vapour curve for argon given in reference [9].	58
3.2	Distribution of experimental points (T,p) at which speed of sound was measured in ethane.	63
3.3	Estimated **uncertainties** and truncation errors on initial conditions for the case $N = 2$ of argon.	67
3.4	Function F along two isotherms for argon.	72
3.5	Deviations of Z and $C_{V,\mathrm{m}}$ from simulations in subcritical region for two different ΔT: (i) for $\Delta T = -0.05$ K and (ii) for $\Delta T = -0.005$ K.	76
3.6	Deviations of Z and $C_{V,\mathrm{m}}$ from simulations of isochoric integration on argon with $\Delta T = \pm 0.5$ K and at $T > T^{\mathrm{c}}$ and fifty isochores up to half of the critical density.	78
3.7	Deviations of Z and $C_{V,\mathrm{m}}$ from simulations of integration on argon along lines at constant fraction of the saturation density.	79
3.8	Parasitic contribution Z_{p} to Z along the isochore at half of the critical density for a gas with a =1/3 resulting from errors in the initial conditions proportional to ρ_n'''.	87
3.9	Parasitic contribution Z_{p} to Z along a line at constant fraction of the saturation density of a gas with a =1/3 resulting from errors in the initial conditions proportional to ρ_n'''.	87
3.10	$\Delta C_{V,\mathrm{m}}/R$ calculated from equation (3.5.11) along the isochore at half of the critical density for a gas with a =1/3 resulting from errors in the initial conditions proportional to ρ_n'''.	88
3.11	$\Delta C_{V,\mathrm{m}}/R$ calculated from equation (3.5.11) along a line at constant fraction of the saturation density for a gas with a =1/3 resulting from errors in the initial conditions proportional to ρ_n'''.	88
3.12	Parasitic contribution Z_{p} to Z along the isochores for argon .	90
3.13	Ripples in $C_{V,\mathrm{m}}$ from preliminary integration of argon at 450 K.	91

Figure.	Caption	Page.
3.14	Error in $C_{V,\mathrm{m}}$ at 450 K from simulations with an error on the speed of sound.	92
5.1	Cross-section of spherical resonator.	109
5.2	Cross-section of spherical resonator and thermostat.	110
5.3	Deviation Δp of the readings of the high-pressure transducer after recalibration from those measured with the oil-piston gauge and the low-pressure transducer.	117
5.4	Resonance of mode (1, 1) in ethane at the $T = 275$ K and $p = 0.5$ MPa.	123
6.1	Diagram of the fractional uncertainty $\delta u/u$ in the speed of sound u as a function of the reduced temperature T/T^{c} and pressure p/p^{c}.	132
6.2	Deviations of speed of sound $\Delta u(0,n) = [u(0,n)/\langle u\rangle - 1]$ of argon determined from different radial modes along the isotherm at 350 K.	139
6.3	Fractional deviations $\Delta u/u$ of the speeds of sound u of argon reported by Ewing and Goodwin[7] from those interpolated from the results of this work.	140
6.4	Y_β as a function of amount-of-substance density ρ_n at selected temperatures. Curves are quadratic polynomials fitted to the results.	143
6.5	Deviations $\delta\beta_a$ of second acoustic virial coefficients of argon from values calculated with the interatomic potential-energy function of Ewing and Trusler.	146
6.6	Third acoustic virial coefficients γ_{a} of argon.	146
6.7	Fourth acoustic virial coefficients δ_a of argon.	147
6.8	Fractional deviations $\Delta u/u$ of the speed of sound u of ethane reported by Boyes[20] from those interpolated from the results of this work.	154
6.9	Fractional deviations $\Delta C_{p,\mathrm{m}}^{\mathrm{pg}}/C_{p,\mathrm{m}}^{\mathrm{pg}}$ of the perfect-gas heat capacities of ethane determined from acoustic measurements from those calculated by means of equation (6.4.2).	156
6.10	Deviations $\Delta\beta_a$ of the second acoustic virial coefficients β_a of ethane from values calculated with a site-site intermolecular potential model.	158

Figure.	Caption	Page.
6.11	Comparison of the third acoustic virial coefficients γ_a of ethane. Solid curve is a graphical interpolation of the data reported here.	158
6.12	Estimated frequency range for non-radial mode (1, 1) of carbon dioxide at several temperatures.	160
6.13	Fractional deviations $\Delta u/u$ of the speeds of sound u derived from mode (1, 1) from the actual speed of sound as a function of the mass of the fluid M_{fl} before applying the correction for the coupling of the gas and shell motion.	161
6.14	Excess half-widths Δg on carbon dioxide: a) before corrected for sound absorption, b) after corrected for sound absorption.	166
6.15	Y_β on carbon dioxide as a function of amount-of-substance density ρ_n. Curves are quadratic polynomials fitted to the results.	167
6.16	Fractional deviations $\Delta C_{p,\mathrm{m}}^{\mathrm{pg}}/C_{p,\mathrm{m}}^{\mathrm{pg}}$ of the perfect-gas heat capacities of carbon dioxide determined from limiting slope analysis from those derived from spectroscopic data given in reference [24].	168
6.17	Deviations $\Delta\beta_a$ of the second acoustic virial coefficients β_a of carbon dioxide from values calculated with a site-site intermolecular potential.	170
6.18	Excess half-widths Δg on the mixture carbon dioxide + ethane: a) before corrected for absorption, b) after corrected for absorption.	176
6.19	Fractional deviation $\Delta u/u$ of the speed of sound u of the check measurements from earlier data at the temperature of 275 K in order to verify possible variation of composition of the mixture carbon dioxide + ethane.	180
6.20	Second acoustic virial coefficients of the mixture β_{mix} and interaction second acoustic virial coefficient β_{12} of the system carbon dioxide + ethane.	182
6.21	Second pseudo-acoustic virial coefficients β_{jj} of the system carbon dioxide + ethane.	183

Figure.	Caption	Page.
7.1	Thermodynamic properties of argon at 150 K from two different algorithms. Solid curves are calculated from integration along lines at constant ϕ and symbols are calculated from integration along isochores.	189
7.2	Fractional deviations $\Delta Z/Z$ of the compression factors Z of argon reported by Gilgen *et al.*[2] from the present results for temperatures between 110 K and 153 K.	190
7.3	Fractional deviations $\Delta Z/Z$ of the compression factors Z of argon reported by Gilgen *et al.*[2] from the present results for temperatures between 154 K and 200 K.	191
7.4	Fractional deviations $\Delta Z/Z$ of the compression factors Z of argon reported by Gilgen *et al.*[2] from the present results for temperatures between 220 K and 340 K.	191
7.5	Fractional deviations $\Delta C_{p,\mathrm{m}}/C_{p,\mathrm{m}}$ of the heat capacities at constant pressure $C_{p,\mathrm{m}}$ reported by Baba *et al.* and from reference [8] along three isobars.	192
7.6	Fractional deviations $\Delta Z/Z$ of the compression factors Z of ethane reported by Douslin and Harrison[7] (open symbols) and by Mansoorian *et al.*[9] (solid symbols) from the present results for temperatures between 273.15 K and 323.15 K.	196
7.7	Fractional deviations $\Delta Z/Z$ of the compression factors Z of ethane reported by Douslin and Harrison[7] (open symbols) and by Mansoorian *et al.*[9] (solid symbols) from the present results for temperatures between 348.15 K and 448.15 K.	196
7.8	Fractional deviations $\Delta C_{V,\mathrm{m}}/C_{V,\mathrm{m}}$ of the heat capacities at constant volume $C_{V,\mathrm{m}}$ of ethane reported by Roder[10] along two isochores.	197
7.9	Resulting reduce χ^2 of the fittings procedure of the parameters of the intermolecular potential as a function of the parameter γ when all experimental second acoustic virial coefficients of ethane were included in the fitting.	200

Figure.	Caption	Page.
7.10	Deviations ΔB of the second virial coefficient B of ethane reported by Douslin and Harrison[7] and by Mansoorian[10] from those calculated from the MS intermolecular potential model adjusted by means of second acoustic virial coefficients.	202
7.11	Resulting reduce χ^2 and parameter m from the fitting of a Lennard-Jones intermolecular potential as a function of the site-site separation l_{ss} when all experimental second acoustic virial coefficients of carbon dioxide were included.	204
7.12	Deviations ΔB of the second virial coefficient B of carbon dioxide reported by Duschek *et al.*[12] and by Holste *et al.*[10] from those calculated from the MS intermolecular potential model adjusted by means of second acoustic virial coefficients.	205
7.13	Deviation $\Delta\beta_{12}$ of the interaction second acoustic virial coefficient β_{12} from those calculated from the final fit of the site-site intermolecular potential model.	208
7.14	Deviations ΔB_{12} of the interaction second virial coefficient B_{12} of the system carbon dioxide and ethane reported in the literature from those calculated from the MS intermolecular potential model adjusted by means of second acoustic virial coefficients.	209

List of tables.

Table.	Caption	Page.
5.1	Calibration constants of thermometers.	114
5.2	Difference of readings between the thermometers and the standard thermometer.	114
5.3	Calibration coefficients of pressure transducers.	115
6.1	Speeds of sound u in argon at temperatures from 110 K to 450 K and pressures up to 19 MPa.	135
6.2.	Second β_a, third γ_a and fourth δ_a acoustic virial coefficients and second B and third C virial coefficients of argon at temperatures T.	145
6.3	Speed of sound of ethane at temperatures from 220 K to 450 K and pressures up to 10 MPa.	151
6.4	Vibrational relaxation times of ethane at the density of 1 $kg \cdot m^{-3}$.	154
6.5	Acoustic virial coefficients and molar perfect-gas heat capacities at constant pressure of ethane.	155
6.6	Speed of sound of carbon dioxide at temperatures from 220 K to 450 K and pressures up to 14 MPa.	164
6.7	Vibrational relaxation times of carbon dioxide at the density of 1 $kg \cdot m^{-3}$.	165
6.8	Second acoustic virial coefficients and molar perfect-gas heat capacities at constant pressure of carbon dioxide.	169
6.9	Excess half-width Δg and estimated contribution to the excess half-width g_{diff} arising from diffusion for the mixture ethane + carbon dioxide.	172
6.10	Vibrational relaxation times τ_{BA} of the mixture ethane plus carbon dioxide at the density of 1 $kg \cdot m^{-3}$ with the assumption that τ_{AB} is infinite.	175
6.11	Speed of sound of mixture ethane + carbon dioxide at temperatures from 220 K to 450 K and pressures up to 1.2 MPa.	177

Table.	Caption	Page.
6.12	Particular compositions x for each mixture of carbon dioxide plus ethane **obtained** from the values of A_0.	179
6.13	Second acoustic virial coefficients of mixture β_{mix}, interaction β_{12} and pure components β_{aj}, and pseudo-acoustic virial coefficient β_{ii}. The molar perfect-gas heat capacities corresponds to the actual composition of the mixture at each temperature.	181
7.1	Parameters of intermolecular potential model obtained from fitting of second acoustic coefficient of ethane.	201
7.2	Parameters of intermolecular potential model obtained from fitting of second acoustic coefficient of carbon dioxide.	205
7.3	Parameters of intermolecular potential model obtained from fitting of the interaction second acoustic coefficient of the mixture ethane plus carbon dioxide.	207
A1	Compression factor Z, heat capacities $C_{V,m}$ and $C_{p,m}$ of argon in a temperature range from 110 K to 450 K and densities up to 6.8 mol·dm^{-3}.	212
A2	Compression factor Z, heat capacities $C_{V,m}$ and $C_{p,m}$ of ethane in a temperature range from 220 K to 450 K and densities up to 3.3 mol·dm^{-3}.	233

Chapter 1. Introduction

1. Introduction.

The determination of thermodynamic properties of fluids remains an important activity. Traditionally, this task has been considered as one of great value because, on the one hand, the data required are essential for many engineering applications while, on the other hand, they are of real scientific interest. The objective of this work has been the determination of thermodynamic properties of **compressed** gases over a wide range of temperatures and pressures primarily from measurements of the speed of sound. These thermodynamic properties may be of interest for both scientists and engineers.

Chiefly, for engineering design, the availability of reliable thermodynamic (and transport) property data for large numbers of fluids (especially mixtures) in wide ranges of pressures and temperatures is more important rather than the attainment of very high precision. However, in some cases, both availability and precision are important. For instance, the metering of natural gas requires precise and accurate knowledge of the equation of state of the fluid in order to calculate densities and other thermodynamic properties from measurements of pressure and temperature.[1]

On the scientific side, information about how the components of the matter (molecules) interact has been derived in significant part from the thermodynamic behaviour of fluids. Moreover, the link between the macroscopic properties of a medium and the energy of interaction between the constituent molecules is well understood within the framework of statistical-mechanical theory; an important ingredient for application of the theory is then the detailed form of the energy of interaction. A common, though not totally rigorous, strategy is to propose a particular model for the energy function U defined in terms of a few disposal parameters that are later adjusted to fit values of a macroscopic property of the medium. The models used in this approach are designed to represent the relevant physical features of the interaction between a pair of molecules (i.e. the attractive well and repulsive wall) in a simple way. Once a potential is adjusted in that way, other macroscopic properties can be predicted according to the theory with some confidence. Even though rigorous

studies of the intermolecular potential have been followed, the current situation is still far from satisfactory since for many systems the knowledge of the intermolecular potential is severely restricted by poor or imprecise experimental information, or simply because of the lack of any information at all about molecular interactions.

Computer simulations have provided useful means to overcome partially the scarcities of information but they are time consuming and may not reflect with accuracy all physical phenomena which occur in a fluid, e.g. critical behaviour. Thus, it is not possible to rely only upon computer simulations and an experimental effort must be made in order to obtain thermodynamic properties of fluids. Thus, a lot of research has been conducted with the aim of improving the way in which thermodynamic properties are measured. This has led not only to further development of traditional *pVT* techniques,[2] but also to the appearance of new and sophisticated experimental techniques,[3] ranging from light scattering and dielectric-constant measurements to precision acoustic resonators.

In the past fifteen years,[4] a considerable effort has been made to understand in detail all phenomena taking place inside a closed cavity filled with a fluid in which an acoustic field is produced with the objective of utilising these phenomena in the measurement of the speed of sound. The observation of a resonance response of the acoustic field as a function of the frequency of the sound source for a fixed geometry and at specific temperature and pressure, is the basis of the acoustic resonator technique. The precision of the current fabrication techniques has favoured the use of a simple geometry (the sphere) for the resonator in which, besides the favourable ratio of volume to surface, the spectrum of frequency for the lowest normal modes of the cavity consists of a series of sharp and isolated peaks distributed in a totally predicted manner. Moreover, some of the modes have a single component which make them quite attractive to obtain measurements of great precision.

In this research, the speed of sound in several gases was measured by means of a spherical resonator and the theory of acoustic resonators is therefore discussed in the next chapter.

Acoustical measurements present some advantages over the traditional *pVT* measurements. These include the insensitivity of the technique to adsorption effects which, in the past, has been a source of systematic errors so acute at low temperatures

that unreliable pVT results were often obtained. This deficiency can be easily avoided when acoustic measurements are performed and then used to derived pVT data, even at low temperatures and pressures.[5]

As mentioned earlier, the speed of sound is a property related with other thermodynamic properties and therefore highly precise and accurate determinations would give valuable information above the thermodynamic state of the fluid in general and the equation of state in particular.

A combination of highly-accurate experimental data and a suitable method of analysis can provide a powerful tool for determining highly precise and accurate thermodynamic-property data. This connection has been made in this work by means of a numerical integration of the equations that link the speed of sound and the compression factor. Although the gases for which the thermodynamic properties were derived from measurements of the speed of sound are neither particularly complex nor unstudied, the methods developed here can be extremely useful for deriving properties of other less-studied fluids for engineering applications (such as the use of new refrigerant fluids).

In addition, measurements of the speed of sound can be used to determine parameters in models of the interactions between molecules. In this case, one takes advantage of the close relationship between the energy of interaction of the molecules and the macroscopic properties of a fluid. One of these relationships in particular has been quite useful in the past. This corresponds to the relation between the second virial coefficient and the pair-wise energy of interaction. As we shall see, there is also an analogous relationship between the second acoustic virial coefficient and the pair-wise intermolecular energy. This provides a natural way of connecting speed of sound information with the pair-wise intermolecular potential, although the resulting relationship between the second acoustic virial coefficient and the intermolecular potential is more complex than that for the ordinary second virial coefficient.[6] One can say that the need of second virial coefficients can be completely satisfied by measuring the speed of sound along isotherms, especially if enough information is available in the low-pressure range.

The link between the speed of sound u and the thermodynamic state of a fluid follows from the following mechanical relation:

$$u^2 = (\partial p/\partial \rho)_S, \tag{1.1}$$

where p, ρ and S denote pressure, mass-density and entropy respectively. The passage of a sound wave in a fluid is related directly to changes of the pressure and density at constant entropy. If u is known as a function of the temperature and either pressure or density, then equation (1.1) can be integrated to obtain an equation of state for the fluid. Unfortunately, the partial derivative in (1.1) is an isentropic one and so a direct integration procedure is not available and a suitable transformation of this relationship must be used. This is derived by means of standard thermodynamic relationships and is conveniently expressed in terms of the slowly varying quantity known as the compression factor Z. This dimensionless quantity is defined by the relation

$$Z = pM/\rho RT, \tag{1.2}$$

and is of order unity over a very large region of the phase diagram. In equation (1.2), M denotes molar mass, R represents the universal gas constant and T is the thermodynamic temperature. If u and Z are expressed as functions of $\rho_n = \rho/M$ and T, relation (1.1) can be written as:

$$u^2 = (RT/M)\{[Z + \rho_n(\partial Z/\partial \rho_n)_T] + (R/C_{V,\mathrm{m}})[Z + T(\partial Z/\partial T)_{\rho_n}]^2\}, \tag{1.3}$$

where $C_{V,\mathrm{m}}$ is the molar heat capacity at constant volume.

Providing that initial conditions and an auxiliary relationship between Z and $C_{V,\mathrm{m}}$ are available, equation (1.3) can be integrated numerically in the region where speed of sound data are available. A thorough description of how (1.3) was solved (numerically) is presented in chapter three. A simulation of the numerical method employed to carry out the integration is also discussed there with the aim of verify the suitability of that particular method. Furthermore, propagation of errors from the initial conditions and the speed of sound were studied in detail by means of both simulations and an approximate analytical model of error propagation.

Speed of sound information can also be used to infer some features about the forces between molecules. It is common to express u^2 as an expansion in powers of ρ_n, such that the coefficients are only functions of temperature:

$$(u/u_0)^2 = 1 + \beta_a \rho_n + \gamma_a \rho_n^2 + \delta_a \rho_n^3 + \cdots . \qquad (1.4)$$

In (1.4) u_0 is defined as $\lim_{\rho \to 0} u$ and β_a, γ_a, δ_a, ···, are the second, third, fourth, ···, acoustic virial coefficients. As we shall see, these acoustic virial coefficients are related with the ordinary virial coefficients through ordinary differential equations of second order in such way that the *N*th acoustic virial coefficient is expressed in terms of the *N*th and all lower-order volumetric virial coefficients. These relations for the first three acoustic virial coefficients are given in chapter 3. A further discussion about the relationship between the second acoustic virial coefficient, the second volumetric virial coefficient and the pair-wise intermolecular potential is presented in chapter four from the semiclassical point of view. This served to establish a method for obtaining simple semi-realistic intermolecular potential models from values of the second acoustic virial coefficient. These models can then be utilised to predict some thermodynamic properties, for instance, ordinary second virial coefficients. Thus, this is another means of exploiting speed of sound information to obtain thermodynamic properties.

In chapter five a full description of the experimental apparatus and procedure is presented. Chapters six and seven are devoted to the results of the measurements, the derived thermodynamic properties and the pair-wise intermolecular potentials. Finally, the conclusions are given in the closing chapter of the thesis.

References.

1. Younglove, B.A.; Frederick, N.V.; *Int. J. Thermophys.*, **11**, 897 (1989). Daridon, J.L.; Lagourette, B.; Xans, P.; *Fluid Phase Equilibria*, **100**, 269 (1994).

2. Duschek, W.; Kleinrahm, R.; Wagner, W.; *J. Chem. Thermodynamics*, **22**, 827 (1990). Gilgen, R.; Kleinrahm, R.; Wagner, W.; *Int. J. Thermophys.*, **26**, 383 (1994). Holste, J.C.; Hall, K.R.; Eubank, P.T.; Esper, G.; Watson, M.Q.; Warowny, W.; Bailey, D.C.; Young, J.G.; Bellomy, M.T.; *J. Chem. Thermodynamics*, **19**, 1233 (1987).

3. Weber, L.A.; *Int. J. Thermophys.*, **13**, 1011 (1992). Jaeschke, M.; *Int. J. Thermophys.*, **81**, 81 (1987).

4. Moldover, M.; Mehl, J.B.; Greenspan, M.; *J. Acoust. Soc. Am.*, **79**, 253 (1986). Mehl, J.B.; *J. Acoust. Soc. Am.*, **78**, 782 (1985). Mehl, J.B.; *J. Acoust. Soc. Am.*, **79**, 278 (1986). Ewing, M.B.; McGlashan, M.L.; Trusler, J.P.M.; *Metrologia.*, **22**, 93 (1986). Trusler, J.P.M.; *Physical Acoustic and Metrology of Fluids*, 1991, Adam Hilger: Bristol.

5. Ewing, M.B.; Goodwin, A.R.H.; McGlashan, M.L.; Trusler, J.P.M.; *J. Chem. Thermodynamics*, **19**, 721 (1987). Ewing, M.B.; Goodwin, A.R.H.; McGlashan, M.L.; Trusler, J.P.M.; *J. Chem. Thermodynamics*, **20**, 243 (1988). Ewing, M.B.; Goodwin, A.R.H.; Trusler, J.P.M.; *J. Chem. Thermodynamics*, **21**, 867 (1989).

6. Ewing, M.B.; McGlashan, M.L.; Trusler, J.P.M.; *Molec. Phys.*, **60**, 681 (1987).

Chapter 2. Theory of acoustic resonators.

2.1 Introduction

The theory of acoustic resonators as a tool for measurements of the speed of sound has been extensively discussed in the past two decades.[1-4] These discussions have led to the establishment of a highly accurate model for the behaviour of the acoustic field inside an enclosure. The aim of this chapter is to present in a concise but complete way the theory behind the acoustic experiments performed in this work. This theory constitutes the so-called *acoustic model*. The approximations made in deriving this model are considered in detail and have been ultimately justified by the experimental conditions achieved in practice. A very convenient treatment of the phenomena occurring inside an acoustic resonator can be achieved by splitting the problem into the solution of an idealised case plus a series of small perturbations. Thus, in the next sections, an idealised model of the spherical resonator is described first; then, all the correction terms are introduced as perturbations to the simple case.

2.2 Theory of sound.

The objective of this chapter is not to describe in all generality the theory of sound but to give the essential physics of the specific problem in question within a formal theoretical framework. Therefore, a hydrodynamic description of sound compatible with the so-called acoustic approximation is presented below. Further discussion is provided to deal with the case in which this description starts to fail. The theory is then applied to the description of the acoustic field inside a spherical cavity driven by a source operating near to a resonance frequency of the cavity.

2.2.1 Hydrodynamic description of sound.

It is well known that the propagation of sound can be described properly as the propagation of a mechanical wave, which in the case of a fluid initially at rest, corresponds to a series of compressions and rarefactions of the density around an equilibrium value. There small changes in density ρ are also accompanied by small variations in the other thermodynamic variables, i.e. pressure p and temperature T. The total value of each thermodynamic variable will therefore be expressed as the sum

of the equilibrium value and the small variation due to the acoustic cycle. These variations, denoted by a subscript a, are functions of both time t and position $\boldsymbol{r}$. Furthermore, it is assumed that the fluid is initially at rest so that the hydrodynamic or fluid velocity $\boldsymbol{v}$ arises only from the acoustic perturbation. In addition, it will be assumed that all acoustic quantities are small, so that second order terms may be neglected. Then, under those conditions, the equation of continuity for mass correct to leading order in the acoustic variables is[5]

$$(\partial \rho_a / \partial t) = -\rho \nabla \cdot \boldsymbol{v} . \qquad (2.2.1)$$

The equation of motion is derived from the Navies-Stokes equation. Firstly, an expression for the stress tensor Π must be given. Then, from the divergence of this tensor, the total force acting on an element of volume of the fluid can be obtained. It is usual to express Π as the sum of two components: the total pressure $p + p_a$ and the viscous stress tensor Θ. All tensors are of rank two and, since there are three spatial directions x_i (i = 1, 2, 3), each may have up to nine independent components. However, as the total pressure is isotropic, it appears only on the diagonal of the stress tensor while the components of the viscous stress tensor should be functions only of derivatives of $\boldsymbol{v}$ since the viscous force vanishes when the fluid is at rest or in uniform motion.[6] With the above consideration the stress tensor may be written as

$$\Pi_{ij} = -(p + p_a) I_{ij} + \Theta_{ij} , \qquad (2.2.2)$$

where I_{ij} is an element of the unit matrix. For a Newtonian fluid, the viscous stress tensor is given by[6]

$$\Theta_{ij} = \eta[(\partial v_i / \partial x_j) + (\partial v_j / \partial x_i)] + \eta'(\nabla \cdot \boldsymbol{v}) I_{ij} . \qquad (2.2.3)$$

The coefficients of proportionality η and η' are independent of position and only depend upon the thermodynamic state of the system. In (2.2.3), η is associated only with the shear rate of the fluid, and therefore is known as the coefficient of shear viscosity, while η' is associated with both the (rate of) shear strain and the (rate of) compression of the fluid. It is common to rewrite (2.2.3) in terms of a volumetric

viscosity η_b. This is achieved by inspection of the trace of the viscous stress tensor, which turns out to be $(3\eta'+2\eta)\nabla\cdot\boldsymbol{v}$. This trace can be related with the compression of the fluid $(3\eta_b)\nabla\cdot\boldsymbol{v}$. Thus, $\eta'=\eta_b-(2/3)\eta$ and the final expression of Θ in terms of the two viscosity coefficients is

$$\begin{aligned}\Theta_{ij} &= \eta[(\partial v_i/\partial x_j)+(\partial v_j/\partial x_i)-(2/3)(\nabla\cdot\boldsymbol{v})I_{ij}]+\eta_b(\nabla\cdot\boldsymbol{v})I_{ij}\\ &= \eta[(\partial v_i/\partial x_j)+(\partial v_j/\partial x_i)-2(\nabla\cdot\boldsymbol{v})I_{ij}]+[\eta_b+(4/3)\eta](\nabla\cdot\boldsymbol{v})I_{ij}.\end{aligned} \tag{2.2.4}$$

The equation of motion can be obtained easily from

$$(\rho+\rho_a)(d\boldsymbol{v}/dt)=\nabla\cdot\Pi\,. \tag{2.2.5}$$

Combining (2.2.2) and (2.2.4) into one expression, equation (2.2.5) is written as

$$\begin{aligned}(\rho+\rho_a)(d\boldsymbol{v}/dt)=\nabla\cdot\{&-(p+p_a)I_{ij}+[\eta_b+(4/3)\eta](\nabla\cdot\boldsymbol{v})I_{ij}\\ &+\eta[(\partial v_i/\partial x_j)+(\partial v_i/\partial x_j)-2(\nabla\cdot\boldsymbol{v})I_{ij}]\},\end{aligned} \tag{2.2.6}$$

and it can be further reduced, correct to first order in the acoustic variables, to the convenient expression

$$(\partial\boldsymbol{v}/\partial t)=-(\rho^{-1})\nabla p_a+D_{\mathrm{v}}\nabla(\nabla\cdot\boldsymbol{v})-D_{\mathrm{s}}\nabla\times(\nabla\times\boldsymbol{v})\,, \tag{2.2.7}$$

where $D_{\mathrm{s}}=\eta/\rho$ is known as the viscous diffusivity and $D_{\mathrm{v}}=(4/3)D_{\mathrm{s}}+\eta_b/\rho$ is introduced to simplify the subsequent description. A separation of equation (2.2.7) in terms of two special components of $\boldsymbol{v}$ is useful. These components are called the longitudinal $\boldsymbol{v}_{\mathrm{l}}$ and transverse $\boldsymbol{v}_{\mathrm{r}}$ velocity and they are defined by the relationship $\nabla\times\boldsymbol{v}_{\mathrm{l}}=0$ and $\nabla\cdot\boldsymbol{v}_{\mathrm{r}}=0$ with the additional restriction that $\boldsymbol{v}=\boldsymbol{v}_{\mathrm{l}}+\boldsymbol{v}_{\mathrm{r}}$. Resolving the linearised version of the Navies-Stokes equation (2.2.7) into these components of the velocity, a pair of uncoupled equations is obtained:

$$(\partial\boldsymbol{v}_{\mathrm{l}}/\partial t)=-(\rho^{-1})\nabla p_a+D_{\mathrm{v}}\nabla(\nabla\cdot\boldsymbol{v}_{\mathrm{l}}) \tag{2.2.8}$$

and

$$(\partial\boldsymbol{v}_{\mathrm{r}}/\partial t)=-D_{\mathrm{s}}\nabla\times(\nabla\times\boldsymbol{v}_{\mathrm{r}})=D_{\mathrm{s}}\nabla^2\boldsymbol{v}_{\mathrm{r}}\,. \tag{2.2.9}$$

The propagation of sound in a fluid without viscosity or any other dissipation effect can be derived easily from (2.2.1) and (2.2.8) considering that $\boldsymbol{v} = \boldsymbol{v}_l$ ($\boldsymbol{v}_r = 0$ under those conditions) once the relation between ρ_a and p_a is specified. The acoustic cycle is then assumed to take place under reversible adiabatic conditions, therefore all changes are considered to be isentropic: i.e. $\delta\rho = (\partial\rho/\partial p)_S \delta p$ where S denotes entropy. Moreover, all these changes are such that *local* thermodynamic equilibrium is attained immediately. The latter assumption may fail when the time available for the constituents molecules of the fluid to adjust to the thermodynamic variables becomes insufficient, so the fluid can no longer follow the acoustic perturbation. More details of this case will be discussed in a later section.

Thus, a simple equation describing the behaviour of p_a can be obtained from (2.2.1) and (2.2.8) with D_s set to zero and assuming an isentropic relation between p and ρ:

$$[\nabla^2 - (1/u_0^2)(\partial^2/\partial t^2)]p_a = 0, \qquad (2.2.10)$$

where $u_0^2 = (\partial p/\partial\rho)_S$. Equation (2.2.10) is the well known wave equation and u_0 is identified with the propagation speed of the wave in an ideal fluid. This limiting case is useful, even though dissipation effects occur under any experimental conditions. Its importance rests on the fact that, to a first approximation, all the dissipation effects (friction and thermal conduction) appear as an attenuation of the sound leaving, in a wide range of frequencies, the speed of propagation unchanged; i.e. the speed u corresponds closely to u_0. Moreover, both p_a and $\boldsymbol{v}$ can be obtained from a velocity potential function $\Psi(\boldsymbol{r},t)$, by the simple relationships $p_a = \rho(\partial\Psi/\partial t)$ and $\boldsymbol{v} = -\nabla\Psi$; the introduction of this function is useful for the description of the acoustic field inside of a cavity, as shall we see.

As has been mentioned, changes in density bring about variations in pressure. They are also accompanied by changes in temperature since an isentropic compression in a fluid raises the temperature, while an expansion decreases the temperature. Hence, an oscillatory temperature **distribution** is established repeated at the wavelength of the sound. This unavoidably leads to a heat flow tending to equalise the temperature. This heat flow can be described by Fourier's law

$$\boldsymbol{J}_{\mathrm{h}} = -\kappa \nabla T_a , \tag{2.2.11}$$

where $\boldsymbol{J}_{\mathrm{h}}$ is the heat current density and κ is a constant of proportionality called the coefficient of thermal conductivity. A consistent first-order approximation of the equation of continuity for the acoustic heat density $\rho\, q_a$ is then

$$\begin{aligned} \rho(\partial q_a/\partial t) &= -\nabla \cdot \boldsymbol{J}_{\mathrm{h}} \\ &= \kappa \nabla^2 T_a . \end{aligned} \tag{2.2.12}$$

Introducing the acoustic specific entropy s_a, the latter equation can be related with the changes of the other acoustic variables, since in a first-order approximation heat transfer is reversible. Thus, $\mathrm{d}s = \mathrm{d}q/T$ and the rate of entropy production per unit mass is just

$$(\partial s_a/\partial t) = (c_p/T)(\partial T_a/\partial t) + (1/\rho^2)(\partial \rho/\partial T)_p (\partial p_a/\partial t) . \tag{2.2.13}$$

Here c_p is the specific heat capacity at constant pressure. Finally, eliminating q_a from (2.2.12) the equation obeyed by T_a is obtained:

$$D_{\mathrm{h}} \nabla^2 T_a = (\partial/\partial t)\{T_a - [(\gamma - 1)/\gamma \beta] p_a\} . \tag{2.2.14}$$

In (2.2.14) $D_{\mathrm{h}} = \kappa/\rho\, c_p$ is called the thermal diffusivity, γ denotes the ratio of the heat capacities C_p/C_V and $\beta = (\partial \rho/\partial T)_\rho$ is the thermal pressure coefficient.

2.2.2 Propagational, thermal and shear modes.

The usual way in which the set of equations described in the last section is solved will be outlined in this section. This will lead to the establishment of the different modes of propagation for acoustic disturbances and, eventually, to the boundary-layer problems where the dissipation effects become important.

A linear system of partial differential equations, with the six unknown p_a, T_a, ρ_a and the three components of $\boldsymbol{v}_{\mathrm{l}}$, is formed by the five equations, (2.2.1), (2.2.8) and (2.2.14). An extra relationship is required to close the system.

The last equation is obtained by means of the thermodynamic equation of state which interrelates the acoustic contributions p_a, T_a and ρ_a:

$$\begin{aligned}\rho_a &= (\partial\rho/\partial p)_T p_a + (\partial\rho/\partial T)_p T_a \\ &= (\gamma / u_0^2)(p_a - \beta T_a).\end{aligned} \tag{2.2.15}$$

In principle the system of equation can be employed to obtain a unique solution subject to any boundary conditions. However, since ν_l appears rather than the complete ν, the rotational flow described by equation (2.2.9) comes into play only when there are boundary conditions to satisfy. In summary, equations (2.2.1), (2.2.8), (2.2.14) and (2.2.15) can be used to describe the propagation of sound in free space, while the complementary equation (2.2.9) may be needed to give a full description of sound inside of an enclosure.

The remainder of this section will deal with solutions of the equations for the acoustic variables in free space for the particular case in which all acoustic variables have a harmonic dependence in time expressed by $\exp(i\omega t)$, where ω is the angular frequency of the wave. In this case, the action of the operator $(\partial/\partial t)$ can be replaced by the factor $i\omega$ in any equation for the acoustic variables. In addition to this, the acoustic pressure and temperature must be proportional to each other. Hence, p_a should satisfy the Helmholtz equation

$$(\nabla^2 + k^2)p_a = 0, \tag{2.2.16}$$

where k is called the propagation constant. It is convenient to define a dimensionless propagation constant $\Gamma = k/k_0$, where $k_0 = \omega/u_0$ is the propagation constant for the ideal fluid -see equation (2.2.10). In a similar manner to the replacement of the temporal derivative, it is possible to substitute $-k^2$ for the action of the Laplacian operator ∇^2. With these substitutions, the system of differential equations becomes one of algebraic equations among the acoustic variables in terms of the undetermined parameter Γ. These equations reduce readily to the following quadratic equation in Γ^2:

$$\Gamma^4(\gamma\omega^2\tau_v\tau_h - i\omega\tau_h) + \Gamma^2(1 + i\omega\tau_v + i\gamma\omega\tau_h) - 1 = 0. \tag{2.2.17}$$

Here, $\tau_v = D_v/u_0^2$ and similarly $\tau_h = D_h/u_0^2$. As shown in reference [5], the solutions are found to be

$$\Gamma^2 = [-\mathrm{i}/(2\omega\tau_\mathrm{h})][(1+\mathrm{i}\omega\tau_\mathrm{v}+\mathrm{i}\gamma\omega\tau_\mathrm{h} \pm D)/(1+\mathrm{i}\gamma\omega\tau_\mathrm{v})], \qquad (2.2.18)$$

where D^2 is

$$D^2 = (1+\mathrm{i}\omega\tau_\mathrm{v}-\mathrm{i}\gamma\omega\tau_\mathrm{h})^2 + 4\mathrm{i}(\gamma-1)\omega\tau_\mathrm{h}\,. \qquad (2.2.19)$$

Generally, the factors $\omega\tau_\mathrm{v}$ and $\omega\tau_\mathrm{h}$ are much smaller than unity, so a series expansion of D in terms of these small factors is convenient. Retaining the leading terms of this expansion, D may be written as

$$D \approx 1+2(\gamma-1)\omega\tau_\mathrm{h}\omega(\tau_\mathrm{v}-\tau_\mathrm{h})+\mathrm{i}[\omega(\tau_\mathrm{v}-\tau_\mathrm{h})+(\gamma-1)\omega\tau_\mathrm{h}]. \qquad (2.2.20)$$

Then, two solutions of Γ^2 can be obtained by choosing the plus or minus sign of D in equation (2.2.18). The solution corresponding to $-D$ is known as the propagational mode of sound and the corresponding to $+D$ is called the thermal mode. Each of these modes have different propagation constants; they are given by

$$\Gamma_\mathrm{p}^2 = 1-\mathrm{i}[\omega\tau_\mathrm{v}+(\gamma-1)\omega\tau_\mathrm{h}], \qquad (2.2.21)$$

and

$$\Gamma_\mathrm{h}^2 = -\mathrm{i}/(\omega\tau_\mathrm{h})\,. \qquad (2.2.22)$$

Equation (2.2.21) clearly shows that the propagation constant k_p is a complex quantity with a real part equal to k_0 in the first-order approximation, and a small imaginary part. The latter takes into account the dissipation mechanisms present in any fluid and give rise to a coefficient of absorption α for the sound. The thermal mode has a propagation constant k_h with equal real and imaginary parts, so it is highly damped and unimportant in the bulk of the fluid. The main contribution of the thermal mode to the acoustic pressure is found near to a boundary where the propagational mode cannot satisfy on its own all the boundary conditions. Similarly, the transverse velocity becomes important near to a boundary since one of the boundary conditions imposed on the acoustic field is directly related with the total fluid velocity $\boldsymbol{v}$. A

solution to the equation (2.2.9) can be derived easily, when the temporal dependence for v_r is assumed to be the same as before. This is known as the shear mode and the corresponding propagation constant may be written as

$$\Gamma_s^2 = -i/(\omega\tau_s) \tag{2.2.23}$$

where $\tau_s = D_s/u_0^2$.

With the above dimensionless propagation constants Γ_i, it is always possible to express the T_a and v_l in terms of an appropriated p_a. This will be useful for establishing the boundary conditions that a travelling sound wave impinging on a fluid-solid interface has to satisfy. Thus, it is found that for the propagational mode those relationships are

$$\begin{aligned} T_p &= [(\gamma-1)/\gamma\beta]\{1-i\Gamma_p^2\omega\tau_h\}^{-1}p_p, \\ &\approx [(\gamma-1)/\gamma\beta]\{1+i\omega\tau_h\}p_p, \end{aligned} \tag{2.2.24}$$

and

$$\begin{aligned} v_{l,p} &= (i\omega\rho)^{-1}[-1-i\gamma\omega\tau_v+i\omega\tau_v(\gamma-1)\{1-i\Gamma_p^2\omega\tau_h\}^{-1}]\nabla p_p, \\ &\approx i(\omega\rho)^{-1}[1+i\omega\tau_v]\nabla p_p. \end{aligned} \tag{2.2.25}$$

where p_p is the acoustic pressure for this mode. Equations (2.2.24) and (2.2.25), while approximate, are valid in a large range of frequency and for the purpose of this work can they be seen as the exact relationships. For instance, $\mathrm{Im}(\Gamma_p^2)$ is always smaller than $5\cdot10^{-3}$ while the $\mathrm{Re}(\Gamma_p^2)$ remains unity for argon at 170 kPa and 300 K in a frequency range from 5.5 kHz to 14.0 kHz (this frequency range **corresponds** to the actual experimental interval studied for argon under those conditions of pressure and temperature; it is also a representative frequency-range for all the experiments). Similar expressions may be derived for the thermal mode to the same degree of approximation:

$$T_h = -i(\gamma\beta\omega[\tau_v-\tau_h])p_h, \tag{2.2.26}$$

and

$$\boldsymbol{v}_{\mathrm{l,h}} = (\gamma\beta\tau_{\mathrm{h}} / \rho)\nabla T_{\mathrm{h}}\,. \qquad (2.2.27)$$

The contribution to the fluid velocity due to the propagational and thermal modes will be particularly important near to a wall, where boundary conditions imposed on $\boldsymbol{v}$ cannot be satisfied by the propagational mode alone. This feature produces boundary layers where thermal and shear waves are important. It is in these layers that the effects of the thermal conductivity κ and viscosity η play an important role in the description of sound; far away from such a boundary, in the bulk of the fluid, κ and η are taken into account by means of an absorption coefficient α, defined as $-(\omega/u_0)\cdot\mathrm{Im}(\Gamma_{\mathrm{p}})$.

2.2.3 Boundary layers.

The regions, near to a boundary, where all modes become important are called the thermal and viscous boundary layers. In order to illustrate the phenomena consider the following simple case. Assuming that the wavefunction of the thermal mode is represented by a plane wave travelling in the positive x_3 direction with angular frequency ω, the thermal wave is given by

$$T_{\mathrm{h}} = B\exp(\mathrm{i}\omega t - \mathrm{i}k_{\mathrm{h}}x_3)\,, \qquad (2.2.28)$$

where B is a constant and the eigenvalue $k_{\mathrm{h}} = (\omega/u_0)\Gamma_{\mathrm{h}}$ can be written

$$k_{\mathrm{h}} = (1-\mathrm{i})(\omega / 2D_{\mathrm{h}})^{1/2}\,, \qquad (2.2.29)$$

by means of equation (2.2.22). Substituting equation (2.2.29) in (2.2.28), one finds that T_{h} is a highly-damped wave because k_{h} is a complex quantity. The distance in which the effect of this attenuated wave is important is known as the penetration length δ_{h} which is defined in terms of the thermal diffusivity as

$$\delta_{\mathrm{h}} = (2D_{\mathrm{h}} / \omega)^{1/2}\,. \qquad (2.2.30)$$

Finally, the contribution to the acoustic temperature T_{h} arising form this thermal mode can be expressed as:

$$T_{\mathrm{h}} = B\exp[\mathrm{i}\omega t - (1+\mathrm{i})x_3/\delta_{\mathrm{h}}]. \qquad (2.2.31)$$

In a similar manner, the contribution of the rotational part of the fluid velocity v_{r} (the shear mode) is important only over a small range described by a shear penetration length δ_{s}:

$$\delta_{\mathrm{s}} = (2D_{\mathrm{s}}/\omega)^{1/2}. \qquad (2.2.32)$$

At distances from a boundary (or from a source) beyond the penetration length, the fluid velocity is essentially described by the longitudinal component alone. It is not difficult to see that the boundary layers are strongly related with these penetration lengths.

In order to present this connection, it is useful to introduce the concept of the specific acoustic admittance y associated with the surface that divides two mediums. Let it be assumed that Z_i is the acoustic impedance medium i, (i = 1, 2), then $y = Z_1/Z_2$. For a fluid (denoted as medium 1), the acoustic impedance Z is simply the product of the mass density ρ and the speed of sound u. The acoustic impedance for a solid medium, for instance a wall, may be more complicated since the possibility exists of transverse and longitudinal waves with different speeds of propagation. However, we are not interested here in the nature of the waves propagating through the solid medium and the wall may be considered as one of local reaction. By this assumption, the reaction of a point of the wall to a sound wave entirely depends upon the acoustic pressure p_a acting at that point. Thus, the acoustic impedance of the wall Z_a is determined as the ratio of $p_a(\boldsymbol{r},t)$ acting on a specific point $\boldsymbol{r}$ on the surface to the normal component of the fluid velocity $\boldsymbol{v}\cdot\boldsymbol{n}$, where $\boldsymbol{n}$ is the wall-pointing unit vector normal to the surface. With the above definitions, the acoustic admittance y of the surface between a fluid and a wall can be expressed as

$$y = \rho u/Z_a = \rho u(\boldsymbol{v}\cdot\boldsymbol{n})/p_a. \qquad (2.2.33)$$

By and large, the normal component of the fluid velocity can be determined from the acoustic pressure.[5] In spite of the fact that the total fluid velocity $\boldsymbol{v}$ has contributions from the propagational, thermal and shear modes, all effects of the thermal and viscous layers are automatically included in the description. Assuming that the acoustic

pressure corresponds to a plane monofrequency wave then, to a first-order approximation, the contributions to the normal component of the fluid velocity ($\boldsymbol{v}\cdot\boldsymbol{n}$) resulting from the different modes can be derived as follows. Let the position of the interface that separates a fluid from a solid wall be placed at the plane $x_3 = 0$. Now, assuming that a plane wave is travelling in the bulk of the fluid along to a direction perpendicular to x_2 and towards the wall, the acoustic pressure corresponding to the propagational mode is

$$p_{\mathrm{p}} = f_1(x_1) f_2(x_3) \exp(\mathrm{i}\omega t)\,. \tag{2.2.34}$$

Here, f_1 and f_2 are solutions of

$$\nabla^2 f_1 = -k_t^2 f_1, \tag{2.2.35}$$

and

$$\nabla^2 f_2 = -(k - k_t^2) f_2, \tag{2.2.36}$$

where the k_t is the tangential propagation constant and $k = \omega/u$. These equations neglect the small attenuation in the bulk of the fluid associated with the imaginary part of Γ_{p}. Then, the contribution to v_{l} arising from the propagational mode p_{p} can be derived by means of equation (2.2.25). In a similar manner, a contribution to T_{p} is obtained from (2.2.24). In order to ensure continuity in the temperature across the interface, the variations in temperature arising from T_{p} must be cancelled by the appearance of a thermal mode of the type described by (2.2.26) which, at the same time, gives rise to a contribution of the longitudinal part of the fluid velocity as equation (2.2.27) clearly indicates. The two contributions to v_{l}, in the direction of x_3, can be written as

$$(\boldsymbol{v}_{\mathrm{l}}\cdot\boldsymbol{e}_3) = \{(\mathrm{i}/\omega\rho)(df_2/dx_3) - (1+\mathrm{i})(\gamma-1)(\tau_{\mathrm{h}}/\rho\delta_{\mathrm{h}}) f_2(0) \exp[(1+\mathrm{i})x_3/\delta_{\mathrm{h}}]\} f_1 \exp(\mathrm{i}\omega t), \tag{2.2.37}$$

where the first term arises from the propagational mode and the second term from the thermal mode. Here, $\boldsymbol{e}_3$ denotes the x_3-pointing unit vector. In addition, a finite component of $\boldsymbol{v}_{\mathrm{l}}$ in the direction $\boldsymbol{e}_1$ arises from the propagational mode which must be

cancelled out at the interface. This is achieved by introducing a shear wave which will give rise to a finite contribution of the rotational part of the fluid velocity $\boldsymbol{v}_r$. Thus, the components of $\boldsymbol{v}_l$ and $\boldsymbol{v}_r$ along the direction x_1 are the negative of each other and since $\nabla\cdot\boldsymbol{v}_r$ must vanish, the component of $\boldsymbol{v}_r$ in the direction of x_3 can be **expressed** as:

$$(\boldsymbol{v}_r\cdot\boldsymbol{e}_3) = -(1+\mathrm{i})(k_t/k)^2(\omega\delta_s/2\rho u^2) f_1 f_2(0)\exp[\mathrm{i}\omega t + (1+\mathrm{i})x_3/\delta_s]\}. \quad (2.2.38)$$

Since the direction $\boldsymbol{e}_3$ corresponds exactly to the direction of the normal derivative at the interface ($x_3 = 0$) and the total acoustic pressure is just p_a, the following relation between the fluid velocity $\boldsymbol{v}$ and p_a is obtained:

$$(\boldsymbol{v}\cdot\boldsymbol{n}) = (1/\rho\omega)\{\mathrm{i}(\partial p_a/\partial n) - (\omega/u)p_a[y_h + y_s]\}, \quad (2.2.39)$$

where the acoustic pressure and its normal derivative are evaluated at a point on the surface. In equation (2.2.39), the quantities y_h and y_s play the role of admittances which arising from the thermal and viscous boundary layers respectively and are defined by the expressions

$$\begin{aligned} y_h &= (1+\mathrm{i})(\omega/2u)(\gamma-1)\delta_h, \\ y_s &= (1+\mathrm{i})(\omega/2u)(k_t/k)^2\delta_s. \end{aligned} \quad (2.2.40)$$

Finally, by substituting (2.2.39) into (2.2.33), the following result is obtained

$$(1/p_a)(\partial p_a/\partial n) = -\mathrm{i}(\omega/u)[y_0 + y_h + y_s], \quad (2.2.41)$$

where, y_0 denotes the admittance of the wall.

2.3 Acoustic resonator theory.

In this section the theory of acoustic resonators is outlined with special attention to the spherical geometry. Solutions are first developed for an idealised cavity with simplified boundary conditions. Corrections for non-zero admittance of the wall of the resonator and for imperfect geometry are incorporated in the following sections.

2.3.1 Ideal spherical resonator.

The treatment of acoustic resonators can be conveniently accomplished by splitting the actual problem into two parts: the case of an ideal cavity plus a series of correction terms. These correction terms will take into account all the differences that exist between the ideal and a real cavity. Before starting with the description of an ideal spherical cavity (e.g. perfect geometry and rigid) filled with an ideal fluid, let us briefly establish the problem in which the fluid in question is such that dissipation effects may be assumed to be important only inside boundary layers, characterised by the penetration lengths δ_h and δ_s. Moreover, let the acoustic pressure and fluid velocity be described by a velocity potential Ψ as in the case of an ideal fluid. It easy to show that the propagational mode of the acoustic pressure can still be described by a velocity potential.[5]

If it is assumed that $\Psi = \phi(\boldsymbol{r})\exp(\mathrm{i}\omega t)$ then, the equation that the spatial component of the velocity potential ϕ must satisfy is

$$(\nabla^2 + k^2)\phi = 0\,. \tag{2.3.1}$$

The effect of absorption α is included in (2.3.1) through the propagational constant k, since $k = (\omega/u) - \mathrm{i}\alpha$. Furthermore, $\phi(\boldsymbol{r})$ should satisfy a boundary condition that, from the definition of the velocity potential and (2.2.33) can be conveniently expressed in terms of the specific acoustic admittance $y(\omega,\boldsymbol{r}_s)$ of the surface as

$$\begin{aligned}(\partial\phi/\partial n) &= -\mathrm{i}(\omega/u)[y_{sh} + y_h + y_s]\phi \\ &= -\mathrm{i}(\omega/u)y\phi.\end{aligned} \tag{2.3.2}$$

Here, y_{sh} denotes the purely mechanical contribution to the acoustic admittance of the surface and y_h and y_s are additional contributions from the thermal and shear boundary layers given by (2.2.32). The boundary condition (2.3.2) restricts k to be one of a discrete set of values K_N, where N denotes a trio of indices n, l, m, since the wave equation refers to a three-dimension space. It is convenient to introduce a complex frequency F_N as $F_N = f_N + \mathrm{i}g_N$ in which g_N is the half-width. This F_N is related with K_N as:

$$F_N = (u/2\pi)(K_N + \mathrm{i}\alpha)\,. \tag{2.3.3}$$

The case of an ideal spherical cavity of radius a is then quite simple; one just sets the acoustic admittance of the surface equal to zero, i.e. $(\partial\phi/\partial n) = 0$. This corresponds to a perfectly rigid sphere without boundary layers. The symmetry of the problem immediately indicates that the most appropriate approach is to describe $\phi(\boldsymbol{r}) = \phi(r,\theta,\varphi)$ in spherical polar co-ordinates (r,θ,φ) where r is the radial distance from the centre of the sphere which is taken as the origin of co-ordinates, and θ and φ are the polar and the azimuthal angles, respectively. The general solution of the wave equation in spherical co-ordinates is the product of a spherical harmonic with a linear combination of spherical Bessel and Neumann functions. Since the solution of (2.3.1) has to be finite at the origin of co-ordinates, i.e. at $r = 0$, the Neumann functions are rejected and the solution can be written as

$$\phi_N(r,\theta,\varphi) = j_l(\nu_{ln} r / a) Y_{lm}(\theta,\varphi)\,, \tag{2.3.4}$$

where j_l is the spherical Bessel function of order l and Y_{lm} are the well known spherical harmonics. In equation (2.3.4), ν_{ln} represents the nth root of

$$(dj_l/dr)_{r=a} = 0\,. \tag{2.3.5}$$

Equation (2.3.5) is just an expression of the boundary condition (2.3.2) for the ideal spherical cavity and it turns out that all K_N are real quantities; the coefficients ν_{ln} are related with the propagation constant K_{ln} by means of

$$K_{ln} = \nu_{ln}/a = 2\pi f_{ln}/u\,, \tag{2.3.6}$$

where u is the speed of sound in the fluid inside the cavity and f_{ln} is the natural frequency corresponding to the normal mode (l, n). The boundary condition (2.3.1) imposed on the acoustic field results in the only possible free oscillations inside the cavity being combinations of these normal modes. We will see that the response of the cavity becomes resonant when it is driven by an acoustic source tuned to a frequency near to f_{ln}. If (2.3.6) is expressed in terms of the complex frequency F_N, it is clear that $f_{ln} = \nu_{ln}(u/2\pi a)$ and $g_{ln} = g_b = (u/2\pi)\alpha$.

Unfortunately, an accurate description of the cavity requires the introduction of a source that can drive the cavity in forced oscillations, a more realistic boundary condition, and characterisation of the effects of imperfect geometry. These features are described in detail in the following sections. Only a few more remarks are made for the ideal case since they are valid even for a non-perfectly rigid resonator.

For the specific case of a spherical resonator, the allowed modes are determined by the functions (2.3.3); there, all the modes are $(2l+1)$-fold degenerate since for a given l there are $2l+1$ different values of m which corresponding to different spherical harmonics Y_{lm}, and therefore, $2l+1$ functions sharing the same eigenvalue ν_{ln}. This degeneracy exits for all modes except those with $l = 0$. It easy to see that the modes $l = 0$ are purely radial, and they are therefore known as the radial modes and we will denote them by the symbol $(0, n)$; the first radial mode different from zero is for $n = 2$, with an eigenvalue $\nu_{02} = 4.493409$. Extensive tables of the turning points for the spherical Bessel functions are available in the literature with excellent accuracy, and also asymptotic formula exist.[7] The degeneracy of the non-radial modes make them less attractive for accurate determination of the speed of sound since any imperfection in the resonator geometry may lift, at least partially, the degeneracy producing a very complicated superposition of modes. Thus, normally, only the radial modes of a spherical resonator are used to obtain the speed of sound since they do not suffer from degeneracy problems. Nevertheless, some work has been reported in which non-radial modes $(1, n)$ have been measured.[1]

2.3.2 Driven cavity.

Before considering the problem of a real cavity, it is important to incorporate a point-source of sound. The solutions obtained in the earlier section are then modified by the presence of the sound source. Neglecting all transient effects, the solution for the steady-state follows.

The eigenfunctions ϕ_N form a complete set of orthogonal functions and therefore it is useful to express the solution for the driven cavity in terms of this set of solutions. This is exactly the case that has to be solved when a cavity is driven by an infinitesimal source of strength S_ω placed on the inner surface of the cavity at a position $\boldsymbol{r}_0$. S_ω produces sound at an (real) angular frequency ω. The equivalent to the

velocity potential is now $\Psi(\boldsymbol{r}|\boldsymbol{r}_0,t) = S_\omega G_\omega(\boldsymbol{r}|\boldsymbol{r}_0)\exp(\mathrm{i}\ \omega t)$, where $G_\omega(\boldsymbol{r}|\boldsymbol{r}_0)$ is the so-called Green's function. The introduction of a source of that kind modifies (2.3.1) as[5]

$$(\nabla^2 + k^2)G_\omega(\boldsymbol{r}|\boldsymbol{r}_0) = -\delta(\boldsymbol{r} - \boldsymbol{r}_0)\,, \tag{2.3.7}$$

where $\delta(\boldsymbol{r})$ is Dirac's delta function. Equation (2.3.7) clearly establishes that G_ω plays the role of the spatial distribution for the acoustic field which now has a discontinuous solution at the source point. This spatial distribution should satisfy the boundary condition:

$$(\partial/\partial n)G_\omega(\boldsymbol{r}|\boldsymbol{r}_0)|_{r=r_S} = -\mathrm{i}(\omega/u)G_\omega(\boldsymbol{r}|\boldsymbol{r}_0)y(\boldsymbol{r}_S,\omega)\,. \tag{2.3.8}$$

The next step is to express G_ω as an infinite series of orthogonal functions which we select to be the normal modes of the cavity. Thus,

$$G_\omega(\boldsymbol{r}|\boldsymbol{r}_0) = \sum\nolimits_N C_N \phi_N(\boldsymbol{r},\omega)\,, \tag{2.3.9}$$

where the coefficients C_N are to be determined. This can be achieved easily by substituting (2.3.9) in (2.3.7), multiplying by $\phi_M^*(\boldsymbol{r},\omega)\ dV$ and, finally, integrating over the whole space inside of the cavity. The result is[5]

$$G_\omega(\boldsymbol{r}|\boldsymbol{r}_0) = \sum_N \frac{\phi_N(\boldsymbol{r},\omega)\phi_N^*(\boldsymbol{r}_0,\omega)}{V\Lambda_N^0[K_N^2(\omega) - k^2]}\,, \tag{2.3.10}$$

where the boundary condition (2.3.8) has been automatically satisfied since each term of (2.3.10) does so. V and $\Lambda^0{}_N$ denote the volume of the cavity and a normalisation constant respectively. With help of (2.3.10) is fairly easy to obtain the acoustic pressure p_ω since it is obtained by operating on Ψ with $\rho(\partial/\partial t)$. The result is then:

$$p_\omega(\boldsymbol{r}|\boldsymbol{r}_0) = \mathrm{i}\omega\rho S_\omega \sum_N \frac{\phi_N(\boldsymbol{r},\omega)\phi_N^*(\boldsymbol{r}_0,\omega)}{V\Lambda_N^0[K_N^2(\omega) - k^2]}\,, \tag{2.3.11}$$

which it is convenient to rewrite in a more useful form. Starting by recalling that $k = (\omega/u)$–iα and hence, it is clear that the denominator Nth term of the summation can be recast as:

$$\begin{aligned} K_N^2 - k^2 &= [(2\pi/u)F_N - \mathrm{i}\alpha]^2 - [(2\pi f/u) - \mathrm{i}\alpha]^2 \\ &\approx (2\pi/u)^2\{[F_N^2 - f^2] - 2\mathrm{i}g_N[F_N - f]\}, \end{aligned} \tag{2.3.12}$$

from which one can see that $K^2{}_N - k^2$ has a minimum when $f = (\omega/2\pi)$ approaches Re(F_N). The imaginary terms of (2.3.12) prevents the Nth term from becoming infinite but it is nevertheless usually much greater than any other term in the series. This means that only the modes with natural frequency near to f may have a substantial contribution to the acoustic field. Keeping this in mind, it is appropriate to separate from (2.3.11) the small group of M modes close to f and to express the contribution of the remaining modes as a Taylor's series around a frequency f_0 near to f. Making use of the convenient approximation

$$K_N^2 - k^2 \approx (2\pi/u)^2[F_N^2 - f^2], \tag{2.3.13}$$

valid near to the resonance condition, the acoustic pressure can be finally expressed as

$$p_\omega = \sum_{N=1}^{M}\{A_N/[(F_N/f)^2 - 1]\} + B + C(f - f_0) + \cdots, \tag{2.3.14}$$

where A_N, B and C are complex constants. If the cavity is driven near to a well-resolved radial mode, the summation becomes a single term. Thus, by measuring the amplitude and phase of the acoustic pressure as a function of f near to Re(F_N), a non-linear fit of p_ω using as a model a Lorentzian function can be used to determine the constant A_N, B and C together with F_N.[8] From (2.3.14), it is straightforward to show that the points of half-power correspond to the frequencies $f = f_N \pm g_N$; hence the name of half-width given to g_N.

2.3.3 Real spherical cavity.

In this sections we obtain expressions for the complex natural frequencies F_N of a real spherical resonator containing a real fluid. This situation differs from that considered above on several counts. First, the cavity itself may have imperfect

geometry and its walls will certainly yield slightly to the acoustic pressure leading to a non-zero value for y_{sh}. Second, full account will be taken of the boundary conditions leading to the existence of the thermal and shear boundary layers. Finally, it may be necessary to account for openings in the wall of the cavity. All these effects can be combined into a pair of integral equations which relate the eigenfunctions and eigenvalues of the real enclosure to those obtained above for the ideal case.

So far, it has been shown that a fit of (2.3.14) can yield the values of F_N, which turned out to be directly related with u as (2.3.6) clearly shows. However, this simple case is valid only for an ideal cavity driven with a infinitesimal source. Therefore, a little more work is required to obtain the desired model for a real cavity. Nevertheless, the basic framework has been set up to obtain the behaviour of a real cavity as a perturbation expansion around the reference case of the ideal cavity. In this sort of treatment all the conditions of a real cavity that differ from the ideal case can be seen as small "corrections" to the natural (complex) frequencies of the system. Since, this treatment has been described elsewhere[1,4,5,9] in detail, only the results are given here. It is important to recall that the starting point is that of an ideal cavity with eigenfunctions ϕ_N and eigenvalues K_N.

Let the eigenfunctions and the eigenvalues of the real cavity be denoted by Φ_N and k_N respectively. Then, the actual solution for a real cavity with surface S and acoustic admittance $y(\boldsymbol{r}_s)$, is found by solving the following integral equations:

$$\Phi_N(\boldsymbol{r}) = \phi_N(\boldsymbol{r}) - \iint_S \Phi_N(\boldsymbol{r}_s)[(\partial/\partial n)G'_N(\boldsymbol{r}|\boldsymbol{r}_s) + \mathrm{i}(\omega/u)y(\boldsymbol{r}_s)G'_N(\boldsymbol{r}|\boldsymbol{r}_s)]dS\,, \quad (2.3.15)$$

and

$$k_N^2 = K_N^2 + (1/V\Lambda^0_N)\iint_S \Phi_N(\boldsymbol{r}_s)[(\partial/\partial n)\phi^*_N(\boldsymbol{r}_s) + \mathrm{i}(\omega/u)y(\boldsymbol{r}_s)\phi^*_N(\boldsymbol{r}_s)]dS\,, \quad (2.3.16)$$

where

$$G'_N(\boldsymbol{r}|\boldsymbol{r}_s) = \sum_{M\neq N} \frac{\phi_M(\boldsymbol{r})\phi^*_M(\boldsymbol{r}_0)}{V\Lambda^0_M(K_M^2 - k_N^2)}\,. \quad (2.3.17)$$

Equations (2.3.15) and (2.3.16) can be solved simultaneously by an iterative procedure to any desired degree of accuracy. It has to be mentioned that (2.3.15) and (2.3.16) can include corrections for imperfect geometry together with corrections for a more realistic model of the boundary expressed through the acoustic admittance y. A complete development of this approach is give elsewhere.[3,5,9] Here, it will be sufficient to consider the first order approximation to the eigenvalues k_N. In this approximation, Φ_N in equation (2.3.16) is replaced by the corresponding ϕ_N, giving the following result:

$$k_N = K_N + \mathrm{i}(\omega / 2uK_N V\Lambda_N^0) \iint_S |\phi_N(\boldsymbol{r}_s)|^2 \, y(\boldsymbol{r}_s) dS + (1/2K_N V\Lambda_N^0) \iint_S \phi_N(\boldsymbol{r}_s)[(\partial/\partial n)\phi_N^*(\boldsymbol{r}_s)]dS, \tag{2.3.18}$$

In equation (2.3.18), the first term will take into account the contributions due to the finite acoustic admittance of the boundary while the second term accounts for imperfections in geometry. In the following sections, the corrections represented by (2.3.18) are described in detail for the case of radial modes.

2.3.4 Boundary conditions.

In this section we discuss the boundary conditions that the acoustic field must satisfy at the surface of the enclosure. Let us start by listing the boundary conditions. Moldover *et al.*[1] listed the boundary conditions as following: (i) the temperature and heat current should be continuous at the gas-wall interface, (ii) the tangential component of the fluid velocity must vanish at the wall, and (iii) the ratio of the normal component of the velocity to the acoustic pressure should equal the effective acoustic admittance. Conditions (i) and (ii) have been employed for deriving the total fluid velocity $\boldsymbol{v}$ in equation (2.2.31). Therefore, a relationship like (2.2.33) for p_a or its analogous (2.3.2) for ϕ, will merge all boundary conditions in a single expression. However, Ewing *et al.*[4] have shown that at low densities temperature-jump and molecular slip effects take place. Therefore equation (2.3.2) is not exactly correct. Fortunately, these effects are small and can be easily included by a slight modification

of the admittances y_h and y_s. This modification introduces the thermal accommodation length l_h defined by

$$l_h = (\kappa/p)[\pi MT/2R]^{1/2}[(C_{V,m}/R)+1/2]^{-1}[(2-h)/h], \qquad (2.3.19)$$

where h is the thermal accommodation coefficient, M is the molar mass and R the universal gas constant. Normally, l_h is much smaller than δ_h and h is nearly unity. The final expression given in reference [4] for y_h is then

$$y_h = (\omega/2u)(\gamma-1)[(1+\mathrm{i})\delta_h - 2\mathrm{i}l_h] \qquad (2.3.20)$$

correct to leading order in the small ratio l_h/δ_h. A similar expression is found for the corresponding y_s, where a momentum accommodation length l_s and coefficient h_s are defined. However, for radial modes, where the tangential component of the fluid velocity vanishes automatically at the wall, no contribution of the viscous mode is required in order to satisfy (ii). Thus, no molecular slip takes place and y_s is simply zero. This is not the case for non-radial modes, whose tangential fluid velocity is finite and the molecular slip may become important at low pressures.

2.3.5 Acoustic model.

Since, as shown in the previous section, all boundary conditions can be incorporated in an single expression, it is straightforward to derive an expression for the eigenvalues k_N of the real cavity. For the purpose of determining the speed of sound u, only the eigenvalues k_N are required and therefore no further discussion about the eigenfuctions will be given.

Thus, effects due to thermal and viscous boundary layers, the coupling of shell and gas motion and openings in the surface can be incorporated into the previous description through an appropriate expression for the acoustic admittance y. Geometric imperfections may also be incorporated in this description because the last term in the integrals (2.3.18) is related with the geometry of the enclosure through the normal derivative of each normal mode. In addition, the approximation made in deriving (2.3.18) is consistent with all approximations made so far to expressing the total acoustic admittance y. Furthermore, since y is a linear combination of the

different effects taking place in the real cavity, the integral is a linear operation and equation (2.3.18) uncouples imperfections in geometry from the remaining contributions, it is clear that a simple final expression for k_N (or F_N) can be found. This expression is the so-called *acoustic model.*

After performing the integral, making use of the eigenfunctions and eigenvalues of the ideal cavity given by (2.3.4) and (2.3.6), and splitting the acoustic admittance y into y_h, y_s and y_{sh}, the resonance frequencies and their half-widths may be written as:

$$(f_{ln} + \mathrm{i}g_{ln}) = \nu_{ln}(u/2\pi a) + \mathrm{i}g_b + \sum_j (\Delta f_j + \mathrm{i}g_j), \qquad (2.3.21)$$

where the real part of the small "correction" terms have been conveniently expressed as shifts of the resonance frequencies while the corresponding imaginary parts contribute to enlarge the half-width of the resonance (since all $g_j \geq 0$). It has been assumed in performing the integral from which (2.3.21) was derived, that the acoustic admittance is constant over the whole surface. However, for a hole of finite size, this assumption is no longer valid and one has to solve the integral of a nonuniform boundary admittance. This can be achieved by using a boundary perturbation theory, like that described by Moldover *et al.*[1] In this way the corresponding shift to the resonance frequencies due to a hole in the resonator Δf_0, can be calculated and then incorporated into (2.3.21). Separating real and imaginary parts of (2.3.21) we can rewrite formula of f_{ln} as

$$f_{ln} = (u\nu_{ln}/2\pi a) + \Delta f_h + \Delta f_s + \Delta f_{sh} + \Delta f_0 + \Delta f_{geom}, \qquad (2.3.22)$$

and for g_{ln} as

$$g_{ln} = g_h + g_s + g_o + g_{sh} + g_b. \qquad (2.3.23)$$

The complete derivations of the expression for each term in (2.3.22) and (2.3.23) are given elsewhere.[1,5] However, several comments are appropriate here. Firstly, temperature-jump and molecular slip effects have been included in the expressions for Δf_h and Δf_s, respectively. The latter is applied only for non-radial modes -in this work, measurements of mode (1, 1) are reported. The, formula for that are

$$\begin{aligned} \Delta f_{\mathrm{h}} + \mathrm{i}g_{\mathrm{h}} &= \mathrm{i}(u/2\pi a)y_{\mathrm{h}} / [1 - l(l+1)\nu_{ln}^{-2}], \\ -\Delta f_{\mathrm{h}} &= g_{\mathrm{h}}(1 - 2l_{\mathrm{h}}/\delta_{\mathrm{h}}) / [1 - l(l+1)\nu_{ln}^{-2}], \\ g_{\mathrm{h}} &= (\gamma - 1)(f/2a)\delta_{\mathrm{h}} / [1 - l(l+1)\nu_{ln}^{-2}], \end{aligned} \tag{2.3.24}$$

and

$$\begin{aligned} \Delta f_{\mathrm{s}} + \mathrm{i}g_{\mathrm{s}} &= \mathrm{i}(u/2\pi a)y_{\mathrm{s}} / [1 - l(l+1)\nu_{ln}^{-2}], \\ -\Delta f_{\mathrm{s}} &= g_{\mathrm{s}} - (fl_{\mathrm{s}}/a)l(l+1) / [\nu_{ln}^{2} - l(l+1)], \\ g_{\mathrm{s}} &= l(l+1)(f/2a)\delta_{\mathrm{s}} / [\nu_{ln}^{2} - l(l+1)]. \end{aligned} \tag{2.3.25}$$

Note that equation (2.3.25) gives a shift that vanishes when $l = 0$; this corresponds to the definition of radial modes.

By and large, the coupling between shell and gas motion gives rise to one of the most important shifts Δf_{sh}. The mechanical admittance of a spherical resonator y_{sh} has been amply investigated by Moldover *et al.*[1] and Mehl.[8] They have worked out exact relationships for Δf_{sh} in terms of the elastic properties of the shell. These expressions, generally quite complicated, can be simplified since under experimental conditions the motion of the shell is small. For a radial mode, the following expression for y_{sh} can be used for calculating Δf_{sh}:

$$y_{\mathrm{sh}} = \mathrm{i}2\pi f\rho uaC / [1 - (f/f_0)^2], \tag{2.3.26}$$

with C the static compliance of the shell and f_0 is the frequency of the lowest radial resonance of the shell. For a spherical shell of outer radius b, we found

$$C = \frac{1-\sigma}{2[(b/a)^3 - 1]\rho_{\mathrm{w}}u_{\mathrm{w}}^2}\left(\frac{(b/a)^3}{1-2\sigma} + \frac{2}{1+\sigma}\right), \tag{2.3.27}$$

and

$$f_0 = (u_{\mathrm{w}}/2\pi a)\{2[(b/a)^3 - 1] / [(b/a) - 1][1 + 2(b/a)^3]\}^{1/2}, \tag{2.3.28}$$

where σ, ρ_{w} and u_{w} denote Possion's ratio, density and longitudinal speed of sound for the wall material respectively. From (2.3.26), Δf_{sh} can be calculated. Clearly, no

contribution for the half-width g_{sh} is found in this case since y_{sh} has only imaginary part; thus Δf_{sh} becomes:

$$\Delta f_{sh} = -f\rho u^2 C / [1-(f/f_0)^2], \tag{2.3.29}$$

An expression of y_{sh} for non-radial modes is also available.[8] The exact result is more complicated than equation (2.3.26) and thus y_{sh} can only be calculated numerically, unless further simplification are introduced. Nevertheless, Δf_{sh} for non-radial modes behaves in a similar way as it does for radial modes; the correction is proportional to the fluid density and to the frequency. A special case is the mode (1, 1) where the fluid motion produces a net force on the shell. In this case the coupling between the shell and fluid motion makes a contribution to the half-width g_{sh}. This is as result of the damping of the translational motion of the shell and possibly from losses due to radiation from the exterior surface. Although, by an exact treatment, these losses can be incorporated in an appropriate expression for the shell admittance, an alternative and simplified approach may suffice. This consists of modelling the shell vibrations as those of a driven oscillator, moving in the direction of the polar axis and having an effective mass M_{sh} and a damping coefficient b_m. The driven force F_z is identified as the net force exerted by the fluid on the shell. Thus, following the procedure described in ref. [2] for calculating Δf_{sh} and g_{sh} for a force

$$F_z = [-M_{sh}(\omega^2 - \omega_0^2) + i\omega b_m]s_0, \tag{2.3.30}$$

where s_0 denotes the axial displacement of the shell, we obtained the corrections as:

$$\begin{aligned}
\Delta f_{sh} &= fM_{fl}(\nu_{11}^2 - 2)^{-1} M_{sh}[1-(\omega_0^2/\omega^2)]\{M_{sh}^2[1-(\omega_0^2/\omega^2)]^2 + (b_m/\omega)^2\}^{-1}, \\
\Delta f_{sh} &\approx fM_{fl}/(\nu_{11}^2 - 2)M_{sh} \\
g_{sh} &= (b_m/\omega)fM_{fl}(\nu_{11}^2 - 2)^{-1}\{M_{sh}^2[1-(\omega_0^2/\omega^2)]^2 + (b_m/\omega)^2\}^{-1}, \\
g_{sh} &\approx (b_m/2\pi M_{sh}^2)M_{fl}(\nu_{11}^2 - 2)^{-1}
\end{aligned} \tag{2.3.31}$$

where M_{fl} is the fluid mass and $\nu_{11} = 2.081576$. Once again the shift in frequency is proportional to the fluid density.

According to Mehl,[3] imperfections in geometry are of second-order magnitude in a distortion parameter ε. If the inner surface of the cavity is describe by

$$(r/a) = 1 - \varepsilon h(\theta, \varphi)\,, \tag{2.3.32}$$

a perturbation theory can be applied to obtain the shift in frequency Δf_{geom} which will arise from the distortion function h. The most important result is that to a first-order approximation in ε, no shifts are found for the radial modes. Conversely, the imperfection of the geometry do have an effect at that level on the non-radial modes whose components become split lifting the degeneracy at least partially. Nevertheless, this splitting of the non-radial components is not totally arbitrary, since to a first-order approximation in the parameter ε, the arithmetic mean of the frequencies of each separate component remains unaffected for any mode. No contribution to the half-width is found for any mode. If ε is not small, however, a significant Δf_{geom} may affect even the radial modes. Instead of using the very complicated theoretical expression for Δf_{geom} given in reference [3], a simpler approach has been proposed to take into account that corrections, which has proved to be valid as long as the perturbation remained constant.[10] The shift due to imperfection geometry, according to reference [10], is taken into account by the simple introduction of a perturbed value of the eigenvalues $\Delta \nu_{ln}$. These values were determined from the fractional deviations of the speeds of sound obtained from individual modes from their mean value, after allowing for corrections due to the other known perturbations. In this way corrections to the first five radial modes were derived, using argon as a calibration gas. Then, the expression given for shifts due to imperfections in geometry is

$$\Delta f_{\text{geom}} = f_{ln}(\Delta \nu_{ln} / \nu_{ln})\,, \tag{2.3.33}$$

where each $\Delta \nu_{ln}$ has to be obtained from calibration. For the mode (1, 1), f_{ln} is taken as the average of the three components of the mode.

Finally, the correction due to a hole in the resonator can be calculated exactly for radial modes only. This is because the corresponding eigenfunctions are constant over the surface. For a non-radial mode this symmetry is broken and therefore the angular position of the hole becomes important. Obviously, a somewhat different

formula for Δf_0 would be derived for non-radial modes but, since the magnitude of this shift can be diminished by a careful choice of the length and diameter of the hole, it would suffice to use indistinctly the expression obtaining for the radial modes. This expression is

$$\Delta f_0 + \mathrm{i}g_0 = \mathrm{i}(u/2\pi a)y_0 \Delta S/(4\pi a^2). \tag{2.3.34}$$

where ΔS is the area of the cross section of the hole. y_0 can be identified with the input acoustic admittance of a open tube of length L_0 and radius b_0, and according to reference [5], it can be written as

$$y_0 = -\mathrm{i}\cot(k_{\mathrm{KH}} L_0 - \mathrm{i}z_{\mathrm{r}}), \tag{2.3.35}$$

where k_{KH} is the Kirchhoff-Helmholtz propagation constant in a duct and z_{r} is the specific acoustic terminal impedance of the tube. These two quantities are calculated by means of the following relationships:

$$k_{\mathrm{KH}} = (\omega/u) + (1-\mathrm{i})(\omega/2ub_0)[\delta_{\mathrm{s}} + (\gamma-1)\delta_{\mathrm{h}}], \tag{2.3.36}$$

and

$$z_{\mathrm{r}} \approx (\omega b_0/2u)^2 + \mathrm{i}0.6(\omega b_0/u). \tag{2.3.37}$$

Here, z_{r} has been taken to be equal to the acoustic radiation impedance. Hence, with the help of (2.3.35) to (2.3.37) the shift caused by a hole can be accounted for.

2.3.6 Relaxation in gases.

So far, we have assumed that the hydrodynamic description holds everywhere, except, perhaps, in the thermal and viscous layers; there, the hydrodynamic **description** has been corrected by the incorporation of the thermal and momentum **accommodation** lengths to the expression of the acoustic admittances y_{h} and y_{s} respectively. However, when the period of acoustic wave is of the order of magnitude of the **average** collision time between molecules, the thermodynamic variables cannot follow the acoustic cycle and an irreversible change takes place. It is said that part of the wave energy is absorbed by the internal degrees of freedom of a molecule, which become

excited and, after the wave has passed, release the excess energy into the medium in form of heat.

From a macroscopic point of view, the relaxation of an excited internal mode of a molecule would be seen at first as an extra absorption α_{ex}, at the onset of the mentioned molecular lagging, leaving the speed of sound unaffected. However, as the time available to redistribute the energy between internal modes and the translation one becomes shorter, the extra absorption increases and, eventually, the speed of sound departs from the value given by (2.2.10) becoming a function of the frequency, $u(\omega)$. This is known as dispersion and the speed of sound then differs from that related with the thermodynamic state of the fluid. A complete treatment of this problem is described elsewhere.[5,6,11] Here a brief description is presented when a single internal mode **relaxes**. Let it be assumed that the relaxation phenomena can be described by a first order linear differential equation,

$$-(dx/dt) = (x - x_0)/\tau\,, \tag{2.3.38}$$

where x is the property undergoing relaxation towards the equilibrium value x_0 and τ is the relaxation time associated with the particular process.

In the present case, the internal and translational degrees of freedom can be regarded as two independent thermodynamic systems, each of them with a different temperature: T_{int} and T_{tr} respectively. Each of these systems are then relaxing towards the equilibrium temperature T. Under these circumstances, a change in energy dE can be seen as the sum of two contributions: the change of energy corresponding to the internal mode and that corresponding to the translational mode as:

$$dE = (C_V - C_{int})dT_{tr} + C_{int}dT_{int}\,, \tag{2.3.39}$$

where C_V is the (static) total heat capacity and C_{int} denotes the part of the heat capacity arising from the internal mode. The manner in which equilibrium is attained depends upon the specific conditions prevailing in the medium, (e.g. at constant **temperature**). In the present case, both temperatures are relaxing, but for a harmonic **sound wave** of frequency ω they have the same temporal dependence and moreover they are related by

$$(dT_{\text{int}}/dT_{\text{tr}}) = (1+\mathrm{i}\omega\tau)^{-1}, \tag{2.3.40}$$

in which has been assumed that the displacement of the energy with respect to the equilibrium value is small and therefore, the heat capacities can be considered as constant. Then defining a heat capacity $C_V(\omega)$ as function of the frequency as

$$dE = C_{V'}(\omega)dT_{\text{tr}}, \tag{2.3.41}$$

and combining equations, (2.3.39), (2.3.40) and (2.3.41), one **obtains** finally

$$C_{V'}(\omega) = C_V - \mathrm{i}\omega\tau C_{\text{int}}/(1+\mathrm{i}\omega\tau). \tag{2.3.42}$$

A similar expression is derived for the heat capacity at constant pressure $C_p(\omega)$ thus the ratio of these two frequency-dependent heat capacities γ_ω becomes:

$$\gamma_\omega/\gamma = \{1-[\mathrm{i}\omega\tau\Delta/(1+\mathrm{i}\omega\tau)]\} / \{1-\gamma[\mathrm{i}\omega\tau\Delta/(1+\mathrm{i}\omega\tau)]\}, \tag{2.3.43}$$

where $\Delta = C_{\text{int}}/C_p$. It has been shown that the effect of relaxation is included by substituting γ_ω instead of γ in the expression of the propagational constant Γ.[6,9,11] To a good approximation, the ratio $\mathrm{Im}(\gamma_\omega/\gamma)$ to $\mathrm{Re}(\gamma_\omega/\gamma)$ gives the excess absorption per wavelength $\mu = \alpha_{\text{ex}}\lambda$ which from equation (2.3.43) is then

$$\begin{aligned}\mu/\pi &= [\mathrm{Im}(\gamma_\omega/\gamma)/\mathrm{Re}(\gamma_\omega/\gamma)] \\ &= \omega\tau\Delta(1-\gamma)/[1+\omega^2\tau^2(1-\Delta)(1-\gamma\Delta)].\end{aligned} \tag{2.3.44}$$

At the same degree of approximation, it is found that $u(\omega)$ is related with u_0 through the real part of the ratio (γ_ω/γ) as follows:

$$\begin{aligned}(u/u_0)^2 &= \mathrm{Re}(\gamma_\omega/\gamma) \\ &= 1+[\omega^2\tau^2(1-\gamma)(1-\gamma\Delta)\Delta]/[1+\omega^2\tau^2(1-\gamma\Delta)^2].\end{aligned} \tag{2.3.45}$$

Thus, if the relaxation time τ is known, a correction for both speed of sound and absorption can be worked out, assuming that a single internal mode is undergoing relaxation. Whenever the product $\omega\tau$ is a small quantity (corresponding with an incipient

dispersion regime), equations (2.3.44) and (2.3.45) can be approximated with simpler and more useful formulae as follows:[12]

$$\mu/\pi = (\gamma - 1)\Delta\omega\tau + \mathrm{O}(\omega^3\tau^3)\,, \tag{2.3.46}$$

and

$$(u/u_0) = 1 + (1/2)(\gamma - 1)\Delta[1 - (1/4)\Delta(3+\gamma)](\omega\tau)^2 + \mathrm{O}(\omega^4\tau^4)\,. \tag{2.3.47}$$

Normally, the translational and rotational contributions to the dispersion of sound can be neglected since they have small collision numbers, while the collisions numbers that characterise vibrational relaxation may be quite large. Moreover, it is assumed that all vibrational modes of the molecule are strongly coupled, so a description of relaxation with a single apparent relaxation time may suffice and corrections for dispersion of sound can be obtained from either the pairs of equations (2.3.44) and (2.3.45) or (2.3.46) and (2.3.47).

If, on the other hand, it happens that more than one internal mode is excited and they relax independently of each other with different relaxation times, it is still possible to derive the effects on absorption and dispersion of the sound and generalise equations (2.3.43) to (2.3.45). Let it be assumed that n internal degree of freedom are undergoing relaxation with a corresponding relaxation time τ_n and with a contribution to the relaxing part of the heat capacity $C_{\mathrm{int}} = \Sigma_n C_n$. If all these modes relaxes independently from each other (parallel excitation) the ratio γ_ω/γ can be expressed as

$$\gamma_\omega/\gamma = \{1 - \sum_n [\mathrm{i}\omega\tau_n\Delta_n/(1+\mathrm{i}\omega\tau_n)]\} \,/\, \{1 - \gamma\sum_n [\mathrm{i}\omega\tau_n\Delta_n/(1+\mathrm{i}\omega\tau_n)]\}\,, \tag{2.3.46}$$

where now $\Delta_n = C_n/C_{\mathrm{p}}$. The way of calculating both the excess absorption per wavelength μ and the speed of sound in the disperse regime $u(\omega)$ is still the same as that for the single relaxation case but replacing (2.3.46) instead of (2.3.43). So, a **correction** to the frequency f_{ln} corresponding to dispersion Δf_{rel} can be written as

$$-(\Delta f_{\mathrm{rel}}/f) = (u/u_0) - 1, \tag{2.3.47}$$

with (u/u_0) given by (2.3.42), and then included as another correction Δf_j in the acoustic model.

References.

1. Moldover, M.; Mehl, J.B.; Greenspan, M.; *J. Acoust. Soc. Am.*, **79**, 253 (1986).

2. Mehl, J.B.; *J. Acoust. Soc. Am.*, **78**, 782 (1985).

3. Mehl, J.B.; *J. Acoust. Soc. Am.*, **79**, 278 (1986).

4. Ewing, M.B.; McGlashan, M.L.; Trusler, J.P.M.; *Metrologia.*, **22**, 93 (1986).

5. Trusler, J.P.M.; *Physical Acoustic and Metrology of Fluids*, 1991, Adam Hilger: Bristol.

6. Bathia, A.B.; *Ultrasonic Absorption*, 1985, Dover Publications, Inc.: New York.

7. Olver, F.W.; *Royal Society Mathematical Tables Volume 7: Bessel Functions part III, zeros and associated values*, 1960, Cambridge University Press: Cambridge.

8. Mehl, J.B.; *J. Acoust. Soc. Am.*, **64**, 1523 (1978).

9. Morse, P.M.; Ingard, K.U.; *Theoretical Acoustic*, 1968, McGraw-Hill: New York.

10. Zarari, M.; *PhD Thesis*, University of London (1993).

11. Herzfeld, K.F.; Litovitz, T.A.; *Absorption and Dispersion of Ultrasonic Waves*, 1959, Academic Press: London.

12. Trusler, J.P.M.; Zarari, M.; *J. Chem. Thermodynamics*, **24**, 973 (1992).

Chapter 3. Determination of thermodynamic properties of a fluid from its speed of sound.

3.1 Introduction.

In this chapter, the theory which relates the speed of sound with the thermodynamic properties of the fluid is described. The main objective is to show how accurate and consistent thermodynamic properties can be derived essentially from speed of sound data alone.

Usually, speed of sound data have been employed to test the predictive capabilities of an equation of state rather than to extract thermodynamic properties directly. Here, methods are presented which allow not only pVT data but also heat capacities to be determined from the speed of sound by means of a numerical integration. The input data is the speed of sound in the region of interest plus two initial conditions with which to start the integration. These initial conditions may be selected from the three following quantities: the compression factor Z, its derivative with respect to temperature $(\partial Z/\partial T)$ (with either ρ_n and p held constant) and either of the molar heat capacities $C_{V,\mathrm{m}}$ or $C_{p,\mathrm{m}}$, as functions of the independent variable (ρ_n or p) on the initial isotherm. Simulations of the algorithm proposed here confirm the accuracy and stability of this numerical integration technique. This chapter also includes a study of the propagation of errors from both the initial conditions and the speed of sound itself. An approximate analytical solution has also been developed from which the effects of such errors may be estimated easily. This model was found to be in broad agreement with the results of numerical simulations.

3.2 The speed of sound and the equation of state.

The basic equation that links the speed of sound u with the thermodynamic equation of state of the fluid is

$$u^2 = (\partial p/\partial \rho)_S , \tag{3.2.1}$$

where the partial derivative of pressure p with respect to mass density ρ is taken at constant entropy S. Some authors[1] have remarked that the quantity defined by (3.2.1)

should be called the thermodynamic speed of sound in order to distinguish it from the actual propagation speed of sound in the medium. This is because, at finite frequencies, dissipation and sometimes dispersion effects occur. Here, it will be assumed that the thermodynamic speed of sound can always be obtained from the experimental data and no further distinction will be made.

The simplicity of equation (3.2.1) has inspired many authors to use u as a source of information about thermodynamic properties, for instance, to obtain the relationship $p(T,\rho_n)$ between the pressure p, the temperature T and the amount-of-substance density ρ_n. Unfortunately, even if possible a direct integration of (3.2.1) as it stands would produce a relationship of the type $p(S,\rho_n)$, which is not in the desired form. Thus, different strategies have been followed in the past to solve this problem. In some cases, a functional form for $p(T,\rho_n)$ was assumed and the speed of sound used to optimise parameters;[2] in other cases, some approximations were made in respect of some thermodynamic quantities that vary very slowly in a large temperature and density range (e.g. heat capacities) and then an iterative procedure involving speed of sound information was applied to estimate other thermodynamic properties.[3]

In addition, it has been common in the past to consider the low-density regime, where a virial expansion may represent properly the speed of sound. A brief review of the perfect gas limit and the virial expansion is presented here because they have been used as a guide in several stages of the development of this work.

3.2.1 Perfect gas limit.

In this section and in the one following, expressions are derived for the speed of sound in fluids that obey certain simple equations of state. The first of these is the perfect gas model which, while approximate in general, becomes exact in the limit of zero density. In the second case, deficiencies of the perfect gas model are amended by the incorporation of virial coefficients. In order to derive the relationship between the speed of sound u and an equations of state, let u be expressed in terms of the isothermal compressibility $\kappa_T = \rho^{-1}(\partial\rho/\partial p)_T$ and the heat capacities ratio $\gamma = C_p/C_V$:

$$u^2 = \gamma(\rho\kappa_T)^{-1} = (C_p/C_V)(\rho\kappa_T)^{-1}, \qquad (3.2.2)$$

where C_p and C_V are respectively the heat capacities at constant pressure and volume. For a perfect gas both heat capacities have constant values and $\kappa_T = (1/RT\rho_n)$, where R is the universal gas constant. This reduces the equations (3.2.2) to

$$u^2 = (RT\gamma^{\mathrm{pg}}/M), \tag{3.2.3}$$

where M is the molar mass, the superscript pg denotes a perfect gas property and the subscript m denotes a molar quantity. Equation (3.2.3) clearly indicates that, for a perfect gas, u is independent of the pressure and that it is possible to obtain information about the perfect gas heat capacities from measurements of u since

$$\gamma^{\mathrm{pg}} = C_{p,\mathrm{m}}^{\mathrm{pg}}/(C_{p,\mathrm{m}}^{\mathrm{pg}} - R). \tag{3.2.4}$$

This of course requires the knowledge of the molar mass. The accuracy with which $C_{p,\mathrm{m}}^{\mathrm{pg}}$ may be obtained by acoustic methods is often much better than that obtained from the available spectroscopic data.[4] However, the model of a perfect gas has severe deficiencies and a better approximation is to adopt the virial equation of state.

3.2.2 The virial equation of state.

The virial equation of state expresses deviations from ideality by means of a power series expansion in the amount-of-substance density:

$$(p/RT\rho_n) = 1 + B(T)\rho_n + C(T)\rho_n^2 + D(T)\rho_n^3 + \cdots. \tag{3.2.5}$$

The coefficients $B(T)$, $C(T)$, $D(T)$, ⋯ are called the second, third, fourth, ⋯ virial coefficient and they are functions of temperature only. The virial equation may be derived from statistical mechanics and the virial coefficients are then found to arise from interactions in clusters of two, three, four, ⋯ molecules. When equation (3.2.5) is combined with (3.2.2) and powers of ρ_n are collected, the following series is obtained:

$$u^2 = A_0(1 + \beta_a\rho_n + \gamma_a\rho_n^2 + \delta_a\rho_n^3 + \cdots). \tag{3.2.6}$$

Here, $A_0 = RT\gamma^{\mathrm{pg}}/M$ is the speed of sound in the perfect gas and β_a, γ_a, δ_a, ⋯ are known as the second, third, fourth,⋯ acoustic virial coefficients; these too are

independent of density. The acoustic virial coefficients are related to the ordinary virial coefficients through second order ordinary differential equations in such a way that an acoustic virial coefficient depends upon the ordinary virial coefficients of the same and lower order. The relationships for the first few acoustic virial coefficients are as follows:

$$\beta_a = 2B + 2(\gamma^{pg} - 1)T(dB/dT) + [(\gamma^{pg} - 1)^2 / \gamma^{pg}]T^2(d^2B/dT^2), \qquad (3.2.7)$$

$$\gamma_a = (1 - 1/\gamma^{pg})[B + (2\gamma^{pg} - 1)T(dB/dT) + (\gamma^{pg} - 1)T^2(d^2B/dT^2)]^2 + [(1 + 2\gamma^{pg})C + \{(\gamma^{pg})^2 - 1\}T(dC/dT) + 2^{-1}(\gamma^{pg} - 1)^2 T^2(d^2C/dT^2)]/\gamma^{pg}, \qquad (3.2.8)$$

$$\begin{aligned}\delta_a = {} & (3\gamma^{pg})^{-1}[6(\gamma^{pg}+1)D + 2(\gamma^{pg}-1)(\gamma^{pg}+2)T(dD/dT) + (\gamma^{pg}-1)^2 T^2(d^2D/dT^2)] + \\ & [(\gamma^{pg}-1)^2/\gamma^{pg}][B + (2\gamma^{pg}-1)T(dB/dT) + (\gamma^{pg}-1)T^2(d^2B/dT^2)]^2 \times \\ & [2T(dB/dT) + T^2(d^2B/dT^2)] + \\ & [(\gamma^{pg}-1)/\gamma^{pg}][B + (2\gamma^{pg}-1)T(dB/dT) + (\gamma^{pg}-1)T^2(d^2B/dT^2)] \times \\ & [2C + 2\gamma^{pg}T(dC/dT) + (\gamma^{pg} - 1)T^2(d^2C/dT^2)].\end{aligned} \qquad (3.2.9)$$

Equations (3.2.5) and (3.2.6) are in principle exact when an infinite number of terms are retained but only a truncated series is suitable in practice. The number of virial coefficients retained in order to achieved convergence depends upon the conditions of temperature and density. Experience suggests that, with only B, C and D, it is possible to represent p accurately up to densities of roughly half the critical, except near to the critical temperature.[5] For the speed of sound, similar behaviour is observed. For example, it is quite common experience that speed-of-sound data can be fitted along an isotherm, well within their uncertainty, with four acoustic virial coefficients up to densities of roughly half the critical.[6] However, due to the fact that the predictive ability of the virial series deteriorates very rapidly with increase in density, the usefulness of this approach is confined to the low density range - not beyond of one sixth of the critical density. That is the reason why this route is not as attractive as the

one selected in this work for obtaining information of the thermodynamic properties of a fluid from measurements of the speed of sound.

In any case, a significant part of the present knowledge about intermolecular potentials originated from ordinary and acoustic virial coefficient, although in recent years the value of the latter has increased greatly because of advances in experimental technique.

3.2.3 Relationship between the speed of sound and the compression factor.

Several equivalent forms of (3.2.1) or (3.2.2) may be found by standard thermodynamic manipulations depending upon the selection of independent variables. For a pure fluid, there are two interesting choices: one in which the independent variables are (T,p) and the other with (T,ρ_n) as the independent variables. In the rest of this chapter, a transformation of (3.2.2) will be adopted in which the **pressure** is eliminated in favour of the compression factor $Z = p/(RT\rho_n) = pM/(RT\rho)$. This is useful for gases where Z is generally a slowly varying function of the independent variables -be they (T,p) or (T,ρ_n).

The representation (T,ρ_n) will be considered first since it has been thoroughly studied in this work. The approach described will lead to accurate determination of thermodynamic properties from speed of sound measurements in a very broad temperature and pressure range.

Recalling that the molar heat capacities at constant volume and at constant pressure, $C_{V,\mathrm{m}}$ and $C_{p,\mathrm{m}}$, are related through the thermodynamic equation

$$C_{p,\mathrm{m}} = C_{V,\mathrm{m}} + (T/\rho_n^2)(\partial p/\partial T)^2_{\rho_n}(\partial p/\partial \rho_n)^{-1}_T, \qquad (3.2.10)$$

$C_{p,\mathrm{m}}$ may be eliminated from equation (3.2.2) to obtain

$$Mu^2 = (\partial p/\partial \rho_n)_T + (T/C_{V,\mathrm{m}})[(\partial p/\partial T)_{\rho_n}/\rho_n]^2. \qquad (3.2.11)$$

The next step is to eliminate p in favour of Z and, performing all derivatives, one obtains

$$u^2 = (RT/M)\{[Z + \rho_n(\partial Z/\partial \rho_n)_T] + (R/C_{V,\mathrm{m}})[Z + T(\partial Z/\partial T)_{\rho_n}]^2\}. \qquad (3.2.12)$$

Finally, a relationship between $C_{V,\mathrm{m}}$ and Z is required to obtain a closed system of equations. This is obtained from the following Maxwell relationship,

$$(\partial S_{\mathrm{m}}/\partial \rho_n)_T = -\rho_n^{-2}(\partial p/\partial T)_{\rho_n} \ . \qquad (3.2.13)$$

Taking the derivative of (3.2.13) with respect to temperature, reversing the order of differentiation and writing $C_{V,\mathrm{m}}$ for $T(\partial S_{\mathrm{m}}/\partial T)_{\rho_n}$, following expression is obtained

$$(\partial C_{V,\mathrm{m}}/\partial \rho_n)_T = -(T/\rho_n^2)(\partial^2 p/\partial T^2)_{\rho_n} . \qquad (3.2.14)$$

If the pressure is then eliminated in terms of Z one obtains:

$$(\partial C_{V,\mathrm{m}}/\partial \rho_n)_T = -(R/\rho_n)[2T(\partial Z/\partial T)_{\rho_n} + T^2(\partial^2 Z/\partial T^2)_{\rho_n}] . \qquad (3.2.15)$$

It is also possible to recast (3.2.10) in terms of Z with the result that

$$(C_{p,\mathrm{m}}/R) = (C_{V,\mathrm{m}}/R) + [Z + T(\partial Z/\partial T)_{\rho_n}]^2/[Z + \rho_n(\partial Z/\partial \rho_n)_T] . \qquad (3.2.16)$$

Equations (3.2.12) and (3.2.15) may be solved numerically by an initial value Euler method giving both Z and $C_{V,\mathrm{m}}$ inside the region where the speed of sound is known. Further, by means of equation (3.2.16), $C_{p,\mathrm{m}}$ can be determined as well. Details of the numerical methods used, and an analysis of likely errors introduced into the solution from several sources of uncertainty, are given below. For the sake of completeness, the equations which would be derived instead in the representation with (T,p) as the independent variables follow. Once again, starting from equation (3.2.2), expressing $C_{V,\mathrm{m}}$ in terms of $C_{p,\mathrm{m}}$ and introducing Z the equations analogous to (3.2.12), (3.2.15) and (3.2.16) become:

$$\left.\begin{aligned} u^{-2} &= (M/RTZ^2)\{[Z - p(\partial Z/\partial p)_T] - (R/C_{p,\mathrm{m}})[Z + T(\partial Z/\partial T)_p]^2\}, \\ (\partial C_{p,\mathrm{m}}/\partial p)_T &= -(R/p)[2T(\partial Z/\partial T)_p + T^2(\partial^2 Z/\partial T^2)_p], \\ (C_{V,\mathrm{m}}/R) &= (C_{p,\mathrm{m}}/R) - [Z + T(\partial Z/\partial T)_p]^2/[Z - p(\partial Z/\partial p)_T]. \end{aligned}\right\} \qquad (3.2.17)$$

In this representation, Trusler and Zarari have derived Z and both heat capacities of methane from their speed-of-sound measurements.[7] This proved that highly accurate

thermodynamic properties can be derived from equations (3.2.17): the uncertainty of Z was only ± 0.01 per cent while that in the heat capacities was about ± 0.1 per cent.[7]

The set of equations (3.2.12) and (3.2.15) are exact and thermodynamically consistent. Unfortunately, the system of equations is non-linear and therefore an analytical solution is not practical, especially because a functional form of $u(T,p)$ must be given first. However, a numerical solution may be possible as long as a suitable integration method is available.

It must be stressed that since equations (3.2.12) and (3.2.15) have to be solved numerically, the stability of the numerical method should be investigated. This topic is related with the way in which the integration of equations (3.2.12) and (3.2.15) is carried out. Briefly, it has been pointed out that integration of equations (3.2.12) and (3.2.15) is stable as long as either of the following is satisfied:[8] the integration takes place with increasing temperature along paths $\rho_n(T)$ or $p(T)$ that do not rise faster than any isentrope (for instance, along isochores or isobars), or the integration takes place with decreasing temperature along paths $\rho_n(T)$ or $p(T)$ that decline faster than any isentrope.

Although, a method for integrating equations (3.2.12) and (3.2.15) at both subcritical and supercritical temperatures has been designed, it turns out to be more convenient and refined to transform these equations for the subcritical region. The transformation involves new independent variables (T,ϕ), where ϕ is a dimensionless quantity defined as

$$\phi = (\rho_n/\rho_n^{\mathrm{c}})/\mathrm{f}(T)\,, \tag{3.2.18}$$

and ρ_n^{c} is the amount-of-substance density at the critical point. In this work, the function f(T) was chosen such that these paths were parallel to the saturated vapour density $\rho_n^{\sigma}(T)$. Thus, it was proposed that

$$\mathrm{f}(T) = \rho_n^{\sigma}(T)/\rho_n^{\mathrm{c}}\,, \tag{3.2.19}$$

so that lines at constant ϕ in the space (T,ϕ) mapped on to lines falling parallel to the saturation curve in the space (T,ρ_n).

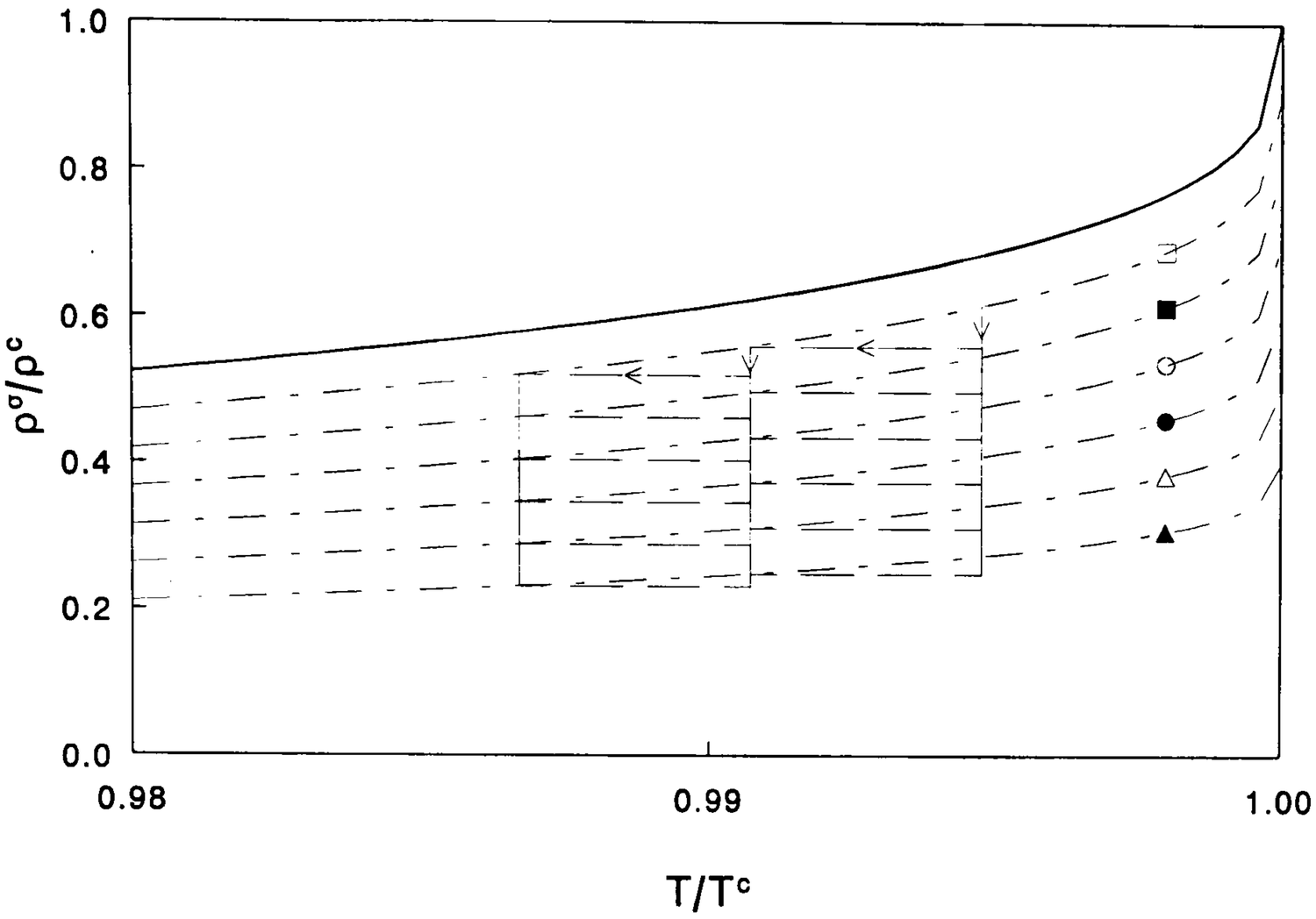


Figure 3.1 Lines at constant ϕ for argon. The function f(T) is obtained from an expression of vapour curve for argon given in reference [9]. (—), saturation curve; (— –), curves at constant ϕ: □, 0.9; ■, 0.8; ○, 0.7; ●, 0.6; △, 0.5; ▲, 0.4. (---), path (along isochores) for the alternative method of integration indicated by the arrows.

As depicted in figure 1, the criterion of stability is satisfied since $(d\rho^{\sigma}/dT) > (\partial\rho/\partial T)_S$. Although figure 1 is based on a correlation of f(T) for simple fluids derived from the principles of corresponding states, it is qualitatively correct for any fluid, so the space (T,ϕ) can be constructed for any system.

To facilitate the use of ϕ as an independent variable in place of ρ_n, the latter was eliminated from equations (3.2.12) and (3.2.15) by means of equation (3.2.18). In order to achieve this, it is necessary to change the direction of all partial derivatives taken at constant density into partial derivatives at constant ϕ. This can be done easily by recalling that, for any variable X depending of density and temperature, a change of the variable held constant can be obtained from

$$(\partial X/\partial T)_{\rho_n} = (\partial X/\partial T)_{\phi} - (\partial X/\partial \rho_n)_T (\partial \rho_n/\partial T)_{\phi}. \qquad (3.2.20)$$

Moreover, it is convenient to introduce a new molar heat capacity, defined by $C_{\phi,\mathrm{m}} = T(\partial S_{\mathrm{m}}/\partial T)_{\phi}$. By means of (3.2.20), the heat capacities $C_{V,\mathrm{m}}$ and $C_{p,\mathrm{m}}$ can be expressed in terms of $C_{\phi,\mathrm{m}}$ as

$$\left.\begin{aligned}
(C_{V,\mathrm{m}}/R) &= (C_{\phi,\mathrm{m}}/R) + T(d\ln f/dT)\{Z + T(\partial Z/\partial T)_{\phi} - \phi T(d\ln f/dT)(\partial Z/\partial\phi)_{T}\} \\
(C_{p,\mathrm{m}}/R) &= (C_{\phi,\mathrm{m}}/R) - T(d\ln f/dT)[Z\{1 + T(d\ln f/dT)\} + T(\partial Z/\partial T)_{\phi}] \\
&\quad + [Z\{1 + T(d\ln f/dT)\} + T(\partial Z/\partial T)_{\phi}]^2 [Z + \phi(\partial Z/\partial\phi)_{T}]^{-1}.
\end{aligned}\right\} \quad (3.2.21)$$

Hence, the system of equations to be solved in the representation (T,ϕ) becomes:

$$\begin{aligned}
u^2 = (RT/M)[&C_{\phi,\mathrm{m}}\{Z + \phi(\partial Z/\partial\phi)_{T}\} + R\{Z + ZT(d\ln f/dT) + T(\partial Z/\partial T)_{\phi}\} \\
&\times\{Z + T(\partial Z/\partial T)_{\phi} - \phi T(d\ln f/dT)(\partial Z/\partial\phi)_{T}\}] \\
&\times[C_{\phi,\mathrm{m}} + RT(d\ln f/dT)(Z + T(\partial Z/\partial T)_{\phi} - \phi T(d\ln f/dT)(\partial Z/\partial\phi)_{T})]^{-1}
\end{aligned} \quad (3.2.22)$$

and

$$\begin{aligned}
-(\phi/R)(\partial C_{\phi,\mathrm{m}}/\partial\phi)_{T} = {} & 2T(\partial Z/\partial T)_{\phi} + T^2(\partial^2 Z/\partial T^2)_{\phi} \\
& - T(d\ln f/dT)\{\phi(\partial Z/\partial\phi)_{T} + T\phi(\partial^2 Z/\partial T\partial\phi)\} \\
& - T^2(d^2\ln f/dT^2)\{\phi(\partial Z/\partial\phi)_{T}\}.
\end{aligned} \quad (3.2.23)$$

Although the integration of the sub-critical region was carried out in the (T,ϕ) space, there is an alternative and equivalent way of performing the integration. Briefly, this alternative method consists of performing the numerical integration with isochoric steps and a negative temperature increment using equations (3.2.12) and (3.2.15). However, following each step, the grid is rescaled so that the greatest density is always a constant fraction of $\rho_{n}^{\sigma}(T)$. This involves a process of interpolation and results in the path sketched in figure 1. The whole procedure is repeated at every single step of the integration and therefore, with the help of this trick, the final results resemble an integration following lines parallel to the saturation curve. Integration in the subcritical region carried out with this alternative method gave essentially the same results as were obtained in terms of the transformed variables ϕ and T.

3.3 Numerical techniques.

This section describes the numerical technique used to obtain the thermodynamic properties of the compressed gas from speed of sound measurements. The method was tested by means of numerical simulations, the results of which are reported. Special attention has been paid to the way in which errors may propagate in the integration procedure affecting the derived thermodynamic properties. One of the most demanding features of the method is the specification of accurate initial conditions.

It has been convenient to separate the integration into two regions, the first for temperatures near and above the critical and the second for temperatures below the critical. The basic numerical methods were however the same in both cases. The underlying reason of this partition is the use of the different paths required for a stable integration. This observation will be further sustained by simulations and by a model for the propagation of errors.

First, a detailed description is given of the algorithm used for the integration. The specification of initial conditions and the method of numerical interpolation used for the speed of sound are both discussed in detail. Second, several tests were performed that show that a predictor-corrector type method allows the integration to be carried out with outstanding accuracy. Finally, a thorough discussion is presented of how likely errors in the source data (initial conditions and speed of sound) may propagate into the derived thermodynamic properties.

3.3.1 Predictor-corrector method.

Equations (3.2.12) and (3.2.15) were solved simultaneously to obtain the compression factor and the heat capacities in the region where speed of sound data were available. Let the region where the speed of sound is known be a rectangle in the variables (T,ρ_n). Moreover, let it be assumed that $Z_0 = Z(T_0,\rho_n)$ and $Z'_0 = (\partial Z_0/\partial T)_{\rho_n}$, are known as functions of ρ_n at the initial temperature T_0 where the integration starts. Then, $(\partial Z_0/\partial \rho_n)_T$ may be calculated by means of a numerical differentiation of Z_0 on the initial isotherm and, using the speed of sound on the same isotherm, $C_{V,\mathrm{m}}$ can be obtained from (3.2.12). Next, $(\partial C_{V,\mathrm{m}}/\partial \rho_n)_T$ is obtained by a numerical differentiation and, finally, $Z''_0 = (\partial^2 Z_0/\partial T^2)_{\rho_n}$ is determined from (3.2.15). At the same time, $C_{p,\mathrm{m}}$ is

determined from (3.2.16). Once Z_0, Z'_0 and Z''_0 are known at the initial temperature and at a series of evenly spaced densities ρ_n, a Taylor's series expansion applied at each density is used to obtain $Z(T_1,\rho_n)$ and $Z'(T_1,\rho_n)$ at $T_1 = T_0+\Delta T$:

$$\left.\begin{aligned} Z(T_1,\rho_n) &= Z(T_0,\rho_n) + \Delta T\, Z'(T_0,\rho_n) + \tfrac{1}{2}(\Delta T)^2 Z''(T=\theta_1,\rho_n), \\ Z'(T_1,\rho_n) &= Z'(T_0,\rho_n) + \Delta T\, Z''(T=\theta_2,\rho_n). \end{aligned}\right\} \quad (3.3.1)$$

Here, θ_i, i =1,2, are temperatures on the interval [T_0, T_1]. The procedure involved first a predictor step in which θ_i was replaced by T_0. This led to estimates of $Z(T_1,\rho_n)$ and $Z'(T_1,\rho_n)$ from which $Z''(T_1,\rho_n)$ was obtained, by the method described above, correct to $O(\Delta T^2)$. Then, Z'' was calculated at the mean temperature $T_m = 2^{-1}\cdot(T_0+T_1)$ and, in the second (corrector) step, equations (3.3.1) were applied again with θ_i replaced by T_m to obtain $Z(T_1,\rho_n)$ and $Z'(T_1,\rho_n)$ correct to $O(\Delta T^4)$ and $O(\Delta T^3)$ respectively. These quantities then served as new initial values for the next step of the numerical integration starting now at $T = T_1$. The entire procedure was repeated until the maximum temperature was reached.

All derivatives with respect to density were determined numerically by finite differences. Generally, the derivative $y'(x)$ of a function $y(x)$ known at evenly spaced ordinates $x_k = k\Delta x$ (k = 1, 2, ···, N) was calculated from the simple 3-point formula

$$y'(x_k) = \frac{y(x_{k+1}) - y(x_{k-1})}{2\Delta x} + O(\Delta x^2) \quad (3.3.2)$$

after dropping the terms $O(\Delta x^2)$. This procedure was applied for all points except $k = N$. At the lowest density (k =1), $y(x_{k-1})$ was set equal to the known value of y (i.e. Z or $C_{l',m}$) in the limit of zero density. At the maximum density ($k = N$) where $y(x_{k+1})$ was unavailable, $y'(x)$ was calculated from the equation

$$y'(x_N) = \frac{4y(x_N) - 7y(x_{N-1}) + 4y(x_{N-2}) - y(x_{N-3})}{2\Delta x} + O(\Delta x^2) \quad (3.3.3)$$

after dropping the terms $O(\Delta x^2)$. This represents a smooth extrapolation of the three-point formula rather than a full four-point finite-difference approximation to $y'(x_N)$.[1]

A variant of this procedure was introduced in order to fully implement the method in the space (T,ϕ). In that representation, equations (3.2.22) and (3.2.23) have to be solved and a calculation of the partial derivative $(\partial^2 Z/\partial T\partial\phi)$ must be included on each isotherm. This can be evaluated by numerical differentiation of $(\partial Z/\partial T)_\phi$ with respect to ϕ, by means of equations (3.3.3) or (3.3.2), subject to the condition $\lim_{\phi\to 0}(\partial Z/\partial T)_\phi = 0$ which follows directly from equations (3.2.18) to (3.2.20). Once the cross derivative was calculated, it was straightforward to determine the second derivative with respect to temperature, $(\partial^2 Z/\partial\phi^2)_T$, in order to carry out the Taylor's expansion and continue with the rest of the procedure.

Any time that equation (3.2.12) was used during the integration, u had to be provided. Two strategies have been followed in the past to give the speed of sound required by (3.2.12) or any of its equivalent thermodynamic expression -for instance, (3.2.2) or (3.2.17). These consist in either smoothing[2,3] or interpolating[7,10] the speed of sound data. When the former is used, either isothermal fits of u are proposed, and hence the integration is restricted to isotherms where u is known[3] or else a double polynomial fit of u in pressure and temperature is performed and it may not be easy to achieve a good fit.[2] These limitations do not occur in the case of two-dimensional interpolation which can be made quite accurate with a suitable spacing of the experimental measurements. In this work, a two-dimension interpolation of u was carried out to provide the information required for the integration algorithm.

---

[1] A Taylor series for $y'(x_{N-1})$ around x_N gives $y'(x_{N-1}) = y'(x_N) + \Delta x y''(x_N) + O(\Delta x^2)$. Assuming then that $y''(x_N)$ can be calculated from a linear extrapolation of the second derivatives $y''(x_{N-j})$, with $j = 1$ and 2, at the middle point between x_N and x_{N-1} as follows:

$$y''(x_N) = y''(x_{N-1}) + 0.5\Delta x\,[\{y''(x_{N-1}) - y''(x_{N-2})\}/\Delta x] = 1.5\,y''(x_{N-1}) - 0.5\,y''(x_{N-2}).$$

Using eq. (3.3.2) to calculate $y'(x_{N-1})$ and a three-point formula to determine the second derivative,

$$y''(x_{N-j}) = 0.5[\,y(x_{N-j+1}) - 2\,y(x_{N-j}) + y(x_{N-j-1})\,]/(\Delta x)^2,$$

the following expressions are obtained:

$$y'(x_N) = y'(x_{N-1}) - \Delta x y''(x_N) + O(\Delta x^2)$$

$$y'(x_N) = (2\Delta x)^{-1}[\,y(x_N) - y(x_{N-2})] + (2\Delta x)^{-1}[\,3y(x_N) - 7y(x_{N-1}) + 5\,y(x_{N-2}) - y(x_{N-3})] + O(\Delta x^2),$$

from which eq. (3.3.3) follows directly after rearranging terms.

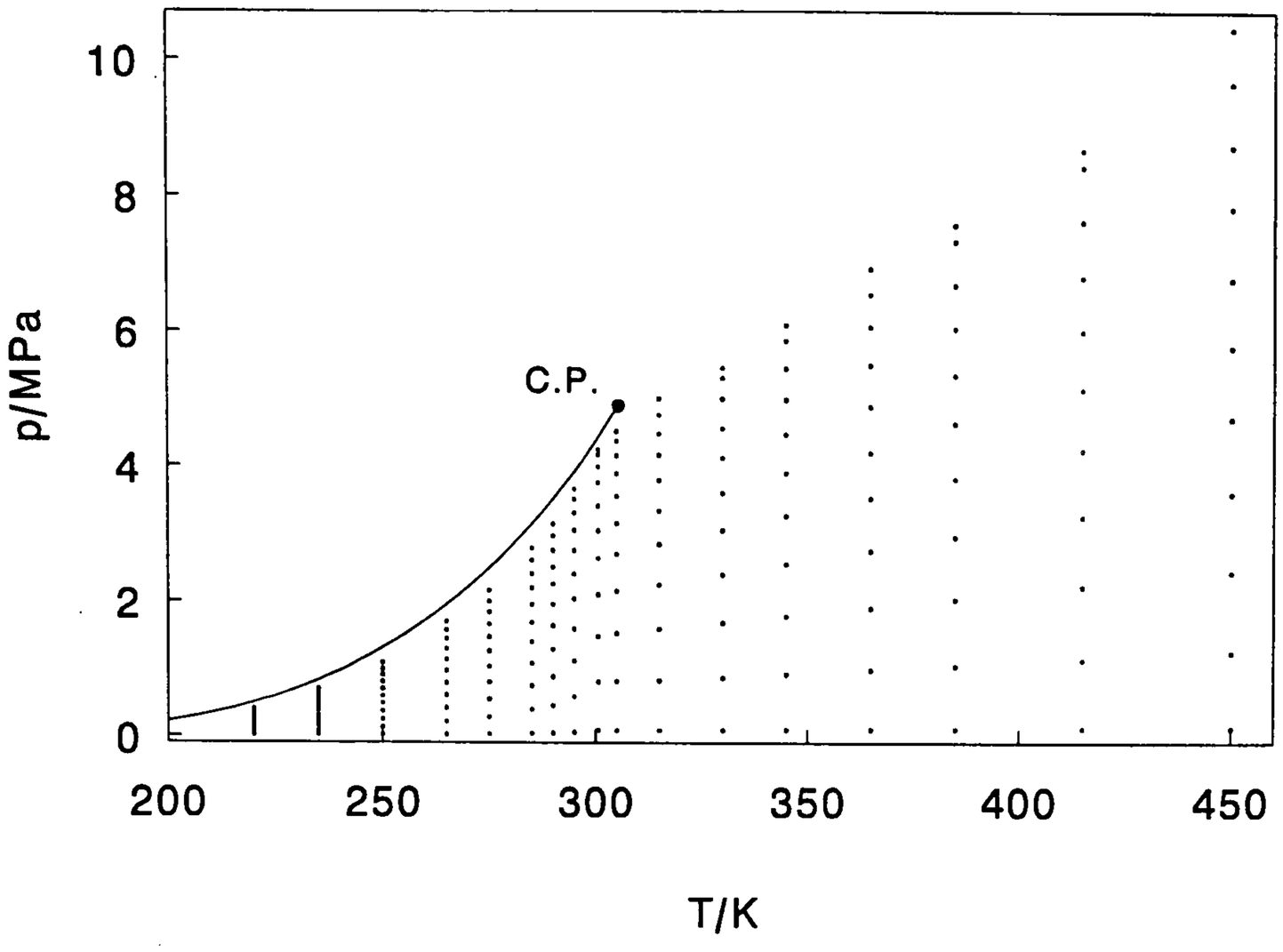


Figure 3.2 Distribution of experimental points (T,p) at which speed of sound was measured in ethane. C.P. denotes the critical point and the solid line is the saturation curve.

Thus, the distribution of experimental points was chosen so that this could be achieved with high precision. The distribution is illustrated in figure 2 for the case of gaseous ethane in the temperature range from 220 K to 450 K.

At temperatures above the critical, the experimental points were chosen to lie approximately on a specified set of isochores while at temperatures in the subcritical region the distributions of points followed paths roughly parallel to the saturation curve.

It is important to note that, even though the experimental quantities were u, T and p, (rather than u, T and ρ_n), the integration could still be carried out with (T,ρ_n) as independent variables because whenever a value $u(T,\rho_n)$ was required, Z had already been evaluated and hence the corresponding (T,p) coordinate could be determined.

3.3.2 Initial conditions.

It must be recalled that the system of equations to be solved was non linear and the initial value method used here to solve them is quite sensitive to small errors in the initial conditions.[7,8] Only one previous attempt at these methods has been reported, in which a numerical integration of equations (3.2.17) was carried out,[7] but there initial conditions were obtained from an analytical equation of state. Here, a method of establishing the initial conditions directly from experimental pVT data is described.

This approach for obtaining the initial conditions at the temperature T_0, i.e. $Z(T_0,\rho_n) = Z_0$ and $Z'(T_0,\rho_n) = Z'_0$, relied upon accurate pVT measurements along several isotherms near to T_0. Details of the source of these data for each of the two substances analysed in this work will be given in chapter 7. Here, the general treatment of initial conditions is presented. Therefore, it is assumed that Z is known, as a function of ρ_n, along $N \geq 2$ isotherms near to T_0. Introducing the notation T_j for these temperatures, $Z_j = Z(T_j,\rho_n)$ will denote the respective compression factors along these isotherms. Rather than seek a correlation of Z_j with temperature, a finite differences approach was applied to obtain Z'_0 from the set Z_j. Let each Z_j be expressed as a Taylor series around T_0,

$$Z_j = Z_0 + Z'_0(\Delta T_j) + \frac{Z''_0(\Delta T_j)^2}{2!} + \frac{Z'''_0(\Delta T_j)^3}{3!} + \cdots, \tag{3.3.4}$$

where $\Delta T_j = T_j - T_0$ and $1 \leq j \leq N$; thus, providing that all the T_j are different, there are N equations of the same kind as (3.3.4). By forming a linear combination of these N equations, each multiplied by a constant α_j, the following relationship was obtained:

$$\sum_{j=1}^{N} \alpha_j Z_j = Z_0 \sum_{j=1}^{N} \alpha_j + Z'_0 \sum_{j=1}^{N} \alpha_j (\Delta T_j) + (Z''_0/2!) \sum_{j=1}^{N} \alpha_j (\Delta T_j)^2 + \tag{3.3.5}$$
$$(Z'''_0/3!) \sum_{j=1}^{N} \alpha_j (\Delta T_j)^3 + \mathrm{O}(\Delta T)^4 .$$

The last term of (3.3.5) represents the truncation error made in each of the individual expansions (3.3.4). The coefficients α_j can be selected to obtain either Z_0 or Z'_0 and to eliminate the first N-1 derivatives in (3.3.5) as is discussed below; this leaves a

truncation error which, in leading order, is proportional to the Nth derivative of Z. In addition, (3.3.5) may give useful information about the precision expected of the initial conditions. The system of equations to obtain the α_j's is linear and for N temperatures it can be written as

$$\left.\begin{aligned}
&\text{(i)}\ \sum_{j=1}^{N}\alpha_j = \begin{cases}1\\0\end{cases}\\
&\text{(ii)}\ \sum_{j=1}^{N}\alpha_j(\Delta T_j) = \begin{cases}0\\1\end{cases}\\
&\text{(iii)}\ \sum_{j=1}^{N}\alpha_j(\Delta T_j)^2 = 0\\
&\vdots\\
&(N)\sum_{j=1}^{N}\alpha_j(\Delta T_j)^{N-1} = 0
\end{aligned}\right\}, \tag{3.3.6}$$

where in (i) and (ii) the upper value corresponds to the solution for Z_0 and the lower one to the solution for Z'_0. It is convenient to express (3.3.6) in matrix form,

$$\boldsymbol{M}\cdot\boldsymbol{a} = \begin{cases}\boldsymbol{b}_1\\\boldsymbol{b}_2\end{cases}, \tag{3.3.7}$$

where $\boldsymbol{M}$ is the following $N\times N$ matrix

$$\boldsymbol{M} = \begin{pmatrix}
1 & 1 & 1 & \cdots & 1\\
\Delta T_1 & \Delta T_2 & \Delta T_3 & \cdots & \Delta T_N\\
(\Delta T_1)^2 & (\Delta T_2)^2 & (\Delta T_3)^2 & \cdots & (\Delta T_N)^2\\
\vdots & \vdots & \vdots & \ddots & \vdots\\
(\Delta T_1)^{N-1} & (\Delta T_2)^{N-1} & (\Delta T_3)^{N-1} & \cdots & (\Delta T_N)^{N-1}
\end{pmatrix}, \tag{3.3.8}$$

and the transpose vectors of $\boldsymbol{a}$ and $\boldsymbol{b}_l$ are given by

$$\begin{aligned} \boldsymbol{a}^{\mathrm{T}} &= (\alpha_1 \quad \alpha_2 \quad \alpha_3 \quad \cdots \quad \alpha_N), \\ \boldsymbol{b}_1^{\mathrm{T}} &= (1 \quad 0 \quad 0 \quad \cdots \quad 0), \\ \boldsymbol{b}_2^{\mathrm{T}} &= (0 \quad 1 \quad 0 \quad \cdots \quad 0). \end{aligned} \tag{3.3.9}$$

Equation (3.3.7) has a unique solution as long as all ΔT_j are distinct. In other words, it is always possible to find a set of $\alpha_j^{(l)}$ which form the solution of (3.3.7) with the independent vector $\boldsymbol{b}_l$. It is also straightforward to study several cases; for instance, $N = 2$, 3, 4, etc. This approach works for any $N \geq 2$ and gives expressions for the initial conditions at least correct to $O(\Delta T^N)$. But it can be seen by (3.3.5) that, at the same time, either Z_0 or Z'_0 has an uncertainty which varies as $\{\sum_j (\alpha_j \delta Z_j)^2\}^{1/2} \approx k_0 \cdot \{\sum_j (\alpha_j Z_j)^2\}^{1/2}$ where δZ_j is the uncertainty of Z_j and k_0 is a fractional uncertainty associated with experimental values Z_j and is assumed to be constant. With the best experimental technique,[11] k_0 might be of the order of $2 \cdot 10^{-4}$. Since Z_j is close to unity and all α_j are of the same order of magnitude, the above uncertainty **turns** out to be roughly proportional to $N^{1/2}$ and it therefore has a minimum for $N = 2$. In fact, for a typical value of k_0, this uncertainty can be regarded as the actual accuracy of the derived initial conditions. Thus, as N become larger, the effect of the experimental uncertainty grows and, although the truncation error declines in theory, there is no improvement in the overall accuracy. This situation is illustrated in figure 3 where the uncertainty is plotted for $N = 2$ together with an estimate of the contribution of the first two neglected derivatives, which correspond to the truncation error the one initial condition or the other. It is clear that in order to implement the above treatment and obtain accurate initial conditions to a higher order in ΔT, k_0 needs to be smaller than it typically is. In other words, for the sort of experimental errors found in pVT data so far, the value of the truncation error associated with $N = 2$ is of only marginal significance. Thus, inclusion of more temperatures in order to eliminate higher derivatives of Z would lead to only a marginal reduction of the overall uncertainty at best.

Based in these observations, it was decided that the only real alternative was to adopt $N = 2$, and if this was unsatisfactory, then some other source of information would be required.

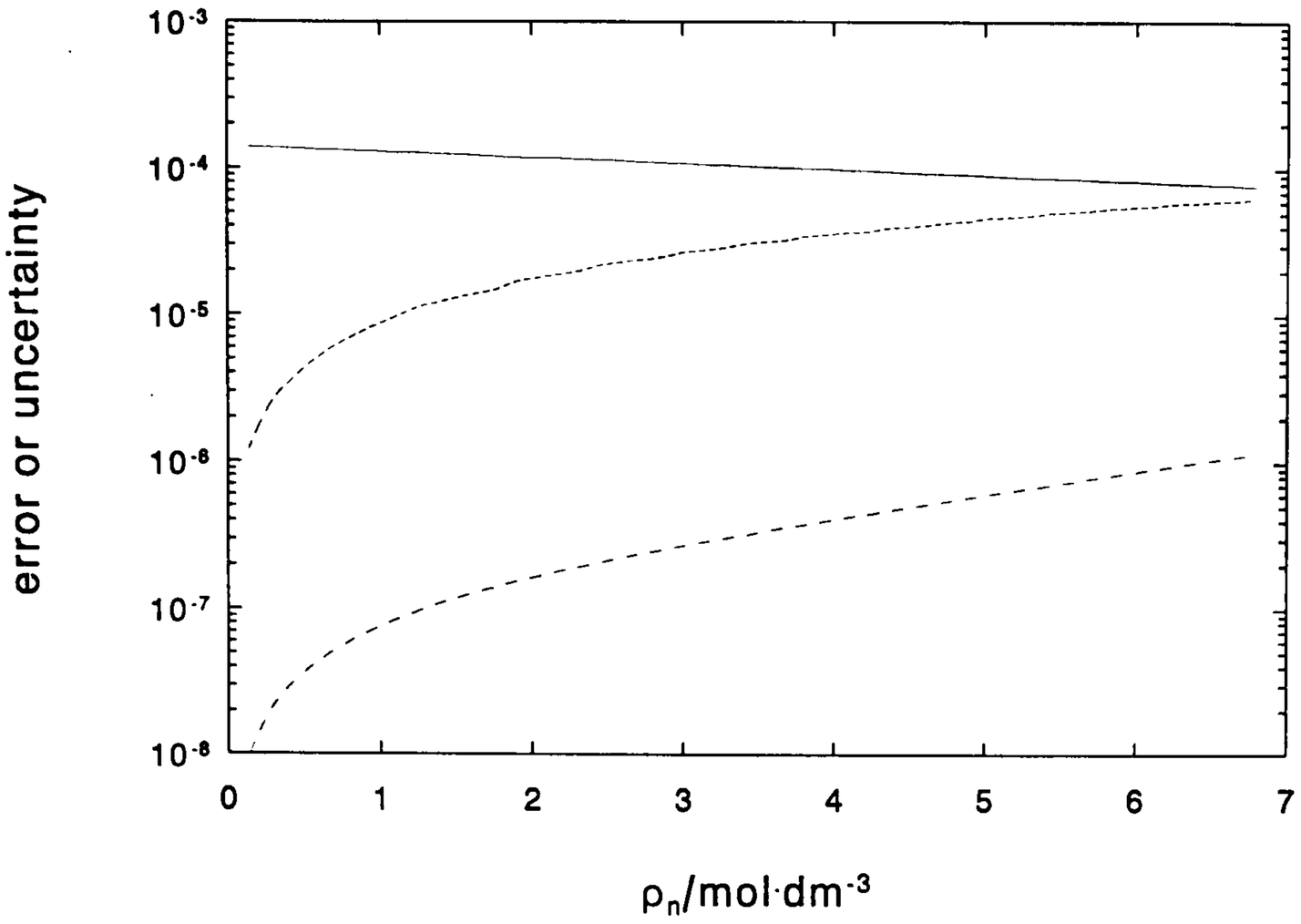


Figure 3.3 Estimated **uncertainties** and truncation errors on initial conditions for the case $N = 2$ of argon. (—), estimated uncertainty of either Z_0 or $Z_0'(\Delta T)$; (---), leading term of the truncation error of Z_0 arising from equation (3.3.5), $|Z_0''/2|(\Delta T)^2$; (····), leading term for Z_0', which is $|Z_0'''/6|(\Delta T)^2$ for the symmetrised-case $N = 2$.

The case $N = 2$ is also interesting as it is the simplest and, in addition, if T_0 is chosen as the average temperature of T_1 and T_2, then $\Delta T_1 = -\Delta T_2 = \Delta T$ and, even when the truncation error in (3.3.5) becomes $O(\Delta T^2)$ for both Z_0 and Z'_0, one more derivative has been cancelled out for the latter. Furthermore, $\boldsymbol{a}^{(1)} = (0.5, 0.5)$ and $\boldsymbol{a}^{(2)} = (1/\Delta T)\cdot(0.5, 0.5)$.

Substituting these vectors in (3.3.5), the final expressions for the initial conditions can be written as,

$$\begin{aligned} Z_0 &= (Z_2 + Z_1)/2 - (Z_0''/2!)(\Delta T)^2 + O(\Delta T)^4 \\ &= (Z_2 + Z_1)/2 - [Z''(T_0 + \xi_2 \Delta T, \rho_n) + Z''(T_0 - \xi_1 \Delta T, \rho_n)]/4 \end{aligned} \tag{3.3.10a}$$

and

$$Z_0' = (Z_2 - Z_1)/(2\Delta T) - (Z_0'''/3!)(\Delta T)^2 + O(\Delta T)^4$$
$$= (Z_2 - Z_1)/(2\Delta T) - [Z'''(T_0 + \zeta_2 \Delta T, \rho_n) + Z'''(T_0 - \zeta_1 \Delta T, \rho_n)]/12, \quad (3.3.10.b)$$

where ξ_i and ζ_i are numbers in the interval (0,1). Although equations (3.3.10) are exact (in any of the two equivalent expressions), we have no knowledge of ξ_i, ζ_i on the right hand side of (3.3.10). Thus, some approximations must be made. First at all, ξ_i and ζ_i were set equal to zero, so the truncation error was proportional to $-Z_0''/2$ and to $-Z_0'''/6$ for Z_0 and Z'_0 respectively. With this degree of approximation a first attempt was made to obtain the thermodynamics properties of the gas, and the results were compared with accurate pVT data. Quantitative details of the results achieved with that approximation are given in chapter 7. Here, a qualitative discussion of the results and their implication are presented. This will serve to show the consequences of the procedure. For this purpose, Z_j was smoothed by means of a four-degree polynomial in density (the constant term was unity) and this usually gave a very precise representation of each Z_j up to densities slightly greater than half the critical

Firstly, it was noticed that the integration routine did not reproduce either Z_2 or Z_1 within the precision with which both were determined -normally $10^{-5} \cdot Z_j$. In fact a small but systematic deviation of the derived Z_1 and Z_2 was found with a nearly linear dependence on density at the two temperatures T_1 and T_2. As the temperature was further incremented, the agreement with the pVT data at first became closer. This particular feature pointed to a systematic error in the values of Z_0 (this suggestion was supported by simulations results described in more detail below).

Late, the disagreement with the pVT data increased reaching a maximum at about 50 K above T_0 where it was about twice the experimental uncertainty in the pVT data. Once again, this systematic pattern can be explained in terms of an inaccurate determination of Z'_0. Therefore, these features suggested that this rough approximation, though giving good results, was not the best one and that both Z_0 and Z'_0 needed to be improved.

Therefore, another source of information was required to overcome this situation. It was noticed that a correction to Z_0 can be obtained from values of the speed of sound. Using the truncated equations (3.3.10) as the initial conditions and combining them with (3.2.12) and (3.2.15), it is possible to estimate Z'' at T_0. This

term is then added to (3.3.10a), still keeping ξ_i equal to zero. A second integration was then performed and, with only this correction, Z_1 and Z_2 were successfully reproduced. However, as the temperature rose, the same pattern found previously appeared essentially unchanged. This reinforced the assumption that the origin of these systematic deviations was an error in Z'_0. Unfortunately, there is no analogous way to correct Z'_0. However, any systematic error in Z'_0 would be consistent with a polynomial in ρ_n with leading term $b\rho_n$, since each Z_j has been fitted by a polynomial in ρ_n with a constant term of unity. Thus, we had to rely on the introduction of a free parameter to adjust the initial values of Z'_0 obtained from the truncated equation (3.3.10b). It was proposed that small differences may be taken into account by incorporating a term proportional to Z'_0 itself. This empirical correction is much less significant for polyatomic gases in which $C_{V,\mathrm{m}}$ is larger than for the case of a monatomic gas such as is argon because the **accuracy** required of Z'_0 is then much less. Thus, Z'_0 was estimated from the formula

$$Z'_0 = [(Z_2 - Z_1)/(2\Delta T_2)](1 + K)\,, \qquad (3.3.11)$$

and K was adjusted to obtain agreement with pVT data on a third isotherm. The value of K determined in that way was so small that the agreement with the two initial isotherms was maintained.

3.3.3 Interpolation of the speed of sound.

As mentioned above, speeds of sound were required at each grid point of the integration characterised by the pairs of co-ordinate (T,ρ_n) or (T,ϕ). For instance, for the usual $|\Delta T|$ of 0.5 K (or 0.01 K at temperatures below T^{c}) and fifty lines at constant of ρ_n (or ϕ), which are fully discussed below, an integration over 1 K would require something like 100 (or 5000) grid-points. It is then evident that an efficient routine to obtain u by a two-dimensional interpolation of the experimental values was required. However, rather than interpolate u itself, it turned out to be more convenient to introduce an intermediate function F that varies more slowly than does u itself. This function was defined by the relation

$$F = (u/u_0)_{\mathrm{exp}} / (u/u_0)_{\mathrm{eos}}, \qquad (3.3.12)$$

where u_0 is the speed of sound in the limit of zero density given by (3.2.3), and subscripts denote properties obtained from either experiment (exp) or an equation of state (eos). For both systems studied in this work, $(u/u_0)_{eos}$ was obtained from the equation of Stewart and Jacobsen.[12] The ratio F was tabulated at each of the experimental state points and, once interpolated to the required state point, the speed of sound was recovered from the relation

$$u = (u/u_0)_{eos}(u_0)_{exp} F . \qquad (3.3.13)$$

This method presented the following advantages. First, F is a smooth and slow-varying function of p and T inside the whole experimental region and never deviates from unity by more than $2.6 \cdot 10^{-2}$. Second, the limit of $u \to u_0$ as $p \to 0$ is achieved exactly while (u/u_0) agrees exactly with $(u/u_0)_{exp}$ at each of the experimental state points. In the case in which u_0 is known exactly, i.e. a noble gas, $(u_0)_{exp}$ is replaced by the actual value at any temperature. Otherwise, a fit of $(u_0)_{exp}$ as a polynomial in T would be accurate enough to describe properly the limit of zero pressure in the whole temperature range.

Even though F is a fairly slowly varying function of (T,p), it proved to be useful to change variables from (T,p) to (τ,ω) defined by

$$\left.\begin{aligned} \tau &= 1/T \\ \omega &= \rho_n^{eos}(T,p)/\rho_n^{c} \end{aligned}\right\} , \qquad (3.3.14)$$

where ω is a reduced density calculated from an equation of state at the state point specified by (T,p). Thus, in practice the two dimension interpolation of u was carried out from data of a table of $F(\tau,\omega)$. To improve the computational efficiency, a partial interpolation in ω was first performed on each isotherm by means of 6-point Lagrange formula. This leads to values of F on each of the isotherms with even spacing $\Delta\omega = 0.004$, in place of the unevenly spaced experimental points with $\Delta\omega \approx 0.05$, and a table of these values was used routinely. Further interpolation with respect to ω required only a 2-point formula for a truncation error not exceeding $10^{-6} \cdot F$.

Interpolation with respect to τ at constant ω was then performed by means of the 6-point Lagrange formula.

Thus, it seems that interpolation in ω involved negligible additional uncertainty given the spacing of the experimental speeds of sound on each isotherm. Comparison for argon with the results of a 5-point interpolation reveal noticeable ripple only near to the greatest density on the isotherm closest to the critical point; even here the ripple only amounted to about $1 \cdot 10^{-5}$ in the function F. However, similar comparisons for the interpolation over τ, reveal ripple of about $8 \cdot 10^{-6}$ over a substantial region of the surface, except once again near to the critical temperature at the maximum density where the ripple increased to about $20 \cdot 10^{-6} \cdot F$. Although this is still too little to affect the derived compression factors by more than $7 \cdot 10^{-5}$, there are some noticeable consequences for the heat capacities which are discussed in more detail below.

In order to get a regular grid for the function F extending up to $\omega = 0.5$ at each value of τ, extrapolations were sometimes necessary from the maximum reduced density actually obtained ω_{max}. When the difference $(0.5 - \omega_{max})$ was small, (no more than $0.05 \cdot \omega_{max}$) a straightforward extrapolation of u was carried out by simply completing the table of F along the isotherm between ω_{max} and 0.5 with the last interpolating polynomial. However, not surprisingly, extrapolations were sensitive to the reduced density range that had to be completed. Figure 4 shows that there is a risk of obtaining a deficient extrapolation when a simple polynomial is used. This is entirely based on observations of how F behaves as a function of T and ρ_n. In order to overcome this potential difficulty, an extrapolation based in a rational polynomial approximation was used in practice. In figure 4, the function F is plotted for two consecutive experimental isotherms; one of them represented u up to half of the critical density while the other has been extended by both a simple extrapolation and by a rational polynomial extrapolation. It is clear that the latter, at least, has the expected behaviour, though is not possible to ensure that the extrapolated values of u were as accurate as those obtained by interpolation. The rational approximation used was

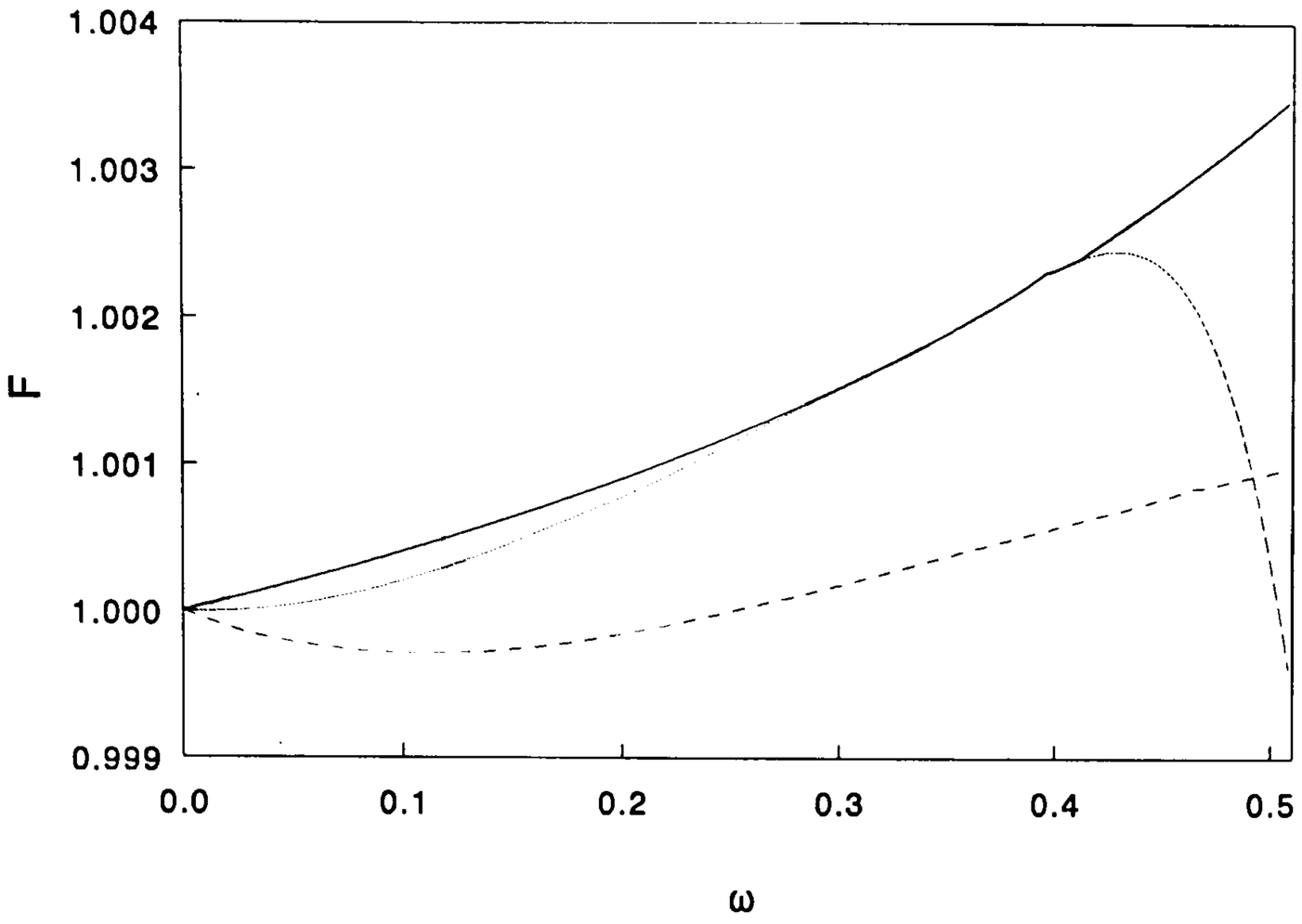


Figure 3.4 Function F along two isotherms for argon. (····), F at $T = 350$ K (no extrapolation); (---), polynomial extrapolation of F at 400 K; (—), rational polynomial extrapolation of F at 400 K with $n = 2$.

$$R(\omega) = P_{2n}(\omega) / Q_{2n}(\omega)$$
$$= [1 + a_1\omega + a_2\omega^2 + \cdots + a_n\omega^n] / [1 + b_1\omega + b_2\omega^2 + \cdots + b_n\omega^n]. \quad (3.2.15)$$

This selection produced a very smooth representation of F which had the same trend in the approach to $\omega = 0.5$ as found on the **remaining** isotherms where there was experimental data available up to $\omega_{max} = 0.5$.

Furthermore, the coefficients where adjusted in such a way that $R(\omega)$ passes exactly through the $2n$-greatest points of F. Extrapolation in this way prevents a very rapid change of F which could be found otherwise if the 6-point interpolation formula were used.

Normally, the degree $n = 2$ or 3 was selected depending upon how large the extrapolation range was. The switch from the polynomial interpolation formula to the rational extrapolation was set at ω_{max} in order to match the value of u on both sides of that point. Moreover, the poles of the rational functions were analysed to guarantee

that they were outside of the range $\omega_{max} \leq \omega \leq 0.5$. This ensures continuity of F, and also of u, along any isotherm in the whole domain of (τ,ω).

3.4 Test of numerical method.

There are two important features that one has to be aware of when selecting a numerical method to solve equations (3.2.12) and (3.2.15): the efficiency and the stability of the method.

The efficiency of the procedure is determined mainly by the algorithm designed to solve the problem. For complex calculations, lack of efficiency may become an acute problem especially if there are limited computational resources. The predictor-corrector method proposed to solve equations (3.2.12) and (3.2.15) can be implemented easily with the advantage that it does not required great computational resources. In the present case, efficiency was not a real concern.

Conversely, stability of the numerical integration is a potentially more serious matter. It may happen that for a given problem a particular numerical method fails to converge into a solution, or it may be quite susceptible of small errors such as truncation errors or other sources of uncertainty. Thus, stability is associated with the feasibility of a numerical method. It is also strongly related with the way in which errors might propagate during the calculations. These two matters, related with stability, have been amply studied.

3.4.1 Simulation of the numerical method: size of steps.

Since in the current predictor-corrector method employed to integrate equations (3.2.12) and (3.2.15), the solution is developed in discrete steps, each obtained from the solution at an earlier stage, the question arose of whether the method might remain stable. Furthermore, all quantities involved in the method are calculated numerically and therefore truncation errors will always exist to a greater or lesser extent. Hence, the tolerable level for this class of error must be considered. These errors are strongly related to the size of the step for both variables (T,ρ_n) or (T,ϕ).

Therefore, a scheme was developed in order to give answers to the questions: simulation of the numerical method. This simulation was able to test the stability of the method in a very broad sense, i.e. it also tested the reliability of the method.

Moreover, the simulation was a way of finding optimum values of the necessary parameters such as the spacing of densities and the size of the temperature increments. It also provided a valuable source of information about how likely errors in the initial conditions might propagate into the solution and how significant might be the integration path.

In the simulations, speeds of sound and initial conditions were calculated from the equation of state of Stewart and Jacobsen[12] and the results of the integration were compared with values calculated from the same equation. The first aspects studied were the required values of the temperature increment and the spacing in ρ_n or ϕ. Since both the initial conditions and the speed of sound were exact and consistent within the simulation, any deviation of the derived properties from those predicted by the equation of state must have their origin in the method itself. One can claim that if, with an adequate choice of both the temperature increment and the spacing in density, the deviations become negligible then the method is intrinsically stable. From our calculations, we found that for densities up to half of the critical, at least thirty isochores are required in order to achieve a truncation error in $\rho_n(\partial Z/\partial \rho_n)_T$ no greater than 10^{-5}. More than thirty isochores would then yield a much smaller truncations error for equations (3.3.2) and (3.3.3) but would also require more computation time. An **acceptable** compromise between between speed and accuracy was found with fifty isochores and this kept errors in $|\rho_n(\partial Z/\partial \rho_n)_T| < 10^{-6}$.

The simulations were performed over an interval of **reduced** temperature (T/T^c) ranging from slightly below 1 up to nearly 3, and the temperature increment ΔT was in the range 2 to 0.1 K. An increment ΔT of 0.5 K was found to be small enough to give negligible errors in (3.3.1) arising from the truncation of the Taylor series and at the same time still large enough to produce an efficient integration. For instance, a simulation over a range of 300 K with a ΔT of 0.1 K may take something like twenty minutes on a 66 MHz Intel 80486 processor. However, for the real integration, this time increases nearly ten fold because of the bidimensional interpolation of u. In all simulations of the integration in the supercritical region, ΔT was a positive quantity and therefore the integration took places along isochores beginning at the lowest temperature and proceeding towards the highest temperature. Under those conditions,

the values calculated for Z were never in error by more than $\pm 10^{-5} \cdot Z$, well within the likely estimated uncertainty for Z from pVT data. For the heat capacities, the fractional errors were never larger than $\pm 3 \cdot 10^{-5}$; at least two orders of magnitude smaller than typical experimental uncertainties. Hence, the integration is stable when it is performed along isochores and with a positive temperature step. In conclusion, two remarks associated with stability of integration along isochores are appropriate: first at all, the choices of ΔT and $\Delta \rho_n$ are independent of each other, at least within a sensible resolution, and second, a stable integration is obtained whenever a positive ΔT is employed.

However, when the variables (T,ϕ) were used to perform the integration in the sub-critical region and the numerical differentiation of all the variables was carried out as described earlier, it was found that the increments ΔT and $\Delta \phi$ were strongly coupled. This is probably caused by the presence of the cross derivative $(\partial^2 Z/\partial T \partial \phi)$ in equation (3.2.23). A failure to determine accurately that derivative would lead to large errors in the derived thermodynamic properties as it is illustrated in figure 5. There, a 20 Kelvin simulation of the integration following lines (50) of constant ϕ, with a $\Delta T = -0.05$ K, clearly shows that with no error in either the initial conditions or the speed of sound, a deviation arose in the cross derivative reaching rapidly a maximum deviation of about 0.1 per cent inside of the first two Kelvin and then slowly declining as the integration proceeded. This deviation produced a gradually increasing error in Z, amounting easily to 0.02 per cent after 15 K of integration, even though the error in the cross derivative has already declined. $C_{V,\mathrm{m}}$ was severely affected within the first few Kelvin and then the errors tended to decay.

As soon as the value of ΔT was decreased to –0.005 K, maintaining the same $\Delta \phi$, all these errors disappeared and, simultaneously, an accurate calculation of the cross derivative was ensured. We were able to formulate an empirical restriction between the increments ΔT and $\Delta \phi$ from these simulation results. Whenever $|\Delta T/\mathrm{K}| \leq 2 \cdot \Delta \phi$ was satisfied, the cross derivative was calculated with enough accuracy to prevent an undesirable growth of errors in the compression factors or heat capacities.

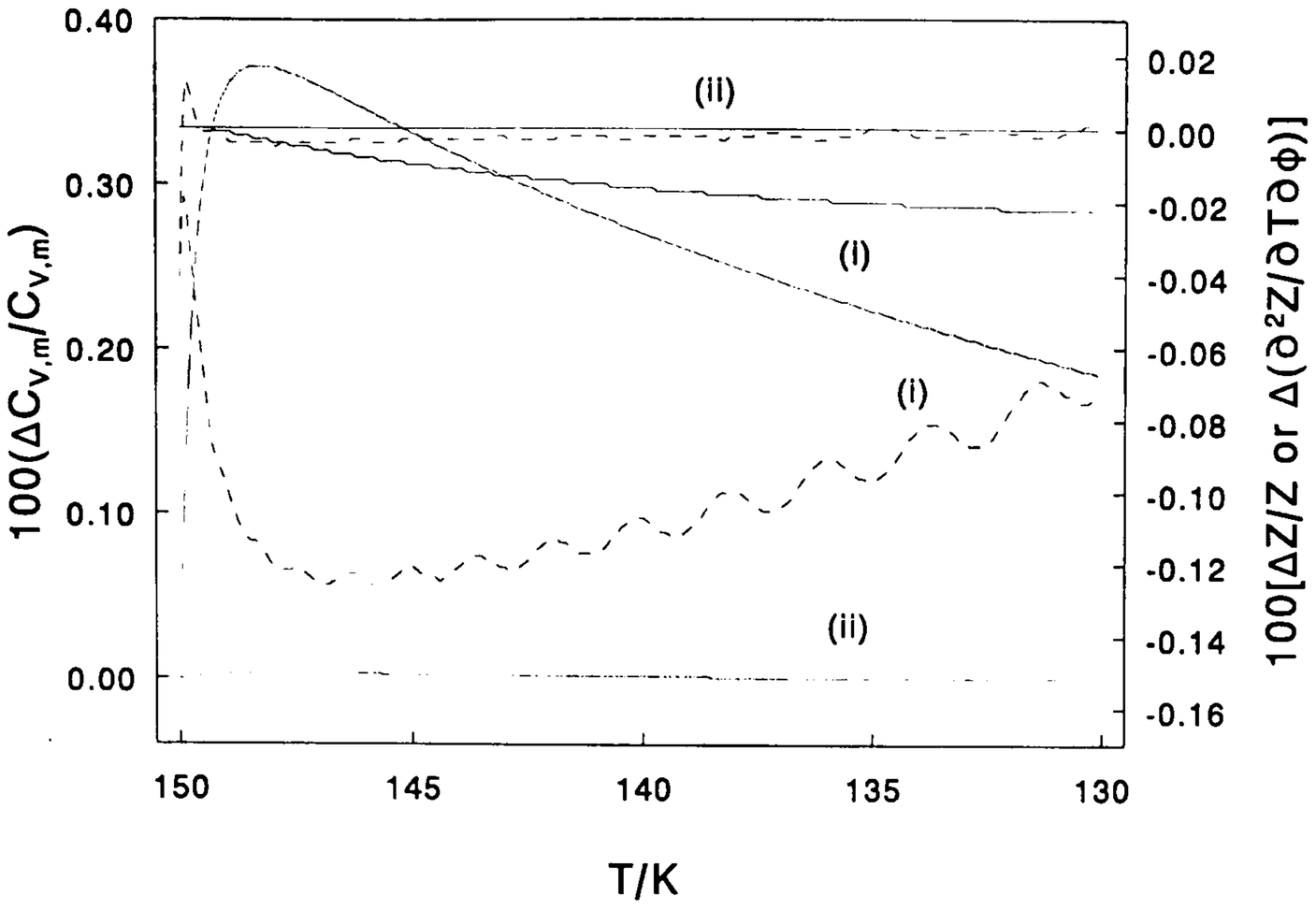


Figure 3.5 Deviations of Z and $C_{V,\mathrm{m}}$ from simulations in subcritical region for two different ΔT: (i) for ΔT = -0.05 K and (ii) for ΔT = -0.005 K. (—), ΔZ; (---), $\Delta(C_{V,\mathrm{m}}/R)$; (····), $\Delta(\partial^2 Z/\partial\phi\partial T)$.

Recalling the need of selecting fifty lines of constant ϕ in order to achieve accurate numerical differentiation with respect to ϕ, the above restriction becomes the criterion required to accomplish accurate calculations.

3.4.2 Simulation of the numerical method: stability.

Once the size of temperature steps and increments $\Delta\rho_n$ or $\Delta\phi$ were defined in a such way as to diminish the effects of truncations error in the numerical formulae, another test was performed. This investigated the way in which the integration might take place. For a given path of integration, there are two possible ways of proceeding: one can use a positive or a negative temperature step. Recalling the remarks made in section 3.2.3 about stability, it is known that integration of the algorithm is always stable if the integration takes place along a path that raises more slowly than the isentrope for a positive temperature step. Thus, a way to **demonstrating** this result is through simulation of the integration with both increasing and decreasing temperature along isochores. For the former, this criterion of stability has been confirmed as

pointed out above. Thus, a simulation along isochores, with the same spacing as before, but starting the integration at the highest temperature, and then going downwards in temperature was attempted.

In this case, errors in the derived thermodynamic properties grew until, at some point, they increased catastrophically as can be seen in figure 6. This suggests that an isochoric integration going downwards in temperature becomes unstable even when the truncation error in a single step is negligible. Larger errors, e.g. errors in the initial conditions and inaccuracies in the speed of sound, may then shorter the region where reliable results may be obtained with a negative temperature increment.

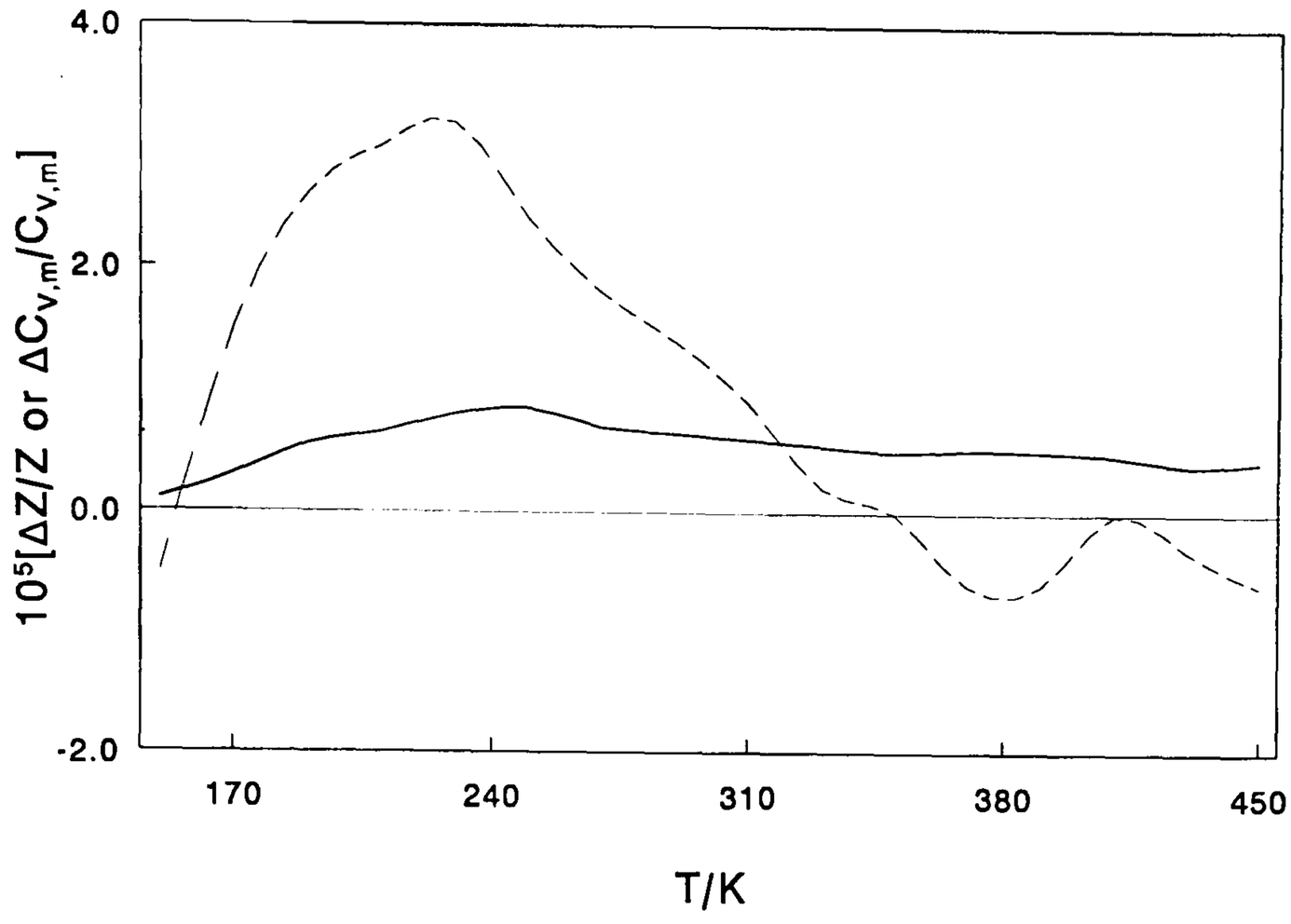
However, it might still be possible to produce an accurate solution along isochores with a negative temperature increment if the temperature range is restricted. For larger temperature intervals, the use of a negative temperature increment must be restricted to integration paths on which ρ_n declines faster than it does on an isentrope in order to maintain stability.

This observation has been sustained, once again, by simulations of integration along lines parallel to the saturation curve. There, likely truncation errors were once again negligible as shown in figure 7.

Further evidence that these two sorts of integrations, along isochores with a positive temperature step and along lines parallel to the saturation curve with a negative temperature step, are stable is provided by an approximate analytical solution which describes the way that errors propagate. This approximation corresponds to a solution of a linearised version of equations (3.2.12) and (3.2.15) and is described in detail below.

Thus, we can say that a stable integration is always obtained in both the supercritical and sub-critical region by a simple adjustment of the size and sign for the increments in both independent variables, bearing in mind the restriction between ΔT and $\Delta\phi$. However, truncation errors are the less demanding source of inaccuracies in the derived thermodynamic properties and, as a matter of fact, errors in both the initial conditions and in the speed of sound may contribute to the error in Z and the heat capacities in a more serious way.

a)



b)

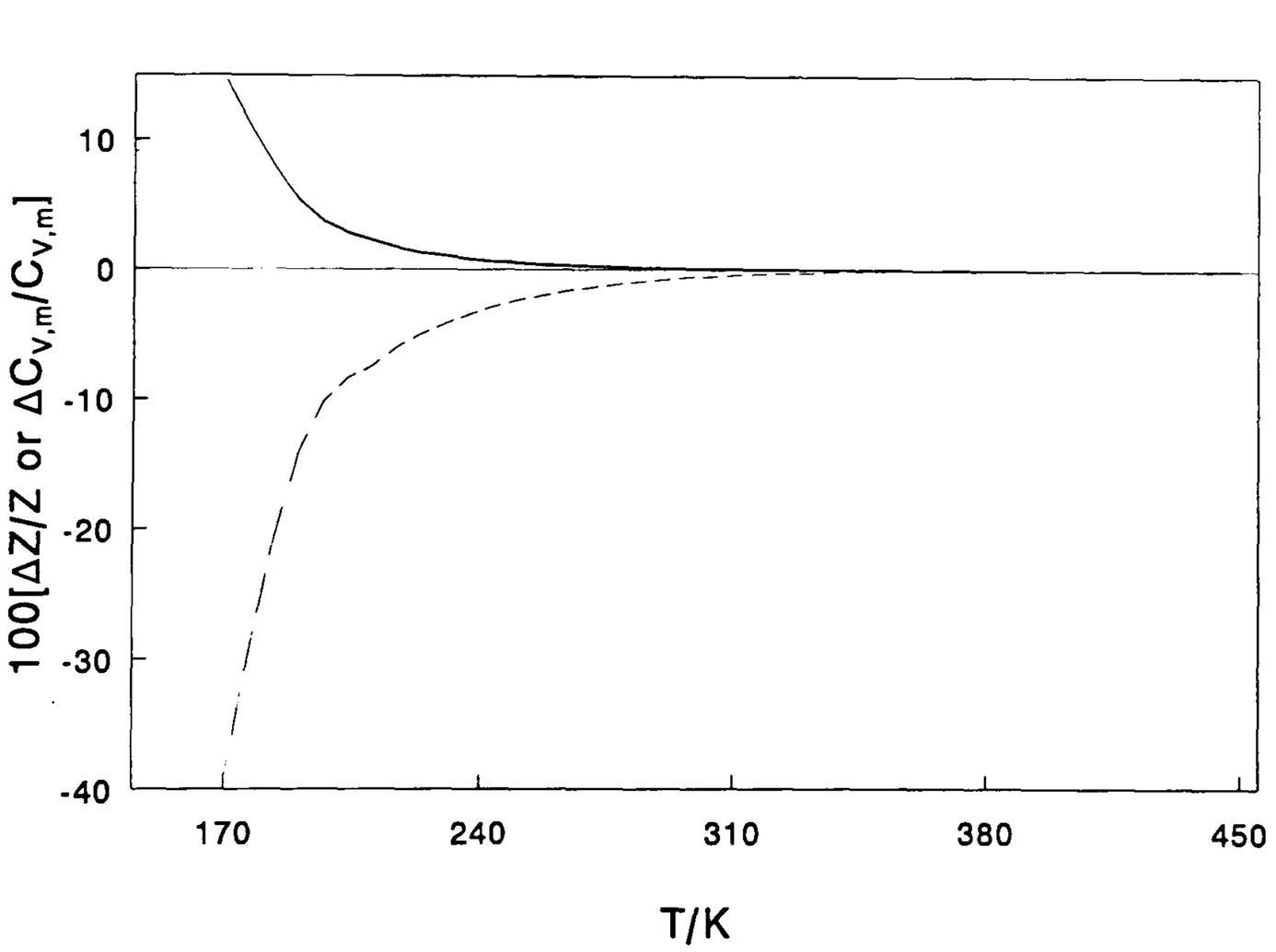


Figure 3.6 Deviations of Z and $C_{V,\mathrm{m}}$ from simulations of isochoric integration on argon with $\Delta T = \pm 0.5$ K and at $T > T^{c}$ and fifty isochores up to half of the critical density. Isochore at half of the critical density: (—), ΔZ; (---), $\Delta(C_{V,\mathrm{m}}/R)$. a) for $\Delta T > 0$ and b) for $\Delta T < 0$.

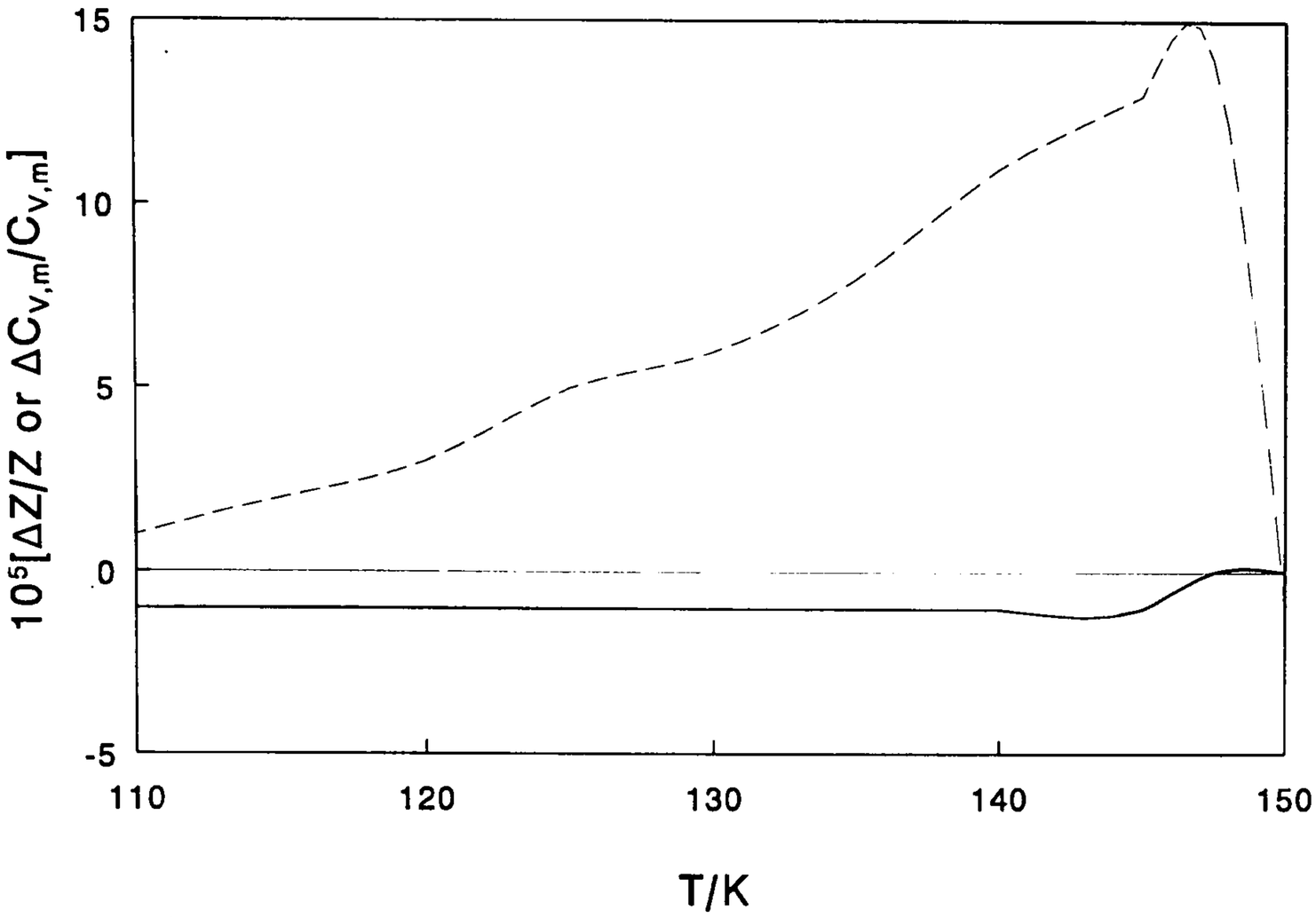


Figure 3.7 Deviations of Z and $C_{V,\mathrm{m}}$ from simulations of integration on argon along lines at constant fraction of the saturation density, ϕ. Results for $\phi = 0.75$. (—), $\Delta Z/Z$; (---), $\Delta C_{V,\mathrm{m}}/C_{V,\mathrm{m}}$.

3.5 Error propagation in numerical integration.

Since the differential equations relating u, Z and $C_{V,\mathrm{m}}$ are non-linear and they are solved by an initial value method, it is quite important to study the propagation of errors from the initial conditions. This would complete the discussion of stability begun above.

When the initial conditions in a simulation were perturbed with small fractional uncertainties, the errors in the derived properties always decayed along isochores tracked with the appropriate increment in temperature. Conversely, small errors in the initial values tend to grow after a while without limit if the temperature is decreased along isochores. Unless the density domain of the integration is restricted, this catastrophic behaviour is always found sooner or later; the larger the errors in the initial conditions, the sooner the deviations became catastrophic. For the typical order of magnitude of these errors, $2\times10^{-4}\cdot Z$, the results from the integration suggested that the accuracy of the derived properties did not deteriorate substantially within few

Kelvin of the initial temperature. Although all these results were obtained from simulations, they are strongly supported by an approximate analytical model developed for the propagation of errors.

3.5.1 Analytical solution.

When appropriate approximations are made, the way in which small errors on initial conditions and speeds of sound may propagate into the solution is described by an analytical solution. Let the actual solution Z obtained from equations (3.2.12) and (3.2.15) be composed of two parts, the true solution Z_t plus a parasitic term Z_p; the latter will ultimately describe the manner in which errors of both initial conditions and speed of sound propagate into the solution. Let the initial conditions be set at T_0 as follows:

$$Z = Z_t(T_0, \rho_n) + \varepsilon_0(\rho_n) \tag{3.5.1}$$

and

$$(\partial Z/\partial T)_\rho = (\partial Z_t/\partial T)_\rho + \varepsilon_1(\rho_n), \tag{3.5.2}$$

where ε_0 and ε_1 are functions that represent experimental errors and give rise to contribution to Z_p. Furthermore, it is assumed that the experimental values of u^2 have a fractional error $\delta(T,\rho_n)$; in practice all the above errors are quite small, thus the parasitic term Z_p is much smaller than Z_t. In this case, an approximation to the non-linear problem can be justified. Starting by replacing Z by $Z_t + Z_p$ and u^2 by $u^2(1+\delta)$ in equations (3.2.12) and (3.2.15) and recalling that Z_t satisfies these equations, the equation obeyed by Z_p can be derived with the result:

$$\begin{aligned} u^2(M\delta/RT) = {} & Z_p + \rho_n(\partial Z_p/\partial\rho_n)_T + \\ & \{(C^t_{V,m}/R) - I(Z_p)\}^{-1} \times (R/C^t_{V,m}) I(Z_p)\{Z_t + T(\partial Z_t/\partial T)_\rho\}^2 + \\ & \{(C^t_{V,m}/R) - I(Z_p)\}^{-1} \times 2\{Z_p + T(\partial Z_p/\partial T)_\rho\}\{Z_t + T(\partial Z_t/\partial T)_\rho\} + \\ & \{(C^t_{V,m}/R) - I(Z_p)\}^{-1} \times \{Z_p + T(\partial Z_p/\partial T)_\rho\}^2, \end{aligned} \tag{3.5.3}$$

where

$$I(Z) = \int_0^{\rho_n} \rho^{-1}\{2T(\partial Z/\partial T)_\rho + T^2(\partial^2 Z/\partial T^2)_\rho\}d\rho \qquad (3.5.4)$$

and

$$(C^{\mathrm{t}}_{V,\mathrm{m}}/R) = (C^{\mathrm{pg}}_{V,\mathrm{m}}/R) - I(Z_{\mathrm{t}})\,. \qquad (3.5.5)$$

Equation (3.5.3) is the exact equation that describes Z_{p}, and can be solved once Z_{t} is known. However, providing that Z_{p} is much smaller than Z_{t}, a **linearized** version of (3.5.3) is more useful. After neglecting all the products between small quantities, equation (3.5.3) may be expressed as

$$\begin{aligned}(u^2 M/RT)\delta = \{Z_{\mathrm{p}} + \rho_n(\partial Z_{\mathrm{p}}/\partial\rho_n)_T\} + a^2\{Z_{\mathrm{t}} + T(\partial Z_{\mathrm{t}}/\partial T)_\rho\}^2 I(Z_{\mathrm{p}}) \\ +2a\{Z_{\mathrm{t}} + T(\partial Z_{\mathrm{t}}/\partial T)_\rho\}\{Z_{\mathrm{p}} + T(\partial Z_{\mathrm{p}}/\partial T)_\rho\},\end{aligned} \qquad (3.5.6)$$

where $a = (C^{\mathrm{t}}_{V,\mathrm{m}}/R)^{-1}$; once Z_{t} and $C^{\mathrm{pg}}_{V,\mathrm{m}}$ are given, equation (3.5.6) may be solved. An analytical solution can be found in the case that $Z_{\mathrm{t}} = 1$, i.e. for the perfect gas model. In this case, equation (3.5.6) simplifies to

$$Z_{\mathrm{p}}(1+2a) + \rho_n(\partial Z_{\mathrm{p}}/\partial\rho_n)_T + 2aT(\partial Z_{\mathrm{p}}/\partial T)_\rho\} + a^2 I(Z_{\mathrm{p}}) = (a+1)\delta. \qquad (3.5.7)$$

The solution to this integral-differential equation can be found easily if a is assumed to be constant (in general a is a function of temperature) and δ is a given function of temperature and density. The homogeneous solution $Z_{\mathrm{p,h}}$ for (3.5.7) is then

$$Z_{\mathrm{p,h}} = \sum_k [c_k \cos\{\gamma_k \ln(T/T_0)\} + d_k \sin\{\gamma_k \ln(T/T_0)\}](T/T_0)^{-\beta_k}\rho_n^{m_k}\,, \qquad (3.5.8)$$

where

$$\left.\begin{aligned}\beta_k &= (2a)^{-1}(a+2m_k), \\ \gamma_k^2 &= (4a^2)^{-1}\{4m_k(a+1) - a^2\}\end{aligned}\right\}, \qquad (3.5.9)$$

and the exponent m_k is a free parameter. The constants c_k and d_k are then completely defined by the functions ε_0 and ε_1; moreover, possible values of the exponents m_k are restricted by the functional form of those errors, which will be assumed to be analytical in the limit of zero density.

The particular solution $Z_{\mathrm{p,p}}$ of (3.5.7) depends upon the specific form of δ, thus errors in the speed of sound can be assessed to determine the way in which they may affect compression factors and heat capacities. A simple but useful form of δ that could describe errors similar to those expected from experiments, is

$$\delta = \sum_j b_j \rho_n^{n_j} (T/T_0)^{\alpha_j} \ . \tag{3.5.10}$$

This is a double polynomial in T and ρ_n in which the b_j are constants. If this functional form of δ is assumed, then the following particular solution $Z_{\mathrm{p,p}}$ is found:[9]

$$Z_{\mathrm{p,p}} = \sum_j (b_j/\chi_j)\rho_n^{n_j} (T/T_0)^{\alpha_j}, \tag{3.5.11}$$

where

$$\chi_j = \{n_j(n_j+1) + 2an_j(1+\alpha_j) + a^2\alpha_j(1+\alpha_j)\}. \tag{3.5.12}$$

Once $Z_{\mathrm{p}} = Z_{\mathrm{p,h}} + Z_{\mathrm{p,p}}$ is found, the corresponding error $\Delta C_{V,\mathrm{m}}$ in the isochoric heat capacity can also be obtained. This error is equal to $I(Z_{\mathrm{p}})$ and by replacing Z_{p} with (3.5.8) and (3.5.11), the following expression is obtained

$$\begin{aligned}
\Delta C_{V,\mathrm{m}}/R =& -\sum_j (b_j/\chi_j)(\rho_n^{n_j}/n_j)\alpha_j(1+\alpha_j)(T/T_0)^{\alpha_j} \\
&+\sum_k \{c_k(\gamma_k^2 - \beta_k^2 + \beta_k) + d_k(2\beta_k - 1)\gamma_k\} \\
&\times \cos\{\gamma_k \ln(T/T_0)\}(T/T_0)^{-\beta_k}(\rho_n^{m_k}/m_k) \\
&+\sum_k \{d_k(\gamma_k^2 - \beta_k^2 + \beta_k) - c_k(2\beta_k - 1)\gamma_k\} \\
&\times \sin\{\gamma_k \ln(T/T_0)\}(T/T_0)^{-\beta_k}(\rho_n^{m_k}/m_k).
\end{aligned} \tag{3.5.13}$$

The particular solution is then completely determined by δ, and the constants c_k, d_k and m_k should be adjusted to satisfy the erroneous initial condition at T_0.

From this particular solution $Z_{p,p}$, we can see that errors in the speed of sound contribute to the error in the solution which is of the same order of magnitude because χ_j has a value of order unity, except for an error in which the function δ contains a term with values of n_j and α_j such that χ_j vanishes; the effect of such an error in u is catastrophic. However, the equation $\chi_j = 0$ has a real root when

$$n_j = a^2 / [4(1+a)], \tag{3.5.14}$$

and

$$\alpha_j = -(2+3a) / [4(1+a)]; \tag{3.5.15}$$

this value of n_j always corresponds to a term which is nonanalytical in the limit $\rho_n \to 0$. For example, with a monatomic gas n_j is 1/15 (and $\alpha_j = -3/5$). Thus, providing that the fractional error in the speed of sound may be represented by terms which are analytical functions of density, the conclusion that $Z_{p,p}$ is of the same order as δ is strictly valid. With current measurement techniques, this source of error may be one order of magnitude smaller than typical uncertainties in direct pVT measurements. For the heat capacity, errors in u may have a larger effect, even when they can be represented by analytical functions of density. A further discussion of this situation is presented in the next section.

Hereafter, we will review the repercussions of errors in the initial conditions alone (with $\delta = 0$). Since at $T = T_0$

$$Z_p = \varepsilon_0 = \sum_k c_k \rho_n^{m_k}, \tag{3.5.16}$$

and

$$T_0 (\partial Z_p / \partial T)_{\rho_n} = \varepsilon_1 = \sum_k (\gamma_k d_k - \beta_k c_k) \rho_n^{m_k}, \tag{3.5.17}$$

the parameters c_k, d_k and m_k are determined completely by the functions ε_0 and ε_1. It follows from equations (3.5.9) that, provided

$$m_k \geq a^2 / 4(1+a), \tag{3.5.18}$$

γ_k and β_k are both positive-real, and the kth term in the series $Z_{\mathrm{p,h}}$ has the form of a damped oscillation which ultimately decays to zero along an isochore as $T \to \infty$. On the other hand, terms with $\beta_k < 0$ diverge with increasing T. In practice, this is prevented as the functional form of Z is known to be that of the virial series in the low-density limit.

Now, it is fairly easy to show along which paths of integration Z_{p} would always decay. Assuming that (3.5.18) is valid, then equation (3.5.8) can be expressed as

$$Z_{\mathrm{p}} \propto (T/T_0)^{-\beta_k} \rho_n^{m_k} . \tag{3.5.19}$$

Also, the integration path may be represented by

$$\rho_n \propto (T/T_0)^{x}, \tag{3.5.20}$$

which describes $\rho_n(T)$. Then, from equations (3.5.9), (3.5.19) and (3.5.20), we can see that Z_{p} is proportional to

$$Z_{\mathrm{p}} \propto (T/T_0)^{-\beta_k + x m_k} = (T/T_0)^{s_k}, \tag{3.5.21}$$

where

$$s_k = -(1/2) + m_k [x - (1/a)] . \tag{3.5.22}$$

Accordingly, for $T > T_0$ (the supercritical region), Z_{p} will decay as long as $s_k < 0$, implying that

$$m_k [x - (1/a)] < (1/2), \tag{3.5.23}$$

and, since m_k is positive for analytical errors in ε_0 and ε_1, then we obtain the very important result

$$x < a^{-1}. \tag{3.5.24}$$

This result clearly states that whenever a path of integration of the form (3.5.20) has an exponent x smaller than a^{-1}, an stable integration would be obtained since errors in the initial conditions will eventually decay as T is increased. The case $x = a^{-1}$ represents the limit of stability for the integration where the integration path precisely coincides with an isentropic path for this ideal-model gas. This can be seen easily by recalling that for an adiabatic process the product pV^{γ} is equal to a constant and hence, for a perfect gas $TV^{(\gamma-1)}$ is constant. This can be expressed alternatively by $\rho_n \propto T^{1/(\gamma-1)}$, and, since $1/(\gamma-1) = (C_{V,\mathrm{m}}/R) = a^{-1}$, a path of the type (3.5.20) will represent an isentrope for $x = a^{-1}$.

Furthermore, the condition of stability can be recast in terms of slopes of the isentropes and the integration path. Taking the derivative with respect to temperature of the integration path -equation (3.5.20)- it is found that (3.5.24) becomes

$$(d\rho_n/dT)_x < (d\rho_n/dT)_S, \tag{3.5.25}$$

where subscripts indicate that the derivative was taken along a line at constant x or S. Equation (3.5.25) represents the condition of stability for $T > T_0$. It establishes that an integration remains stable as long as the slopes of the integration path rise slower than the isentropes do.

The analysis of case $T < T_0$, follows a similar approach except that all the inequalities are now reversed. Therefore, the condition of stability there is expressed by forcing s_k to be positive. This leads directly to the stability condition

$$x > a^{-1}, \tag{3.5.26}$$

Once again, equation (3.5.26) may be represented in terms of slopes, giving the final stability condition

$$(d\rho_n/dT)_x > (d\rho_n/dT)_S. \tag{3.5.27}$$

This condition expresses that an integration with a negative temperature step ($T < T_0$) will remain stable as long as the slopes of the integration path are larger than that of

the isentropes. Since paths parallel to the saturation curve (paths at constant ϕ) satisfy this criterion, a stable integration will be obtained. This is precisely the anticipated result.

The analytical model used above is of course based on the erroneous assumptions that Z_t is unity and a is constant. However, the actual behaviour of the errors in a real gas would not be very different. This can be verified by plotting the predicted error in Z and $C_{V,m}$ from equations (3.5.8) and (3.5.13), respectively, for given error functions ε_0 and ε_1 and then comparing with results from simulation where the initial conditions were perturbed with the same errors.

However, the stability analysis just discussed seems to be a general property of the equations studied and therefore it can be seen as an exact result, independent of the equation of state model used in the derivation.

3.5.2 Predictions and simulations of errors.

In order to test the predictions of the above model, simulations with perturbed initial conditions were performed. Several functional forms for the errors ε_0 and ε_1 were suggested in such a way that they may represent typical uncertainties in pVT data obtained with current techniques ($\varepsilon_0 = 2 \cdot 10^{-4}$ and $\varepsilon_1 = 2 \cdot 10^{-3}$). This was important because in this work the initial conditions were derived from experimental pVT data and therefore, are quite likely to affect the accuracy of the derived thermodynamic properties.

Based on the information given by the analytical solution for the error propagation discussed above, the most interesting cases correspond to integer exponents m_k. Figures 8, 9, 10 and 11 shown the behaviour of the errors in Z and $C_{V,m}$ for $m_k = 1, 2$, in both supercritical and subcritical region. This is achieved by taking T_0 close to T^c and using equations (3.2.22) and (3.2.23) to integrate along lines parallel to the saturation curve for $T < T_0$. Generally speaking, the larger the exponent m_k the faster that errors in Z and $C_{V,m}$ decay if only the Z_0 is in error ($\varepsilon_1 = 0$). However, for errors in the derivative of Z at the initial temperature the situation is less favourable because the errors in Z started to grow before reaching a maximum and finally decaying.

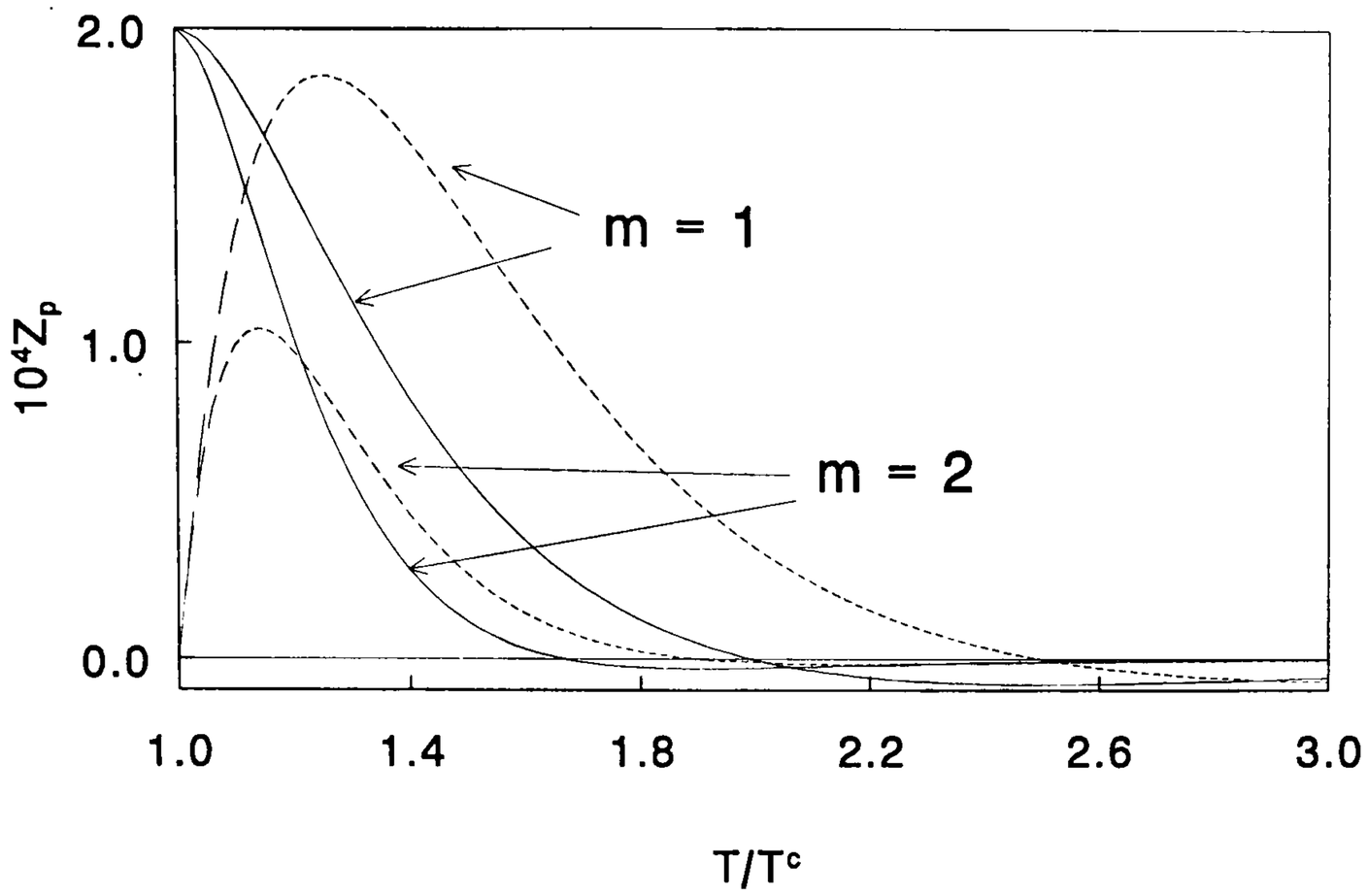


Figure 3.8 Parasitic contribution Z_p to Z along the isochore at half of the critical density for a gas with a =1/3 resulting from errors in the initial conditions proportional to ρ_n''' . (—), $Z_p = 2\times10^{-4}$ at T_0; (---), $T(\partial Z_p / \partial T)_{\rho_n} = 2\times10^{-3}$ at T_0.

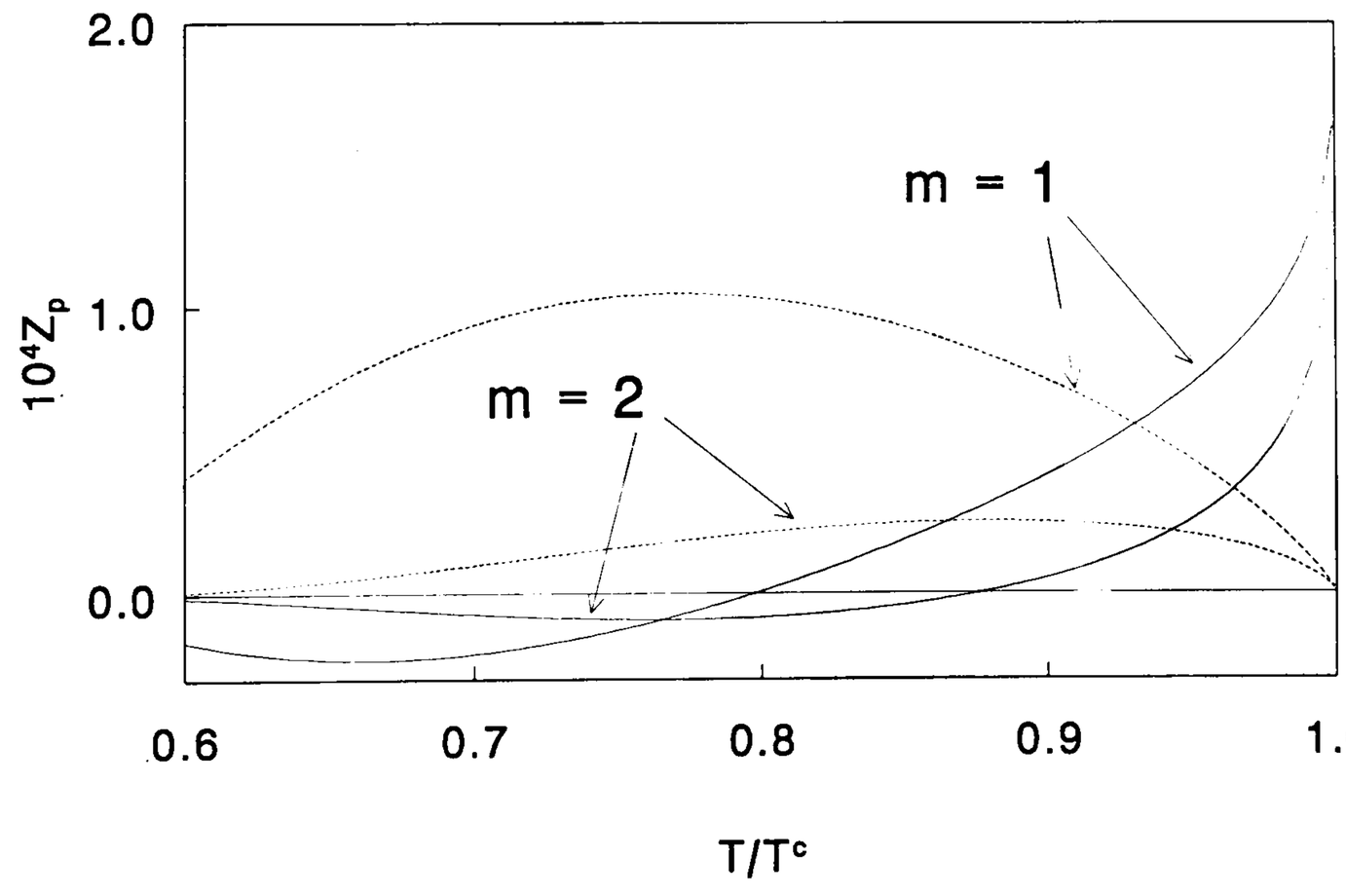


Figure 3.9 Parasitic contribution Z_p to Z along a line at constant fraction of the saturation density of a gas with a =1/3 resulting from errors in the initial conditions proportional to ρ_n''' . (—), $Z_p = 2\times10^{-4}$ at T_0; (---), $T(\partial Z_p / \partial T)_{\rho_n} = -2\times10^{-3}$ at T_0.

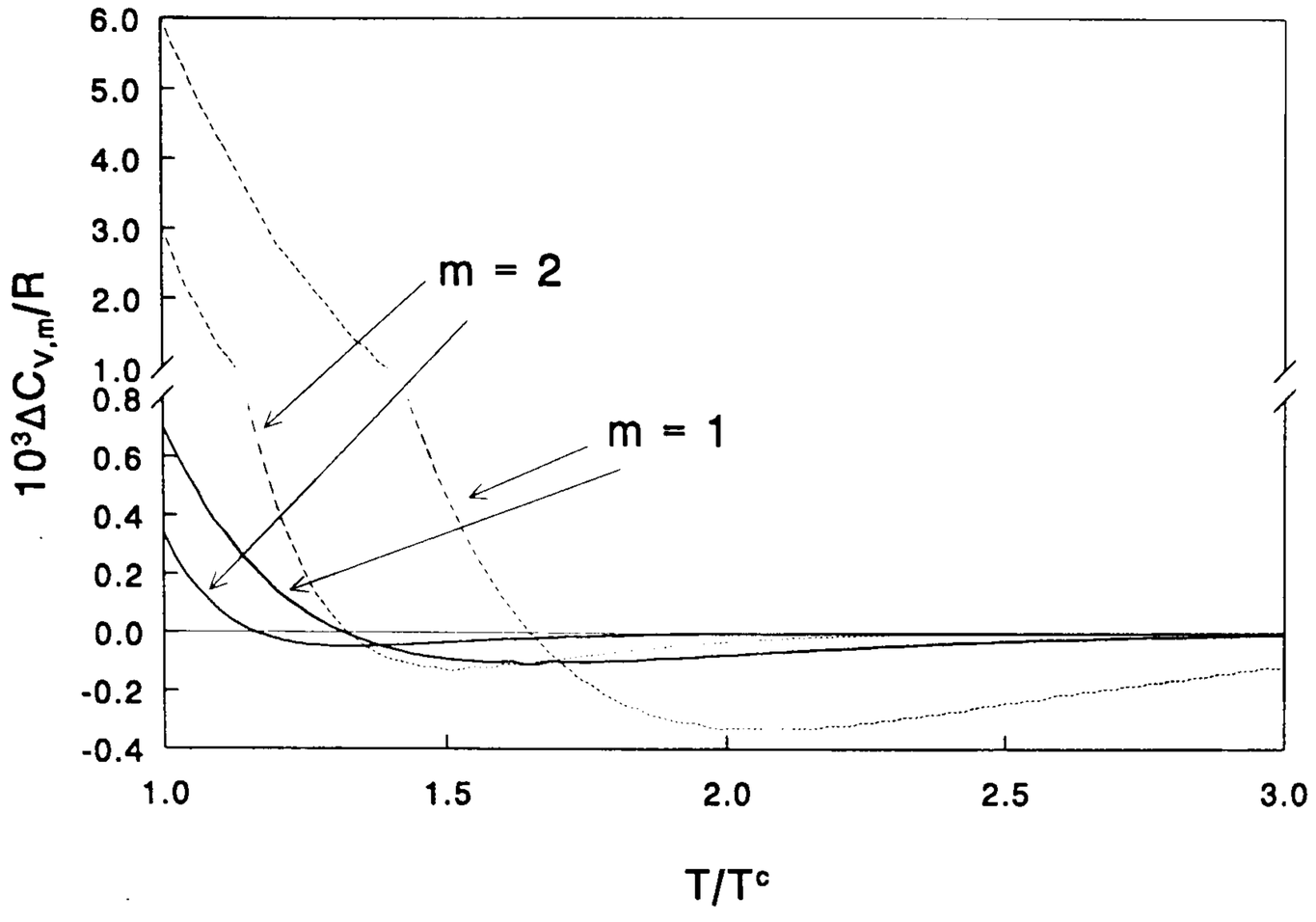


Figure 3.10 $\Delta C_{V,\mathrm{m}}/R$ calculated from equation (3.5.11) along the isochore at half of the critical density for a gas with a =1/3 resulting from errors in the initial conditions proportional to ρ_n''' . (—), $Z_\mathrm{p} = 2\times10^{-4}$ at T_0; (---), $T(\partial Z_\mathrm{p}/\partial T)_{\rho_n} = 2\times10^{-3}$ at T_0.

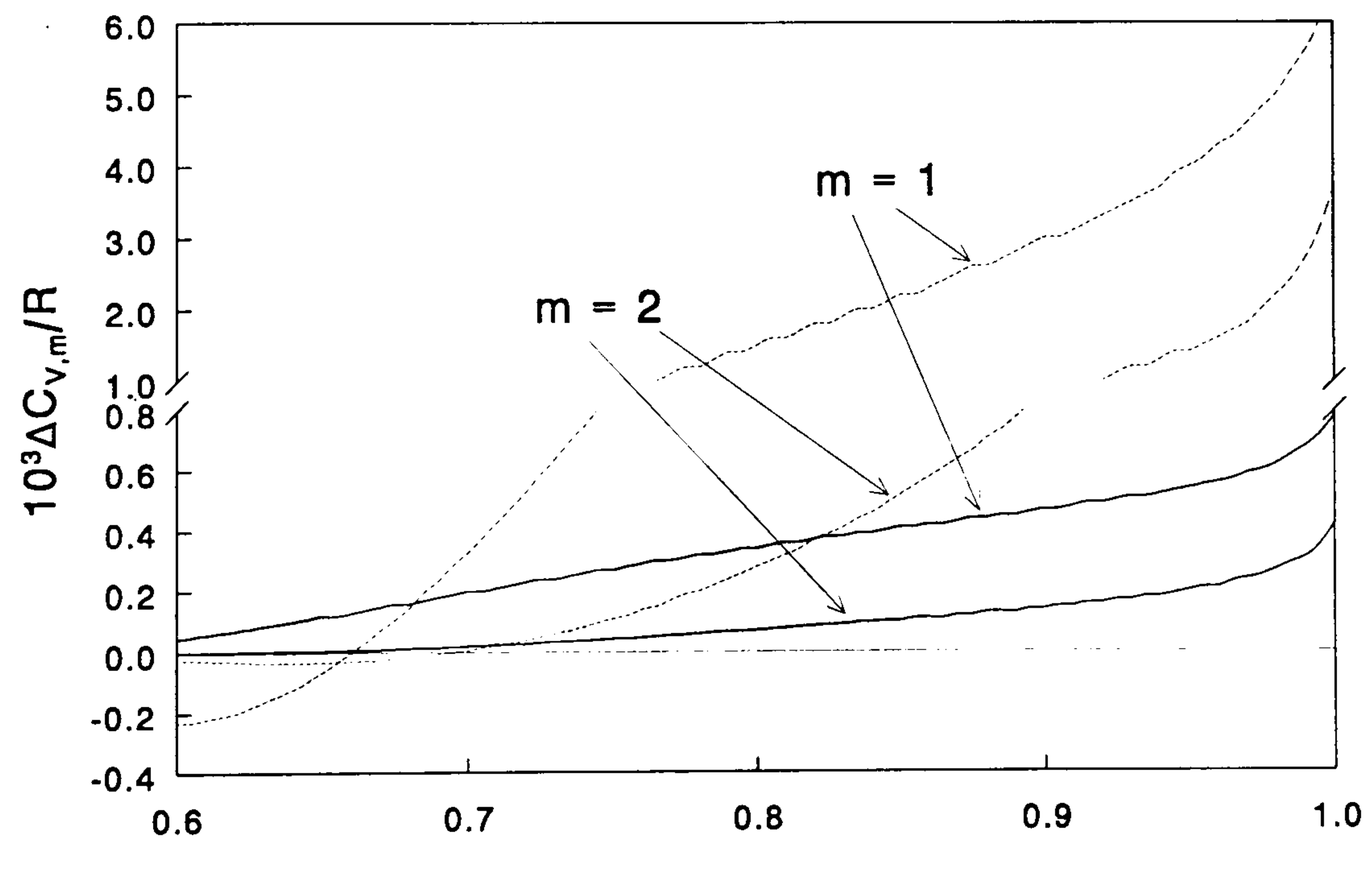


Figure 3.11 $\Delta C_{V,\mathrm{m}}/R$ calculated from equation (3.5.11) along a line at constant fraction of the saturation density for a gas with a =1/3 resulting from errors in the initial conditions proportional to ρ_n''' . (—), $Z_\mathrm{p} = 2\times10^{-4}$ at T_0; (---), $T(\partial Z_\mathrm{p}/\partial T)_{\rho_n} = 2\times10^{-3}$ at T_0.

Although, the quantitative agreement between the simulated results and those predicted by the analytical error model tend to be less good with an increase in density, the qualitative trends are remarkable good as figure 12 clearly indicates.

3.5.3 Propagation of errors into the heat capacities.

As mentioned in the previous section, errors in the speed of sound might have a more profound effect on the heat capacities. After a preliminary analysis, it was found that, with increasing temperature along an isochore, small ripples appeared in the derived values of $C_{V,\mathrm{m}}$. These ripples became quite obvious as soon as the temperature reached the region where $C_{V,\mathrm{m}}$ varied only slowly with density (e.g. about $0.08 \cdot R$ between zero density and $\rho_n^{\mathrm{c}}/2$ for argon at $T \geq 420$ K). For instance, at 450 K in argon the amplitude of the ripples was about $0.002 \cdot R$ which, although small, could be easily detected in a plot, as shown in figure 13.

This observation suggested that a likely source for this effect was errors in the speed of sound, chiefly in the way that u was obtained by interpolation. In order to discard as possible source for this strange behaviour the extrapolation routine of the speed of sound, another integration was performed with a more modest density range in argon to avoid the usage of extrapolated data. Once again, the pattern shown in figure 13 appeared.

This suggested that the ripples were caused by errors in u associated with the interpolation routine. In order to confirm this, some simulations were performed with a perturbation in the speeds of sound which tried to resemble the likely errors that the interpolation may generate. Thus, u was perturbed by a fractional error δ in the form of

$$\delta = \delta_0 \sin[\theta_n \omega + \theta_m \Delta_1 (T_0 \tau - 1)], \tag{3.5.28}$$

where $\theta_n = 2n\pi$, $\theta_m = m\pi$ and $\Delta_1 = [(T_0/T_{\mathrm{f}}) - 1]^{-1}$; n and m are positive integers and T_{f} represents the final temperature at which speed of sound is available.

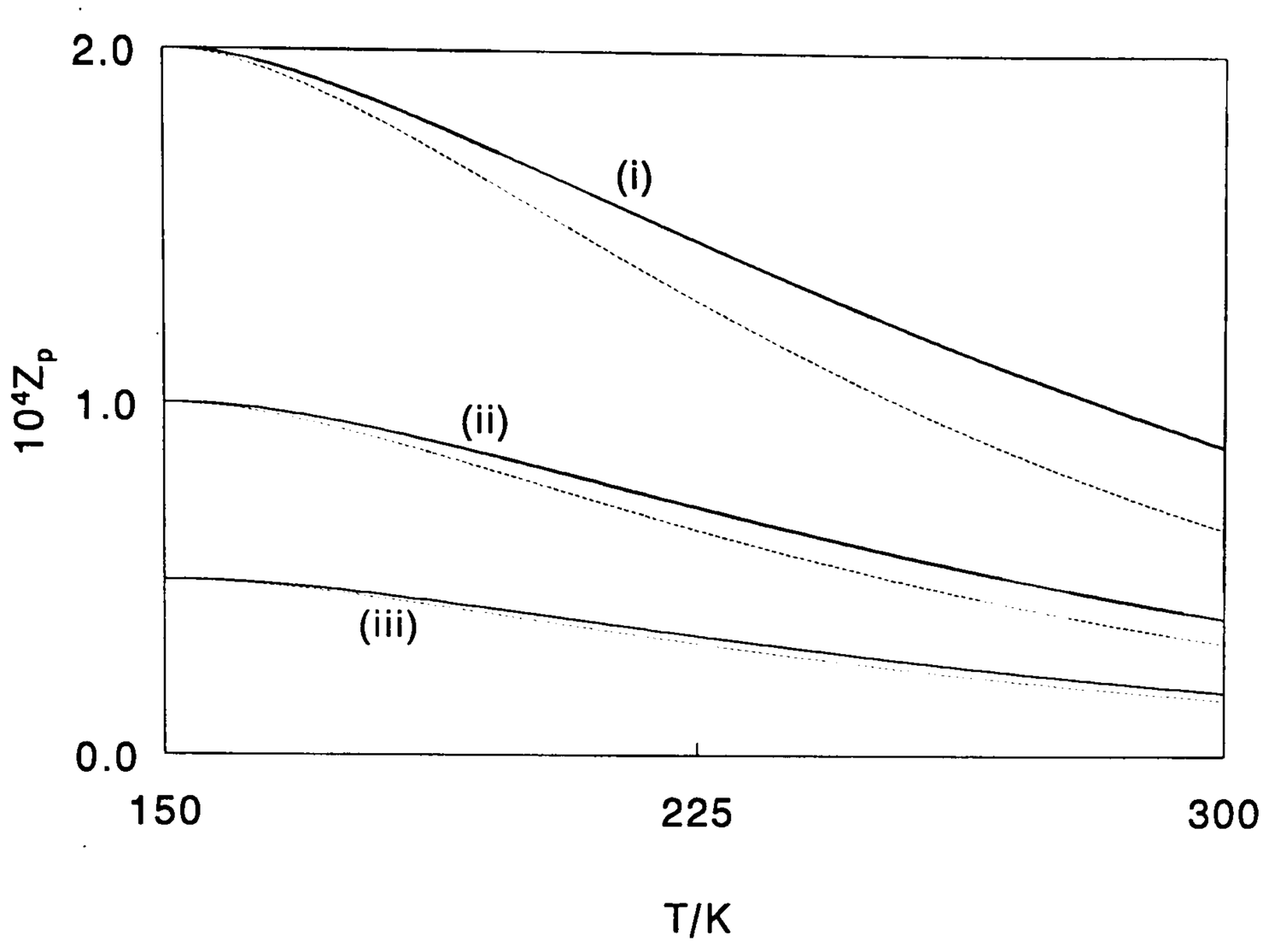


Figure 3.12 Parasitic contribution Z_p to Z along the isochores for argon gas resulting from an error in the initial values of Z given by $\varepsilon_0 = 4\times10^{-4}(\rho_n/\rho_n^c)$. (i) $\rho_n = \rho_n^c/2$; (ii) $\rho_n = \rho_n^c/4$; (iii) $\rho_n = \rho_n^c/8$. (—), numerical solution of equations (3.2.12) and (3.2.15) with properties from ref. [12]; (---), Eq. (3.5.6).

Equation (3.5.28) defined in that way has the property of being zero at regular increments of the interpolating variables, τ and ω. Then, n is equal to the number of densities measured along an isotherm minus one and m is the number of isotherms minus one. Although the actual spacing of the speed of sound in both τ and ω is not exactly regular, equation (3.5.28) may still be a good approximation to the likely type of error produced by the interpolation routine. This seems to be the case since a δ_0 of about $30\cdot10^{-6}\cdot u$ yields ripples in $C_{V,m}$ similar to those observed in practise with little effect (<0.01 per cent) on the derived values of Z, as can be seen in figure 14. At the beginning of the simulation no ripples are presented but they become quite obvious and regular as the temperature is increased.

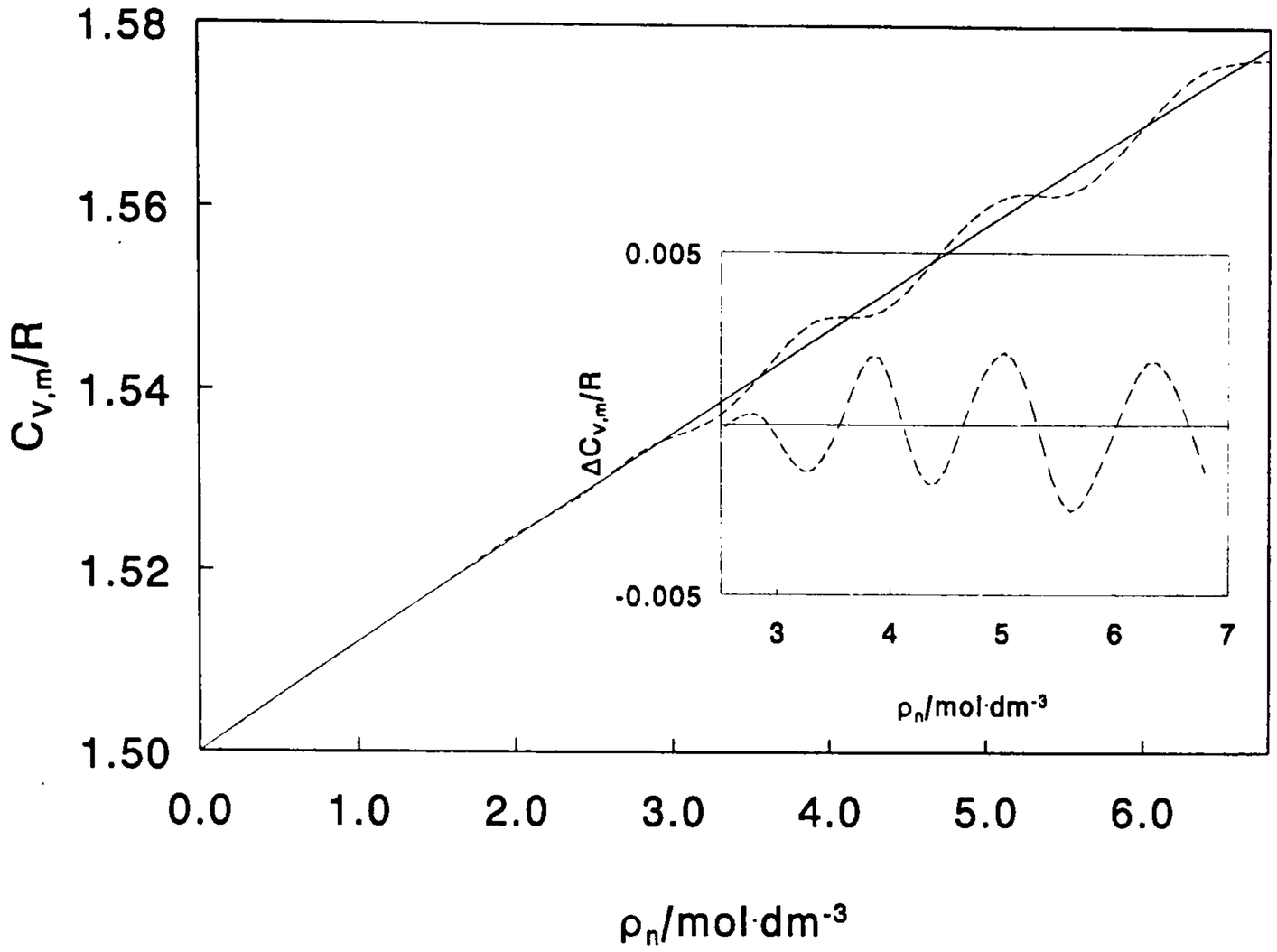


Figure 3.13 Ripples in $C_{V,\mathrm{m}}$ from preliminary integration of argon at 450 K. Representation of $C_{V,\mathrm{m}}$: (---), unsmoothed values; (—), values from a fourth degree polynomial in density. Insert is an amplification of ripples of $C_{V,\mathrm{m}}$.

Once the possible origin of these ripples was established, attempts were made to overcome this difficulty by "filtering out" errors in the values of u. The strategy followed consisted of smoothing the derived $C_{V,\mathrm{m}}$ by means of a fourth degree polynomial in ρ_n before allowing the integration routine to take the next temperature step. This smoothing routine acted as an effective filter preventing the growth of noticeable ripples in $C_{V,\mathrm{m}}$ but, at the same time, not altering the derived values of Z significantly (in fact, by no more than $8 \cdot 10^{-5}$).

In addition, a flag was incorporated in the predictor-corrector method to switch on or off this filter. The criterion to use the filter in the calculation of $C_{V,\mathrm{m}}$ was to observe any possible indication of ripples in $C_{V,\mathrm{m}}$ along the last isotherm, were presumably $C_{V,\mathrm{m}}$ would be more affected, and accordingly, recalculated the whole surface if any indication of ripples appeared within the resolution achieved.

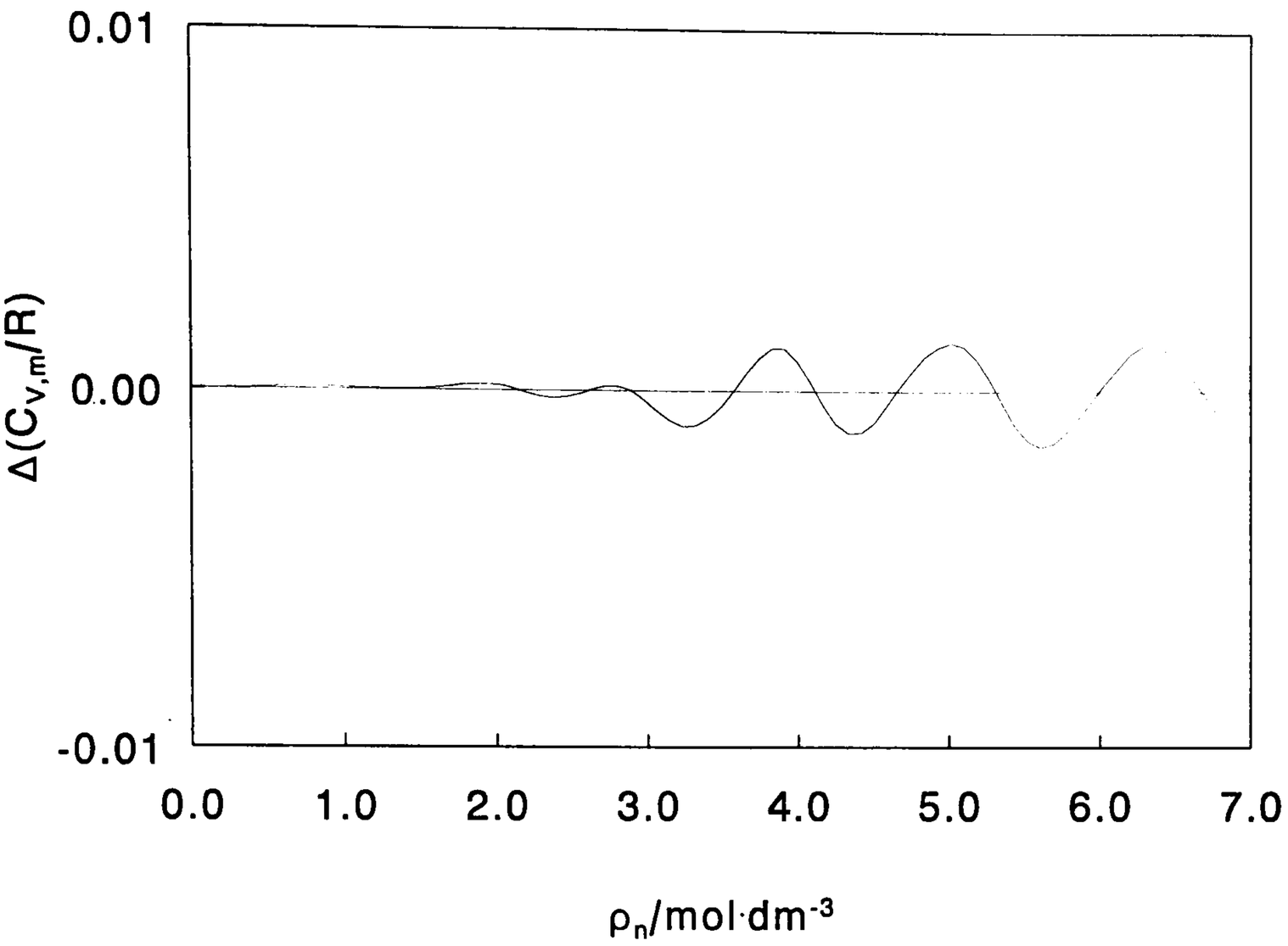


Figure 3.14 Error in $C_{V,\mathrm{m}}$ at 450 K from simulations with an error on the speed of sound given by equation (3.5.26).

When the filter was actived, all isobaric heat capacities $C_{p,\mathrm{m}}$ were obtained from the smoothed values of $C_{V,\mathrm{m}}$ by means of (3.2.16). For the sub-critical region the corresponding smoothing took place in $C_{\phi,\mathrm{m}}$ and both $C_{V,\mathrm{m}}$ and $C_{p,\mathrm{m}}$ were then obtained by (3.2.21); this ensured that all the heat capacities were always smooth functions in any region, supercritical or subcritical.

References.

1. Rowlinson, J.S.; Swinton, F.L.; *Liquids and liquid mixtures*, 1982, 3rd edn., London:Butterworths.

Le Neindre, B.; Vodar, B. (eds); *Experimental Thermodynamics, Volume II: Experimental Thermodynamics of Non-reacting Fluids*, 1975, London:Butterworths.

2. Seldam, C.A. ten; Biswas, S.N.; *J.Chem.Phys.*, **94**, 2130 (1991).

3. Daridon, J.L.; Lagourette, B.; Xans, P.; *Fluid Phase Equilibria*, **100**, 269 (1994). Davis, L.A.; Gordon, R.B.; *J.Chem.Phys.*, **46**, 2650 (1967). Kell, G.S.; Whalley, E.; *J.Chem.Phys.*, **62**, 3496 (1975).

4. Ewing, M.B.; Goodwin A.R.H.; Trusler, J.P.M.; *J. Chem. Thermodynamics*, **21**, 867 (1989). Esper, G.; Lemming, W.; Beckermann, W.; Kohler, F., *Fluid Phase Equilibria*, **105**, 173 (1995).

5. Prausnitz, J.M.; Lichtenlhaler, R.N.; de Azevedo, E.G.; *Molecular Theory of Fluid Phase Equilibria*, 1986, Englewood Cliffs, NJ: Prentice-Hall

6. Estrada-Alexanders, A.F.; Trusler, J.P.M; *J. Chem. Thermodynamics*, **27**, 1075 (1995).

7. Trusler, J.P.M.; Zarari, M.; *J. Chem. Thermodynamics*, **24**, 973 (1992).

8. Estrada-Alexanders, A.F.; Trusler, J.P.M; Zarari, M.P.; *Int. J. Thermophys.*, **16**, 663 (1995).

9. McGlashan, M.L.; *Chemical Thermodynamics*, 1979, London: Academic Press.

10. Estrada-Alexanders, A.F.; Trusler, J.P.M; *Int. J. Thermophys.*, (in press).

11. Gilgen, R.; Kleinrahm, R.; Wagner, W.; *Int. J. Thermophys.*, **26**, 383 (1994).

12. Stewart, R.B.; Jacobsen, R.T.; *J. Phys. Chem. Ref. Data*, **18**, 639 (1989).

Chapter 4. Intermolecular potential and virial coefficients.

4.1 Introduction.

Recently, knowledge about the interaction between molecules has been boosted by the development of sophisticated experimental techniques and the use of faster computers. One of the experimental sources recently used to gain information about the interactions occurring between molecules is the speed of sound, u. For example, one may rely upon the expansion of u as a series in powers of density as described in chapter three. The coefficients of this expansion are known as the acoustic virial coefficients and they are directly related to ordinary virial coefficients (see §3.2.2). Moreover, it is well known that the ordinary second virial coefficient, and therefore also the acoustic one, is linked to the interaction potential energy of a pair of molecules. Since the acoustic virial coefficient β_a can be determine with better precision than the corresponding ordinary virial coefficient B, the former may be regarded as an excellent source of information. This is the method used in this work to deduce precise model intermolecular potentials from speed of sound measurements.

In this chapter, a brief review of the relevant theory concerning the link between the second virial coefficient and the intermolecular potential is given. A description of the simple but anisotropic site-site model potential is included here. This kind of potential may describe the pair-wise interaction between both like and unlike non-spherical molecules. The aim is to use values of second acoustic virial coefficients to adjust disposal parameters in an assumed intermolecular potential model, by means of a non-linear regression routine, in order to predict ordinary second virial coefficient from the final potential model. This approach may generate a potential model of more general utility but it will not provide an accurate description of the true intermolecular potential surface; that would require much more information.

4.2 Decomposition of the energy of interaction.

Before starting the discussion regarding the link between intermolecular interactions and virial coefficients, it is convenient to describe briefly the way in which the energy of interaction U_N of a system with N molecules can be expressed. For the present purposes only a qualitative discussion will suffice.

The most simple non-trivial system that one can study is that composed of just two molecules ($N = 2$). In that case, there is only one contribution to the energy of interaction U_2: that which arises from the interaction between molecule 1 and molecule 2, denoted by U_{12}. Now, let it be assumed that a third molecule is added to the system ($N = 3$). The energy of interaction U_3 for this case is not as simple as before. Traditionally, one has assumed for simplicity that the energy of a system of three interacting molecules is the sum of interactions between pairs of molecules: $U_3 = U_{12} + U_{13} + U_{23}$. However, it is well known that this simple picture is just a crude approximation and that a better description is obtained when one includes a contribution arising from the simultaneous mutual interaction of the three molecules U_{123} which would not exist otherwise. The energy associated with this situation is known as the non-additive contribution to the intermolecular potential of three molecules. Thus, the energy of a system of three molecules is given by $U_3 = U_{12} + U_{13} + U_{23} + U_{123}$.

Obviously, as N increases, so too does the complexity of the description of the energy of the system. One way of tackling the problem is to consider the energy as the sum of energies arising from the pair-wise interactions and those arising from the non-additive contributions. The latter, in principle, would take into account (mutual) interactions among trios of molecules, those among quartets, and so on. Thus, the energy of a macroscopic system U may be expressed as follows[1]

$$U = \sum_{i<j}^{N} U_{ij} + \sum_{i<j<k}^{N} U_{ijk} + \cdots . \qquad (4.2.1)$$

Normally, one assumes, without further justification, that the dominant term of the expansion (4.2.1) is that corresponding to the interaction between pairs. From the remaining non-additive contributions, there is some knowledge of the functional form of the energy of interaction U_{ijk} arising from dispersion forces.

Thus, the expansion of the energy of a system is truncated after the second term, and from those two terms, the pair-wise interaction energy U_{ij} seems to be the most significant. This is based upon the argument that encounters of two molecules are much more frequent than those of three or more molecules simultaneously, especially at low densities. Since the properties of a macroscopic system can be related with the energy of molecules in isolate clusters (with many fewer molecules than the full system contains) through a rigorous statistical treatment the previous expansion is convenient.

Statistical-mechanical theory provides exact relationships between the energy of just of one of these clusters with each of the virial coefficients: the resultant energy of all possible interactions in a cluster formed by two, three, four, ···, molecules is directly related to the second, third, fourth, ···, virial coefficients. Details of procedure to obtain those relationships are given elsewhere.[2,3] The important result is that the virial equation of state has a solid theoretical grounding and a straightforward physical meaning, but at the same time, it has the disadvantage of being expressed as an infinite series in density.

4.3 Intermolecular potential model.

The pair-wise intermolecular potential U_{ij}, which hereafter is denoted simply by U, has been the object of numerous studies because it is particularly important in the description of the macroscopic properties of fluids, especially for gases at low or moderate densities.[3] There are several ways in which an anisotropic interaction potential $U(\boldsymbol{r}_{12},\omega_1,\omega_2)$ may be represented.[1] Here $\boldsymbol{r}_{12}$ is the distance between molecules and ω_j represents the two angles that describes the orientation of a linear molecule. One common way of decomposing U is

$$U(\boldsymbol{r}_{12},\omega_1,\omega_2) = U_r(r_{12}) + U_a(\boldsymbol{r}_{12},\omega_1,\omega_2)\,. \tag{4.3.1}$$

by combining a purely radial contribution U_r and an angular part U_a. The latter consists of a series of angular-dependent terms that might be derived in part from theory. The most important of angular-dependent contributions are multipolar interactions, induction and dispersion forces and overlap between electronic clouds when the two molecules became close.[4,5] Often, U_r is represented by one of the great

variety of simple model potentials which mimic the two main features of the interactions between molecules with the use of only a few disposal parameters. These features are the attractive and the repulsive forces between molecules; the former may act on a large range while the latter is really important only when the molecules become very close each other.

An alternative way of study an anisotropic potential is to split once again the intermolecular potential in a radial part U_r and in an angular part U_a but now with U_r expressed as

$$U_r(\boldsymbol{r}_{12}) = \langle U(r_{12},\omega_1,\omega_2)\rangle_{(\omega)}, \tag{4.3.2}$$

where $\langle\ldots\rangle_{(\omega)}$ denotes an unweighted average over all possible orientations:

$$\langle U(\boldsymbol{r},\omega_1,\omega_2)\rangle_{(\omega)} = \Omega^{-2}\int d\omega_1 d\omega_2 U(\boldsymbol{r},\omega_1,\omega_2). \tag{4.3.3}$$

Here, Ω is a normalisation constant. Consequently, from **equations** (4.3.1) to (4.3.3) follow that $\langle U_a(\boldsymbol{r}_{12},\omega_1,\omega_2)\rangle_{(\omega)} = 0$. This approach can then be combined with an expansion in spherical harmonic components of all anisotropic contributions as described earlier.[1,5]

Although an expansion in spherical harmonics can represent accurately the full potential, a large number of terms may be required. A simpler but approximate treatment which still incorporates anisotropy is afforded by a site-site model.[1,4] The model consists of placing so-called interaction sites on each molecule, which interact with the sites on a second molecule in accordance with a radial potential U_r. The anisotropy of the model is then implicit in the different distances between sites for a given orientation of the pair. The total intermolecular potential U is given by[4]

$$U(r_{12},\omega_1,\omega_2) = \sum_{\alpha\beta} U_r(r_{\alpha\beta}), \tag{4.3.4}$$

where the summation goes over all pair of sites on the different molecules. For instance, if a site is placed over each atom in a molecule then in an interaction between two N_2 molecules the summation is over 4 terms, while for CH_4-CH_4 there are 25 interactions. However, it is not always the rule to place an interaction site on

each atom and it is sometimes possible to simplify the description of the potential using fewer sites than there are atoms in a molecule. In this work, the site-site approach was followed. The radial potential U_r used in (4.3.4) might be anything as long as it contained the well-known physical features of the interaction between molecules: an attractive and a repulsive part. Below, a flexible model potential studied in this work is presented together with the formulas used to calculated the site-site distances $r_{\alpha\beta}$ in molecules containing two interaction sites.

4.3.1 Maitland-Smith potential.

The Maitland-Smith interaction energy potential is a generalisation of the well known Lennard-Jones potential (n-6):

$$U_{\mathrm{MS}}(r) = \varepsilon[6(r/r_{\mathrm{m}})^{-n} - n(r/r_{\mathrm{m}})^{-6}]/(n-6), \qquad (4.3.5)$$

where ε and r_{m} are the **depth** and separation at the minimum of the potential. The main difference between the Maitland-Smith and Lennard-Jones potentials is that the repulsive exponent n in the former is not fixed but raises with r according to[6]

$$n = m + \gamma[(r/r_{\mathrm{m}}) - 1]. \qquad (4.3.6)$$

In (4.3.6), m and γ are parameters. The Lennard-Jones potential is recovered by setting γ equal to zero.

This model is quite flexible on account of the four parameters ε, r_{m}, m and γ. As a final remark, it is also convenient to introduce the distance at which the potential becomes zero, $r = \sigma < r_{\mathrm{m}}$. For the Maitland-Smith potential, σ and r_{m} are related by means of the transcendental equation:

$$\sigma = r_m \{n(\sigma)/6\}^{1/[6-n(\sigma)]}. \qquad (4.3.7)$$

Solution of equation (4.3.7) does not represent a major problem unless $n(\sigma) = 6$. This is prevented by restricting that the values of m are larger than γ.

4.3.2 Site-site distances between like and unlike molecules.

Once a radial potential has been selected to represent the interactions between two sites on different molecules, the anisotropy of the total potential is implicitly given by the distances between the sites for a particular orientation of the molecules. Let us consider first two molecules, whose centres of mass are separated by a distance r. Moreover, let the orientation of the molecular axis of each molecule be described by the angles θ_i and φ_i with $i = 1, 2$. The number of site-site distances to be calculated is $M_1 \times M_2$, where M_j (with $j = 1, 2$) is the number of sites placed in molecule j. If the molecules are of the same chemical species, $M_1 = M_2$; this is also the case when the interacting molecules have the same number of sites even if they are of different chemical species. Here, the site-site distances are describe by $r_{\alpha\beta} \equiv r_{i,j}$, where the first subscript is for the molecule 1 ($i = 1,.., M_1$) and the second one is for the molecule 2 ($j = 1,.., M_2$). Anisotropy in the molecular interactions appears even in the case of an atom-diatomic molecule system ($M_1 = 1$ and $M_2 = 2$). However, in the present case, we are interested in the next more complicated case in which both M_1 and M_2 are two (not necessarily for a diatomic-diatomic system). For two molecules with only two sites placed along their molecular axis and with site-site distances given by the lengths $2l_1$ and $2l_2$ for molecules 1 and 2 respectively, the following expressions for the distances $r_{i,j}$ are obtaining

$$r_{1,1}^2 = r^2 + l_1^2 + l_2^2 + 2r[l_2 c_2 - l_1 c_1] - 2l_1 l_2 [c_1 c_2 + s_1 s_2 \cos\varphi_{12}], \qquad (4.3.8a)$$

$$r_{1,2}^2 = r^2 + l_1^2 + l_2^2 - 2r[l_2 c_2 + l_1 c_1] + 2l_1 l_2 [c_1 c_2 + s_1 s_2 \cos\varphi_{12}], \qquad (4.3.8b)$$

$$r_{2,1}^2 = r^2 + l_1^2 + l_2^2 + 2r[l_2 c_2 + l_1 c_1] + 2l_1 l_2 [c_1 c_2 + s_1 s_2 \cos\varphi_{12}], \qquad (4.3.8c)$$

$$r_{2,2}^2 = r^2 + l_1^2 + l_2^2 - 2r[l_2 c_2 - l_1 c_1] - 2l_1 l_2 [c_1 c_2 + s_1 s_2 \cos\varphi_{12}]. \qquad (4.3.8d)$$

Here, c_j and s_j represent respectively $\cos\theta_j$ and $\sin\theta_j$. Equations (4.3.8) simplify further for the case of like molecules, ($l_1 = l_2$). The pair-wise intermolecular potential may be expressed as

$$U(r,\theta_1,\theta_2,\varphi_1,\varphi_2) = \sum_{i,j=1}^{2} U_r(r_{i,j}) \\ = U_{\mathrm{MS}}(r_{1,1}) + U_{\mathrm{MS}}(r_{1,2}) + U_{\mathrm{MS}}(r_{2,1}) + U_{\mathrm{MS}}(r_{2,2}), \tag{4.3.9}$$

for two sites in each molecule. This is the formula according to which the non-linear fitting of second acoustic virial coefficient, described in detail below, was performed.

4.4 Second virial coefficient and the pair-wise intermolecular potential.

The major importance of the second virial coefficient B is the simple and direct relation with the energy of interaction between a pair of molecules. This energy is a function which depends upon the separation and relative orientations between the pair. Except for monatomic or nearly spherical molecules, the orientation between two molecules must be considered as important. Statistical-mechanical theory describes formally the way in which B is related with U; this relationship can be derived either assuming that molecules interact according to the laws of the classical mechanics or from a formal quantum theory. It has been pointed out that, except for very light molecules (such as H_2 and He), it is a good approximation to assume that the molecules obeyed classical mechanics and, if necessary, quantum effects can be incorporated as small corrections. Details of this semi-classical approach have been given elsewhere.[2-5] Here, only the relationship between B and U is given for the case of linear molecules. Thus, in the rest of the discussion, it is going to be assumed that the molecules can be modelled as rigid, with moment of inertia I and mass m.

4.4.1 Pure component.

For molecules of the same chemical species inside a container of volume V, the second virial coefficient B is related with the pair-wise intermolecular potential U by[3]

$$B(T) = -(L/2V\Omega^2)\iint_{(\tau)}[\exp\{-U/kT\} - 1]d\tau_1 d\tau_2, \tag{4.4.1}$$

where L and k are the Avogadro and Boltzmann constants respectively and Ω is a normalisation constant equal to 4π. The double integral (4.4.1) is evaluated over all possible positions and orientations $d\tau_j$ of each molecule within V. The position and

orientation of molecule j in a reference frame can be given by the position of the centre of mass $\boldsymbol{r}_j$ and the orientation of the molecular axis, described by two angular variables θ' and φ'. Since U is a function of the separation $r_{12} = |\boldsymbol{r}_1 - \boldsymbol{r}_2|$ and the relative orientation, a translation of the origin of coordinates would change neither U nor B. It is convenient to set the origin of coordinates at the centre of mass of one molecule, for instance molecule 1, and to direct the z axis along the line that joins the two centres of mass, in which the orientation of the molecules is specified by the new variables θ and φ. Moreover, due to the symmetry of problem, U depends upon the difference of the azimuthal angles $\varphi_{12} = \varphi_1 - \varphi_2$ between the molecules rather than upon each separate φ_j. Thus, a second transformation of variables is appropriate in which φ_1 and φ_2 are replaced in favour of φ_1 and φ_{12}. Following those transformations, it is straightforward to perform the integration over the position of molecule 1 and over the azimuthal angle φ_1. The results of these integrations combine with the change of variable from $\boldsymbol{r}_2$ to r_{12} in such a way that a factor of $8\pi^2 V$ is finally obtained and B is then expressed as

$$B = -(L/4)\int_0^{\infty} r_{12}^2 dr_{12} \int_0^{\pi} \sin\theta_1 d\theta_1 \int_0^{\pi} \sin\theta_2 d\theta_2 \int_0^{2\pi} f_{12}(r_{12}, \theta_1, \theta_2, \varphi_{12}) d\varphi_{12}, \qquad (4.4.2)$$

where the Mayer function f_{12} has been introduced,[2]

$$f_{12} = \exp\{-(U/kT)\} - 1, \qquad (4.4.3)$$

and θ_j is the polar angle of the molecule j. Equation (4.4.2) represents the classical limit of the second virial coefficient for linear molecules. Formally, the upper limit for the radial integration should be at most of the order of $V^{1/3}$ but, since f_{12} is a function that rapidly decays towards zero as r_{12} increases, it is possible to extend the integration to infinite.[2] In the case that U is only a function of r_{12}, equation (4.4.2) reduces further to[4]

$$B = -2\pi L \int_0^{\infty} f_{12}(r_{12}) r_{12}^2 dr_{12} = 2\pi L \int_0^{\infty} [1 - \exp\{-U(r)/kT\}] r^2 dr. \qquad (4.4.4)$$

As mentioned previously, quantum effects can be incorporated into the calculation of the B through small corrections characterised by a series in even powers of the Plank's constant h. This expansion is given by:[3,5]

$$B = B_{class} + (\hbar^2/\mu)B_{t1} + (\hbar^2/\mu)^2 B_{t2} + \cdots + \\ + (\hbar^2/I)B_{r1} + (\hbar^2/I)^2 B_{r2} + \cdots . \tag{4.4.5}$$

In equation (4.4.5), B_{class} is given by (4.4.4), $\mu = m_1 m_2/(m_1+m_2)$ is the reduced mass and $\hbar = h/2\pi$. The first corrections at order $\hbar^2$ are:[5]

$$B_{t1} = [L/48(kT)^3]\int_0^\infty \int_{(\Omega)} \exp(-U/kT)(\partial U/\partial r_{12})^2 r_{12}^2 dr_{12} d\Omega , \tag{4.4.6}$$

$$B_{r1} = [L/96(kT)^3]\int_0^\infty \int_{(\Omega)} \exp(-U/kT)[(\partial U/\partial \theta_1)^2 + (\partial U/\partial \theta_2)^2 \\ + (\sin\theta_1)^{-2}(\partial U/\partial \varphi_1)^2 \\ + (\sin\theta_2)^{-2}(\partial U/\partial \varphi_2)^2] r_{12}^2 dr_{12} d\Omega , \tag{4.4.7}$$

with

$$\int_{(\Omega)} d\Omega = \int_0^\pi \sin\theta_1 d\theta_1 \int_0^\pi \sin\theta_2 d\theta_2 \int_0^{2\pi} d\varphi_{12} . \tag{4.4.8}$$

It has been pointed out that the expansion (4.4.5) is not completely correct due to the omission of a coriolis-type rotation-translation term: $(\hbar^2/2\mu)B_{cl}$.[7,8] The expression of this term for linear molecules is[8]

$$B_{cl} = (\pi L)/[6\Omega(kT)^3]\int_0^\infty \int_{(\Omega)} \exp(-U/kT) F(r_{12}, \theta_1, \theta_2, \varphi_{21}) dr_{12} d\Omega , \tag{4.4.9}$$

where

$$F(r_{12},\theta_1,\theta_2,\varphi_{12}) = (\partial U/\partial\theta_1)^2 + (\partial U/\partial\theta_2)^2 + [\csc^2\theta_1 + \csc^2\theta_2 - 2](\partial U/\partial\varphi_{21})^2$$
$$-2(\partial U/\partial\varphi_{21})\sin\varphi_{12}[\cot\theta_2(\partial U/\partial\theta_1) + \cot\theta_1(\partial U/\partial\theta_2)]$$
$$+2\cos\varphi_{12}[(\partial U/\partial\theta_1)(\partial U/\partial\theta_2) - \cot\theta_1\cot\theta_2(\partial U/\partial\varphi_{21})^2]. \quad (4.4.10)$$

These expressions can be then used to relate U with the second acoustic virial coefficient β_a. To do this, one combines (4.4.2) with (3.2.7) to obtain

$$\beta_a = (L/2)\int_0^\infty r_{12}^2 dr_{12}\int_0^\pi \sin\theta_1 d\theta_1\int_0^\pi \sin\theta_2 d\theta_2 \times$$
$$\int_0^{2\pi}\{1-[1+(P_a-2Q_a)(U/kT)+Q_a(U/kT)^2]\exp(-U/kT)\}d\varphi_{12}. \quad (4.4.11)$$

Here, $P_a = (\gamma^{pg}-1)$ and $Q_a = (\gamma^{pg}-1)^2/2\gamma^{pg}$. An equivalent and useful way of expressing (4.4.11) is by means of an unweighted average over all possible relative orientations of the two molecules expressed by the following relation[9]

$$\beta_a = 4\pi L\langle\int_0^\infty\{1-[1+(P_a-2Q_a)(U/kT)+Q_a(U/kT)^2]\exp(-U/kT)\}r_{12}^2 dr_{12}\rangle_{(\omega)}. \quad (4.4.12)$$

Values of β_a calculated by means of equation (4.4.11) -or equivalently (4.4.12)- are exact at high temperatures, in accordance to the classical mechanics treatment. The small quantum corrections to B -equations (4.4.6) to (4.4.10)- can be incorporated into the numerical calculations easily, though the final formula for β_a is not written down because it is very lengthy. Thus, for a given model of the intermolecular potential energy U, equation (4.4.12) may be evaluated and compared with values of β_a obtained from measurements of the speed of sound. This procedure can then be repeated with a slightly different choice of the set of parameters defining U in order to assess whether or not the changes would reproduce better the experimental β_a. In others words, a non-linear fit of a set of M_p parameters defining U may be obtained by minimising the statistical function:[9]

$$\chi^2 = \sum_{i=1}^{N} \{[\beta_a(T_i) - \beta_{\text{fit}}(T_i)]/\sigma_i(\beta_a)\}^2, \qquad (4.4.13)$$

assuming that there are N determinations of $\beta_a(T_i)$, i =1, 2,···, N each associated with a standard deviation $\sigma_i(\beta_a)$, and denoting the values of β_a calculated from the model potential at the temperature T_i by $\beta_{\text{fit}}(T_i)$. Moreover, an useful quantity is the so-called reduce χ^2 defined as the ratio of χ^2 to the number of degree of freedom of the fit.

This method alone may not be sufficient when one is interested in a more realistic intermolecular potential in which all features attached to the potential are incorporated into the description -multipolar moments, induction and dispersion energies, overlap interactions, etc. However, for a simple model of the intermolecular potential with a few free parameters to be determined, non-linear fitting of β_a, alone should be sufficient. A simple model including anisotropy would be still quite useful. This sort of approach will lead to the establishment of a semi-realistic model potential which at least may predict properly the second virial coefficient. This is the objective pursued in this work.

4.4.2 Binary mixture.

In a binary mixture an extra degree of freedom appears which is associated with the composition of the mixture. The thermodynamics properties become functions not only of density and temperature but also of the composition of the mixture, which can be characterised by the mole fraction x of one of the components. A generalisation of a second virial coefficient for the mixture can be then given:[3]

$$B_{\text{mix}} = x^2 B_{11} + 2x(1-x)B_{12} + (1-x)^2 B_{22}, \qquad (4.4.14)$$

where x is the molar fraction of component 1 and B_{jj} is the second virial coefficient of the pure component j. B_{12} is then called the interaction second virial coefficient and physically can be interpreted as the contribution to B_{mix} which arises from the interaction energy between a pair of unlike molecules; it therefore depends upon the intermolecular potential U_{12} between a molecule of component 1 and a molecule of component 2. It is straightforward to work out the relationship between B_{12} and U_{12}. As a matter of fact, equation (4.4.2) still holds to relate B_{12} with the corresponding

U_{12}. Even quantum corrections to B_{12} can be applied in the same manner as for a pure component.

A relationship similar to (3.2.7) between second acoustic coefficient for a mixture β_{mix} and B_{mix} can be derived. For a binary mixture, this relation is:

$$(\beta_{\text{mix}}/2) = B_{\text{mix}} + P_a T(dB_{\text{mix}}/dT) + Q_a T^2 (d^2 B_{\text{mix}}/dT^2), \qquad (4.4.15)$$

which differs from (3.2.7) in the sense that both P_a and Q_a are functions of the mixture composition. Thus, one can not easily define a β_{12} by analogy with B_{12}. However, if one does assume that β_{mix} may be decomposed in manner similar to (4.4.14)

$$\beta_{\text{mix}} = x^2\beta_{11} + 2x(1-x)\beta_{12} + (1-x)^2\beta_{22}, \qquad (4.4.16)$$

then β_{ii} do not coincide with the second acoustic virial coefficients of the pure component i, $\beta_{a,i}$. This is because the coefficient P_a and Q_a in (4.4.15) are not simply mole-fraction-weighted averages of the pure component values. Accordingly, each pseudo acoustic virial coefficient β_{ij} is related with the second virial coefficient B_{ij} by means of

$$(\beta_{ij}/2) = B_{ij} + P_a T(dB_{ij}/dT) + Q_a T^2 (d^2 B_{ij}/dT^2), \qquad (4.4.17)$$

where P_a and Q_a refer to the mixture and are composition dependent. In (4.4.17), the composition-dependent β_{12} is then directly related with the unlike B_{12} and therefore to the intermolecular potential U_{12}. However, in order to implement equation (4.4.16) and obtain β_{12} from β_{mix} a calculation of the pseudo virial coefficient β_{jj} has to be made. Ewing and Trusler have proposed a method to determine these pseudo virial coefficients from information on the pure components.[10] The method consisted of calculating β_{jj} from

$$\beta_{jj} = \xi_{jj}(\beta_{a,j} - 2b_0) + 2b_0, \qquad (4.4.18)$$

where b_0 is a constant and the ratio ξ_{jj} is defined by

$$\xi_{jj} = (\beta_{jj} - 2b_0)/(\beta_{a,j} - 2b_0), \qquad (4.4.19)$$

and calculated from an intermolecular potential. The constant b_0 is chosen in such way that the denominator in (4.4.19) is different of zero inside the temperature range of interest. Thus, providing that one has an intermolecular potential that reproduces the acoustic virial coefficients of the pure components, equations (4.4.16), (4.4.18) and (4.4.19) can be employed to obtain β_{12}, which may then be used to optimise parameters of U_{12} by means of (4.4.17) and (4.4.13).

References.

1. Gray, C.G.; Gubbings, K.E.; *Theory of Molecular Fluids. Vol. 1: Fundaments*, Claredon Press: Oxford (1984).

2. Mayer, J.E.; Mayer, M.G.; *Statistical Mechanics*, John Wiley: New York (1940).

3. Mason, E.A.; Spurling, T.H.; *The International Encyclopedia of Chemical Physics. Vol.2: The Virial Equation of State*, Pergamon Press: Oxford (1969).

4. Maitland, G.C.; Rigby, M.; Smith, E.B.; Wakeham, W.A.; *Intermolecular Forces. Their Origin and Determination*, Claredon Press: Oxford (1981).

5. Hirshfelder, J.O.; Curtiss, C.F.; Bird, R.B.; *Molecular theory of gases and liquids*, John Wiley: New York (1954).

6. Maitland, G.C.; Smith, E.B.; *Chem. Phys. Lett.*, **22**, 443 (1973).

7. Pack, R.T.; *J. Chem. Phys.*, **78**, 7217 (1983).

8. Trusler, J.P.M., unpublished results.

9. Ewing, M.B.; Trusler, J.P.M.; *Physica A.*, **184**, 415 (1992).

10. Ewing, M.B.; Trusler, J.P.M.; *Physica A.*, **184**, 437 (1992).

Chapter 5. Apparatus and experimental procedure.

5.1 Introduction.

In this chapter the apparatus and experimental procedure are described. A discussion of pressure and temperature measurements including the calibration of the pressure transducer and thermometers is presented. A description of the electroacoustic transducers is also given because these were modified slightly in order to permit measurements of the speed of sound at temperatures higher than previously achieved. Further discussion concerning with the mechanical stability of the resonator and the reproducibility of the measurements is also presented here. Finally, the experimental procedure is outlined together with the systems studied in this work.

5.2 Description of the apparatus.

Most of the apparatus described below has been in operation for the past five years, thus its performance and capability are well known and speeds of sound of several systems have been measured in that period.[1-5] Although some improvements have been made on the whole system, most of the original features have been preserved. A description of the resonator and its environment follows.

5.2.1 Spherical resonator.

The acoustic resonator used in this work and shown in figure 1 is a spherical cavity fabricated from type 321 stainless steel, having an inner radius of approximately 40 mm and a wall thickness of 10.5 mm. The resonator was manufactured as hemispheres which were electron-beam-welded together at the equator. The external surface is also spherical except for cylindrical bosses at the top and the bottom of the shell which were used to hold the hemispheres during fabrication.

The gas admission port consisted of a 41 mm long tube with 1 mm internal diameter embedded in the upper boss of the sphere from which it protruded vertically by about 10 mm. This narrow tube was then accommodated inside the fixed inlet tube (2.6 mm id.) which terminates at its lower end in a circular flange bolted to the boss. This joint was sealed by means of a PTFE-coated stainless steel O-ring.

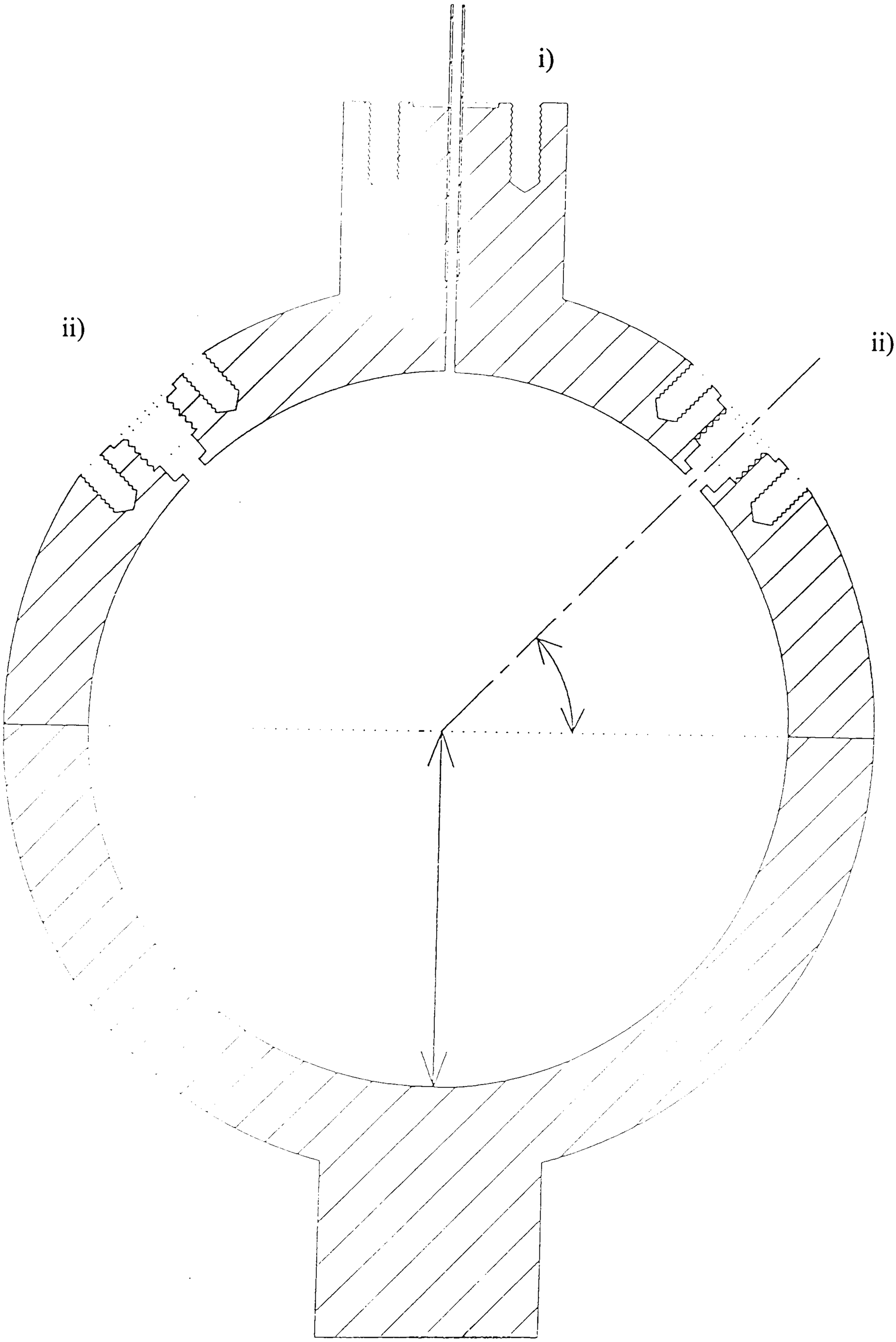


Figure 5.1 Cross-section of spherical resonator. i) gas entry port; ii) holes for housing electro-acoustic transducers.

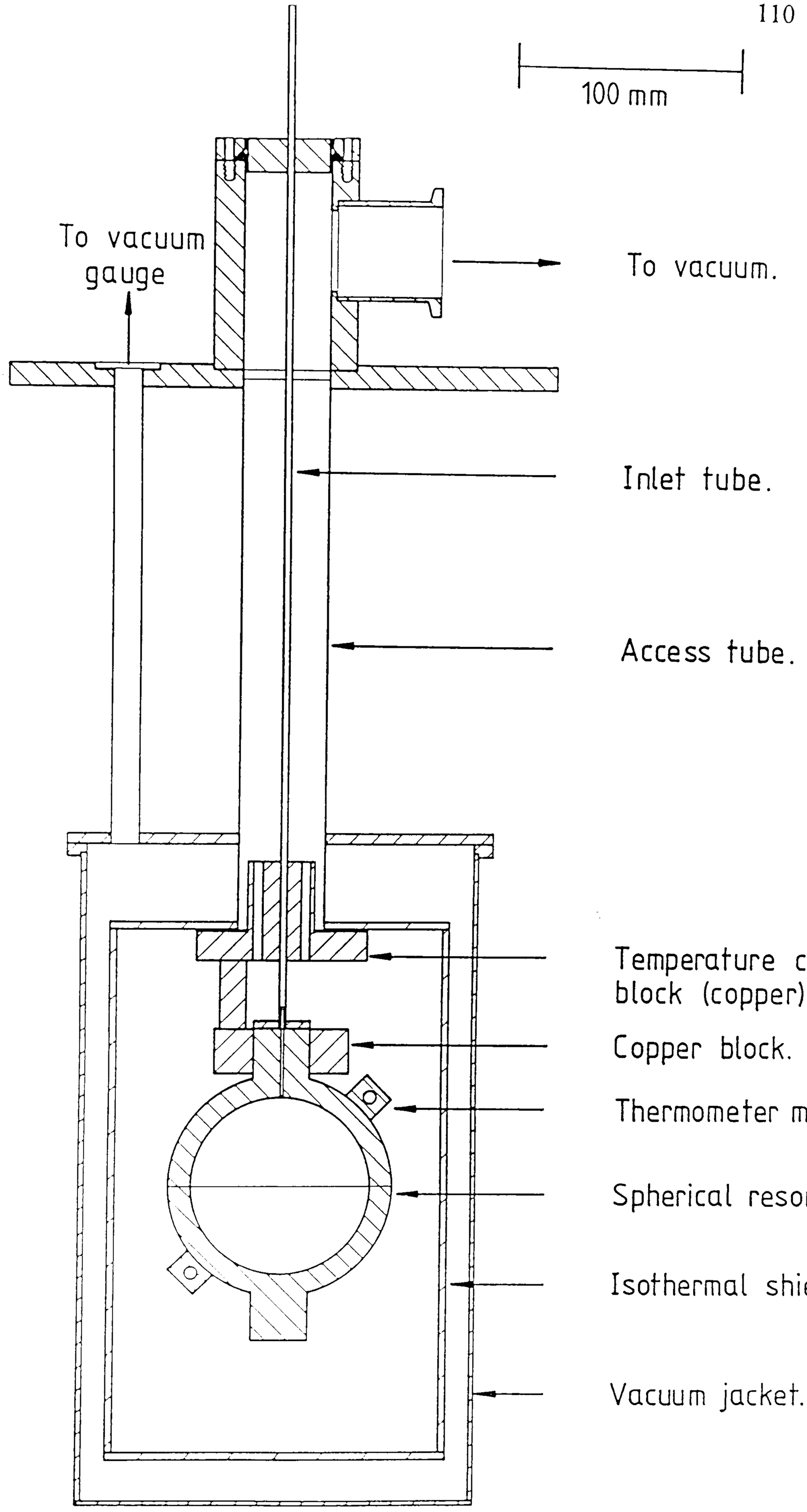


Figure 5.2 Cross-section of spherical resonator and thermostat.

In addition to the hole for gas entry, two orifices separated by 90° were drilled in the northern hemisphere of the resonator as shown in figure 1 and used to house the electroacoustic transducers. One of these was for the source of sound and the other for the detector. Further details of the assembly and operation of these transducers are described below.

As shown in figure 2 (which is another cross section of the apparatus but rotates by ninety degrees with respect to figure 1), the resonator is suspended from the upper boss inside a vacuum cryostat and firmly held in position by a copper clamp which also provided the thermal path between the resonator and the location at which the temperature was controlled. This enabled the necessary heat exchange to achieve thermal equilibrium. Moreover, the isothermal shield surrounding the resonator was important for promoting the thermal equilibrium, especially at high temperatures where radiation heat losses can be significant. However, the temperature control of the resonator was achieved mainly by heat conduction from the controlled copper block connected to the clamp that held the resonator by the copper post. Thermal equilibrium was attained by driving the control block in a proportional-integral servo loop. The isothermal shield had independent temperature control which **proved** to be useful especially at temperatures (above 400 K) where heat-radiation might cause **difficulties** in the control of the resonator's temperature. A booster heater was placed on the equator of the resonator to allow rapid changes in temperature and a fast recovery of the resonator after a release of gas. Programmable d.c. power supplies controlled by an HP workstation were used to drive the control block, shield base, shield side and resonator heaters. The maximum voltage delivered into the heaters was 30 V, but near control conditions it was considerably smaller, especially for the heater on the resonator.

The upper end of the gas inlet tube was connected to the pressure transducer and a system of valves placed inside an oven. The oven was normally off except when the experimental conditions were such that condensation of the gas would occur; in that case the oven was run at a moderated temperature just high enough to prevent condensation. Heaters housed on the inlet tube were also employed to prevent condensation there and to permit a smooth temperature profile between the resonator

and the oven. Crude temperature control of the oven and the inlet tube, say ± 1 K, seemed to be satisfactory.

The thermostat was designed for operation at temperatures from 80 K to 500 K, although in practice it was never set above 450 K. For temperatures below ambient, the thermostat was immersed in a Dewar filled with liquid nitrogen.

5.2.2 Temperature measurements.

Two of the key measured variables are temperature and pressure. They are of major importance and thus a detailed description of the thermometers follows and, in next section, the pressure transducers used in these experiments are described.

A new set of thermometers was used in this work to measured the temperature at several locations in the apparatus. They differs in design and number from the previous set of thermometers.[1,2] In total, five thermometers were fabricated especially for the present system. All were strain-free four-wires platinum resistance element package in cylindrical ceramic envelopes and approximately 50 mm long and 3 mm diameter. They were encapsulated in 0.5 mm thick glass tubes (outside diameter 5 mm) which were filled with an inert gas to enhance their response to temperature changes.

All the thermometers are housed in small metallic blocks. Two of these blocks were made of aluminium with one of their surface machined to match the curvature of the outer surface of the resonator, to which they were attached above and below the equator, as shown in figure 2. The other blocks, made of copper, were distributed around the thermostat; two of them on the isothermal shield and the other on the control block.

The thermometers were calibrated on ITS-90 by comparison with a standard thermometer (Tinsley serial number B249) which was itself calibrated on ITS-90 at the UK NPL prior to the measurements. This calibration held in the temperature range from the triple point of argon (83 K) to the freezing point of tin (505 K). The comparison took place at eight different temperatures in the above range, including the triple-point of water. The latter was measured at the beginning and repeated at the end of the calibration procedure. The ratios of resistances R_j/R_s, where R_j denotes the resistance of each thermometer and R_s represents a standard resistance (Tinsley model

5685 A, serial No. 259310) were measured with an AC resistance bridge (Automatic System Laboratories, model F17A). The standard resistance has a calibrated value of approximately 25 Ω at 293.15 K and is described by

$$R_s(T)/\Omega = 24.99988\{1 - 9.8\times10^{-8}[(T/K) - 293.15]^2\}\ . \qquad (5.2.1)$$

For each thermometer to be calibrated, the ratio $W = R(T_{90})/R(273.16\ \mathrm{K})$, was derived from the readings of R_j/R_s by means of equation (5.2.1) and with the resistance at the temperature of the triple-point of the water; here T_{90} is the temperature on the ITS-90. The calibration proceeded by fitting for each thermometer the ratios W at different temperatures to the following expressions[6]

$$W - W_{\mathrm{ref}} = a(W-1) + b(W-1)^2\,, \qquad (5.2.2)$$

and

$$W - W_{\mathrm{ref}} = c(W-1) + d(W-1)\ln W\,, \qquad (5.2.3)$$

where W_{ref} is a function of T_{90} defined by the ITS-90 standard and a and b are the calibration constants for $T > 273.16$ K while c and d correspond to $T < 273.16$ K. The two coefficients (for each temperature range) were determined from two points of the calibration rather than from a linear regression with all the information. These coefficients are given in table 1. Finally, during the experiments, all temperatures were determined from the resistance of the standard resistance by solving equations (5.2.2) and (5.2.3) by means of a simple Newton-Rhapson method.

The temperatures used to determine the calibration coefficients and the differences between the readings of each calibrated thermometer at the remaining temperatures and those obtained from the standard are given in table 2. The two thermometers that best reproduced their resistance readings at the triple-point of water (which also showed the smallest temperature differences from the standard thermometer) were selected for use on the resonator while the remaining thermometers were placed one on the control block and two on the isothermal shield (base and side); from each of these the temperature was inferred at those positions.

Table 5.1 Calibration constants of thermometers. Labels are as follow: 1) South sphere; 2) North sphere; 3) Control block; 4) Side shield; 5) Base shield.

j	a	b	c	d
1	$-5.035995\cdot10^{-4}$	$2.346425\cdot10^{-5}$	$-3.668175\cdot10^{-4}$	$-1.506903\cdot10^{-6}$
2	$-4.129805\cdot10^{-4}$	$-1.042040\cdot10^{-4}$	$-4.967975\cdot10^{-4}$	$-1.154610\cdot10^{-4}$
3	$-4.049632\cdot10^{-4}$	$-1.224446\cdot10^{-4}$	$-5.203358\cdot10^{-4}$	$-1.325574\cdot10^{-4}$
4	$-4.443676\cdot10^{-4}$	$3.060598\cdot10^{-5}$	$-3.038232\cdot10^{-4}$	$8.981468\cdot10^{-6}$
5	$-3.694536\cdot10^{-4}$	$-1.195541\cdot10^{-4}$	$-2.922011\cdot10^{-4}$	$5.017839\cdot10^{-5}$

Table 5.2 Difference of readings between the thermometers and the standard thermometer, $\Delta_j = (T_j - T_S)$. Thermometer labelled with j = 1, 2 correspond to those placed on the resonator. The temperatures selected to fit the coefficients were 100 K, 223 K, 298 K and 423 K.

T_S/K	Δ_1/mK	Δ_2/mK	Δ_3/mK	Δ_4/mK	Δ_5/mK
162.2403	1.0	0.9	-10.5	-12.9	1.8
371.1382	-0.6	-0.4	-1.6	0.2	-0.3
470.7775	-0.6	-1.2	4.2	6.3	-5.8

It must be stressed that the reproducibility of readings of these thermometers at the temperature of the triple-point of water was better than 5 mK during the calibrationand subsequent comparisons in the past two years have shown that their accuracy is better than 3 mK.

5.2.3 Pressure measurements.

Two Digitquartz pressure transducers were employed to measure the pressure; one was a Parascientific model 43K-101 with a pressure range from 0 to 20 MPa (serial No. 39004) while the other was a Parascientific model 2200A-101 with a more modest pressure range of 1.4 MPa (serial No. 51434). Hereafter, they will be mentioned as the high- and low-pressure transducers respectively. In both cases the pressure p is determine by measurements of the periods τ_p and τ_T of two quartz-crystal oscillators associated with the pressure and the temperature respectively and given by means of the following relations:

Table 5.3 Calibration coefficients of pressure transducers.

Coefficients	Pressure transducer	
	high	low
$U_0/\mu s$	5.869693	5.855695
$Y_1/°C\cdot\mu s^{-1}$	-3941.386	-3932.606
$Y_2/°C\cdot\mu s^{-2}$	-11128.22	-11762.27
$Y_3/°C\cdot\mu s^{-3}$	0.0	-7454.8.98
C_1/MPa	-60.70921	6.804023
C_2/MPa·μs^{-1}	9.93851	-0.01122356
C_3/MPa·μs^{-2}	254.5736	-11.62871
D_1	0.042475	0.220697
$D_2/\mu s$	0.145081	0.0
$T_1/\mu s$	31.080942	27.78001
T_2	2.261544	0.3450925
$T_3/\mu s^{-1}$	47.37557	15.34603
$T_4/\mu s^{-2}$	0.0	-61.47034
$T_5/\mu s^{-3}$	0.0	12.91698

$$\left.\begin{aligned} p &= C[1-(\tau_0/\tau_p)^2]\{1-D[1-(\tau_0/\tau_p)^2]\} \\ C &= C_1 + C_2U + C_3U^2 \\ D &= D_1 + D_2U \\ \tau_0 &= T_1 + T_2U + T_3U^2 + T_4U^4 + T_5U^5 \\ U &= \tau_T - U_0. \end{aligned}\right\} \qquad (5.2.4)$$

All coefficients C_j, D_j and T_j are given in table 3 together with U_0 (the zero-pressure period) for each pressure transducer. For the low-pressure transducer, the coefficients were taken directly from the manufacturer's calibration certificate while for the high-pressure transducer, some of them correspond to a recalibration performed near to the beginning of this work and the remaining to the original

calibration. New values were determined for C_1, D_1, D_2 and T_1 as described in the following.

The high-pressure transducer was calibrated against a certified oil-lubricated piston gauge. The pressure transducer and the oil-arm of the balance were connected through a Differential Pressure Cell (Ruska). This served both to isolate the gas from the oil by means of a metallic diaphragm housed inside the D P C and to accurately null the pressure difference between the two media. This calibration ranged from a pressure of 2.0 MPa to a pressure slightly above 20 MPa. Pressures, approximately evenly spaced were determined at increments of 2.0 MPa going first upwards from the lowest pressure to the highest and then reversing the sign of the increment. Small differences in the nominal pressure were found due to hysteresis effects, but using the average of both determinations a satisfactory fit for the calibration constant was obtained. The actual calibration followed a standard procedure described elsewhere.[7] The masses used during the calibration had been already characterised and from them the corresponding pressures were determined after applying all the appropriate corrections arising from the contribution of atmospheric pressure, buoyancy forces acting on the piston and the masses, the surface tension between the piston and the oil, and the deformation of the piston area with pressure and temperature. In addition, the transducer was kept under vacuum for several hours with the purpose of recording its zero-pressure period both before and after the calibration. This quantity is required to obtain a complete calibration for this type of pressure gauge.

For pressures below 1.4 MPa, an indirect calibration was performed by a simple comparison of the pressure readings between high- and low-pressure transducers when they were interconnected simultaneously to the resonator. This comparison presumed that the manufacturer's calibration of the low-pressure transducer was accurate (within the claimed uncertainty of 0.01 per cent of the full scale). From the results of this comparison between transducers, an irregular deviation in the reading of the high-pressure transducer was found that can be represented as a distorted gaussian function. The deviation was confined to a small range of about 200 kPa and had a maximum amplitude of roughly 1.5 kPa. Therefore a complete calibration required a combination of the results of both procedures from which an estimated overall uncertainty of the pressure was derived.

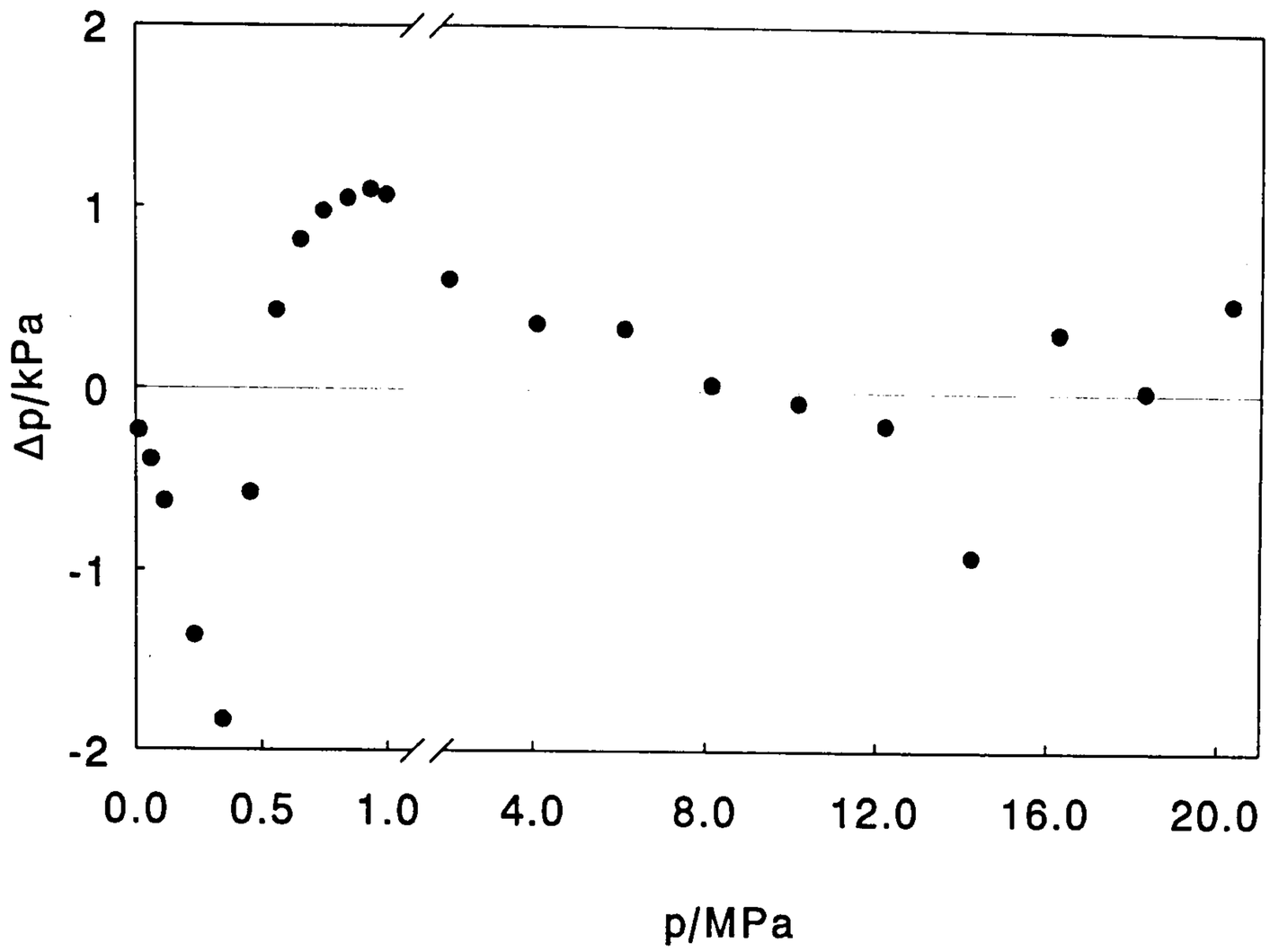


Figure 5.3 Deviation Δp of the readings of the high-pressure transducer after recalibration from those measured with the oil-piston gauge and the low-pressure transducer.

It seems that the pressure readings from high pressure transducer were not in an error larger than 0.5 kPa after application of the new calibration constants except in the region of the low pressure deviation which is discussed further below. Deviations of the true pressures from those determined from the high-pressure transducer after obtaining the calibration constants from a regression analysis are plot in figure 3.

Some additional remarks regarding the pressure measurements are appropriate. It was found that the low-pressure irregularity of the high-pressure transducer was not entirely reproducible and it apparently depended on the recent hydrostatic and thermal history. The location of the peak deviation varied by 200 kPa or 300 kPa with an average location at about 500 kPa. Some experimental evidence suggested that this deviation might vanish altogether if the transducer were at a temperature slightly higher than ambient. However, this evidence was not conclusive because of the lack of reproducibility of the behaviour. It was therefore normal practice during the measurements to skip the interval from 350 kPa to 650 kPa when working with this pressure transducer. If measurements in this interval were necessary because, for

instance, the pressure range was restricted by the saturation curve, pressure readings were taken using the low-pressure transducer instead.

5.2.4 Electroacoustic transducers.

The mechanical design of the electroacoustic transducer was the same for both source and detector. The active element of these transducers was a 3 mm diameter circular diaphragm made of polyamide film, 12 μm thick, with a 50 nm layer of gold on one side. They were placed nearly flush to the inner shell surface (see figure 1) and held in position by means of a ceramic sleeve. The back plate was held inside the ceramic sleeve and gently pushed towards the diaphragm by means of a small spring attached to the electrical feed-through in the cover plate. This cover plate was bolted directly to the resonator into 6 threaded blind holes. A pin-hole was made in the centre of each of these diaphragms to allow for the free passage of gas into and out of the trapped volume between the diaphragm and the back plate. This also reduces the acoustic stiffness of the system and enhances the sensitivity of transducer.[8]

In fact, this kind of electroacoustic transducer is known under the generic name of solid-dielectric capacitance transducer. These devices produce a net force upon the diaphragm when an electric field is applied across the plates of the transducer and this is responsible for the movement of the diaphragm. Conversely, if the separation of the plates is changed by movements of the diaphragm when the device is maintained under conditions of constant electric charge, a small potential difference can be detected and amplified. An interested property of these devices is that the force between the plates is proportional to the square of the electrical field, which in practice means that an alternate voltage with frequency f will produce a force, and hence sound, at frequency $2f$. This has an advantage as direct 'crosstalk' picked up by the detector may be filter out without affecting the acoustic signal at $2f$.

An electrical signal of frequency f and RMS amplitude 180 V was fed to the source transducer with no additional d.c. bias voltage, whereas the detector was charged with a 100 V d.c. bias voltage. An HP synthesiser, model 3325B, was used to generate the input electrical signal with high stability and accuracy and accordingly with the manufacturer specifications, it was estimated to be better than $\pm 1 \cdot 10^{-7} f$

during the time of collection of data. The necessary high voltage was obtained by means of a step-up transformer.

Unfortunately, both the displacement amplitude of the diaphragm and the acoustic pressure are very small and therefore a weak output electrical signal is obtained from the detector side. Amplification of the detected signal is therefore vital. However, since the electroacoustic transducer has a capacitance of the order of only 10 pF any small capacitance of a cable attached to the detector will act as a potential divider even though the length of this cable may be short. The simplest approach to overcome this problem has been to attach a pre-amplifier with unity gain just behind the detector. This had the effect of eliminating the capacitance of the cable since the output impedance of the pre-amplifier is low (on the order of 1 kΩ or less). Although this solution had been used in the past for this apparatus and had given satisfactory results,[1-3] there is a great disadvantage: the maximum temperature at which measurements can be made is restricted by the operational temperature range of the pre-amplifier. This restriction prevents measurements of the speed of sound at temperatures above around 375 K since the performance of the pre-amplifier declines with an increase in temperature.

The alternative solution to this problem, implemented in this work, consisted of connecting the detector to a remote unity-gain pre-amplifier through a tri-axial cable with an active guard. Here, the centre core carries the detected signal while the outer shield is ground. These are screened from each other by a co-axial guard which is fed with the output of the pre-amplifier. Since the pre-amplifier has a voltage gain near to unity no difference of potential exists across the capacitance between the guard and the signal wire even for cables as long as half of meter. This enables one to place the pre-amplifier where the temperature is close to the ambient. The design and specifications of this kind of pre-amplifier are discussed elsewhere.[9] Finally, the signal passing through this pre-amplifier was fed to a lock-in amplifier which measured its amplitude and phase. With this configuration, reliable measurements of the voltage can be made; in most cases, values of the resonance amplitude voltages were between 50 μV to 1 mV, though sometimes amplitudes as small as 5 μV were observed and it was still possible to measure them with an acceptable signal-to-noise ratio.

5.2.5 Radius of resonator.

One of the most important aspect of the measurements is to have an accurate calibration of the radius of the resonator. Indeed, the absolute accuracy of the speed of sound can be no better than that of the radius as equation (2.3.6) clearly suggests. In this sense, the technique is not an absolute one and a calibration of a is essential.

The problem is best split into two. Firstly, calibration of the zero-pressure radius a_0 using a gas with a known molar mass and perfect-gas heat capacity such as argon. Secondly, assuming that the resonator obeys the law of elasticity for an isotropic elastic shell, calculation of the dilation under the influence of the internal pressure p. Knowledge of Young's modulus and Poisson's ratio for the wall material is required for this purpose.

In the case of any mechanical instability, the situation is less promising. Whether or not any thermal or mechanical strain has changed the radius over time may be, at least partially, confirmed by making periodic checks on a_0. In the present case, such checks were made frequently as the resonator has been submitted to a very wide operational range of temperature and pressure. In fact, evidence of a problem was observed before this work started.[5] Thus, several times during nearly two years a_0 at 300 K was remeasured obtaining a reproducibility within 20 ppm, which is in fact the accuracy claimed in the initial calibration.[5] Unfortunately, a fractional change of a_0, at 300 K, amounting to about 50 ppm, was observed recently after taking the resonator to a pressures of 33 MPa. A new calibration was therefore carried out in the temperature range of 250 K to 350 K. It was found that a_0 has indeed changed and the new correlation differed from the previous one, in the worse case by about 55 ppm. So far, there is no satisfactory explanation of the change although it could be due to yielding in the highly pre-stressed welded area between the hemispheres. Nevertheless, the only measurements performed after this change were those on to the binary mixture. It should be noticed that, despite imperfect knowledge of the radius, it is still possible to derive accurate acoustic virial coefficients as described in § 3.2.3.

5.3 Experimental procedure.

In all experiments the procedure has been the same; the speed of sound was measured along isotherms, starting at the maximum pressure and then releasing gas to lower the pressure in predetermined decrements. Usually, these decrements were calculated to correspond to either a fraction of the critical density or, at temperatures below the critical temperature, a fraction of the saturated-vapour density. In this manner, the spacing of points in the (T,ρ_n) or (T,ϕ) plane formed a nearly rectangular grid. Only for the binary mixture was regular decrement in pressure itself preferred.

A correction to the pressure reading was applied to take into account the hydrostatic head of fluid (roughly h = 81.0 cm long) between the equatorial plane of the resonator and the pressure transducer. For this purpose, the temperature at four points along the inlet tube was measured together with the temperature of the oven where the pressure transducer was housed. Linear variations of density along the inlet tube were assumed and the correction for the hydrostatic head was calculated from:

$$\Delta p = \int_0^h g\rho(z)dz \approx \sum_{j=1}^{6} g\langle\rho\rangle_j h_j \qquad (5.3.1)$$

where g is the acceleration of the gravity, $\langle\rho\rangle_j$ is the average density in the interval h_j defined as the distances between adjacent thermocouples whose readings gave the temperature profile along the inlet tube. The densities were calculate from an equation of state.[10] This correction was applied for all experiments and, for instance, in argon it was never larger than 2.3 kPa.

The speed of sound was inferred from measurements of the frequencies at which a resonance inside of the acoustic cavity was observed. Normally, the non-degenerated radial resonance were used, though in exceptional cases a non-radial mode was included in the measurements.

5.3.1 Fit of radial modes.

At each state point, the pressure, temperature and the frequency of up to five radial resonance were determined and stored by an HP workstation for later analysis. The complex resonance frequency $F_N = f_{0n} + \mathrm{i}g_{0n}$ was determined from the measured complex voltage $W = U + \mathrm{i}V$ at the detector. Normally, eleven evenly spaced values of

W distributed around the estimated resonance frequencies were used, ranging from $f_{0n} - g_{0n}$ to $f_{0n} + g_{0n}$. The data were used to determine the parameters A, F_N, B and C in the equation

$$W = A/(F_N^2 - f^2) + B + C(f - f_0), \tag{5.3.2}$$

by means of a non-linear fitting routine of the type described by Mehl.[11] As normal practice, two slightly different fits of W to equation (5.3.2) were performed; in the first, C was constraint to be zero, while in the second it was a free parameter to be determined. A statistical comparison of both fits was used to select the most appropriate one. In most cases, three-term fits were adequate and the incorporation of the linear term in (5.3.2) neither improved the goodness of the fit nor changed significantly the complex frequency F_N already derived. However, it has been pointed out that, under some circumstances, neglecting such contributions would lead to systematic errors which may compromise the accuracy of the frequencies determined.[12]

Two set of measurements of the radial modes were taken at each state point and normally a reproducibility better of 1 ppm in f_{0n} was observed in successive set of measurements under conditions of thermal equilibrium.

5.3.2 Fit of non-radial mode (1, 1)

For the non-radial mode (1, 1), the procedure to obtain f_{11} and g_{11} was similar to that used for the radial modes except for the fact that the resonance model to which the data were fitted was more complicated because of the need to include three Lorentzian functions and 7 complex parameters in the fit. From (2.3.14), the following model is appropriate:

$$W = \sum_{i=1} A_i / (F_i^2 - f^2) + A_4 . \tag{5.3.3}$$

where all A_i and F_i are complex. This model is based on the fact that for an imperfect sphere, the degeneracy of the mode (1, 1) is, at least partially, lifted. Although the degeneracy of mode (1, 1) is completed lifted in the present resonator, two components out of the three for mode (1, 1) are quite close in frequency and are

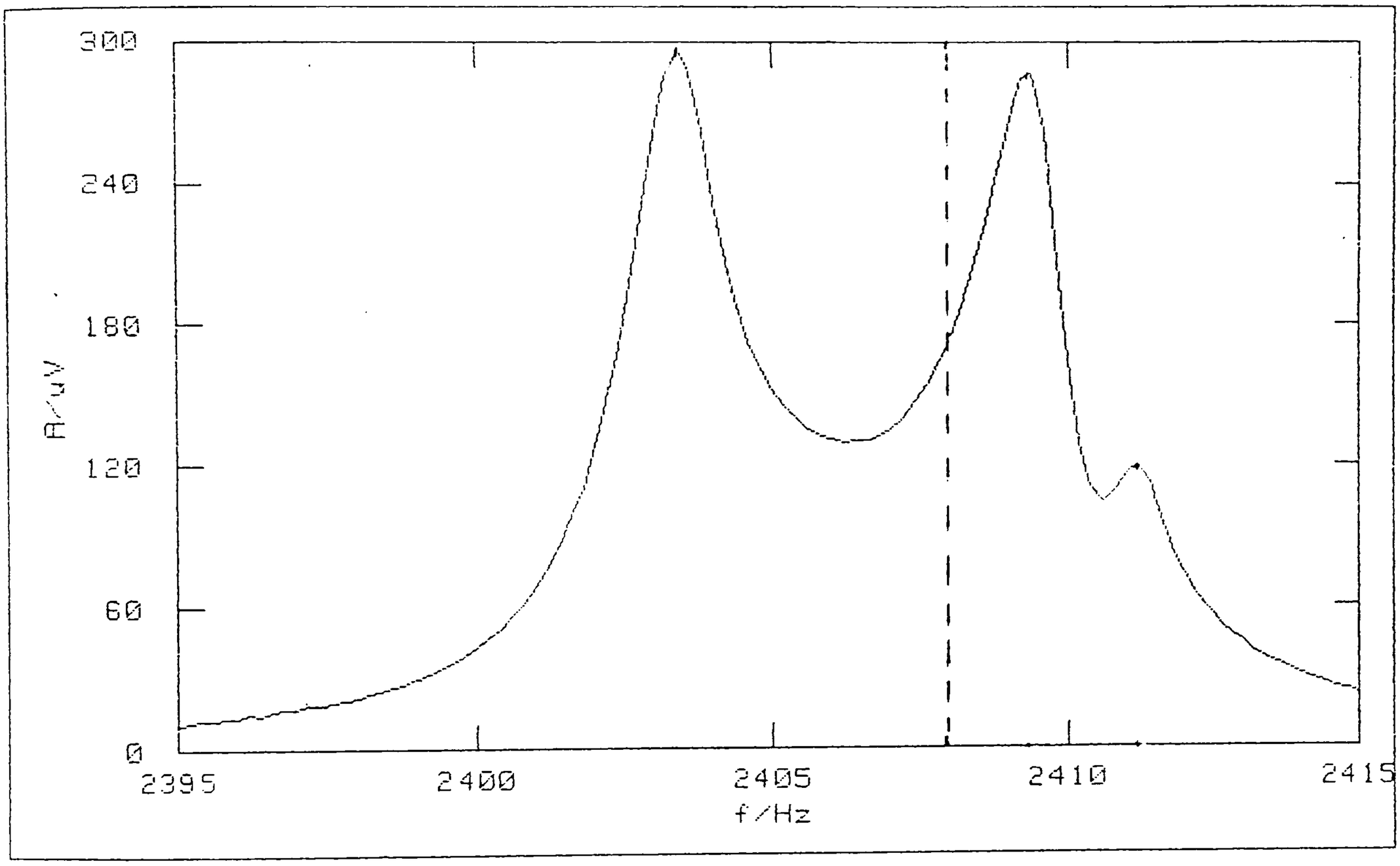


Figure 5.4 Resonance of mode (1, 1) in ethane at the $T = 275$ K and $p = 0.5$ MPa. Under these conditions, the three components are resolved giving a f_m (---) of about 2407.6 Hz.

difficult to resolve unless large quality factors for the resonance are observed -normally a g_{11} no greater than 1 Hz is required. Therefore, it is expected that mode (1, 1) can be fitted to (5.3.3) as long as g_{11} remains small.

Since the half-widths of any resonance suffer a significantly enlargement at low pressure, there may be a good opportunity for carrying out measurements of this mode only in an intermediate pressure range. Figure 4 illustrated this point. The gas used for the determination of the triplet is ethane. For high pressures, mode (1, 1) is well-resolved but, as the pressure is reduced, and hence g_{11} is enlarged, two of the components start to merge. Eventually, all three components fused together with the appearance of a very broad resonance at sufficiently low pressure. Under those circumstances, the model completely failed to yield any sensible result. Although (5.3.3) can be used in a straightforward way to determine the frequencies corresponding to each component of the triplet,[12] it was decided to take advantages of the relationship existing among all components of mode (1, 1).

From the solution of the wave equation for an ideal cavity, one can see that the components of mode (1, 1) will produce a pressure field proportional to

$$p_\omega(\boldsymbol{r}|\boldsymbol{r}_0) \propto \sum_{j=1}^{3} \frac{\phi_{N_j}(\boldsymbol{r},\omega)\phi^*_{N_j}(\boldsymbol{r}_0,\omega)}{\Lambda^0_{N_j}[F^2_{N_j} - f^2]}, \tag{5.3.4}$$

where $\boldsymbol{r}_0$ and $\boldsymbol{r}$ are the position of the source and detector and ϕ_{N_j} are given by (2.3.4). and the indices N_j represent the set of numbers (n_j, l_j, m_j) with $j = 1, 2, 3$. In fact, all $n_j = 1$, all $l_j = 1$ and $m_j = 0 \pm 1$. Assuming that the co-ordinates of $\boldsymbol{r}_0$ and $\boldsymbol{r}$ are $(r_0 = a, \theta_0 = \pi/4, \varphi_0 = \pi/2)$ and $(r = a, \theta = \pi/4, \varphi = 3\pi/2)$ respectively, together with the expression for the normalisation constant

$$\begin{aligned}\Lambda^0_N &= (3/2) j_l^2(k_{ln}a)[\{1 - l(l+1)\nu_{ln}^{-2}\}/(2l+1)][(l+|m|)!/(l-|m|)!] \\ &= (1 - 2\nu_{11}^{-2})[j_1^2(k_{11}a)/2][(l+|m|)!/(l-|m|)!],\end{aligned} \tag{5.3.5}$$

one finds that the (5.3.4) can be reduced to

$$p_\omega(\boldsymbol{r}|\boldsymbol{r}_0) = a_1 \exp(i[\delta+\pi])/[F_1^2 - f^2] + a_2 \exp(i\delta)/[F_2^2 - f^2] + a_3 \exp(i[\delta-\pi])/[F_3^2 - f^2] + A_4 + \cdots, \quad (5.3.6)$$

where a_i are now real parameters and δ denotes an arbitrary phase. Moreover, Moldover *et al.* have shown, that to a first order approximation, all components have the same halfwidth $g_i = g_{11} = g$ and the average frequency f_m corresponds to f_{11} in the ideal cavity.[13] In other words, f_m defined by $(f_m - f_1) + (f_m - f_2) + (f_m - f_3) = 0$, is identified with f_{11} with an eigenvalue $\nu_{11} = 2.081576$. Introducing the real parameters $X_i = f_m - f_i$, the complex resonance frequencies F_i may be written

$$F_i = (f_m - X_i) + ig = (f_{11} - X_i) + ig_{11}. \quad (5.3.7)$$

It turns out to be useful to express one of the X_i in terms of the other two, for instance, $X_3 = -(X_1 + X_2)$. Finally, the model (5.3.3) can be expressed in a simplified way,

$$W = \frac{a_1 \exp(i[\delta+\pi])}{(f_m - X_1 + ig)^2 - f^2} + \frac{a_2 \exp(i\delta)}{(f_m - X_2 + ig)^2 - f^2} + \frac{a_3 \exp(i[\delta-\pi])}{(f_m + X_1 + X_2 + ig)^2 - f^2} + A_4, \quad (5.3.8)$$

where we have reduced the number of parameters to be fitted from 14 in (5.3.3) to 10, or 8 if the constant background term is neglected. Once again the strategy of constraining one complex parameter, namely A_4, in a first fit was applied. In fact, a small modification of the existing algorithm to fit radial modes was required to cope with (5.3.8). Since for the present resonator X_i is of the order of few Hz, the pattern described by the triplet may extent over roughly 10 Hz. This means that a substantial number of points are required to cover the whole resonance. Thus, the number of points recorded was increased to 44 and the range was increased to between 5 and 6 times g_{11}. It is important to comment that since the model used to fit W is a non-linear function, the determined F_{11} may depend strongly on the initial guess for the eight parameters. Apart from f_{11}, X_1 and X_2, for which sensible guesses can be proposed, the initial guess for the remaining parameters may be quite ambiguous and it is easy to make a poor choice that may introduce a systematic error in F_{11}.

Normally, there was no problem in finding and measuring the lowest five radial modes. However, in some cases, the frequency range of one the modes was such that coupling with shell motion would affect them considerably. In addition, a special situation occurred in carbon dioxide, where vibrational relaxation strongly enhanced the sound absorption. The latter difficulty was particularly acute in carbon dioxide during measurements carried out at 220 K and 250 K where strong sound absorption resulted in loss of the modes with $n > 2$. In that case, the mode (1, 1) was employed in addition to the mode (0, 2).

5.4 Substances.

The speed of sound was measured in the following four gaseous systems: argon, ethane, carbon dioxide and a binary mixture containing approximately 60 mole per cent carbon dioxide plus 40 mole per cent ethane.

5.4.1 Argon.

Research grade argon was supplied by British Oxygen Company with a claimed purity of 99.9999 mole per cent; no attempt at purification was made. Twenty one isotherms were measured in argon covering the temperature range from 110 K to 450 K. Nine of these isotherms were below the critical temperature $T^{c} = 150.8$ K, 150 K being the isotherm closest to T^{c}. For all $T \geq 150$ K the pressure reached was estimated to correspond to one half of the critical density, $\rho_n^{c} = 13.41$ mol·dm^{-3}, except for 400 K and 450 K where the pressure was restricted to be at most 19 MPa since maximum working pressure of the pressure transducer is 20 MPa. On the other hand, for $T < 150$ K the maximum pressure reached corresponded to roughly 80 per cent of the saturated vapour density ρ_n^{σ}. The distribution of temperatures was chosen to give nearly even spacing in reciprocal temperature.

5.4.2 Ethane.

Research grade ethane was supplied by Praxair with a claimed purity of 99.997 mole per cent. In order to reach the much higher pressure required to perform the experiment at half of the critical density, a stainless-steel sample cylinder of 330 cm^3 volume was filled with the contents of the gas cylinder. A heater was wrapped around

this sample cylinder to raise the temperature and thence the pressure. Unfortunately, in some initial experiments, the gas was contaminated, and as consequence of this, inconsistent results were obtained. Therefore, before restarting the measurements two initiatives were taken. Firstly, the resonator was baked at 450 K for more than 72 hours keeping it under vacuum during that period of time. Secondly, a series of degassing cycles were applied to the gas contained inside of the sample cylinder until the residual pressure of the frozen sample was negligible (below 100 Pa). Finally, several flushes to the resonator and pipes with this "clean" ethane were performed before taking any measurements. In this case, seventeen isotherms were measured covering the temperature range from 220 K to 450 K. Ten of them were below $T^{c} = 305.33$ K, 305 K being the isotherm closest to T^{c}. For all $T \geq 300.65$ K the pressure reached was estimated to correspond to half of the critical density, $\rho_n^{c} = 6.875$ mol·dm^{-3}; for the isotherm at 300.65 K this density corresponds to nearly 96 per cent of ρ_n^{σ}, and contrary to other reported research,[14] no pre-condensation phenomena were observed. At 450 K the greatest pressure reached 10.5 MPa.

5.4.3 Carbon dioxide.

Research grade carbon dioxide was supplied by British Oxygen Company with a claimed purity of 99.999 mole per cent; no purification was attempted. For this system, seven isotherms were measured covering the range from 220 K to 450 K and with a pressure distribution similar to that described earlier; at 450K the greatest pressure reached was 14.1 MPa. Since the critical temperature for carbon dioxide, $T^{c} = 304.11$ K, is quite similar to that of ethane, the same sort of difficulties were found in reaching the desired pressure (that corresponding to half the critical density, $\rho_n^{c} = 10.627$ mol·dm^{-3}). Thus, a quantity of the gas was condensed in the sample cylinder mentioned above and the temperature raised until the desired pressure was reached. This procedure was followed for the isotherms at 350 K, 400 K and 450 K.

5.4.4 Mixture of carbon dioxide and ethane.

Seven isotherms for a binary mixture of carbon dioxide and ethane were measured in the range from 220 K to 450 K and pressures up to 1.2 MPa. The carbon dioxide used for preparing the mixtures was the same as that use for the measurements on the pure

component while for ethane a new sample, but from the same manufacturer, was used since the previous supply was exhausted at the end of the measurements on the pure component. The purity of this new ethane was again claimed to be 99.997 mole per cent and no further purification was attempted. The mixture was prepared in the same sample cylinder used in previous systems by condensing back the contents of the resonator, which was employed as a *pVT* cell to measure approximately the amount of substance of each component. Firstly, the carbon dioxide was transferred from the sample cylinder into the resonator. After estimating the amount of substance from the temperature, pressure and volume of the sphere, the contents of the resonator where condensed into the previously evacuated sample cylinder (which was immersed in liquid nitrogen). The desired amount of substance was obtained after several cycles of this procedure. Next, the ethane was added by the same method. After completing the transference process, the sample cylinder was removed from the liquid nitrogen and brought gently to room temperature. The nominal composition was planned to be 0.6 mole fraction of carbon dioxide since this nearly corresponds to the azeotropic composition of the mixture at 220 K and this allowed a slightly wider pressure range. The pressure at the azeotrope at 220 K is roughly 800 kPa.[15] In any case, the actual composition was worked out from an analysis of the zero-density speed of sound, as described in next chapter.

References

1. Trusler, J.P.M.; Zarari, M.; *J. Chem. Thermodynamics*, **24**, 531 (1992).

2. Trusler, J.P.M.; Wakeham, W.A.; Zarari, M.; *High. Temp. High. Press.*, **25**, 293 (1993).

3. Trusler, J.P.M.; *J. Chem. Thermodynamics*, **26**, 751 (1994).

4. Trusler, J.P.M.; Wakeham, W.A.; Zarari, M.; *Int. J. Themophys.*, **17**, 35 (1996).

5. Estrada-Alexanders, A.F.; Trusler, J.P.M; *J. Chem. Thermodynamics*, **27**, 1075 (1995).

6. National Physical Laboratory, *Certificate of Calibration: Platinum resistance thermometer serial number B249*, april 1990.

7. Roe, D.R.; *PhD Thesis*, University of London (1972).

8. Trusler, J.P.M.; *Physical Acoustic and Metrology of Fluids*, 1991, Adam Hilger: Bristol. (pag . 160)

9. Horowitz, P.W.; Hill, W.; *The Art of Electronics*, 1980, 1st ed., Cambridge University Press: Cambrigde.

10. Lee, B.I.; Kesler, M.G.; *AIChE Journal*, **21**, 510 (1975).

11. Mehl, J.B.; *J. Acoust. Soc. Am.*, **64**, 1523 (1978).

12. Ewing, M.B.; Trusler, J.P.M.; *J. Chem. Phys.*, **90**, 1106 (1989).

13. Moldover, M.; Mehl, J.B.; Greenspan, M.; *J. Acoust. Soc. Am.*, **79**, 253 (1986).

14. Mehl, J.B.; Moldover, M.R.; *J. Chem. Phys.*, **77**, 455 (1982).

15. Brown, T.S.; Kidnay, A.J.; Sloan, E.D.; *Fluid Phase Equilibria*, **40**, 169 (1988).

Wei, M.S.-W.; Brown, T.S.; Kidnay, A.J.; Sloan, E.D.; *J. Chem. Eng. Data*, **40**, 726 (1995).

Chapter 6. Experimental results.

6.1 Introduction.

The results of the speed-of-sound measurements on the four gases studied in this work are presented in this chapter together with the zero-density sound speeds and acoustic virial coefficients determined from them.

6.2 Analysis of uncertainties in speed of sound.

Before discussing the results, an analysis of the likely experimental uncertainties in u is presented. The acoustic model employed to determine the speed of sound from the measured resonance frequencies follows from equation (2.3.22) and may be expressed as

$$(u/a_0) = (2\pi a/a_0)(f_{ln} - \sum_j \Delta f_j) / \nu_{ln} \,. \qquad (6.2.1)$$

This gives directly (u/a_0), where a_0 is the mean radius of the resonator at the temperature in question but at zero pressure. The summation includes all the small corrections described earlier. In addition, the experimental half-widths g_{ln} were systematically compared with those predicted by equation (2.3.23). The aim of this test was to verify that all transport and thermodynamic properties involved in calculating the frequency shifts were essentially correct. Although this would not be consider as a definitive proof that the behaviour of the resonator follows the acoustic model, it is indeed a very good indication. When dealing with polyatomic gases, the analysis of the excess half-widths Δg_{ln}, defined as the difference between the experimental and calculated g_{ln}, gives information about any relaxation phenomena taking place. Commonly, a small Δg_{ln} is found even for a monatomic gas and this most probably reflects the presence of a real additional loss mechanism. Therefore, rather than trying to null Δg_{ln} for a polyatomic gas, it is more realistic to allow for a small but finite Δg_{ln}. It seems that an acceptable tolerance in the present resonator is about $\Delta g_{ln} / f_{ln} = 10^{-5}$. A larger value of Δg_{ln} may indicate that a correction for relaxation in the gas has to be made or that a serious error has occurred.

In the rest of this section we concentrated on the analysis of sources of uncertainties associated with all factors involved in the calculation of u from experimental quantities. The description of the radius calibration will be presented together with the results for argon since from these measurements a_0 was determined. An extensive assessment of the propagation of uncertainties was performed in connection with the measurements on argon.[1] All estimates of uncertainty were carried out numerically by perturbing the associated variable by an amount equal to its estimated uncertainty and determining the change in the computed speed of sound. Similar results are expected with other gases and the conclusion will therefore be applied to each set of measurements.

From equation (6.2.1) it is easy to see that sources of uncertainties in u arise from the measured f_{0n}, the radius of the resonator and from each of the correction terms. Furthermore, estimates are included of $(\partial u/\partial p)_T \delta p$ and $(\partial u/\partial T)_p \delta T$ corresponding to the effects of uncertainties δp and δT in the measured pressure and temperatures. As discussed in connection with the calibration of the thermometers, the uncertainty of the measured temperature is estimated to be ± 3.0 mK but the precision is much better than 1 mK. This level of uncertainty in the temperature seems to be negligible since u is a very smooth function of temperature and normally the temperature control was better than 1 mK while experiments were carried out. Furthermore, most of the temperature uncertainty is concentrated in the characterisation of a_0. This is not the case for the pressure, where the maximum likely uncertainty δp = 1.5 kPa can give rise to an uncertainty of up to $60 \cdot 10^{-6} \cdot u$ at the highest pressure along the isotherm at 150 K in argon. The second largest source of uncertainty arises from inaccurate knowledge of the elastic constants used in the calculations of both the ratio (a/a_0) and the correction for coupling between the gas and the shell motion. The estimated 5 per cent uncertainty in both Young's modulus and the Poisson's ratio[2] produced an uncertainty which increases with pressure and reaches about $35 \cdot 10^{-6} \cdot u$ at p = 19 MPa.

The remaining sources of uncertainty for u/a_0 are those associated with the transport properties and the thermodynamic properties employed in the calculations.

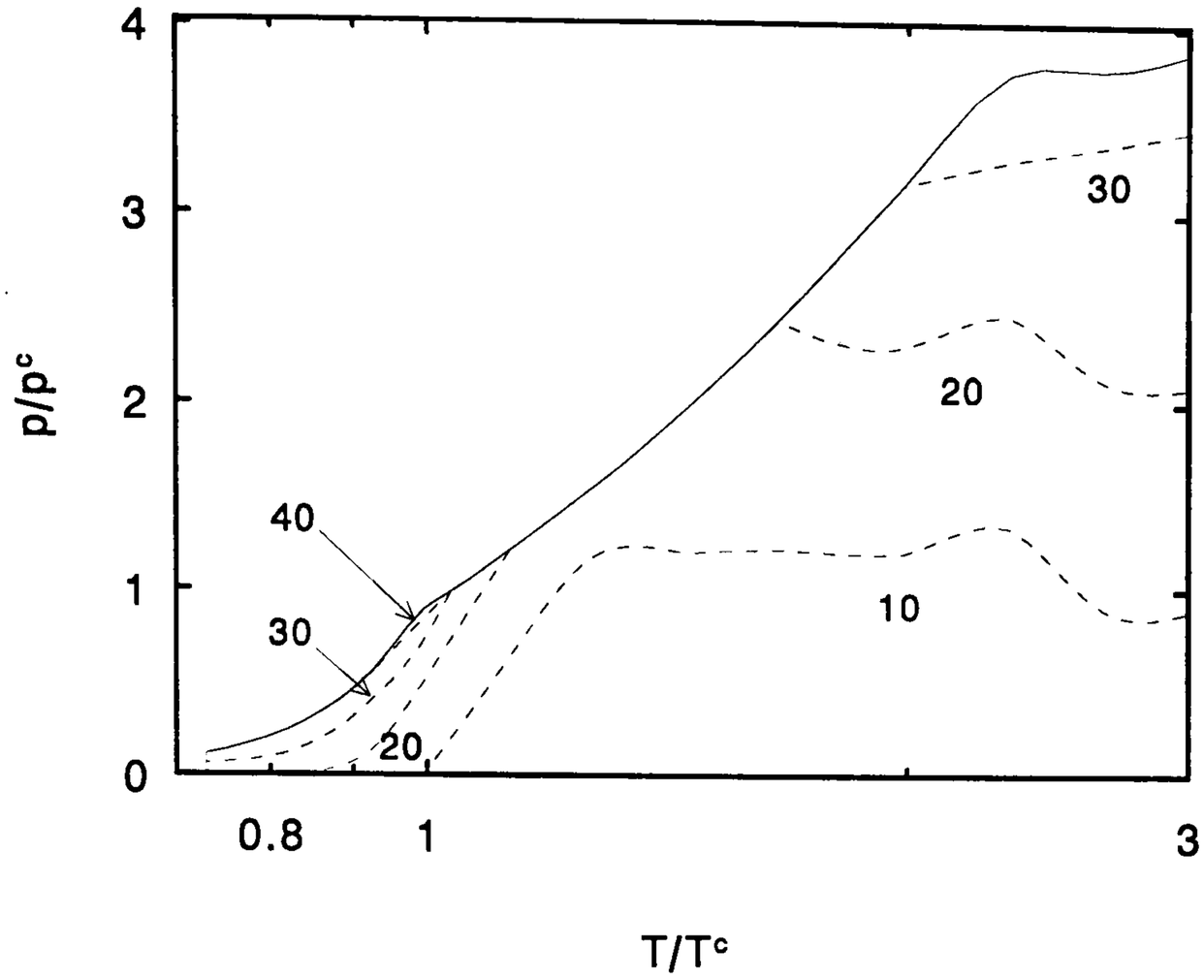


Figure 6.1 Diagram of the fractional uncertainty $\delta u/u$ in the speed of sound u as a function of the reduced temperature T/T^c and pressure p/p^c. (- - -), contour of constant $\delta u/u$ labelled with the value of $10^6 \cdot \delta u/u$; (——), boundary of the measurements.

For the former, numerical calculation have shown that uncertainties in the thermal conductivity κ amounting to 4 per cent[3] introduced uncertainties of only $5 \cdot 10^{-6} \cdot u$ in the worse case while for the viscosity η, a similar level of imprecision,[3] had negligible effect. Since the worst case corresponds to a low pressure where the thermal boundary layer corrections become significant, it is expected that the uncertainty of the thermal conductivity will be much less important in the dense fluid and thus the probably errors arising from this source could be neglected in most cases. Similarly, likely errors in the Lee-Kesler equation of state[4] used to determine the equilibrium properties were inconsequential since the corrections do not demand highly accurate determination of the density and heat capacities. Finally, the uncertainty of u arising from the determination of a_0 was estimated to be $10 \cdot 10^{-6} \cdot u$ in the worst case. A linear combination of all significant sources of uncertainty was adopted as an upper-bound of the probable error in the speed of sound. This is illustrated for argon in figure 1 in terms of reduced variables p/p^c and T/T^c (p^c = 4.9383 MPa and

T^c = 150.8 K). Only in a small region near to the critical pressure and temperature does the uncertainty exceed $40 \cdot 10^{-6} \cdot u$. Since the major sources of the uncertainties are entirely dependent on either the properties of the resonator (elastic constants) or the enhanced curvature of u in the region close to the critical point (as consequence of the nonanalytical behaviour near to the critical point), it is suggested that the diagram of uncertainties depicted in figure 1 gives a good idea of the uncertainties for values of u determined with this resonator for any other gas if the state point (T,p) is expressed in terms of reduced variables.

Only one more factor will modify these estimates: uncertainty arising from corrections due to relaxation in the gas. A significant error will arise from neglecting that phenomena at low pressures for polyatomic but one may expect that the error will be reduced or eliminated by the application of the appropriate correction. Based on the experience of this work, one can claim that the accuracy of the speed of sound deteriorates only slightly (possibly up to three times the bound of uncertainty given above) in the few measurements performed on carbon dioxide (the system studied in this work with the most severe dispersion absorption) at low pressures.

6.3 Argon.

Highly-accurate determinations of the speed of sound of argon were obtained in a temperature range from 110 K to 450 K, reaching pressures up to 19 MPa. The main objective of this set of measurements was to derive the thermodynamic properties of argon by means of the numerical integration discussed in chapter 3. In addition, the radius of the resonator was calibrated, as described below, from these measurements since both the molar mass and the perfect-gas heat capacities are known. The method of analysis used for obtaining the radius gave also values of the acoustic virial coefficients.

6.3.1 Speed of sound.

The speed of sound was determined according to the acoustic model (6.2.1) mostly from the five lowest radial modes. For most of the isotherms the quality factor of each resonance $Q = (f/2g)$ was between values of 8000 to 12000 which implies that very sharp resonances were found in most cases. However at 450 K, Q diminished to

values of no larger than 5000; in addition, a decline of the signal-to-noise ratio (which otherwise was very favourable) was observed at that temperature. This condition affected the observed resonances in such a way that only modes (0, 2) to (0, 4) could be measured. After all the measurements were taken in argon, it was found that the deterioration of the signal-to-noise ratio was due to a small electrical leakage in the electrical feedthrough mounted in the cover plate of the detector transducer. Nevertheless, good results were obtained at 450 K by simply increasing the time constant of the lock-in amplifier to counter the noise. Thus, it was not necessary to repeat those measurements. The fault was late repaired by replacing the damage cover plate with a new one.

The same equation of state[4] used in the analysis of uncertainties was then used to evaluate all the thermodynamic properties required for the corrections to the experimental frequencies. Transport properties for argon were obtained from the correlation of Younglove and Hanley.[3]

The values of (u/a_0) determined from the five radial modes at each state point generally agreed to better than $\pm\, 2{\cdot}10^{-5}$ (u/a_0) over the entire range of measurements. However, larger deviations were found at pressures as low as 5 MPa for temperatures of 350 K and above. This disagreement did not show any systematic trend for higher order modes (0, n), with $n \geq 3$. In figure 2 this behaviour is illustrated for the isotherm at 350 K. The tendency of one or more of the modes to depart from the average of the remaining modes has been observed previously in this[5] and others resonators.[6] When this behaviour was observed, the affected mode or modes were rejected from the analysis either at individual state points or along the complete isotherm. The value u/a_0 at each state point was obtained as a weighted average of the remaining modes, where the statistical weight is given by the lesser of $(2{\cdot}10^{-6}{\cdot}f/\delta f)^2$ and unity, with δf being the estimated uncertainty of the resonance frequency. Generally, the fractional imprecision of a resonance frequency $\delta f/f$ was less than 10^{-6} so that all selected modes received the same weight. Finally, using the correlation for a_0 discussed below, the absolute speed of sound u was determined; the final results for argon are reported in table 1. Small corrections were applied to reduce all values to the specified temperature for each isotherm.

Table 6.1 Speeds of sound u in argon at temperatures from 110 K to 450 K and pressures up to 19 MPa. For uncertainties in u, see figure 6.1.

p/kPa	u/m·s^{-1}	p/kPa	u/m·s^{-1}	p/kPa	u/m·s^{-1}	p/kPa	u/m·s^{-1}
			T = 110.00 K				
546.88	185.618	398.11	188.563	235.70	191.493	61.25	194.381
501.33	186.551	344.47	189.560	178.24	192.471	6.83	195.234
450.17	187.564	290.89	190.526	119.89	193.437		
			T = 120.00 K				
995.48	189.434	745.20	193.729	453.21	198.119	112.71	202.639
933.16	190.560	654.27	195.158	343.90	199.630	59.47	203.301
842.92	192.123	557.60	196.614	232.59	201.109	12.09	203.880
			T = 130.00 K				
1729.36	190.782	1312.63	197.357	807.43	203.841	215.90	210.244
1605.56	192.903	1155.04	199.513	618.16	206.002	104.34	211.348
1460.87	195.187	982.50	201.728	413.17	208.217	21.28	212.154
			T = 135.00 K				
2217.80	190.683	1738.91	198.139	1090.57	205.981	302.09	213.753
2098.40	192.749	1528.10	200.893	837.33	208.636	31.02	216.138
1924.65	195.486	1316.43	203.443	572.96	211.240		
			T = 140.00 K				
2842.29	189.228	2263.13	198.466	1447.16	207.824	404.88	217.187
2689.29	192.046	1999.75	201.787	1120.70	210.977	201.69	218.811
2485.07	195.324	1744.12	204.709	782.33	214.017	41.82	220.054
			T = 143.00 K				
3286.94	187.620	2632.11	198.464	1718.39	208.648	496.60	219.060
3094.05	191.430	2364.84	201.795	1336.10	212.174	52.20	222.349
2881.30	194.934	2055.43	205.246	930.69	215.623		

Table 6.1 -continued

p/kPa	u/m·s^{-1}	p/kPa	u/m·s^{-1}	p/kPa	u/m·s^{-1}	p/kPa	u/m·s^{-1}
			T = 146.00 K				
3722.20	186.827	3076.12	197.941	2047.61	209.187	604.19	220.863
3580.57	189.890	2811.54	201.255	1635.98	212.835	62.27	224.629
3357.78	193.835	2468.41	205.058	1126.50	216.961		
			T = 148.00 K				
4112.10	184.175	3494.87	196.229	2412.06	208.395	716.43	221.816
3969.88	187.856	3183.49	200.301	1889.95	212.968	74.47	226.104
3772.17	191.822	2832.96	204.241	1349.21	217.242		
			T = 150.00 K				
4428.49	184.033	3755.82	197.021	2635.19	209.081	774.72	223.179
4287.32	187.826	3453.18	200.829	2093.11	213.649	71.44	227.670
4059.51	192.371	3081.42	204.850	1415.36	218.768		
			T = 156.08 K				
4923.47	197.396	4124.78	205.556	2789.85	215.911	836.23	228.080
4745.07	199.451	3752.41	208.721	2218.46	219.728	83.18	232.240
4446.59	202.552	3285.01	212.355	1575.35	223.746		
			T = 163.15 K				
5567.54	209.801	4492.35	215.308	2978.11	223.375	863.57	233.878
5264.84	211.238	4058.46	217.648	2351.37	226.589	88.54	237.492
4876.39	213.248	3551.52	220.360	1653.48	230.066		
			T = 170.00 K				
6064.00	221.065	4847.85	224.056	3173.40	230.219	893.60	239.304
5694.60	221.700	4340.25	225.801	2472.50	232.997	82.89	242.514
5297.00	222.688	3799.75	227.800	1675.80	236.181		
			T = 180.00 K				
6761.72	235.521	5347.67	235.983	3417.30	239.900	950.97	246.942

Table 6.1 -continued

p/kPa	u/m·s^{-1}	p/kPa	u/m·s^{-1}	p/kPa	u/m·s^{-1}	p/kPa	u/m·s^{-1}
6399.80	235.320	4753.71	236.921	2657.64	241.925	99.62	249.570
5886.94	235.450	4124.64	238.204	1832.53	244.292		
			T = 190.00 K				
7621.95	248.826	5850.55	247.062	3698.43	248.991	1009.53	254.317
7072.60	247.811	5176.91	247.318	2857.32	250.422	96.86	256.490
6472.16	247.217	4456.48	247.972	1894.88	252.347		
			T = 205.00 K				
8599.18	266.383	6602.84	262.520	4064.44	261.981	1104.69	264.965
8110.16	265.075	5790.71	261.917	3125.88	262.611	115.84	266.480
7389.49	263.596	4952.11	261.746	2121.78	263.636		
			T = 220.00 K				
9916.43	283.452	7349.81	276.882	4472.01	274.206	1190.32	275.187
9070.47	280.773	6389.73	275.518	3396.05	274.148	117.41	276.135
8199.04	278.551	5462.52	274.670	2261.85	274.511		
			T = 250.00 K				
12169.04	313.176	8796.08	303.058	5254.53	296.948	1364.50	294.514
11043.88	309.299	7648.13	300.607	3982.70	295.720	142.22	294.473
9961.98	306.050	6453.30	298.546	2657.39	294.904		
			T = 300.00 K				
15752.36	355.638	11203.07	341.520	6451.25	330.824	1698.68	324.119
14341.42	350.864	9641.04	337.545	4909.56	328.233	164.55	322.724
12811.90	346.084	8046.32	333.952	3307.33	325.970		
			T = 350.00 K				
18731.85	390.833	13583.94	375.487	7786.70	361.461	1918.08	351.036
17423.24	386.693	11523.51	370.086	5748.61	357.407	187.88	348.679
15473.18	380.819	9645.05	365.560	3723.17	353.839		

Table 6.1 -continued

p/kPa	u/m·s^{-1}	p/kPa	u/m·s^{-1}	p/kPa	u/m·s^{-1}	p/kPa	u/m·s^{-1}
			T = 400.00 K				
18822.10	414.157	13657.74	400.283	7682.04	386.440	1894.25	375.521
17764.03	411.184	11632.50	395.312	5757.29	382.529	991.24	374.047
15664.24	405.476	9602.14	390.607	3844.77	378.913	193.50	372.796
			T = 450.00 K				
19261.85	437.034	13379.12	422.341	7591.82	409.412	1818.08	398.234
17388.72	432.200	11449.60	417.854	5588.03	405.333	921.98	396.666
15391.01	427.199	9408.93	413.299	3742.32	401.755	191.51	395.418

As a test of the internal consistency of the results, $(u/a_0)^2$ was fitted to polynomials in the density along individual isotherms. In these fits, densities were calculated from the experimental (p,T) by means of the Lee-Kesler equation of state and polynomials of between the 3rd and 5th degree were required depending upon the temperature and the greatest density on each isotherm. Typical deviations of $(u/a_0)^2$ were less than $15 \cdot 10^{-6}$ $(u/a_0)^2$ and imply an internal consistency well within the estimated uncertainty. For temperatures close to the critical, deviations of as much as twice the above figure were observed but this reflects in part the limitations of the polynomial representation.

Although argon is a well-studied fluid, it is surprising to find that few measurements of u have been reported,[7-10] and that most of the available results were reported more than twenty years ago. Only two relatively recent sets of measurements[7,8] are considered accurate enough to be compared fairly with this work. It must be stressed that no previous study has covered such an extensive region of pressure and temperature in the gas phase. Nevertheless, a favourable comparison was found with the speeds of sound reported by Ewing and Goodwin[7] at the three temperatures 255 K, 273.16 K and 300 K with pressures up to 7 MPa.

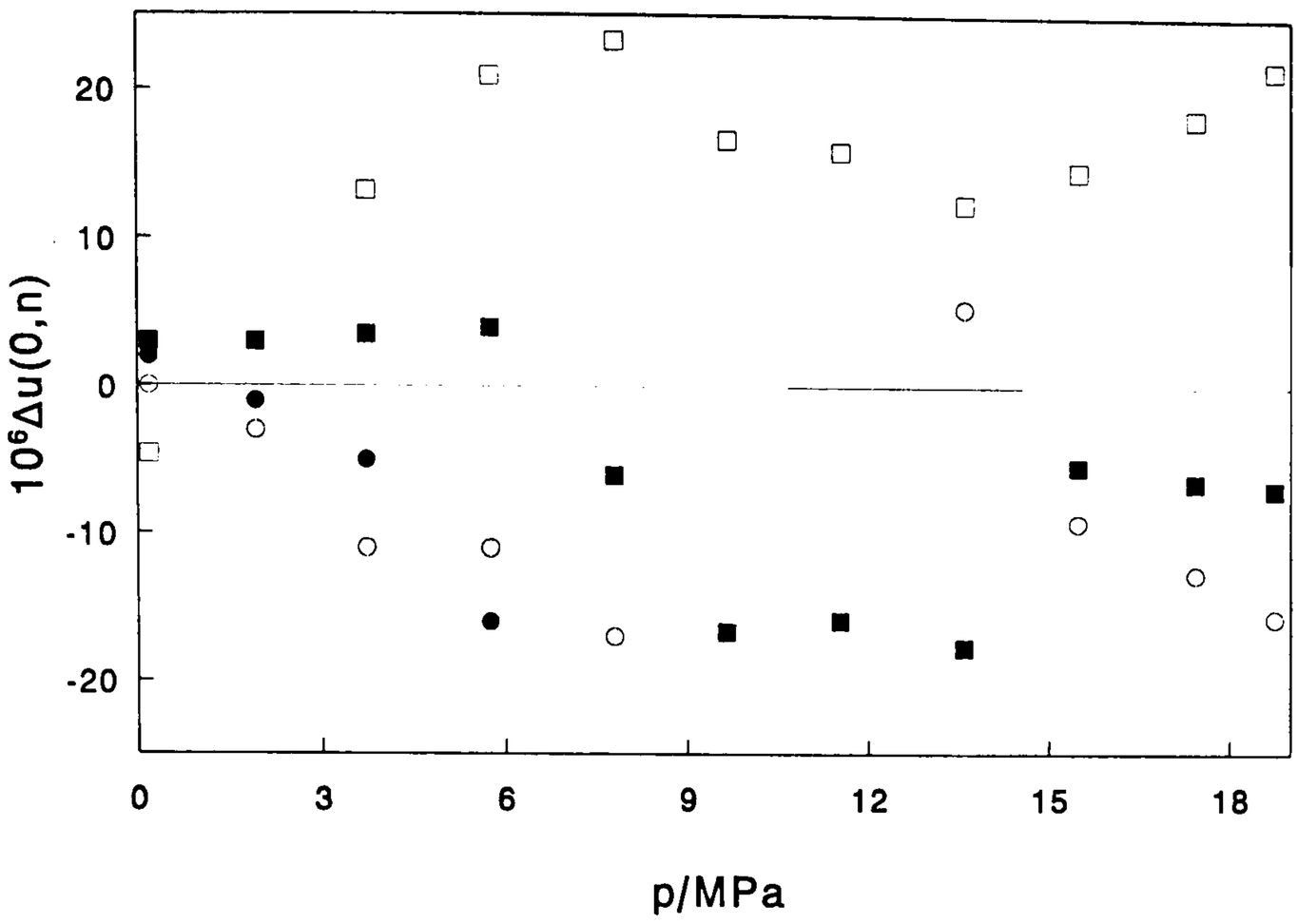


Figure 6.2 Deviations of speed of sound $\Delta u(0,n) = [u(0,n)/\langle u\rangle - 1]$ of argon determined from different radial modes along the isotherm at 350 K. The deviations are plotted against the average speed of sound $\langle u\rangle$ and radial modes cover up to $n = 5$: □, (0, 2); ■, (0, 3); ○, (0, 4); ●, (0, 5).

In order to make comparisons, the interpolation routine for the speed of sound described in connection with the determination of the thermodynamic properties was applied to the present results. It should be noted that the interpolation was of very high accuracy and would not introduce an error larger than $30\cdot10^{-6}\cdot u$; indeed the probable interpolation error is more like $10\cdot10^{-6}\cdot u$ for the region in question. From figure 3, one can see that the 38 values reported by Ewing and Goodwin agree with those interpolated from the present results to within $30\cdot10^{-6}\cdot u$. The RMS deviation of just $12\cdot10^{-6}\cdot u$. Since the values of u reported by Thoen *et al.*[9] and those reported by Goring[10] have only a modest precision of about $5\cdot10^{-3}\cdot u$, a comparison with these data is not particularly meaningful. Nevertheless, it was found that the 71 data points reported by Thoen *et al.* have an RMS deviation of $5\cdot10^{-3}\cdot u$ while a similar comparison with the 9 values of Goring yields an RMS deviation of $1.6\cdot10^{-3}\cdot u$. In each case, small corrections were applied to convert the reported temperatures to the ITS-90 scale used in this work.[11]

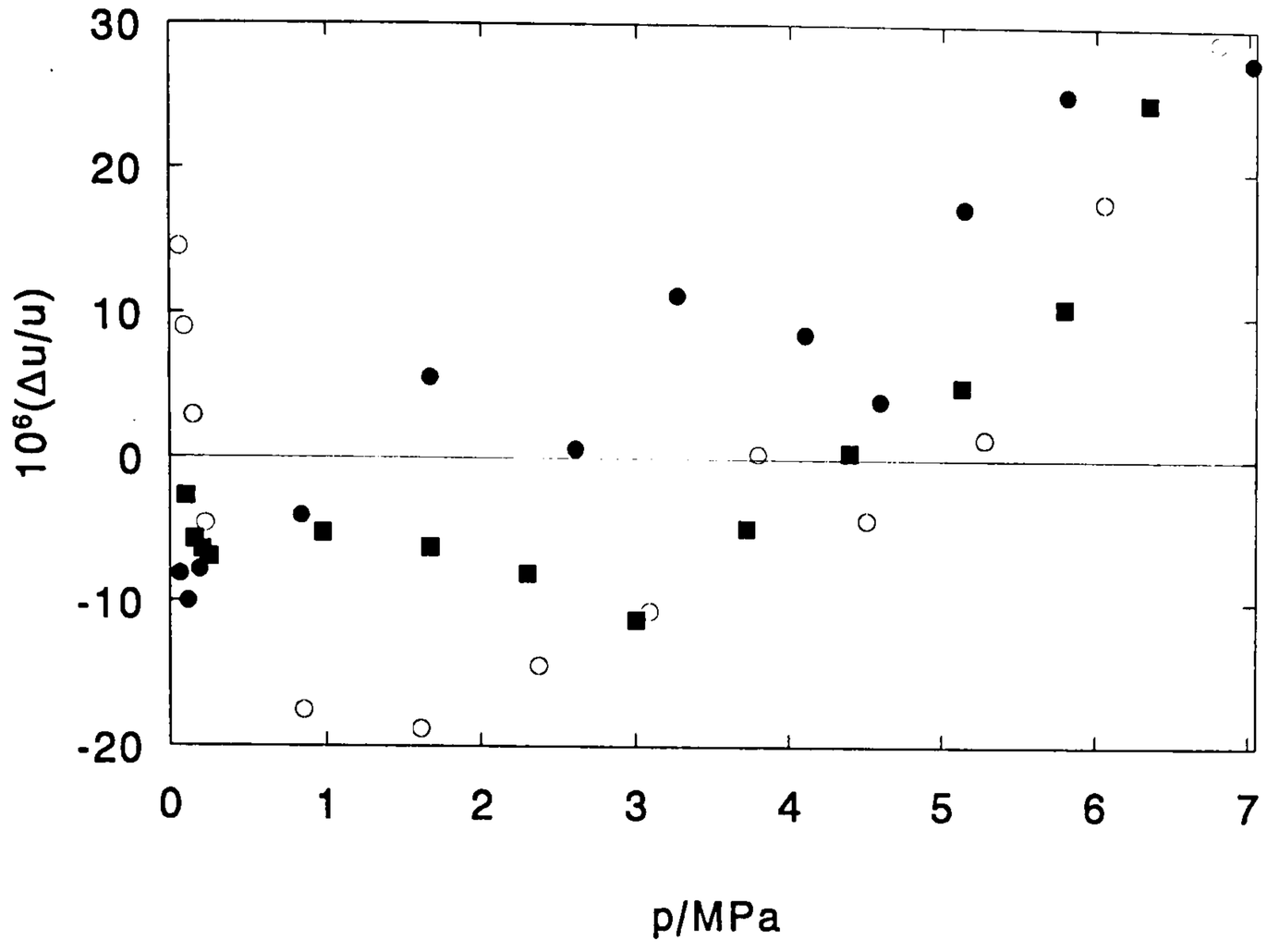


Figure 6.3 Fractional deviations $\Delta u/u$ of the speeds of sound u of argon reported by Ewing and Goodwin[7] from those interpolated from the results of this work. ●, $T = 255.00$ K; ■, $T = 273.16$ K; ○, $T = 300.00$ K.

6.3.2 Radius calibration.

For a monatomic gas, A_0 is a known quantity equal to $(5RT/3M)$. In particular, for argon, the molar mass $M = 0.0399478$ kg·mol^{-1} while the recommended value of the universal gas constant is $R = 8.31451$ J·mol^{-1}·K^{-1}.[12] Once these two constants are given, the radius at zero pressure a_0 can be obtained from the extrapolation of the ratio u/a_0 to the following limit: $\lim_{p\to 0} (u/a_0)^2 = A_0/(a_0)^2$. There are several manners of performing this extrapolation ranging from quite simple graphical analysis and straightforward polynomial fits of $(u/a_0)^2$ as function of p (or alternatively as a function of ρ_n),[13] to more complex analysis such as a simultaneous fit to a (p,T) surface,[14] and iterative limiting slope analysis.[1] In this work, the iterative limiting slope analysis was used, as described below, to obtain not only the limit of $A_0/(a_0)^2$ but also the acoustic virial coefficients. At each temperature values of a_0 were determined with a typical precision of $5\cdot10^{-6}a_0$. The results were used to establish a

simple correlation for a_0 as a function of temperature covering the range from 120 K to 450 K:

$$a_0/\mathrm{mm} = c_0\{1 + c_1[(T/\mathrm{K}) - T_r] + c_2[(T/\mathrm{K}) - T_r]^2\}. \qquad (6.3.1)$$

Here, $c_0 = 40.1695$, $c_1 = 15.3195 \cdot 10^{-6}$, $c_2 = 1.\ 0855 \cdot 10^{-8}$ and $T_r = 300$; the data is then reproduced within 30 ppm or 1.5 μm.

As pointed out in the previous chapter, the spherical resonator has shown a peculiar change this is not well understood.[1] Nevertheless, most of the measurements reported here were carried out in a period of time in which relatively stable conditions prevailed. This was verified by routine determinations of the radius using the same gas (argon). For instance, a check measurement made just after completion of the argon measurements gave a value of $a_0(T = 300\ \mathrm{K})$ 0.5μm or $12 \cdot 10^{-6}$ a_0 greater than the value found at the start of the work. At a later time, a check measurement found that $a_0(T = 170\ \mathrm{K})$ has increased by only 0.2μm from the value used to establish equation (6.3.1). This gave confidence that the resonator remained reasonably stable until the measurements on CO_2 took place.

6.3.3 Acoustic virial coefficients.

As mentioned above, the acoustic virial coefficients were determined by an iterative process of limiting slope analysis. This method consists of an analysis of the low-pressure range of each isotherm in terms of a truncated expansion of u/a_0 in powers of either p or ρ_n. In practice, it has proved to be more accurate to perform the analysis in terms of densities, because of the more rapid convergence achieved, despite of the fact that p is actually the variable directly measured.

Only for the isotherms at 110 K and 120 K, where saturation severely restricted the density range, were the results represented adequately along the entire isotherm using equation (3.2.6) truncated after the fourth acoustic virial coefficient.

Consequently, the remaining isotherms were examined in terms of the limiting slope analysis. Since u/a_0 is the experimental accessible quantity, the analysis started by writing the expansion of $(u/a_0)^2$ in powers of the amount-of-substance density

$$(u/a_0)^2 = (A_0/a_0^2)(1 + \beta_a\rho_n + \gamma_a\rho_n^2 + \delta_a\rho_n^3 + \cdots), \qquad (6.3.2)$$

Next, a function Y_β is introduced in the analysis by means of the definition

$$Y_\beta = [\{(u/a_0)^2/(A_0/a_0^2)\} - 1]/\rho_n, \tag{6.3.3}$$

and we observe that Y_β has the property of approaching β_a with slope γ_a as $\rho_n \to 0$. Obviously, the exact value of the ratio (A_0/a_0^2) is unknown at the start of the analysis and therefore and iterative process is required. First, (A_0/a_0^2) was estimated from the value of $(u/a_0)^2$ at the lowest density on the isotherm using equation (6.3.2) truncated after the term in ρ_n^2 and setting β_a and γ_a to zero. The deliberate strategy of including a measurement at a very low density (typically $\rho_n^c/200$ or less) resulted in a good initial guess of the value of (A_0/a_0^2) which was relatively insensitive to the crude initial estimates of the acoustic virial coefficients. In the second step of the analysis, Y_β was calculated at each of the remaining densities on the isotherm and β_a and γ_a were obtained from the zero-density intercept and slope. An improved estimate of (A_0/a_0^2) was then obtained from the lowest point on the **isotherm** making use of (6.3.2) with the values of β_a and γ_a just determined. This process was iterated until no further change in (A_0/a_0^2), β_a and γ_a was found (typically after 5 cycles).

Several strategies can be adopted for the extrapolation of Y_β to the limit of zero density such as graphical analysis, numerical analysis of finite differences or polynomial fits. In this work a polynomial fit was employed for that purpose. After several attempts, it was concluded that a density range which included the lower five densities (excluding the lowest one) was adequate and that Y_β was then properly represented with a quadratic polynomial in ρ_n. In figure 4, some examples of these functions Y_β are shown. At first glance, Y_β seems to be a linear function of ρ_n but detailed analysis reveals a small curvature which is accurately represented by a quadratic polynomial. Although, each of the three coefficients of the quadratic polynomial of ρ_n would be enough to determine each of the three first acoustic virial coefficients, the practical usage of (6.3.3) was restricted to determinations of β_a and γ_a only. Higher order acoustic virial coefficients should be determined as follows. After (A_0/a_0^2) and β_a are known, a new function Y_γ is defined as

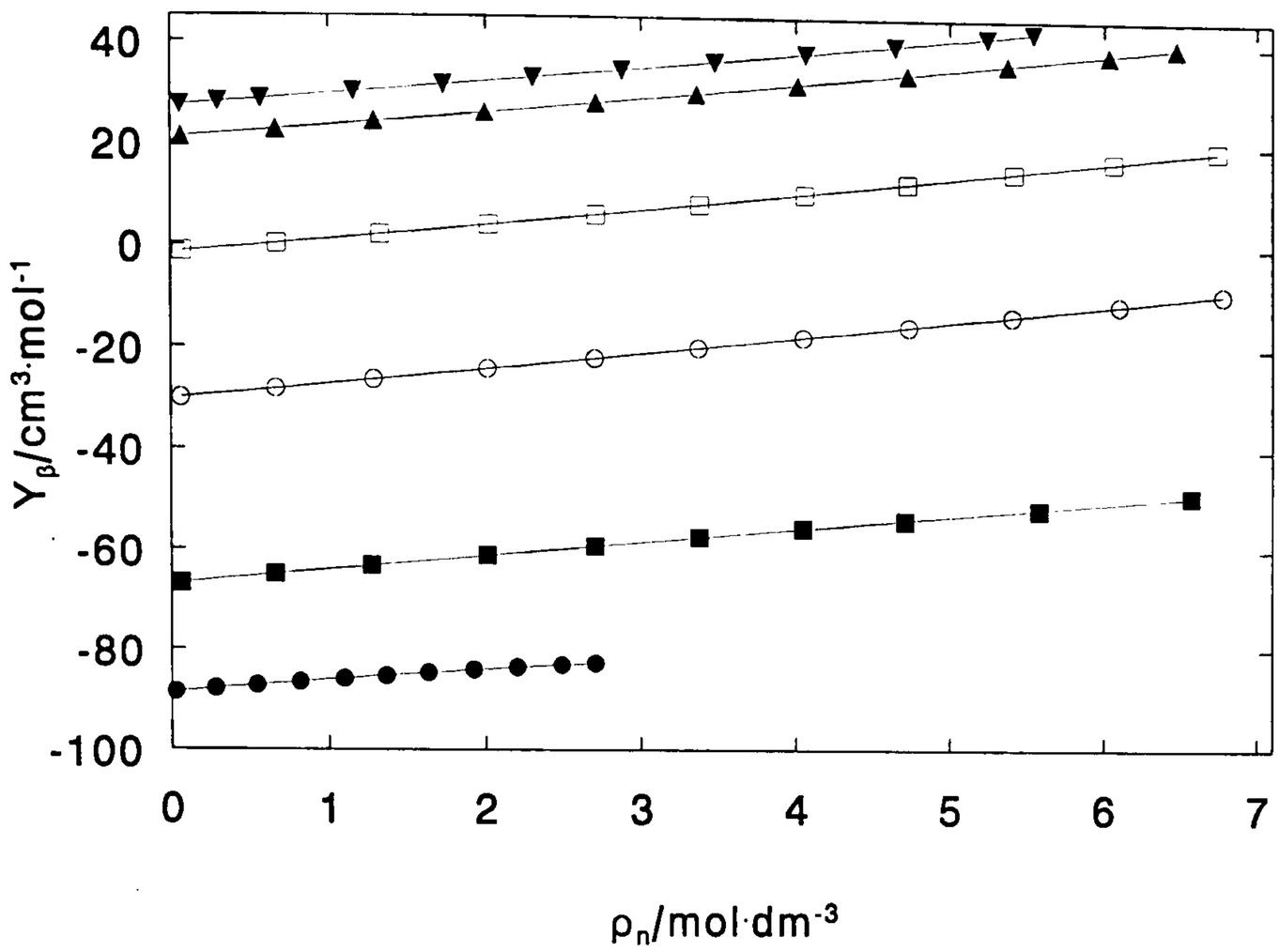


Figure 6.4 Y_β as a function of amount-of-substance density ρ_n at selected temperatures. Curves are quadratic polynomials fitted to the results. ●, 135 K; ■, 150 K; ○, 190 K; □ , 250 K; ▲, 350 K; ▼ , 450 K;

$$Y_\gamma = (Y_\beta - \beta_a)/\rho_n, \tag{6.3.4}$$

from which γ_a and δ_a may be obtained as the zero-density intercept and slope. Once again, Y_γ can be represented by a suitable polynomial in ρ_n but this time no iterative procedure is required. The final values of both β_a and γ_a were obtained from equation (6.3.3) while those of δ_a were obtained from equation (6.3.4). Nevertheless, the values of γ_a determined from (6.3.3) agreed very well, at all temperature, with those obtained from the intercept of (6.3.4).

In principle, the introduction of further functions Y_{α_j}, may lead to determination of the jth and $(j+1)$th acoustic virial coefficients (for $j > 4$). However, in practice this is not possible since a complete virial series from which to calculate the density is unavailable. One can prove by direct substitution in (6.3.2) that densities calculated from a virial series of the type (3.2.8) but truncated after the mth virial coefficient may give correctly the first $(m+1)$ derivatives of $(u/a_0)^2$ in the limit of zero

density. If the model employed to calculate the densities does not reproduce correctly the first m virial coefficients, inaccuracies in the density will affect all acoustic virial coefficients beyond the second.

The effect of carrying out the limiting slope analysis with densities calculated from different models at a single temperature, namely 148 K, was studied. Three models were selected: one in which densities were calculated from the Lee-Kesler equation of state and two which employed truncated virial series, the one truncated after B and the other after C. Values of B and C were calculated from a modified version of HFD-B2 potential for argon,[15] proposed by Ewing and Trusler.[16] The two leading quantum corrections for B were included as was the leading non-additive contribution to the potential energy of three-atoms in the calculation of C. This interatomic potential reproduces, within the experimental uncertainty, the values of B and C reported by Gilger *et al.*[17] but also had the additional advantage of yielding values of B and C at temperatures above 350 K where fewer **accurate** measurements were available.

The results obtained from the three models were compared and it was found that β_a was indeed essentially independent of the model used to calculate $\rho_n(T,p)$ in the limiting slope analysis; the values obtained all agreed to within the combined uncertainties. However, as expected, different third and fourth acoustic virial coefficients were obtained. This test suggests that the Lee-Kesler equation of state may be used in the determination of accurate second acoustic coefficient from the speed of sound for another substance, especially if no accurate second virial coefficients are available.

Table 2 reports values of the second, third and fourth acoustic virial coefficients derived from the limiting slope analysis together with their estimated uncertainties; values of B and C used to determine the densities are also included there. Uncertainties reported for β_a in table 2 do not represent the precision with which β_a can be determined by the limiting slope analysis -typically 0.01 $cm^3 \cdot mol^{-1}$. Instead, more conservative values are given for the total uncertainty which reflect the differences found using different density ranges and different polynomial in the

limiting-slope analysis. For γ_a and δ_a, the same consideration were applied but, in addition, the effects of uncertainties in the calculated densities were included.

Table 6.2. Second β_a, third γ_a and fourth δ_a acoustic virial coefficients and second B and third C virial coefficients of argon at temperatures T. B and C are calculated from interatomic potential-energy function given in ref. 3.

T/K	β_a/cm^3·mol^{-1}	γ_a/cm^6·mol^{-2}	δ_a/dm^9·mol^{-3}	B/cm^3·mol^{-1}	C/cm^6·mol^{-2}
110.00	-144.85 ± 0.05	-511 ± 200	-126.0 ± 76	-154.08	1176
120.00	-118.34 ± 0.05	1590 ± 100	-57.0 ± 29	-131.32	1927
130.00	-97.39 ± 0.03	2346 ± 150	-16.0 ± 7.2	-113.28	2174
135.00	-88.53 ± 0.03	2614 ± 100	-12.6 ± 5.4	-105.59	2204
140.00	-80.63 ± 0.01	2744 ± 50	-3.02 ± 1.2	-98.64	2198
143.00	-76.12 ± 0.02	2760 ± 50	-4.03 ± 1.6	-94.78	2183
146.00	-72.06 ± 0.04	2944 ± 50	-6.71 ± 2.7	-91.12	2162
148.00	-69.55 ± 0.01	3107 ± 50	-8.78 ± 3.1	-88.79	2146
150.00	-66.99 ± 0.01	3101 ± 50	-7.27 ± 2.5	-86.54	2127
156.08	-59.63 ± 0.02	3046 ± 50	-3.41 ± 1.2	-80.17	2064
163.15	-52.12 ± 0.01	3039 ± 50	-1.28 ± 0.4	-73.51	1982
170.00	-45.77 ± 0.01	3104 ± 50	-1.16 ± 0.4	-67.74	1901
180.00	-37.36 ± 0.01	3007 ± 50	1.36 ± 0.5	-60.29	1786
190.00	-30.25 ± 0.01	3026 ± 50	1.27 ± 0.4	-53.82	1679
205.00	-21.03 ± 0.01	2909 ± 50	3.25 ± 1.0	-45.55	1538
220.00	-13.48 ± 0.01	2871 ± 50	3.59 ± 1.1	-38.66	1419
250.00	-1.58 ± 0.01	2746 ± 50	4.83 ± 1.4	-27.81	1239
300.00	11.98 ± 0.01	2569 ± 50	6.43 ± 1.9	-15.33	1052
350.00	20.92 ± 0.01	2468 ± 50	6.98 ± 2.1	-6.95	946
400.00	27.22 ± 0.02	2354 ± 50	8.40 ± 2.5	-0.98	881
450.00	31.79 ± 0.02	2186 ± 50	16.18 ± 4.9	3.47	838

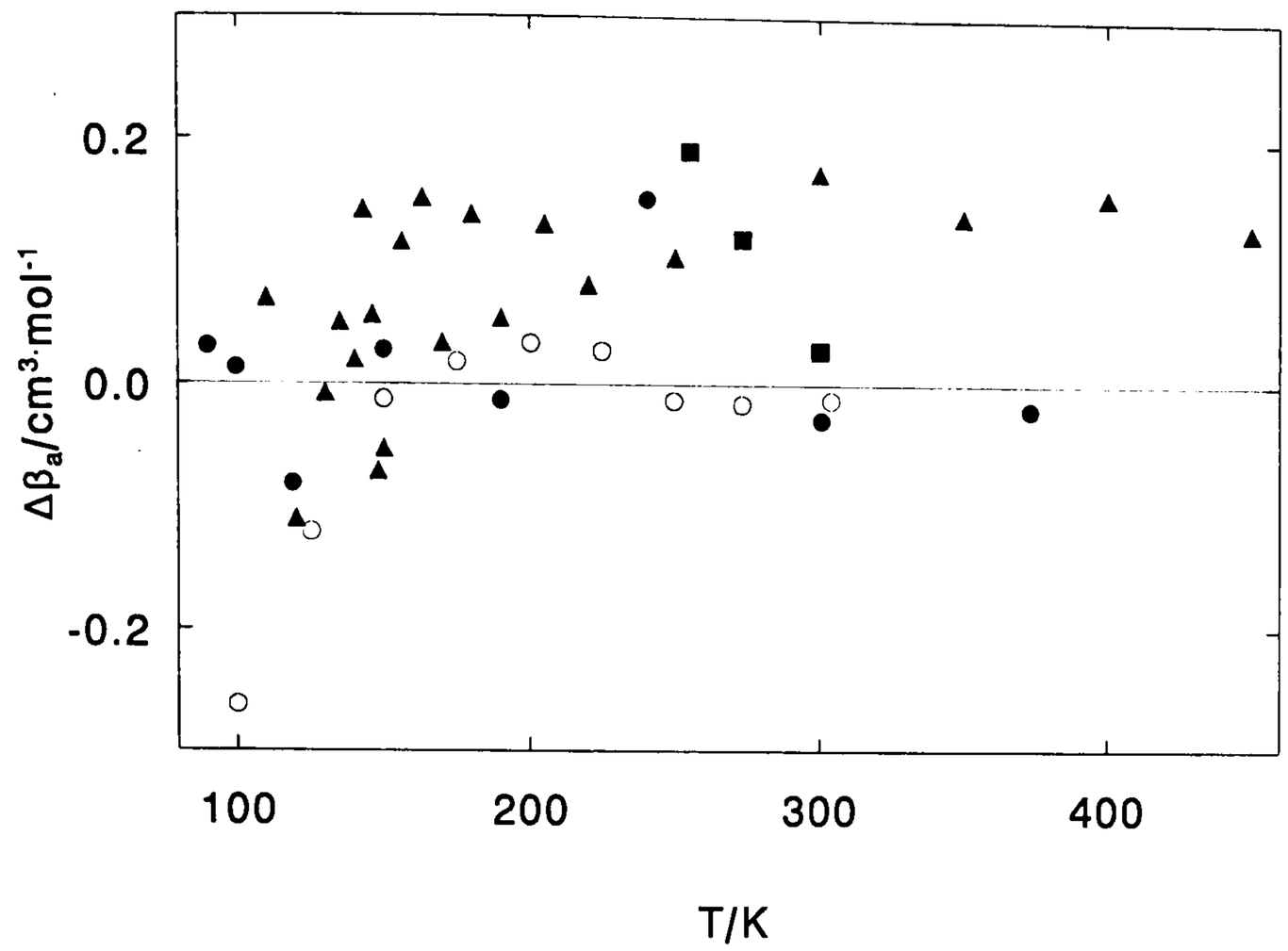


Figure 6.5 Deviations $\delta\beta_a$ of second acoustic virial coefficients of argon from values calculated with the interatomic potential-energy function of Ewing and Trusler.[16] ●, reference 16; ■, reference 7; ○, reference 8; ▲, this work.

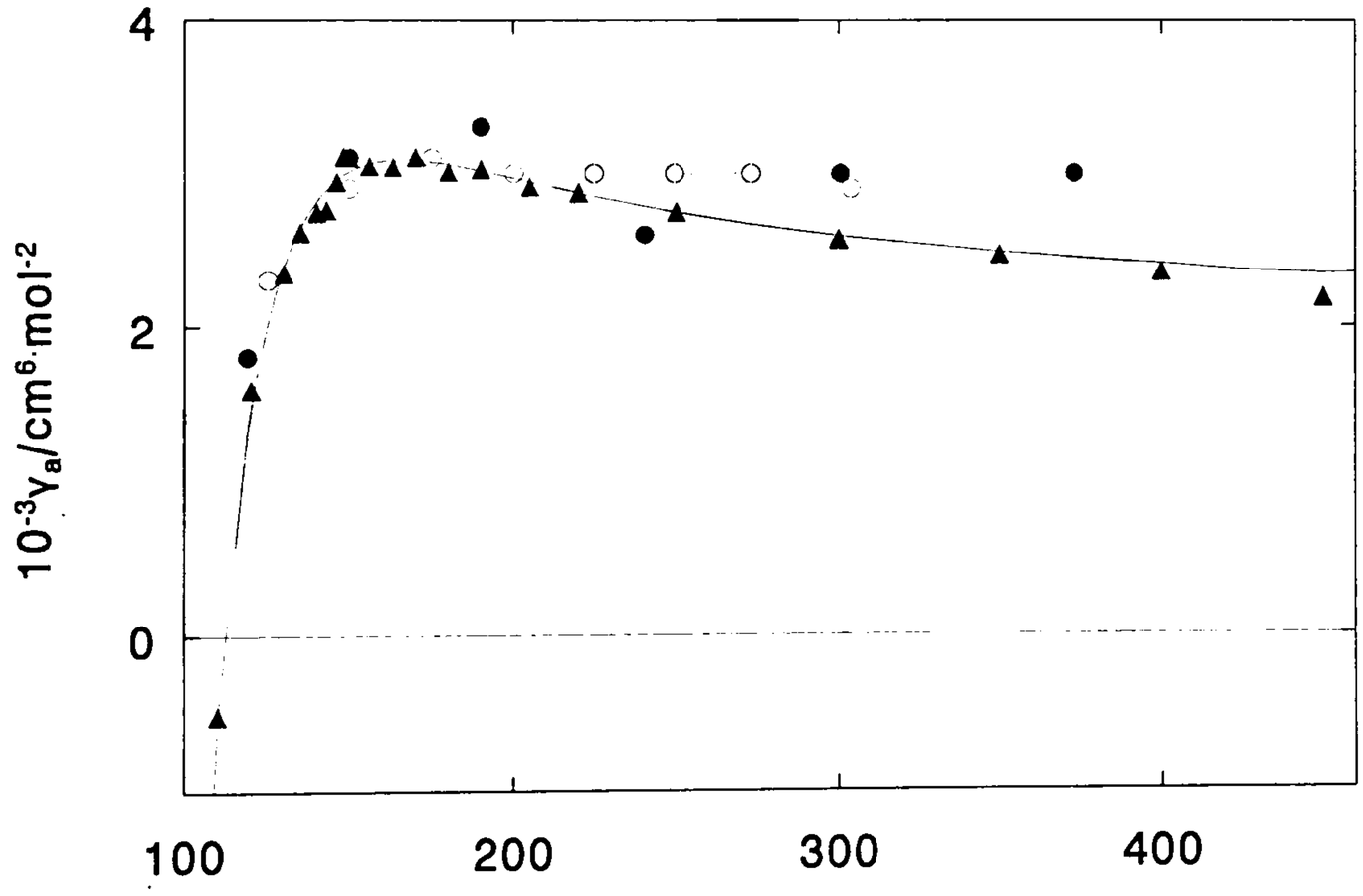


Figure 6.6 Third acoustic virial coefficients γ_a of argon. ●, reference 16; ○, reference 8; ▲, this work.

Values of β_a obtained here are compared with those of others workers in figure 5. Since the temperature range of this work **exceeds** the ranges of previous studies, the comparison included also values of β_a calculated from the interatomic potential proposed in reference [16]. A good agreement has been obtained and the evidence is such that it can be said that β_a is known for argon with an uncertainty of about ± 0.2 $cm^3 \cdot mol^{-1}$ in the full range of temperatures. In the case of γ_a, fewer values have been reported but a satisfactory agreement is noted with those reported by Ewing *et al.*[8] and by Ewing and Trusler[16] and an outstanding agreement with the calculated values as shown in figure 6. Finally, δ_a is plotted in figure 7. There have been no previous determination of fourth acoustic virial coefficients for argon but, despite the large experimental uncertainties, this quantity has been obtained with sufficient precision to establish its probable temperature dependence including the existence of two turning points.

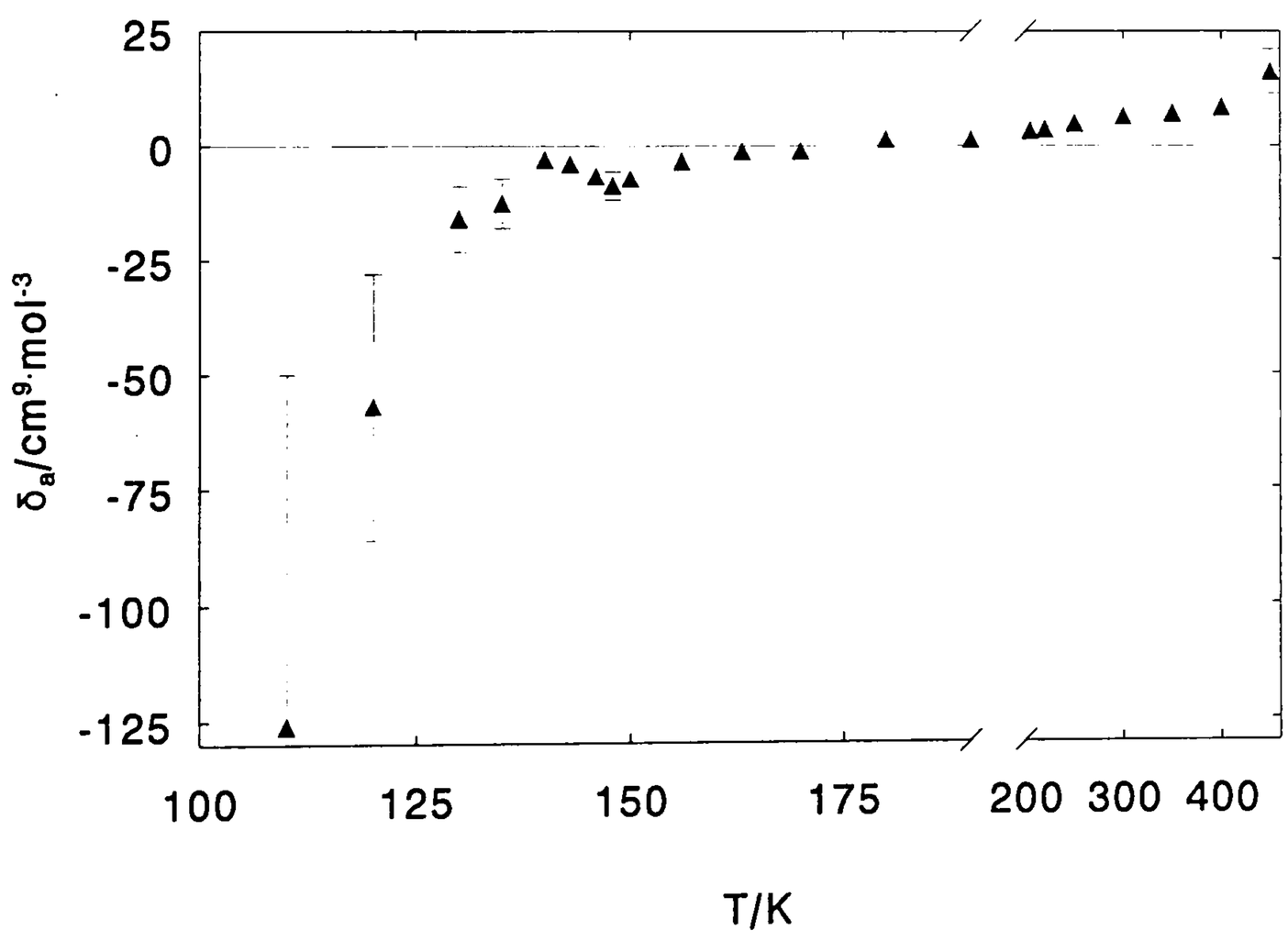


Figure 6.7 Fourth acoustic virial coefficients δ_a of argon. ▲, This work.

6.4 Ethane

The speed of sound in ethane was measured at temperatures between 220 K and 450 K with pressures up to 10.5 MPa with the primary objective of determining the *pVT* surface. The purity of the gas was checked by means of gas chromatography analysis with a flame-ionisation detector. This did not reveal any impurity but the analysis was sensitive mainly to hydrocarbons and a. nonflammable impurity might still be present. Nevertheless, no further attempt at analysis or purification was made. Heat capacities of the perfect-gas and acoustic virial coefficients were derived from the limiting slope analysis. Finally, from values of the second acoustic virial coefficient, parameters of a model intermolecular potential were determined.

6.4.1 Speed of sound in Ethane.

The first five radial modes of the spherical resonator were measured along each isotherm. Typical values of Q in ethane were greater than 15000 and a favourable signal-to-noise ratio was always obtained at all temperatures.

Once again, the equilibrium properties required to determine the small correction terms in the acoustic model were obtained from the Lee-Kesler equation of state.[4] Transport coefficients were obtained from two sources: the viscosity was calculated from a correlation due to Younglove and Ely[18] while the thermal conductivity was obtained from a correlation reported by Vesovic.[19]

Except for few modes rejected at particular state points, the speeds of sound derived from different modes normally agreed within ± 20 ppm. The maximum pressure reached was nearly 10.5 MPa at 450 K. However, in contrast to argon, significant excess half-widths Δg_{0n} were observed at every temperature in a preliminary analysis which did not account vibrational relaxation. These excess half-widths are related with the extra absorption per wavelength μ, discussed in §2.3.5, by means of the relationship

$$(\mu/2\pi) = (\Delta g_{0n}/f_{0n})\,. \tag{6.4.1}$$

The pattern described by the Δg_{0n} is consisted with one in which relaxation takes place. At high pressure, Δg_{0n} was very small ($< 30\cdot10^{-6}\cdot f_{0n}$ for any mode) but Δg_{0n} increased rapidly at low pressures in proportion to p^{-1} at constant f. This

behaviour is attributed to vibrational relaxation of the ethane molecule.[20,21] It is also well known that, in ethane, two groups of vibrational modes tend to relax in parallel with relaxation times τ_1 and τ_2 giving an overall apparent relaxation time τ. Equation (2.3.46) cannot be then employed directly in order to determine both relaxation times unless the contributions of each mode C_j (j =1, 2) to the total part of the heat capacity that is relaxing C_{int} are known. In practice, this may be accomplished only if the full dispersion curve is known or, alternatively, if an arbitrary partition of C_{int} is proposed but the latter would introduce an extra parameter to be determined. The full dispersion curve was not available in this case and since the introduction of an artificial partition might lead only to apparent relaxation times τ_j, the latter did not present any advantages above a simpler approach in which, rather obtaining each τ_j, the analysis of the Δg was carried out in terms of the overall apparent relaxation time τ . Moreover, even before application of a dispersion correction, no disagreement was observed between the speeds of sound derived from different modes even at the lowest pressure on each isotherm. In other words, at most the onset of the dispersion curve was reached and it was therefore assumed that a correction based on a single apparent relaxation time τ would be sufficient. Thus, a non-linear regression of the values Δg_{0n} was carried out to obtain values of τ according with the simple formula (2.3.23). The values of C_{int} required for this analysis were calculated simply by deducting $3R$ to the total molar isochoric heat capacity of the perfect gas. The values of the heat capacity of the perfect gas was obtained from the correlation given in reference [18].

Furthermore, in the non-linear regression the independent variable was the product $\tau\rho$ since this quantity is considered to be a constant along each isotherm. Then, the whole analysis was repeated, applying a correction to both the speed of sound and the halfwidths according to equations (2.3.45) and (2.3.44) respectively. This time, values of Δg_{0n} were not larger than $20 \cdot 10^{-6} \cdot f_{0n}$, which was considered as a reasonable agreement, and it was found that a perturbation of the value of $\tau\rho$ amounting to 10 per cent would not change significantly the values of Δg. As expected, the correction to the speed of sound, according to equation (2.3.44), turned out to be very small indeed; the maximum correction applied to the speed of sound

amounted to an insignificant 0.4 ppm in the 'worst' case (the state point at 13.87 kPa and 220 K). This negligible change is consistent with the previous observation regarding the region of the dispersion curve reached.

Finally, in table 3, the speeds of sound in ethane are reported after accounting for corrections due to dispersion. Small corrections have also been applied to reduce all points to the stated temperature along each isotherm. In addition, values of τ at an arbitrary density of 1 kg·m^{-3} are report in table 4.

The speed of sound was fitted to a polynomial in density along each isotherm as a test of internal consistency. The densities were once again calculated from the equation of state of Lee and Kesler.[4] Normally, a 4 or 5 term fit was required to accommodate all data within about $10^{-5}\cdot u$, except in the temperature range from 290 K to 305 K, where six terms fits were needed to achieve the same class of agreement. This is not surprising since the critical temperature of ethane is 305.33 K.

The values of the speed of sound were compared with those recently reported by Boyes.[20] Since those results were also obtained by means of a spherical resonator, it is assumed that their accuracy is comparable to the accuracy of the values reported here. In order to carry out the comparison, an interpolation routine for the speed of sound was implemented in similar a way to that used for argon. This comparison is shown in figure 8. It can be seen that u itself may disagree by ± 120 ppm, more than was expected, but when the same comparison was made in terms of the ratio (u/u_0), the agreement improved considerably with differences always within ± 20 ppm. At 250 K, where only interpolations in density were carried out, the agreement in both u or (u/u_0) was within 20 ppm; conversely, at 330 K, where once again interpolation of u was required only in density, (u/u_0) agreed within 20 ppm but u itself did not. From the remaining temperatures, only at 230 K was a favourable comparison of u itself achieved. This evidence points to a small inconsistency between the absolute values of u derived from both set of measurements. Possible explanations for this disagreement might be differences in purity between the samples or an inaccurate knowledge of the radius of either resonator. In either case, the inconsistency of u_0 would be reflected clearly in a comparison of the derived heat capacities of the perfect gas.

Table 6.3 Speed of sound of ethane at temperatures from 220 K to 450 K and pressures up to 10 MPa.

p/kPa	u/m·s^{-1}	p/kPa	u/m·s^{-1}	p/kPa	u/m·s^{-1}	p/kPa	u/m·s^{-1}
			T = 220 K				
407.33	258.377	289.44	263.192	169.72	267.770	44.45	272.277
364.99	260.146	254.41	264.562	125.97	269.374	13.87	273.340
326.79	261.703	209.49	266.280	86.68	270.787		
			T = 235 K				
704.82	258.301	513.41	265.475	307.07	272.510	79.25	279.629
641.60	260.751	445.56	267.860	.232.95	274.894	15.97	281.509
576.68	263.181	380.92	270.064	156.09	277.295		
			T = 250 K				
1088.81	257.188	806.68	266.939	489.41	276.641	132.15	286.415
994.83	260.580	702.03	270.266	371.54	279.983	21.03	289.263
908.11	263.577	594.35	273.554	251.33	283.269		
			T = 265 K				
1699.24	250.690	1298.04	264.165	793.56	278.447	217.86	292.460
1577.76	255.039	1139.43	268.913	611.62	283.094	21.89	296.830
1444.57	259.523	973.27	273.620	422.24	287.706		
			T = 275 K				
2164.86	246.338	1666.31	262.608	1040.57	279.335	286.49	296.332
2000.96	252.090	1474.27	268.081	804.38	284.960	30.68	301.550
1845.79	257.144	1265.61	273.661	554.36	290.600		
			T = 285 K				
2793.14	238.207	2208.15	257.483	1407.67	278.178	398.68	299.455
2616.76	244.592	1960.43	264.398	1086.81	285.391	39.64	306.185
2417.68	251.148	1691.54	271.347	754.83	292.390		

Table 6.3 -continue.

p/kPa	u/m·s^{-1}	p/kPa	u/m·s^{-1}	p/kPa	u/m·s^{-1}	p/kPa	u/m·s^{-1}
			T = 290 K				
3153.27	233.445	2516.51	254.573	1646.67	276.739	456.53	301.062
2975.21	240.042	2266.31	261.506	1294.83	284.477	48.09	308.404
2764.29	247.079	1964.34	269.225	886.73	292.836		
			T = 295 K				
3671.86	222.894	3062.86	245.176	2045.61	272.009	592.58	301.319
3525.96	229.072	2764.49	253.914	1601.54	281.767	60.51	310.542
3320.06	236.735	2418.04	263.058	1123.41	291.418		
			T = 300.65 K				
4258.65	211.299	3771.18	232.122	2648.37	263.702	812.30	300.657
4183.63	215.319	3424.76	243.218	2110.23	275.775	92.16	312.673
4007.44	223.236	3054.03	253.572	1486.06	288.357		
			T = 305 K				
4533.51	213.491	3903.71	236.573	2711.50	267.061	818.99	303.091
4387.53	219.847	3570.99	246.129	2163.94	278.574	87.43	314.813
4168.56	227.991	3169.65	256.440	1534.71	290.605		
			T = 315 K				
5017.28	225.752	4180.67	246.778	2859.69	274.340	831.81	308.502
4777.79	232.130	3806.10	255.181	2258.73	285.289	92.09	319.322
4497.48	239.217	3355.53	264.634	1601.72	296.409		
			T = 330 K				
5477.16	246.466	4581.34	260.891	3065.92	284.953	876.13	315.972
5329.11	248.776	4143.36	268.016	2407.19	294.769	96.03	325.977
5019.77	253.736	3622.35	276.334	1690.88	304.959		

Table 6.3 -continue.

p/kPa	u/m·s^{-1}	p/kPa	u/m·s^{-1}	p/kPa	u/m·s^{-1}	p/kPa	u/m·s^{-1}
			T = 345 K				
6110.77	261.334	5008.16	273.490	3281.72	294.867	930.13	323.110
5880.00	263.637	4493.29	279.769	2569.08	303.656	99.71	332.479
5469.60	268.092	3920.89	286.893	1794.95	312.994		
			T = 365 K				
6944.18	279.852	5521.82	289.632	3546.67	307.590	995.00	332.405
6565.10	282.011	4910.43	294.869	2766.84	315.160	105.59	340.899
6088.10	285.237	4220.86	301.176	1917.60	323.451		
			T = 385 K				
7589.48	297.689	6063.52	304.424	3834.97	319.432	1053.61	341.463
7350.52	298.456	5370.83	308.615	2971.08	326.080	111.96	349.095
6701.31	301.118	4652.28	313.468	2043.22	333.458		
			T = 415 K				
8686.30	321.575	6813.20	325.360	4254.71	336.355	1144.13	354.533
8436.78	321.803	6014.69	328.212	3265.39	341.752	120.86	361.051
7637.33	323.135	5156.81	331.904	2235.91	347.795		
			T = 450 K				
10458.36	347.557	7826.69	347.641	4724.24	354.985	1251.07	369.136
9660.73	346.872	6780.50	349.374	3605.41	359.023	126.69	374.524
8736.36	346.872	5773.98	351.792	2443.60	363.780		

6.4.2 Heat capacities of perfect gas.

The determination of the heat capacities of the perfect gas and the acoustic virial coefficients was based on the limiting slope analysis of Y_β discussed earlier. The densities required for the limiting slope analysis were obtained in two ways: first from Lee-Kesler equation of state; and second, from a virial equation truncated after the

third virial coefficient. The coefficients B and C were calculated from a correlation given in reference [20] which is based on acoustic measurements. Both models for the density led to essentially the same β_a and γ_a, and the final results correspond to the equation of state of Lee and Kesler.[4]

Table 6.4 Vibrational relaxation times of ethane at the density of 1 kg·m^{-3}.

T/K	τ/ns	T/K	τ/ns	T/K	τ/ns
220.00	7.7178	290.00	12.051	345.00	14.442
235.00	9.9149	295.00	12.499	365.00	14.392
250.00	10.628	300.65	14.703	385.00	14.267
265.00	10.566	305.00	14.794	415.00	14.249
275.00	11.375	315.00	14.648	450.00	13.940
285.00	11.508	330.00	14.512		

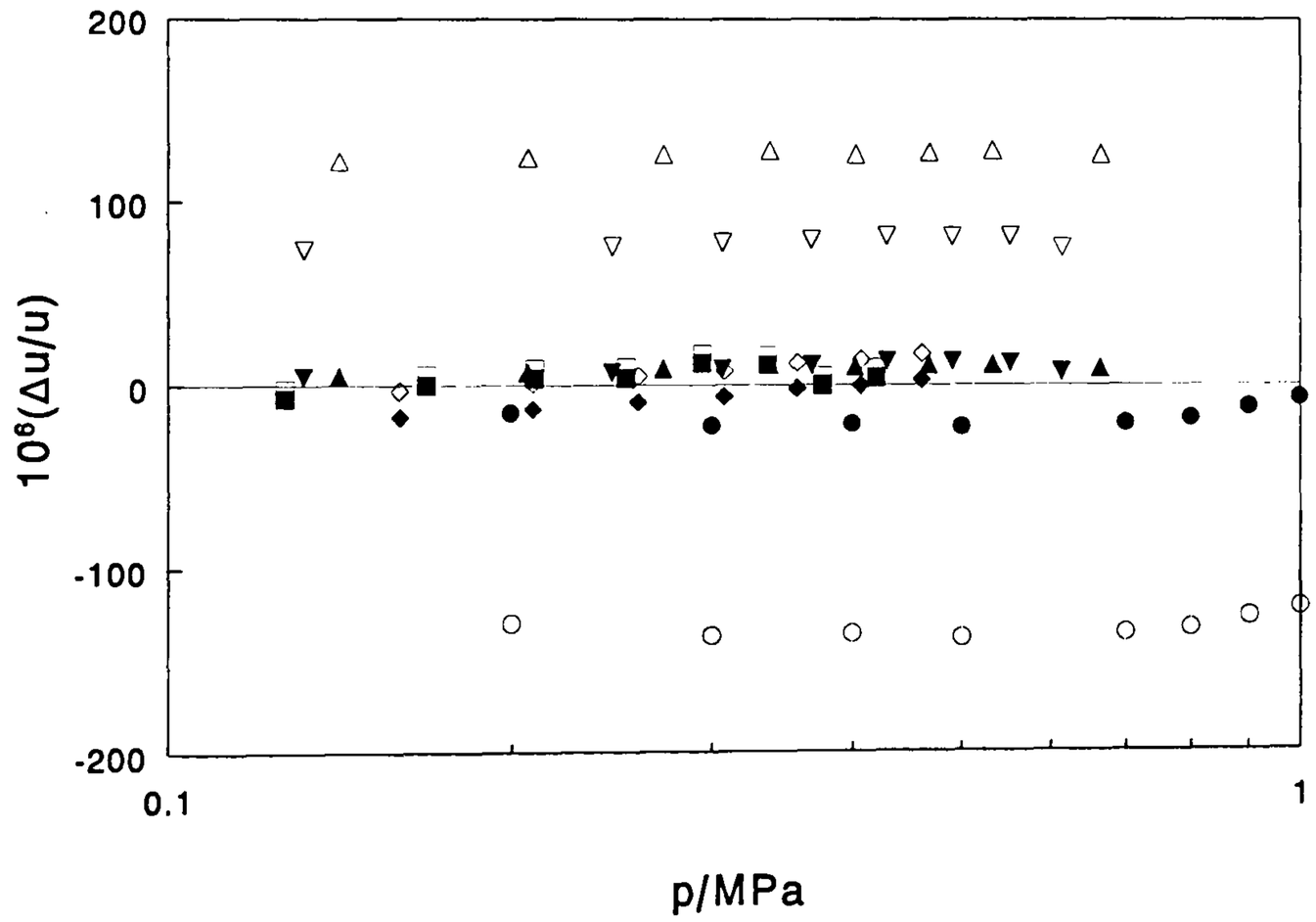


Figure 6.8 Fractional deviations $\Delta u/u$ of the speed of sound u of ethane reported by Boyes[20] from those interpolated from the results of this work. Open symbols for comparison between absolute speed of sound u and filled symbols for comparison of the ratio (u/u_0). ■, $T = 230$ K; ◆, $T = 250$ K; ●, $T = 300$ K; ▼, $T = 330$ K; ▲, $T = 360$ K.

Table 6.5 Acoustic virial coefficients and molar perfect-gas heat capacities at constant pressure of ethane.

T/K	$C_{p,\mathrm{m}}^{\mathrm{pg}}/R$		β_a/cm^3·mol^{-1}		γ_a/cm^6·mol^{-2}	
220.00	5.3007	0.0002	-458.505	0.030	40449	937
235.00	5.4711	0.0002	-405.867	0.106	46984	1668
250.00	5.6537	0.0003	-360.946	0.127	41193	1547
265.00	5.8469	0.0003	-322.674	0.064	33965	485
275.00	5.9822	0.0003	-300.384	0.037	31142	222
285.00	6.1212	0.0003	-280.262	0.031	29328	138
290.00	6.1921	0.0003	-270.870	0.052	28563	201
295.00	6.2639	0.0003	-262.003	0.052	28092	156
300.65	6.3452	0.0003	-252.055	0.039	27148	87
305.00	6.3993	0.0003	-245.024	0.034	26734	76
315.00	6.5481	0.0004	-229.585	0.032	25478	71
330.00	6.7762	0.0004	-208.641	0.037	23810	82
345.00	7.0064	0.0004	-189.752	0.052	22261	116
365.00	7.3200	0.0005	-167.531	0.052	20480	117
385.00	7.6344	0.0005	-147.913	0.065	18894	143
415.00	8.0958	0.0006	-123.052	0.011	17621	24
450.00	8.6295	0.0007	-98.483	0.007	16141	16

Exactly, the same strategy followed for argon was employed in this case. The speed of sound measured at a low pressure point ($\rho_n \approx \rho_n^{\mathrm{c}}/200$ or less) on each isotherm was used to establish the initial estimate of A_0 in the iterative process. Once, the procedure converged, values of A_0, β_a and γ_a were obtained, and from A_0 and the recommended value of molar mass of ethane (M = 0.03007 kg·mol^{-1}), values of the heat capacity at constant pressure were determined according to

$$(C_{p,\mathrm{m}}^{\mathrm{pg}}/R) = [1-(RT/MA_0)]^{-1}. \qquad (6.4.2)$$

In table 5, the values of $C_{p,\mathrm{m}}^{\mathrm{pg}}$, β_a and γ_a obtained from the limiting slope analysis are reported. Uncertainties in the acoustic virial coefficients were worked out in a similar way as for argon, while the uncertainty in the heat capacities was calculated from the gaussian error propagation formula based on likely uncertainties in all the variables involved in (6.4.2).

Values of the perfect-gas heat capacities of ethane have been reported from spectroscopic data.[22] These determinations can be fitted in the temperature range from 200 K to 500 K to within ± 0.06 per cent by the following equation:

$$(C_{p,\mathrm{m}}^{\mathrm{pg}}/R) = -1.91108 + 2.2604\times10^{-2}(T/K) + 5.07766\times10^{2}(T/K)^{-1} - 8.20908\times10^{-9}(T/K)^{3}. \quad (6.4.2)$$

In figure 9 deviations of the heat capacities derived in this work from equation (6.4.2) are plotted together with those determined from acoustic measurements by Boyes[20] and by Esper *et al.*[14]

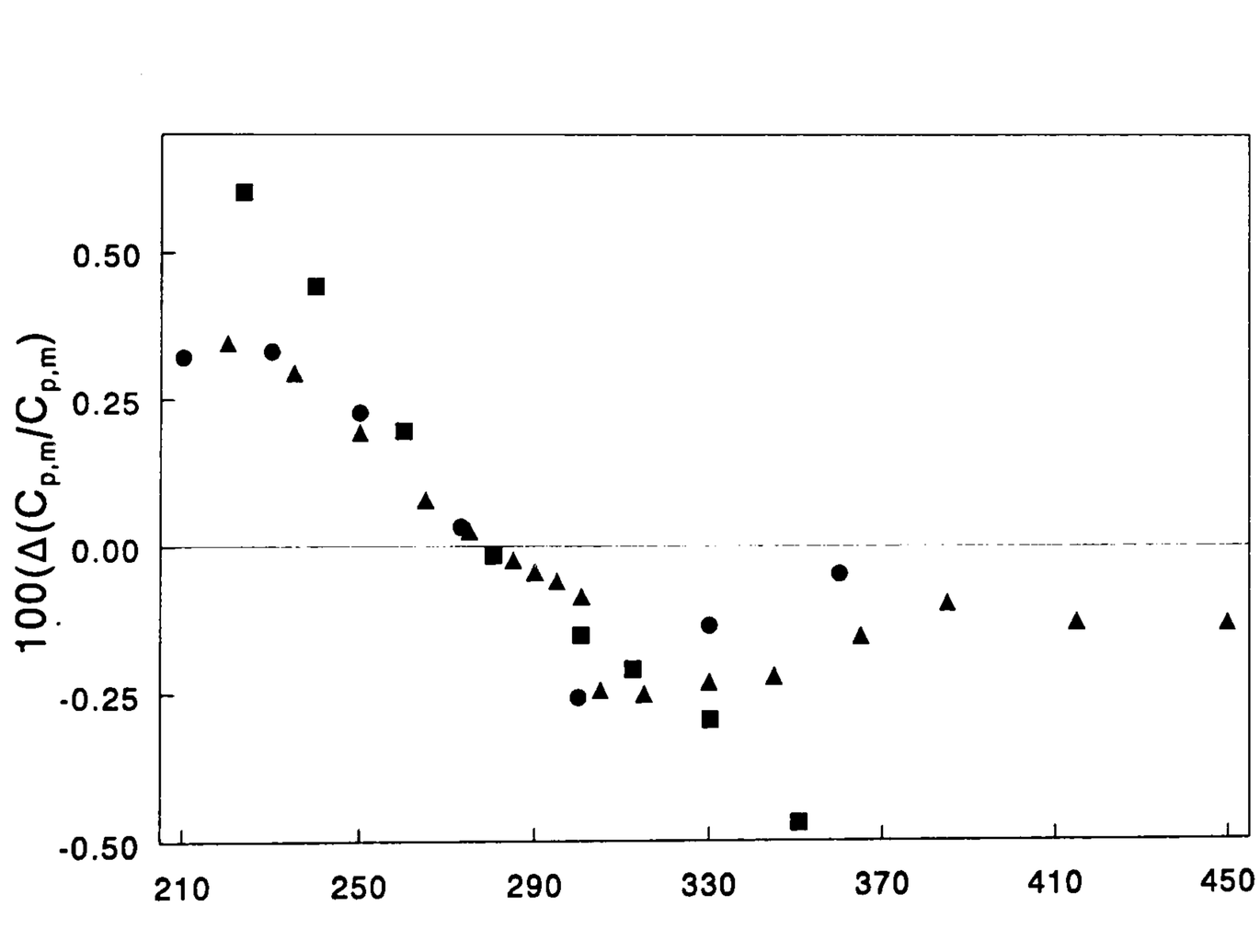


Figure 6.9 Fractional deviations $\Delta C_{p,\mathrm{m}}^{\mathrm{pg}}/C_{p,\mathrm{m}}^{\mathrm{pg}}$ of the perfect-gas heat capacities of ethane determined from acoustic measurements from those calculated by means of equation (6.4.2). ■, ref. 14; ●, ref. 20; ▲, this work.

Although the agreement between equation (6.4.2) and the acoustic determination of the heat capacities is not very good, it is evident that the agreement between the present results and those of Boyes at temperatures below 290 K is very close.

At higher temperature this agreement deteriorated somewhat towards a value no better than about 0.1 per cent. Values reported by Esper *et al.* tend to deviate in a systematic way from the correlation and only at a few temperatures do they agree with the other sources. The observed degree of disagreement could well be due to impurities. Unfortunately, the above comparison is not conclusive so the purity of the samples is not a resolved matter.

6.4.3 Acoustic virial coefficients.

Second acoustic virial coefficient β_a have been also reported by both Boyes[20] and Esper *et al.*[14] Only the former included determinations of third acoustic virial coefficients because the latter measured u at pressures no greater than 0.5 MPa.

Since the values of β_a listed in table 5 are mostly at different temperatures of those reported elsewhere,[14,20] a smoothing of the data has to be made in order to carry out comparisons. A convenient way of achieving the above is to use the present values of β_a to determining the parameters of an intermolecular potential model by means of a non-linear regression algorithm, which is described in detail in chapter seven.

Once the model was obtained, it was used to calculate β_a at each temperature reported in references [14] and [20] and the differences between the experimental β_a and the values calculated in this way are compared in figure 10. It is evident that the intermolecular potential proposed was capable of reproducing the second acoustic virial coefficients obtained in this work quite well for $T \geq 235$ K and where they also agreed within $\pm$ 1.0 $cm^3 \cdot mol^{-1}$ with the values reported by Boyes. Less satisfactory agreement was found with values reported by Esper *et al.* but their values have a larger uncertainty which might be as much as 3.0 $cm^3 \cdot mol^{-1}$.[14] Finally, in figure 11 the third acoustic virial coefficients listed in table 5 are plotted. The only other determinations of this quantity appears to be that of Boyes[20] whose results are also plotted in figure 11; both sets of third acoustic virial coefficients are in fair agreement for temperatures above 273 K but they differ notably at lower temperatures.

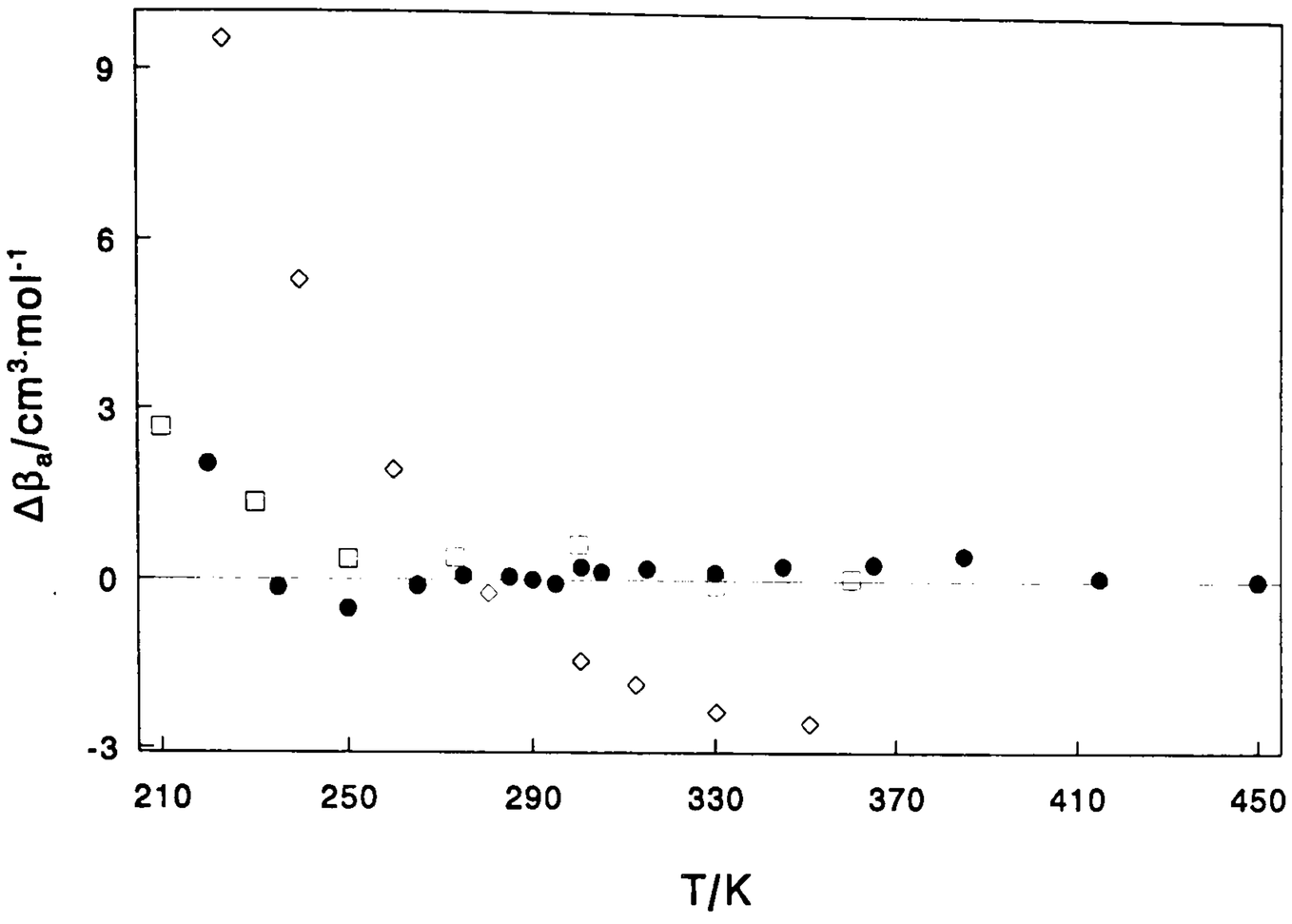


Figure 6.10 Deviations $\Delta\beta_a$ of the second acoustic virial coefficients β_a of ethane from values calculated with a site-site intermolecular potential model. ◇, ref. 14; □, ref. 20; ●, this work.

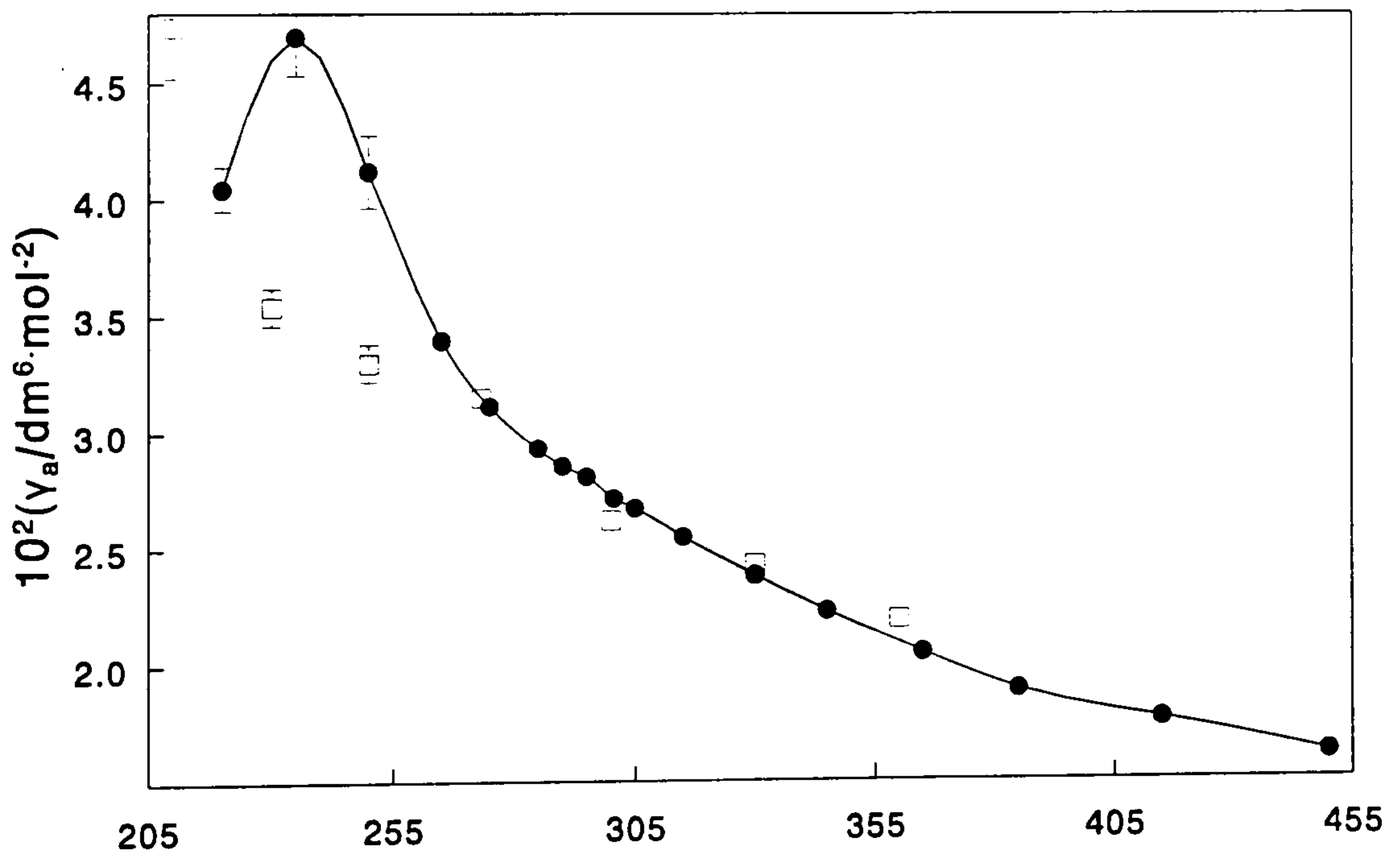


Figure 6.11 Comparison of the third acoustic virial coefficients γ_a of ethane. Solid curve is a graphical interpolation of the data reported here. □, ref. 20; ●, this work.

Furthermore, the trend shown by the present values of γ_a resembles closely that obtained in the case of argon while the values reported by Boyes have a completely different trend. This may be explained by the fact that the pressures reached in Boyes' measurements of the speed of sound were substantially lower than those achieved in this work and his results do not establish γ_a precisely. The present results are believed to be the more reliable.

6.5 Carbon Dioxide.

Measurements of the speed of sound in carbon dioxide differed from those in the other two system studied in several ways. Firstly, the speed of sound was badly affected by vibrational relaxation and the experimental frequency range overlapped with the dispersion region at low temperatures. This led to low quality factors Q: they never exceeded 5000 and were as small as a few hundred at low pressures. Further, at the temperature of 220 K where the measurements were restricted by the vapour-pressure curve to a pressure < 450 kPa, the mode (0, 2) was the only distinguishable radial mode, but was affected by overlap with the nearby non-radial mode (3, 1). This made the measurement of the speed of sound under those conditions very difficult. It was therefore decided to measure also the non-radial mode (1, 1), which is a three-component multiplet but appears at a much lower frequency than any radial mode and hence is less affected by relaxation absorption.

6.5.1 Non-radial mode (1, 1)

In order to use the non-radial mode, which in the present slightly distorted resonator has the appearance of a partially-resolved triplet, two pieces of information are needed: one is the effective mass of the shell and the other is shift to the eigenvalue ν_{11}. The former is required to calculate the correction for the coupling of the gas and shell motion, while the latter characterises the effect of imperfection in geometry. Further, the correction due to the viscous boundary layer has also to be included since for mode (1, 1) the tangential component of the fluid velocity is finite at the wall. This correction can be calculated from formula (2.3.25) assuming that the molecular slip is characterised by a momentum accommodation length l_s given by

$$l_s = (\eta / p)(\pi RT/2M)^{1/2}[(2 - h_s)/h_s], \qquad (6.5.1)$$

where h_s is the momentum accommodation coefficient, assumed to be unity.

In order to obtain the effective mass of the resonator and evaluate the effects of imperfection in geometry, measurements in a calibration gas were made and analysed according to the model proposed in chapter five.

Furthermore, a region in which both gases (calibration and test gas) had the same speed of sound and, therefore, the same resonance frequency for the mode (1, 1), was chosen. This may be important since the effective mass may be frequency dependent and it was intended to transfer the information from one gas to another. Thus, it seemed sensible to carry out this calibration procedure as close as possible to conditions prevailing during the work on carbon dioxide.

The frequency range for mode (1, 1) of carbon dioxide for the working density range of each of the seven isotherms was estimated by assuming the simplest case in which the resonator is considered as an ideal cavity. Values of speed of sound required for such estimations were calculated from a correlation based on the principle of the corresponding states.[4] In figure 12, these intervals of frequency are shown.

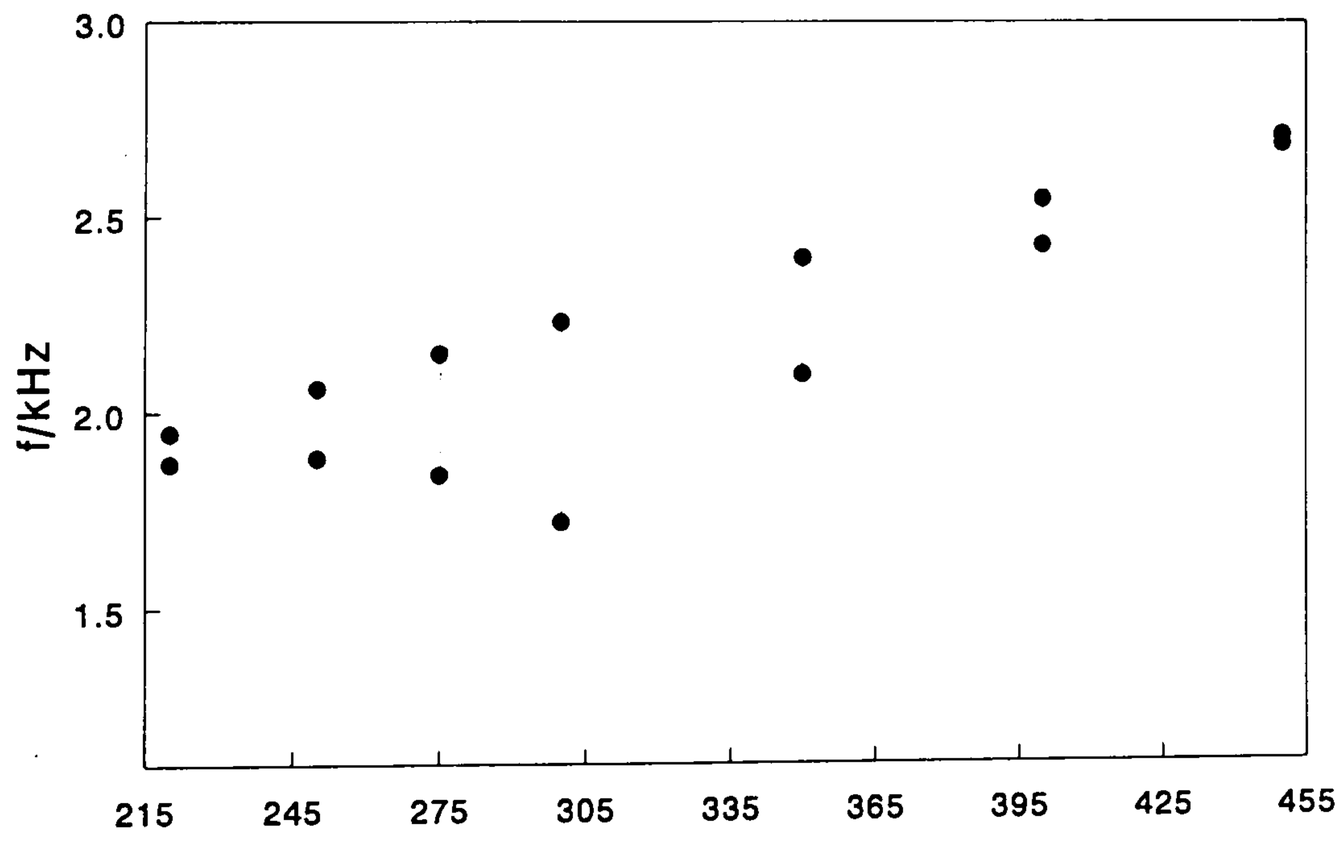


Figure 6.12 Estimated frequency range for non-radial mode (1, 1) of carbon dioxide at several temperatures.

The problem with dispersion would be more acute at low temperatures because of the restricted pressure range at which one had to work. Thus, argon was chosen as the calibration gas and measured at a temperature of 170 K since, for this temperature, the frequency range of mode (1, 1) varied from 1.8 kHz at a pressure of roughly 6.5 MPa to nearly 2.0 kHz at the limit of zero-pressure. With this choice, frequencies corresponding to mode (1, 1) for carbon dioxide at 220 K and 250 K were included.

Thus, measurements in argon at 170 K and pressures up to 6.2 MPa were performed for modes $(1, 1)$ and $(0, n)$, with $n = 2, 3$. In an initial analysis, all corrections were applied for each mode according to the equation (6.2.1) except for corrections for both the shell-gas coupling and imperfection in geometry for the mode (1, 1). Thus, the differences between the values of u derived from mode (1, 1) with the accurate values derived from the two radial mode, Δu, reflected the corrections omitted in mode (1, 1). When Δu was plotted as a function of density, a nearly straight line was obtained, as can be seen in figure 13.

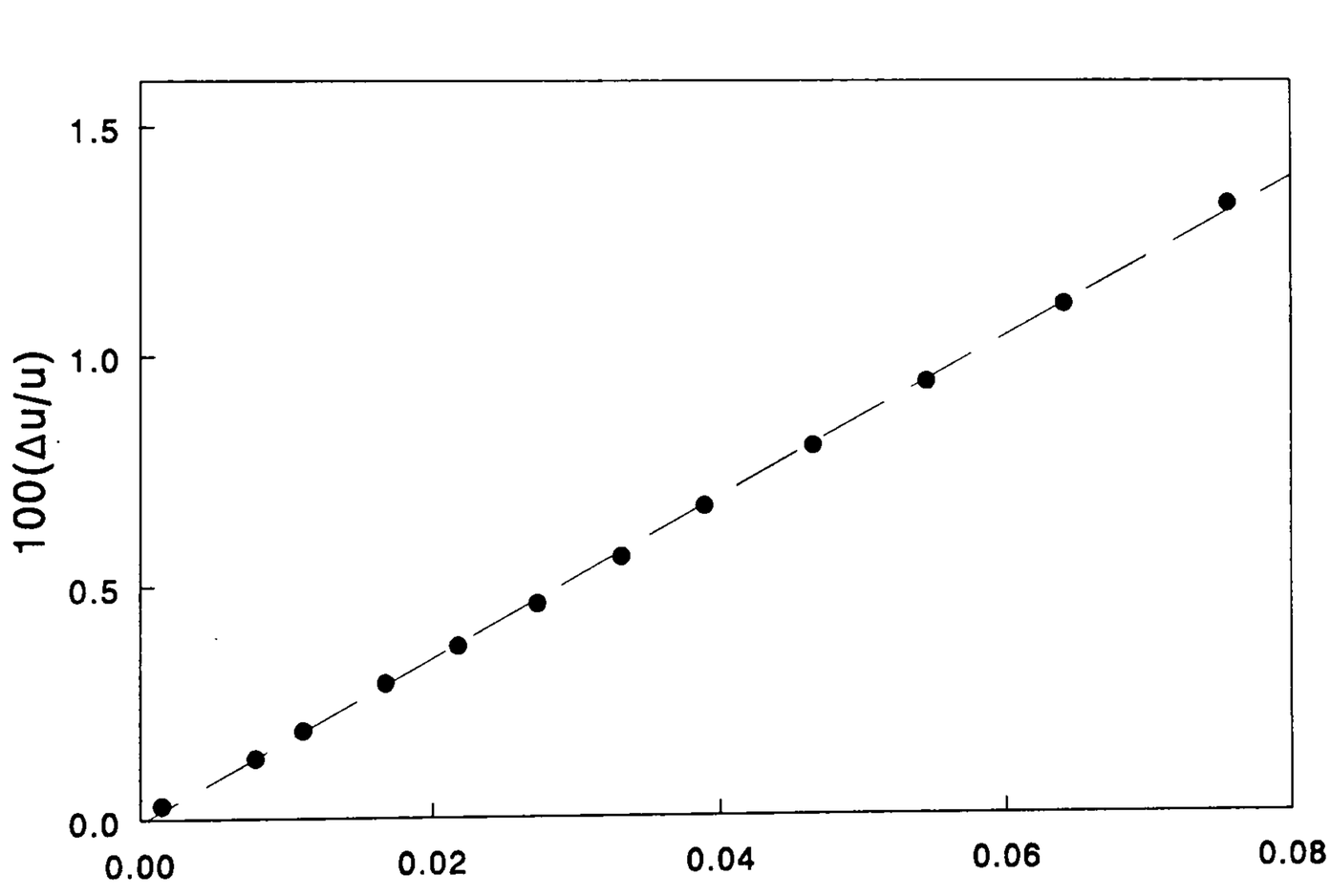


Figure 6.13 Fractional deviations $\Delta u/u$ of the speeds of sound u derived from mode (1, 1) from the actual speed of sound as a function of the mass of the fluid M_{fl} before applying the correction for the coupling of the gas and shell motion. Measurements correspond to argon at a temperature of 170 K.

This is exactly the expected trend, since the correction for the coupling of gas and shell motion for any mode is proportional to ρu^2 at constant frequency according to equation (2.3.31) and u varied over a range of only 8 per cent.

Furthermore, the value of Δu at zero density is related with the imperfection in geometry and it was assumed that this correction was independent of the gas density. Thus, the shift of the eigenvalue $\Delta\nu_{11}$ that would bring both set of measurements into agreement was determined. Once, this was achieved the remaining disagreement between the values of u determined from mode (1, 1) and from mode (0, 2) should be entirely due to the shell motion correction. A linear regression of these data was then carried out from which the effective mass of the shell M_{sh} required by (2.3.31) was obtained. An analysis of half-widths g_{11} was also performed and, after allowing for all known contributions (corrections for openings and the viscous and thermal boundary layers), significant excess half-widths Δg_{11} were always obtained. However, these did not behave as predicted by a model of the shell and gas motion including a damping term. In other words, a single constant damping coefficient was unable to bring the final Δg_{11} within a range of $\pm\ 20\cdot10^{-6}\cdot f_{11}$. From this calibration procedure, the following values for the shift of the eigenvalue and the effective mass of the resonator were obtained: $\Delta\nu_{11} = -346.8\cdot10^{-6}$ and $M_{sh} = 2.495 \pm 0.005$ kg.

The value of $\Delta\nu_{11}$ is consistent with the order of magnitude of the corresponding shifts of the radial-mode eigenvalues which range from $-206\cdot10^{-6}$ to $744\cdot10^{-6}$. The mass of the resonator can be estimated by a simple geometric calculation which gives a value of (2.1 ± 0.1) kg. The figure does not compare favourably with the value derived from acoustic measurements but the fact that the effective mass exceeds the true mass is not surprising as the resonator is held firmly by a clamp which couples it to other massive objects.

In conclusion, it seems that a reliable analysis of the experimental frequencies of the non-radial mode (1, 1) can be made with the inclusion of the two corrections described. No further attempts were made to account for the half-widths.

6.5.2 Speed of sound.

The speed of sound was determined from the non-radial mode (1, 1) and the four lowest radial modes (0, 2) to (0, 5). However, at temperatures below 300 K, the restricted pressure range available combined with strong relaxation effects limited the measurements to modes up to (0, 4). Moreover, at the temperatures of 250 K and 220 K the only distinguishable resonances were (1, 1) and (0, 2). Thus, mode (1, 1) was measured only along the isotherms at 220 K and 250 K while on the remaining five isotherms only radial modes were measured. At 250 K, very good agreement between speed of sound derived from the (0, 2) radial and the (1, 1) non-radial modes was achieved: u from both modes agreed within ± 20 ppm. However, at 220 K this level of agreement was not achieved. Instead, a systematic deviation between u from different modes was observed. This trend persisted even after corrections for dispersion were included. Thus, the measurements of mode (1, 1) at 220 K were rejected for the final analysis.

Thermodynamic properties involved in the calculation of the corrections were obtained from the Lee-Kesler equation of state[4] while transport properties required for the calculations were obtained from a correlation due to Vesovic *et al.*[23]

From a preliminary analysis of the speed of sound, excess half widths were derived and, in a similar manner to the case of ethane, relaxation times τ for carbon dioxide were determined. Only excess half-widths from the radial modes were employed in this calculation. In table 6, speeds of sound of carbon dioxide are reported after allowing for dispersion corrections; further small corrections were applied to reduce all results to the nominal temperature.

In order to derive relaxation times τ required for the correction due to dispersion, it was **assumed** that a single relaxation mechanism was present and that equation (2.3.43) could be used. Values of C_{int} used in the non-linear regression analysis of the Δg_{0n} were obtained from a correlation given in reference [23] at each temperature.

In table 7, the relaxation times at a density of 1 $kg \cdot m^{-3}$ derived from the non-linear regression are listed. Figure 14 illustrated the sort of agreement obtained for the excess half widths Δg before and after the corrections for absorption were applied.

Table 6.6 Speed of sound of carbon dioxide at temperatures from 220 K to 450 K and pressures up to 14 MPa.

p/kPa	u/m·s^{-1}	p/kPa	u/m·s^{-1}	p/kPa	u/m·s^{-1}	p/kPa	u/m·s^{-1}
			T = 220 K				
517.38	224.907	412.32	227.208	313.14	229.244	265.25	230.154
457.69	226.227	363.61	228.220				
			T = 250 K				
1369.02	228.999	1179.46	232.218	913.95	236.436	629.76	240.652
1292.99	230.312	1050.84	234.296	773.66	238.544	477.05	242.820
			T = 275 K				
3213.11	219.898	2476.72	231.531	1541.61	243.557	812.74	251.675
2977.63	223.921	2185.95	235.519	1191.23	247.560	420.54	255.667
2721.41	227.948	1878.10	239.480				
			T = 300 K				
6100.00	205.863	5303.53	219.148	3643.25	238.812	2021.54	254.000
6007.50	207.702	4836.31	225.367	2893.08	246.164	1085.78	261.777
5706.35	213.030	4286.21	231.903				
			T = 350 K				
9270.57	250.173	7121.80	257.385	5176.38	265.648	2848.13	276.295
8721.45	251.703	6214.62	261.118	4067.08	270.669	1482.73	282.641
7984.38	254.135						
			T = 400 K				
13214.84	287.460	10157.55	286.895	6359.03	291.833	3337.10	298.545
12432.26	286.822	8989.99	287.866	4876.29	294.901	1728.71	302.735
11298.06	286.524	7686.45	289.557				

Table 6.6 -continued

p/kPa	u/m·s^{-1}	p/kPa	u/m·s^{-1}	p/kPa	u/m·s^{-1}	p/kPa	u/m·s^{-1}
			T = 450 K				
14188.33	317.053	10616.70	314.758	7282.88	315.586	3788.09	318.904
13706.86	316.526	9039.79	314.832	5609.73	316.903	1963.14	321.416
12169.42	315.310						

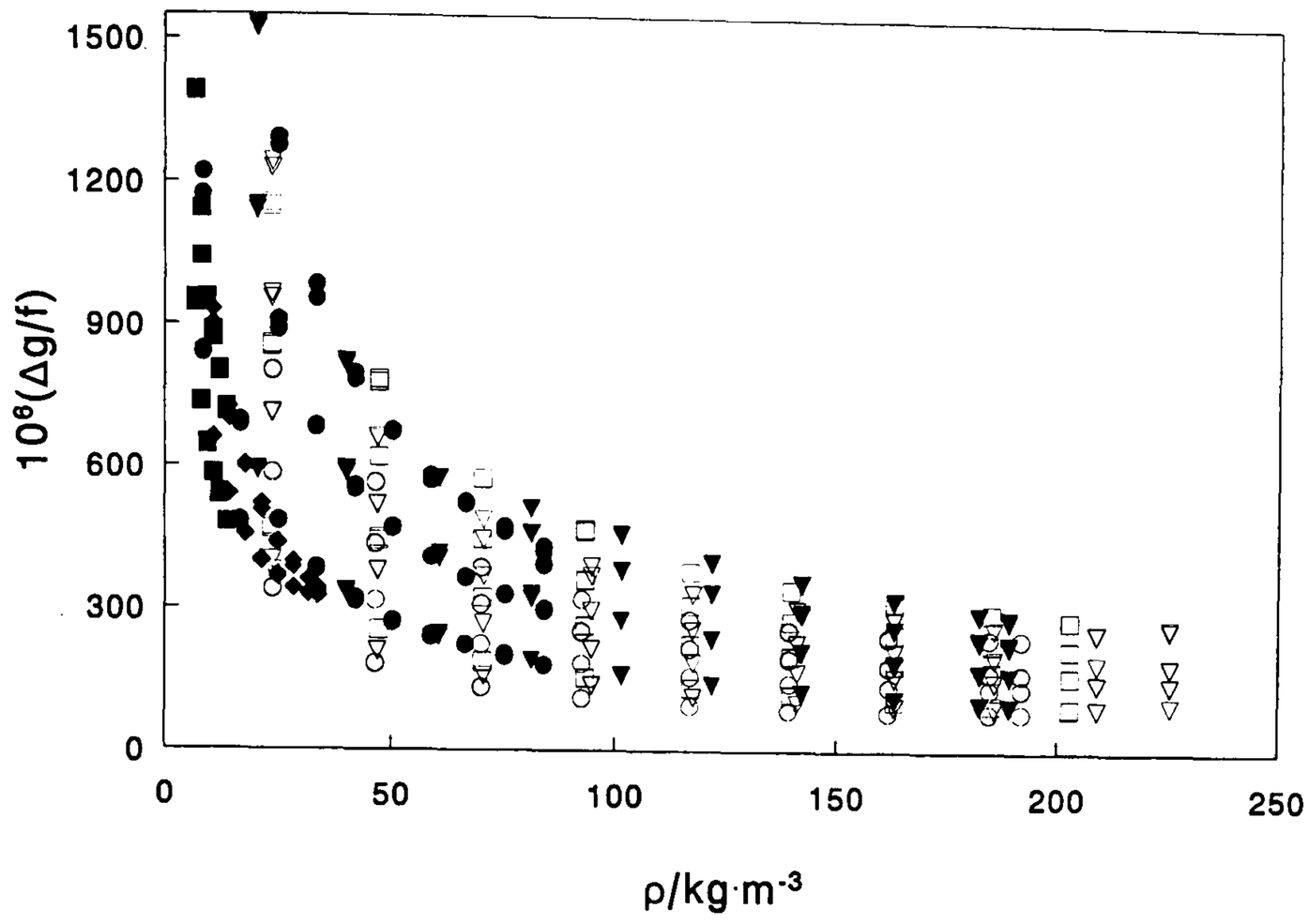
Table 6.7 Vibrational relaxation times of carbon dioxide at the density of 1 kg·m^{-3}.

T/K	τ/μs	T/K	τ/μs
220	15.502	350	8.891
250	13.197	400	6.737
275	12.883	450	5.250
300	11.678		

The values of τ are three order of magnitude larger than those for ethane which is consistent with the marked dispersion found in the experiments. For instance, the correction for dispersion to the speed of sound at 220 K and at a pressure of 265.25 kPa rose to about -55 ppm in u. The magnitude of the correction declined rapidly with increasing of either temperature or pressure.

Once again, the internal consistency of the speed of sound was tested by fits in powers of the density along each of the isotherms. At temperatures above 275 K, four or five terms fits were used to accommodate the data within 20 ppm, while at 250 K the standard deviation of the fit deteriorated to 42 ppm. At 220 K, the measurements covered the range from a maximum pressure of 520 kP down to just 265 kPa below which relaxation absorption prevented useful results being obtained. Only six points were measured in that interval and, in the end, the lowest pressure was rejected from the final analysis. Despite these limitations, a two-term fit for the isotherm at 220 K gave a standard deviation of just 83 ppm. This figure does not seem too high when one takes into account all the difficulties.

a)



b)

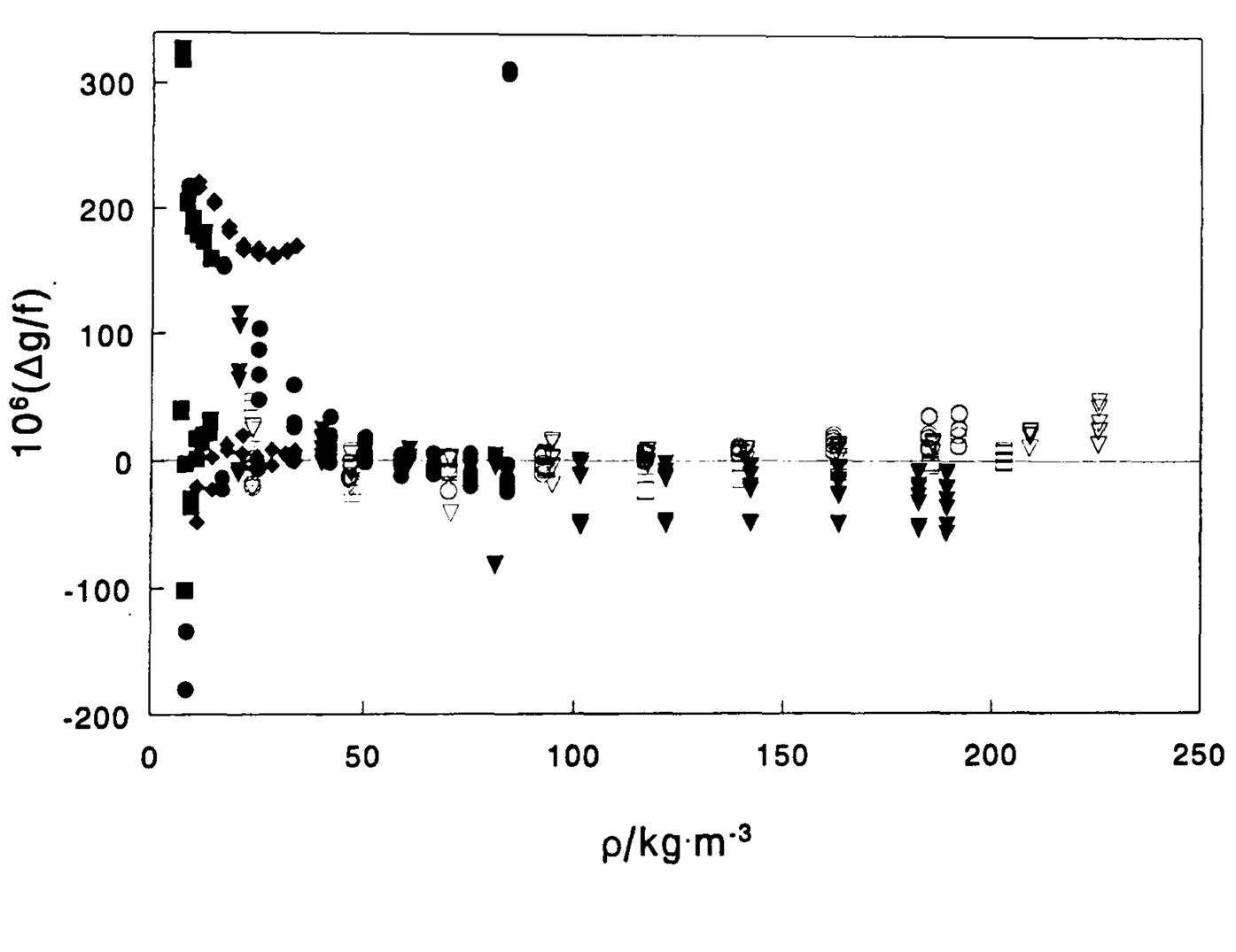


Figure 6.14 Excess half-widths Δg on carbon dioxide: a) before corrected for sound absorption, b) after corrected for sound absorption. ■, T = 220 K; ◆, T = 250 K; ●, T = 275 K; ▼, T = 300 K; □, T = 350 K; ▽, T = 400 K; ○, T = 450 K.

No other work reported in the literature has involved speeds of sound in carbon dioxide in the region where the present measurements were carried out.

6.5.3 Heat capacities and second acoustic virial coefficient.

As in the cases of argon and ethane, a limiting slope analysis was carried out in order to derive heat capacities and acoustic virial coefficients. Unfortunately, on this occasion the initial estimate of A_0 was obtained from a value of u at a much larger pressure than previously since sound-speed measurements at pressures lower than 265 kPa were not feasible at any temperature. However, Y_β behaved in a similar manner to the cases of argon or ethane, on most isotherms, i.e. it was nearly linear when plotted against densities calculated from an equation of state.[4]

Only for the isotherms at 220 K and 250 K was a smooth dependency of Y_β on density not found. This can be seen in figure 15. Consequently, the limiting slope analysis was carried out with the initial guess for A_0 taken as the value of u^2 at the lowest available pressure only for $T \geq 275$ K. Even these cases, convergence required more iterations (never less than twenty five) but eventually a good fit was obtained.

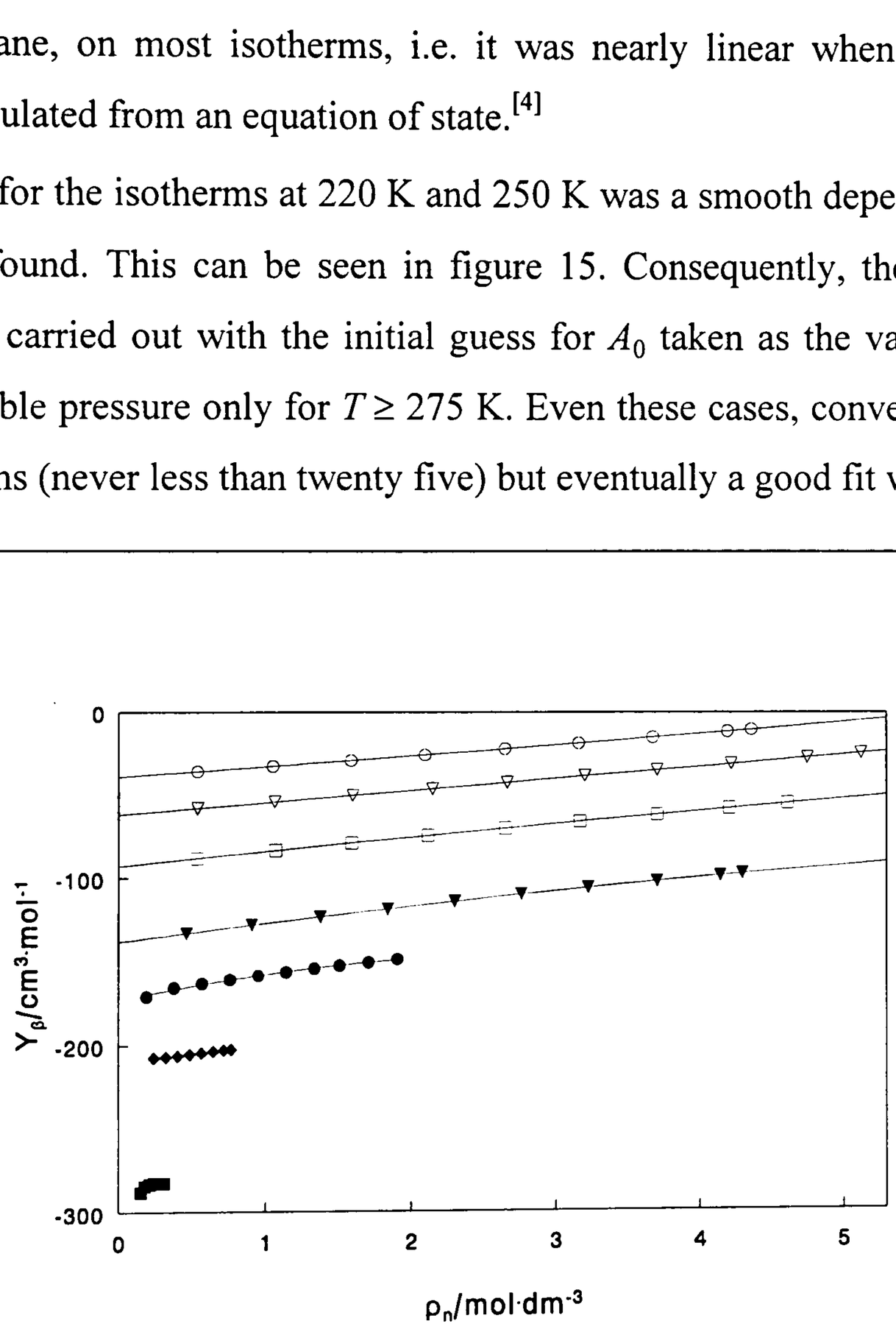


Figure 6.15 Y_β on carbon dioxide as a function of amount-of-substance density ρ_n. Curves are quadratic polynomials fitted to the results. ■, T = 220 K; ◆, T = 250 K; ●, T = 275 K; ▼, T = 300 K; □, T = 350 K; ▽, T = 400 K; ○, T = 450 K.

Then, from the values of A_0, the recommended value of the molar mass (M = 0.044009 kg·mol^{-1}) and the slope of Y_β at zero-density, heat capacities of the perfect gas and second acoustic virial coefficients were determined.

As a further test, a slightly variation of the limiting slope analysis was performed. This time A_0 was constrained to be the value calculated from an empirical correlation of the perfect-gas heat capacities reported by Woolley for carbon dioxide (which were based in spectroscopic information).[24] The calculated values had an estimated uncertainty of 0.0007·R whereas the correlation

$$\begin{aligned}(C_{p,\mathrm{m}}^{\mathrm{pg}}/R) = 2.141799 + 9.271544\times10^{-3}(T/\mathrm{K}) \\ -5.878347\times10^{-6}(T/\mathrm{K})^2 + 24.47833(T/\mathrm{K})^{-1},\end{aligned} \tag{6.5.2}$$

reproduced them within ± 0.04 per cent. Once A_0 was fixed, a single regression analysis of Y_β provided both second and third acoustic virial coefficients. The maximum changes were for β_a and $C_{p,\mathrm{m}}^{\mathrm{pg}}$, respectively, of just 0.75 cm^3·mol^{-1} and 0.0058·R, both being at 450 K.

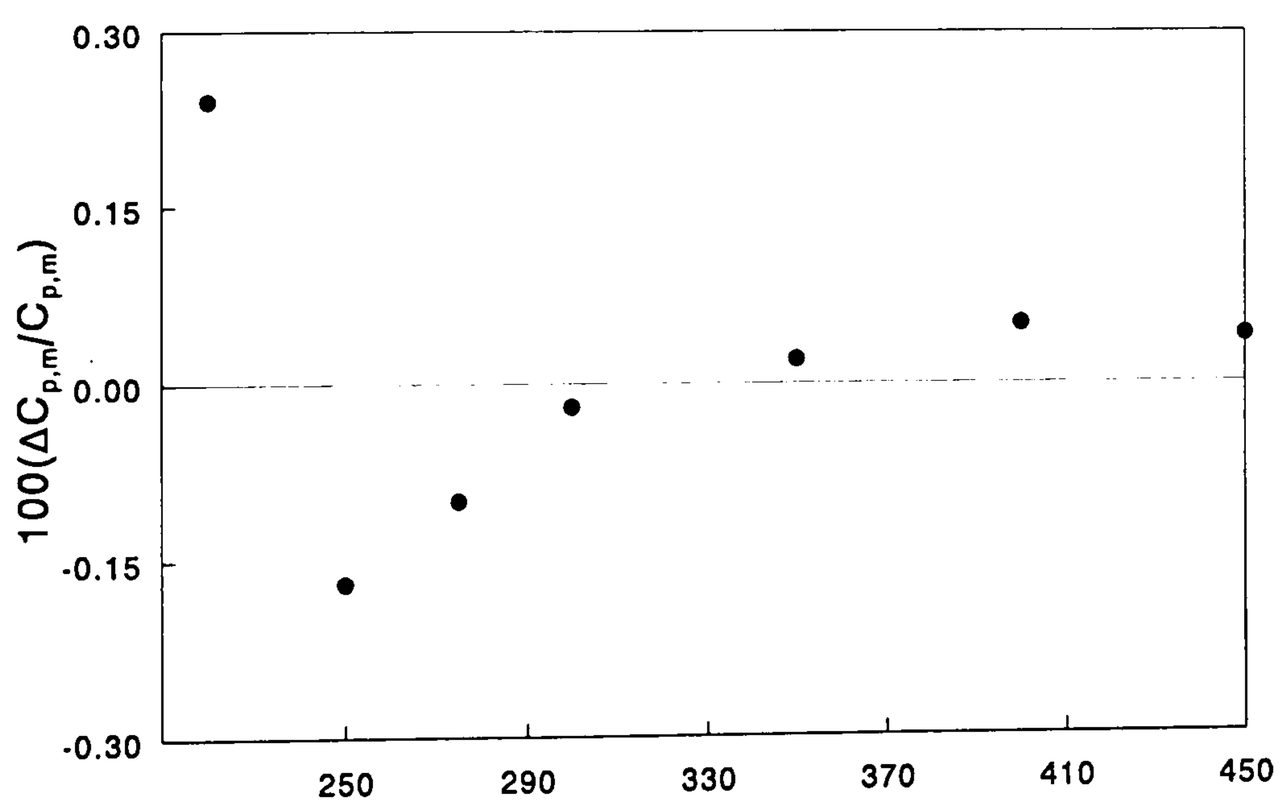


Figure 6.16 Fractional deviations $\Delta C_{p,\mathrm{m}}^{\mathrm{pg}}/C_{p,\mathrm{m}}^{\mathrm{pg}}$ of the perfect-gas heat capacities of carbon dioxide determined from limiting slope analysis from those derived from spectroscopic data given in reference [24]. ●, this work.

Table 6.8 Second acoustic virial coefficients and molar perfect-gas heat capacities at constant pressure of carbon dioxide.

T/K	$C_{p,\mathrm{m}}^{\mathrm{pg}}/R$	β_a/cm^3·mol^{-1}
220	5.3007 ± 0.0002	-458.51 ± 0.03
250	5.6537 ± 0.0003	-360.95 ± 0.13
275	5.9822 ± 0.0003	-300.38 ± 0.04
300	6.3452 ± 0.0003	-252.06 ± 0.04
350	7.0064 ± 0.0004	-189.75 ± 0.05
400	8.0958 ± 0.0006	-123.05 ± 0.01
450	8.6295 ± 0.0007	-98.48 ± 0.01

This means that extrapolation of A_0 from a comparatively large pressure may still be a reasonably accurate way of performing the limiting slope analysis.

For isotherms at 220 K and 250 K, heat capacities and second acoustic virial coefficients were derived from straightforward polynomial fits of the speed of sound as a function of density. The final values of the heat capacities and second acoustic virial coefficients are listed in table 8, together with their estimated uncertainty obtained from the precision of the fits.

The heat capacities were compared with those reported by Woolley and the differences are plotted in figure 16. This comparison is favourable taking into account all the difficulties in determining the resonances frequencies.

There appear to have been no previous measurements of the speed of sound in carbon dioxide in the low density range reported here, so no other values of the acoustic virial coefficients were available for comparison. However, second acoustic virial coefficients were used to determine the parameters of an intermolecular potential, a procedure which can be seen as a test of internal consistency. Figure 17 shows the deviations found for the experimental points from values calculated from the final potential. The maximum deviation is 3.7 cm^3·mol^{-1} at 220 K, but most of the points are reproduced much better. Details of fitting procedure follow are given in the next chapter.

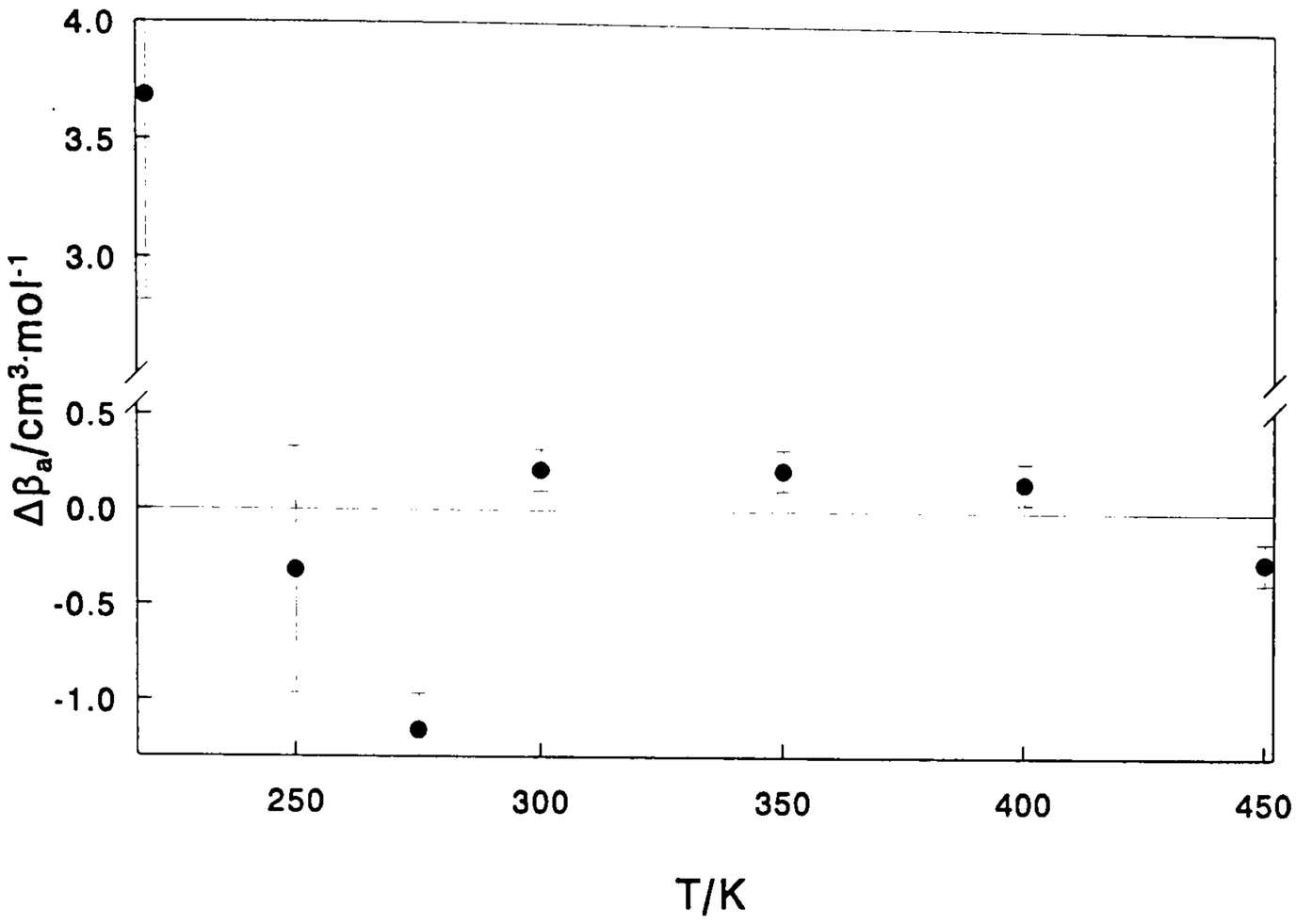


Figure 6.17 Deviations $\Delta\beta_a$ of the second acoustic virial coefficients β_a of carbon dioxide from values calculated with a site-site intermolecular potential. ●, this work.

6.6 Binary mixture $(1\text{-}x)C_2H_6 + xCO_2$.

A binary mixture with mole fraction of carbon dioxide $x \approx 0.6$ was studied with the aim of obtaining interaction virial coefficients for the system carbon dioxide-ethane from the measurements of the speed of sound. Measurements were performed in a rather moderate pressure range (not beyond 1.25 MPa) along seven isotherms. The temperatures at which these measurements took place were the same as those studied for carbon dioxide. An important difference from the latter measurements was the fact that the mixture presented much larger quality factors Q (of the order of several thousands) even at pressures as low as 50 kPa. The acoustic virial coefficients were obtained from polynomial fits of the speed of sound as function of density and the composition of each sample was determined from the value of the zero-density sound speed estimated in this way.

6.6.1 Speed of sound.

At all seven temperatures measurements with the lowest five radial modes were carried out. Even at the temperature of 220 K, no difficulties were found detecting all radial modes and therefore there was no need to measure non-radial modes. The pressure range at 220 K was restricted to pressures no greater than 612 kPa in order to maintain the sample within one-single phase region. Sufficient information was obtained in the literature to worked out the dew point at that temperature for the chosen composition.[25,26] At the other temperatures, the dew pressure was always far above of the maximum pressure measured.

All thermodynamic properties required for the calculation of the corrections were derived from the equation of state of Lee and Kesler,[4] assuming for the binary mixture a fixed nominal composition of $x = 0.6$ mole at any temperature. Transport properties involved in the above correction terms were also derived for a fixed composition of $x = 0.6$. In this case, an empirical correlation for thermal conductivity and viscosity was fitted to values for this particular mixture obtained from the values of the pure components by means of a computational package.[27] This programme calculates the transport properties of a binary mixture from the transport properties of the pure components by a suitable kinetic theory which is based upon a rigid-sphere model of the fluid mixture.[28]

The precision of the empirical correlation are about ± 0.01 and ± 0.02 per cent of the viscosity and thermal conductivity, respectively, inside of a temperature range from 220 K to 460 K, and densities up to 500 $mol \cdot m^{-3}$, whereas the accuracy of the values themselves may be no better than 2 per cent.[27]

At first glance, all resonances were quite strong and relatively sharp though an excess halfwidth larger than the usual level persisted. Besides all absorption mechanisms described for a pure gas, in a mixture another source of absorption of sound is found. Since in an acoustic wave gradients of both temperature and density occur in the bulk of the fluid, a tendency to unmix exists and this process is not entirely reversible. The main consequence is additional sound absorption.[29] This additional contribution to the absorption coefficient α_{diff} has been worked out for a

binary mixture of ideal gases.[30] For a mixture $(1-x)A + xB$, the final expression of α_{diff} is[31]

$$\alpha_{\text{diff}} = (\omega^2/2u^3)\gamma x(1-x)D\{[(M_B-M_A)/M]+[(\gamma-1)/\gamma x(1-x)]K_T\}, \quad (6.6.1)$$

where M_A and M_B are the molar masses of the two components, D is the binary diffusion coefficient and K_T is the thermal difussion ratio; γ and M are the ratio of the heat capacities and the molar mass of the mixture. The contribution to the half-widths arising from **difussion** g_{diff} is then simply $(u\alpha_{\text{diff}}/2\pi)$. An attempt was made to calculate this correction but no information on the coefficients D and K_T was available for this particular mixture ($x = 0.6$, $A = C_2H_6$ and $B = CO_2$). Thus, a rough estimation of the magnitude of g_{diff} was made by assuming that the mixture was in fact an equimolar mixture of nitrogen and carbon dioxide because data was available for these components: $D = 0.118$ $m^2 \cdot s^{-1}$ and $K_T = 0.0583$ at $T = 250$ K and $p = 101.3$ kPa.[32] Small corrections to the above values were applied to calculate g_{diff} at a pressure of 150 kPa ($D\rho$ is approximately constant). The estimated values of the g_{diff}, for data at 250 K and 150 kPa, are listed in table 9 together with the experimental excess half-widths Δg_{0n}. One can see immediately that, under these conditions, diffusion effects are negligible (their contribution was never larger than 0.5 per cent of Δg_{0n}) so no further attempt to calculate g_{diff} was made. In addition, table 9 offers an idea of the sort of sound dispersion presented in the mixture which was **definitely** less severe than for pure carbon dioxide.

Table 6.9 Excess half-width Δg and estimated contribution to the excess half-width g_{diff} arising from diffusion for the mixture ethane + carbon dioxide.

n	$f(0,n)$/Hz	g_{diff}/Hz	$(g_{\text{diff}}/f)\cdot 10^6$	$(\Delta g(0,n)/f)\cdot 10^6$
2	4620.21	$1.5\cdot 10^{-3}$	0.3	58.0
3	7943.55	$4.4\cdot 10^{-3}$	0.6	79.7
4	11212.56	$8.8\cdot 10^{-3}$	0.8	109.6
5	14464.48	$14.7\cdot 10^{-3}$	1.0	136.5

A preliminary analysis was carried out in order to determine the relaxation time and thence apply the appropriate dispersion corrections. However, the relaxation time for a mixture is composition dependent and is affected by relaxation times for the pure components.

According to Herzfeld and Litovitz,[29] a relaxation correction can be worked out in a mixture of two gases A and B with the composition $(1-x)A + xB$. The main assumption is that each of the pure gases could be treated as having a single relaxation time. These relaxation times will be denoted by τ_A and τ_B, respectively. Furthermore, τ_{AB} will denote the relaxation time of one molecule A embedded in a fluid B (assumed to be composed of spherical molecules) while τ_{BA} will denote a relaxation time for the inverse condition. The number of deactivations per second of molecule A in the mixture is

$$(1-x)/\tau_A + x/\tau_{AB}, \tag{6.6.2}$$

since it makes only $(1-x)$ times as many collisions with other molecules A than it would have made if only A had been present, and x times as many with B molecules than if these alone had been present. Similarly, the number of deactivations per second of a molecule B is

$$x/\tau_B + (1-x)/\tau_{BA}. \tag{6.6.3}$$

The mixture is then treated as one gas with two degrees of internal freedom excited in parallel. For this purpose, it has been assumed that none of the unlike molecule can interchange energy between their internal degrees of freedom. Hence, one has

$$\tau_1^{-1} = (1-x)/\tau_A + x/\tau_{AB}, \tag{6.6.4}$$

$$\tau_2^{-1} = x/\tau_{AB} + (1-x)/\tau_B, \tag{6.6.5}$$

and with each of these relaxation times the part of the heat capacity that undergoes relaxation is calculated as

$$C_1 = (1-x)C_{\text{int},A}\,, \tag{6.6.6}$$

$$C_2 = xC_{\text{int},B}\,. \tag{6.6.7}$$

Thus, with the above definitions for τ_j and C_j, equations (2.3.41) and (2.4.43) can be utilised to worked out the dispersion correction. However, it should be noted that even when both relaxation times for the pure components τ_A and τ_B are known, with only one piece of information (excess half-widths) it will not be possible to work out both relaxation times for the unlike interactions τ_{AB} and τ_{BA}. A simplification of the problem can be accomplished by assuming a value for one of these times; for instance, let it be assumed that an excited molecule A can not exchange energy with an unexcited molecule B, which mean that is τ_{AB} infinite. Another possible assumption is to consider that any molecule being of species A or B, may deactivated an excited molecule A, which would imply that τ_{AB} is just τ_A. Somewhere in between these two extremes the actual value of τ_{AB} should be found. Obviously, either of the above assumptions will lead to a value of τ_{BA} which may not be the actual one but it would be sufficiently accurate to produce a satisfactory regression of the excess half-widths.

Thus, the excess half-widths determined from a preliminary analysis of the speed of sound were fitted to a model described by equations (2.3.41) and (2.3.43) with each τ_j (j =1,2) given by equations (6.6.4) and (6.6.5). The relaxation times of the pure components were obtained from the experimental values given in tables 4 and 7 while the part of the heat **capacities** that undergoes relaxation, $C_{\text{int},A}$ and $C_{\text{int},B}$ were respectively computed at each temperature from $C_{p,\text{m}}^{\text{pg}} - 4R$, with $C_{p,\text{m}}^{\text{pg}}$ calculated by equation (6.4.2), and from the correlation given in reference [23].

The values of the relaxation times τ_{BA} at a density of 1 kg·m^{-3} which corrected the excess half-widths under the assumption that τ_{AB} is infinite are listed in table 10. The values of τ_{BA} derived from the non-linear regression of Δg were quite insensitive to variations in composition. For instance, 0.1 per cent change of the nominal composition x, would affect values of τ_{BA} by no more than 0.25 per cent. Larger changes in τ_{BA} would be obtained if a different assumption for τ_{AB} were made.

Table 6.10 Vibrational relaxation times τ_{BA} of the mixture ethane plus carbon dioxide at the density of 1 kg·m^{-3} with the assumption that τ_{AB} is infinite.

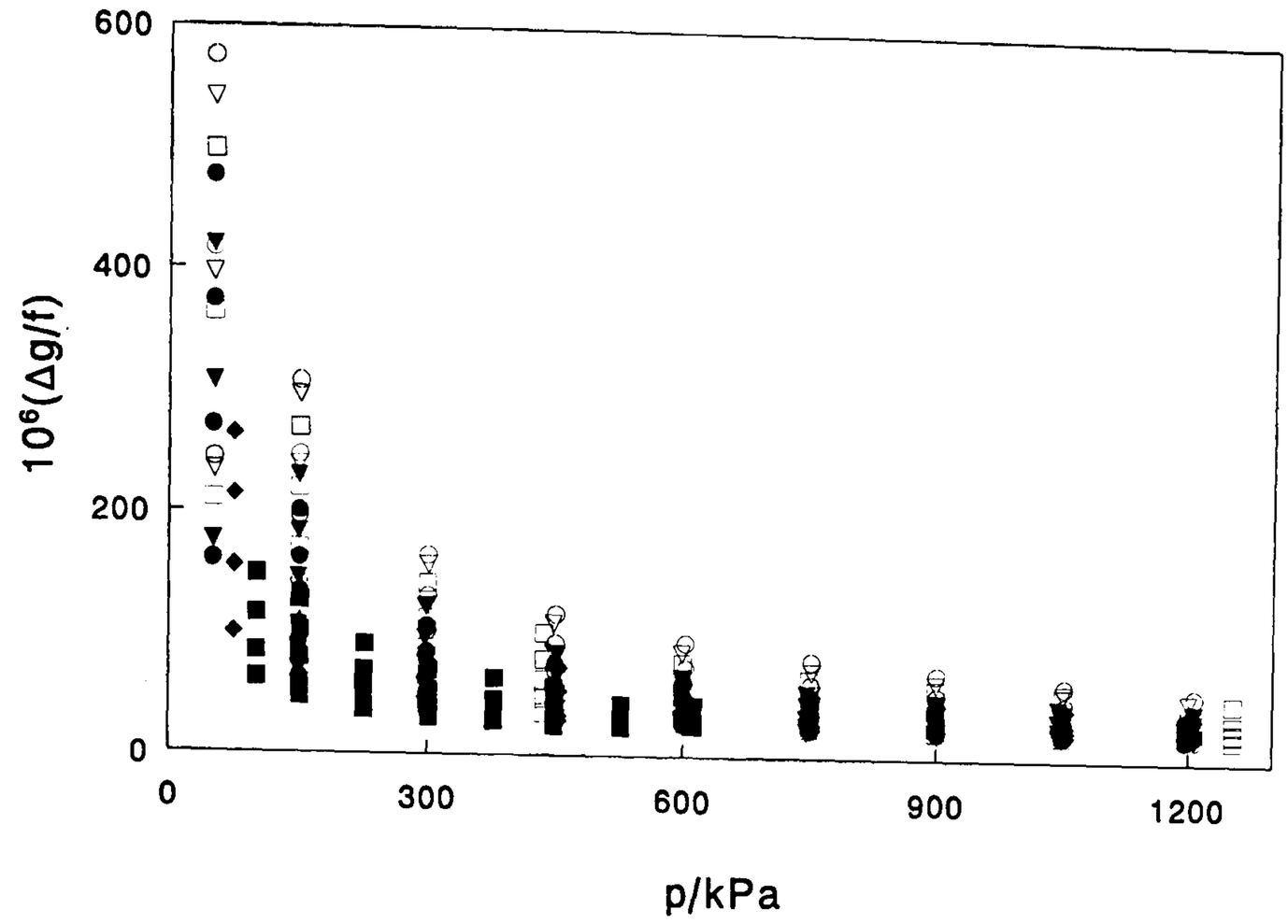
T/K	τ_{BA}/ns	T/K	τ_{BA}/ns
220	152.92	350	95.65
250	135.10	400	82.54
275	121.32	450	71.78
300	110.11		

For example, when τ_{AB} is assumed to be the same as τ_A, the resultant values of τ_{BA} from the regression analysis may differ from those reported in table 10 by five per cent at 220 K and up to 22 per cent at 450 K. However, in both cases, the corrections to Δg and to u are essentially the same. For an infinite τ_{AB} the maximum correction to u for dispersion is about -12.2·10^{-6}·u, at 275 K and 50.11 kPa, whereas for a τ_{AB} equals to τ_A, at the same state point, the correction varied to -15.0·10^{-6}·u; in both cases, the calculated Δg was the same. In other words, both assumptions about the value τ_{AB} lead to similar solutions for the sound dispersion for the mixture. In figure 18, values of Δg are plotted before and after the correction accounting for relaxation was carried out. Finally, in table 11, speed of sound for the mixture $(1-x)\,C_2H_6 + x\,CO_2$ on seven different isotherms are reported. Also included are a set of check measurements at 275 K which are commented on further in the next section. Finally, no comparisons of the speeds of sound determined for this particular mixture were made because, to the best of our knowledge, no other study has reported the speed of sound for this system.

6.6.2 Composition of the mixture.

Generally, all radial modes agreed among themselves to within ± 10 ppm after all corrections were carried out. Once the internal consistency of the data had been proved, a determination of the actual composition of each sample followed since, as has been mentioned already, for each isotherm a fresh sample of the mixture was taken from the sample cylinder. Even when a lot of care was taken during the process of filling, it may still be possible for there to be slightly different composition each

a)



b)

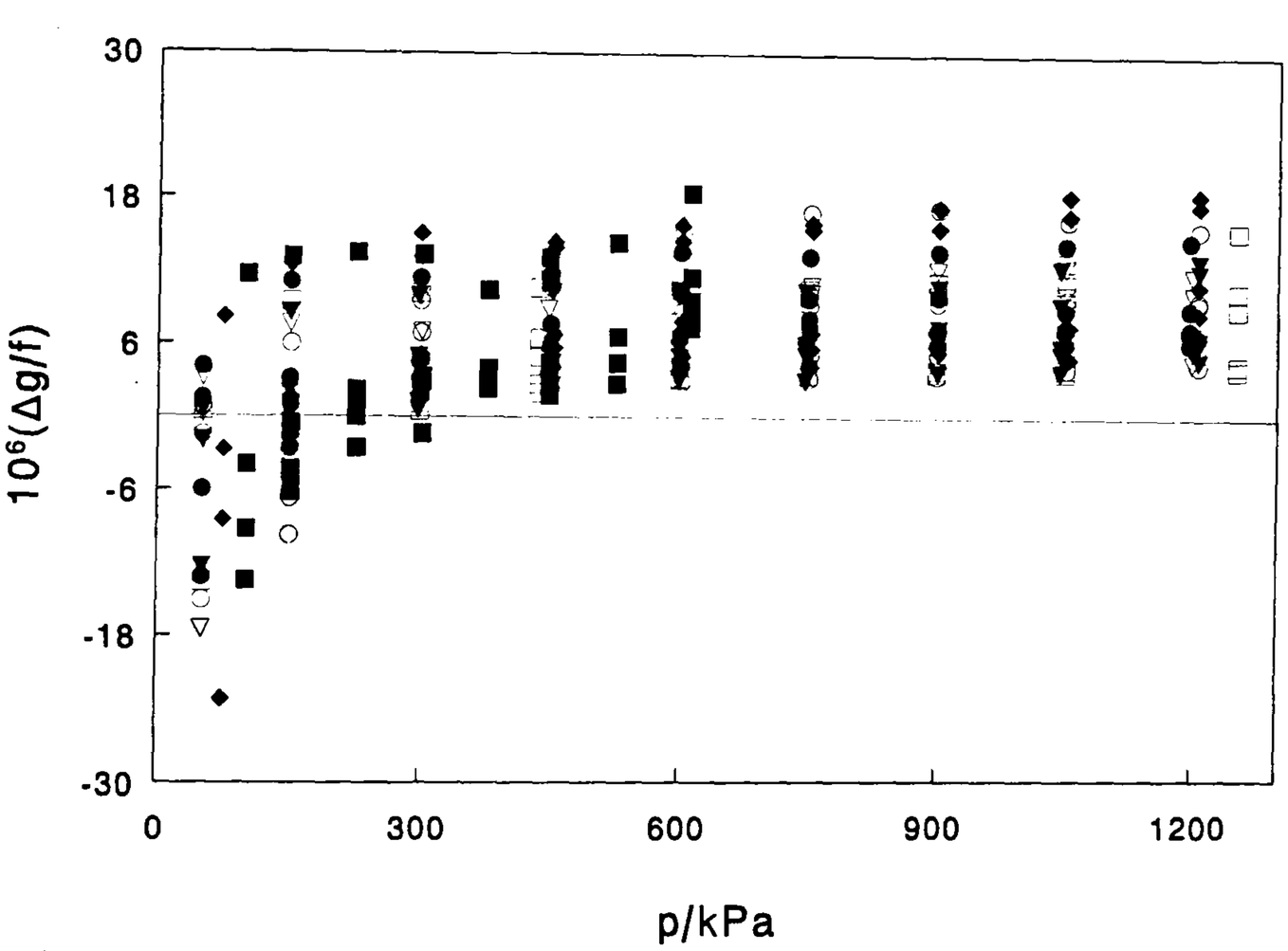


Figure 6.18 Excess half-widths Δg on the mixture carbon dioxide + ethane: a) before corrected for absorption, b) after corrected for absorption. ■, T = 220 K; ◆, T = 250 K; ●, T = 275 K; ▼, T = 300 K; □, T = 350 K; ▽, T = 400 K; ○, T = 450 K.

Table 6.11 Speed of sound of mixture ethane + carbon dioxide at temperatures from 220 K to 450 K and pressures up to 1.2 MPa.

p/kPa	u/m·s^{-1}	p/kPa	u/m·s^{-1}	p/kPa	u/m·s^{-1}	p/kPa	u/m·s^{-1}
			T = 220 K				
612.01	232.817	448.26	237.029	301.39	240.571	150.82	244.009
526.45	235.056	377.33	238.764	225.89	242.317	100.55	245.116
			T = 250 K				
1206.47	240.986	752.22	249.427	453.50	254.510	150.59	259.361
1053.45	243.940	601.86	252.026	299.60	257.009	74.47	260.535
901.28	246.762						
			T = 275 K				
1195.92	257.764	600.42	265.556	50.11	272.272	†750.55	263.713
1049.76	259.733	449.26	267.444	†1195.26	257.849	†598.63	265.641
900.06	261.710	298.93	269.288	†1049.72	259.807	†450.31	267.492
749.31	263.663	150.01	271.086	†900.59	261.773	†450.12	267.493
			T = 300 K				
1206.63	271.817	745.25	276.384	451.74	279.218	149.63	282.081
1043.77	273.445	598.98	277.803	297.07	280.690	50.55	283.004
900.47	274.863						
			T = 350 K				
1252.27	295.886	748.60	298.886	435.84	300.748	149.97	302.448
1049.43	297.094	598.26	299.781	298.68	301.564	50.37	303.032
898.65	297.992						
			T = 400 K				
1199.26	317.216	751.33	318.872	446.87	320.007	149.73	321.084
1050.01	317.765	597.93	319.443	300.25	320.550	50.44	321.319

† Check measurements

Table 6.11 -continued.

p/kPa	u/m·s^{-1}	p/kPa	u/m·s^{-1}	p/kPa	u/m·s^{-1}	p/kPa	u/m·s^{-1}
899.30	318.322						
			T = 450 K				
1206.53	336.077	750.53	337.108	450.17	337.802	150.18	338.483
1051.78	336.424	602.02	337.451	299.41	338.150	50.40	338.629
899.59	336.768						

time that the resonator was filled. One way of monitoring possible changes in composition of the mixture is by analysing the intercept of u^2 versus ρ_n which, for instance, can be obtained from polynomial fits.

This method of monitoring the composition of the **mixture** takes advantages of the fact that A_0 is a quite sensitive (and usually single-valued) function of the composition for a binary mixture. For a mixture, A_0 may be expressed as:

$$A_0 = RT[(R + C^{pg}_{V,mA}) / C^{pg}_{V,mA} M_A][(1 + a_1 x) / (1 + a_2 x + a_3 x^2)], \qquad (6.6.8)$$

where the coefficients a_j, j = 1, 2, 3 are given by,

$$a_1 = (C^{pg}_{V,mB} - C^{pg}_{V,mA})/(R + C^{pg}_{V,mA}), \qquad (6.6.9)$$

$$a_2 = (M_B/M_A) + (C^{pg}_{V,mB}/C^{pg}_{V,mA}) - 2, \qquad (6.6.10)$$

$$a_3 = [1 - (M_B/M_A)][1 - (C^{pg}_{V,mB}/C^{pg}_{V,mA})]. \qquad (6.6.11)$$

Equation (6.6.8) is quadratic in x and both roots are real but only one of them lies in the physical interval of (0,1). Thus, for a given value of A_0, equation (6.6.8) can be solved for x. These values of A_0 were obtained from polynomial fits of u reported in table 11 with densities calculated from the Lee-Kesler equation of state[4] at the nominal mole fraction composition of x = 0.6 and with heat capacities of the pure components calculated from equation (6.4.2) and from reference [23]. Values of A_0

and x derived in this way are listed in table 12. Uncertainties in x were determined from a gaussian quadrature formula involving all sources of uncertainty, i.e. uncertainties in A_0 and in the heat capacities of the perfect gas for each component.

The average composition is $\langle x \rangle = 0.5975$ with a standard deviation $\sigma_x = 0.0017$; even though this level of agreement seems to be very good in fact it is at least one order of magnitude worse than experience dictates.[33] If the value at 450 K is removed from the average then better agreement is achieved among the remaining compositions but, even under those conditions, a disagreement of at least six time that reported in reference [33] persisted.

In fact, it was clear that a variation of the composition took place during successive fillings even when the sample was kept in the single-phase region and with a temperature gradient along the side of the sample cylinder to promote convection mixing. Further evidence was obtained from the check measurement at 275 K which showed some changes from the initial measurements; this can be seen in figure 19 where values of u obtained during the check measurements are compared with the values calculated from a three-term fit to the first set of data. The representation for the first data set was good, accommodating all u within 5 ppm.

Table 6.12 Particular compositions x for each mixture of carbon dioxide plus ethane obtanied from the values of A_0.

T/K	x		A_0/m^2·s^{-2}	
220	0.59704	± 0.00038	61146.57	± 0.72
250	0.59662	± 0.00020	68471.93	± 0.31
275	0.59670	± 0.00018	74455.43	± 0.37
300	0.59670	± 0.00016	80359.51	± 0.42
350	0.59597	± 0.00015	92012.82	± 1.60
400	0.59797	± 0.00016	103462.44	± 2.84
450	0.60143	± 0.00013	114821.38	± 2.23

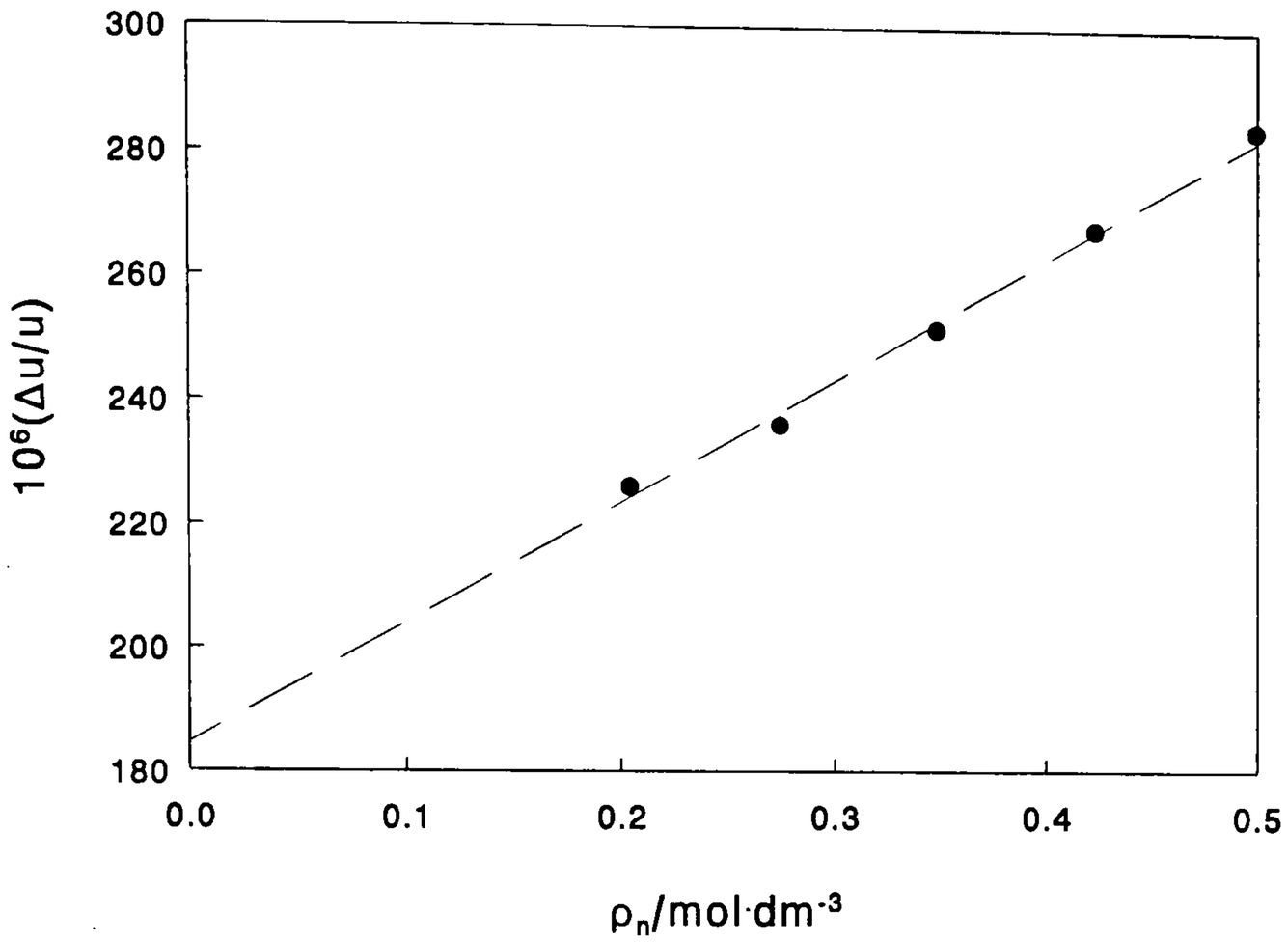


Figure 6.19 Fractional deviation $\Delta u/u$ of the speed of sound u of the check measurements from earlier data at the temperature of 275 K in order to verify possible variation of composition of the mixture carbon dioxide + ethane.

The change in the of intercept between the two sets was $337 \cdot 10^{-6} \cdot A_0$ implying a reduction of the carbon dioxide contents in the mixture from a mole fraction of 0.5967 to a mole fraction of just 0.5953, which is a change of 0.23 per cent of x.

Moreover, the variation of x did not have a systematic behaviour with time; measurements started at the lowest temperature and then **proceeded** upwards in temperature except for the check measurement at 275 K, which was the last one to be carried out. At the beginning, x tended to decrease with each sample measured but after reaching 350 K, the mole fraction increased for the remaining two temperatures in steps much bigger and finally, it once again decreased for the check measurements to a composition below that reported at 350 K. This very odd behaviour of the composition has not been completely understood. In addition, the fits of the speed of sound at 400 K and at 450 K were less satisfactory than for the rest of the isotherms. This is reflected in part in the relatively larger uncertainty attached to A_0 at these temperatures. But the plausible uncertainty of the speed of sound for those isotherms is not sufficient to explain on its own such variations in composition.

6.6.3 Acoustic virial coefficients.

Since the main objective was to obtain interaction second acoustic virial coefficients β_{ij} for the mixture, only second acoustic virial coefficients of the mixture β_{mix} were determined. In this case a straightforward polynomial fit gave a value of β_{mix} for each temperature. Except for the isotherm at 400 K, where a four-term fit was used, the remaining isotherms were fitted with a three-term polynomial. Moreover, only β_{mix} derived from the first set of measurements taken at 275 K was used in the rest of the analysis.

In order to obtain β_{ij} from the experimental values of β_{mix}, the method of the ratios discussed in §4.2.2 was applied. For this purpose, the ratios ξ_{ii} were calculated from the intermolecular potential determined previously for each component from the speed of sound measurements. All calculation were carried out with the set of parameters derived with the inclusion of the first quantum correction.

Table 6.13 Second acoustic virial coefficients of mixture β_{mix}, interaction β_{12} and pure components $\beta_{a,j}$, and pseudo-acoustic virial coefficient β_{ii}. The molar perfect-gas heat capacities $C_{p,m}^{mix}$ corresponds to the actual composition of the mixture at each temperature.

T/K	β_{12}/cm^3·mol^{-1}	β_{11}	β_{22}	$^{\ddagger}\beta_{a1}$	$^{\ddagger}\beta_{a2}$	$C_{p,m}^{mix}/R$
220	-288.20 ± 0.41	-293.67	-429.12	-283.88	-460.74	4.52882
250	-220.17 ± 0.26	-224.84	-335.99	-211.10	-360.71	4.78098
275	-180.27 ± 0.11	-183.50	-278.03	-169.47	-300.40	4.99973
300	-150.49 ± 0.10	-149.86	-232.59	-137.94	-253.29	5.22459
350	-103.30 ± 0.23	-103.75	-166.52	-92.95	-184.06	5.68520
400	-62.98 ± 0.90	-71.94	-120.55	-62.09	-135.10	6.13491
450	-43.57 ± 0.44	-48.88	-85.23	-39.46	-98.32	6.55340

‡Values calculated from intermolecular potential models including first quantum correction.

Values of the mixture composition x, need to calculate γ^{pg}, and from it, the functions P_a and Q_a for the mixture, were taken from the values reported in table 12. Heat capacities of the perfect gas of each of the two pure component were obtained in the same way described in connection with the analysis of the composition of the mixture. Table 13 lists values of β_{mix}, β_{ij} and $\beta_{a,j}$ with $j = 1,2$ and $i \leq j$. In the same table 13, values of the molar perfect-gas heat capacity at constant pressure for each particular mixture have been included. The uncertainty associated with β_{12} was worked out from all sources of uncertainties, namely, β_{mix}, β_{jj} and x, combined according to the usual gaussian propagation formula. In figure 20 and 21, all the resulting second acoustic virial coefficients are plotted. There, it can be seen that each β_{jj} did not correspond to the actual $\beta_{a,j}$, in the same way that β_{mix} **differed** from β_{ij}; this was previously pointed out in chapter four.

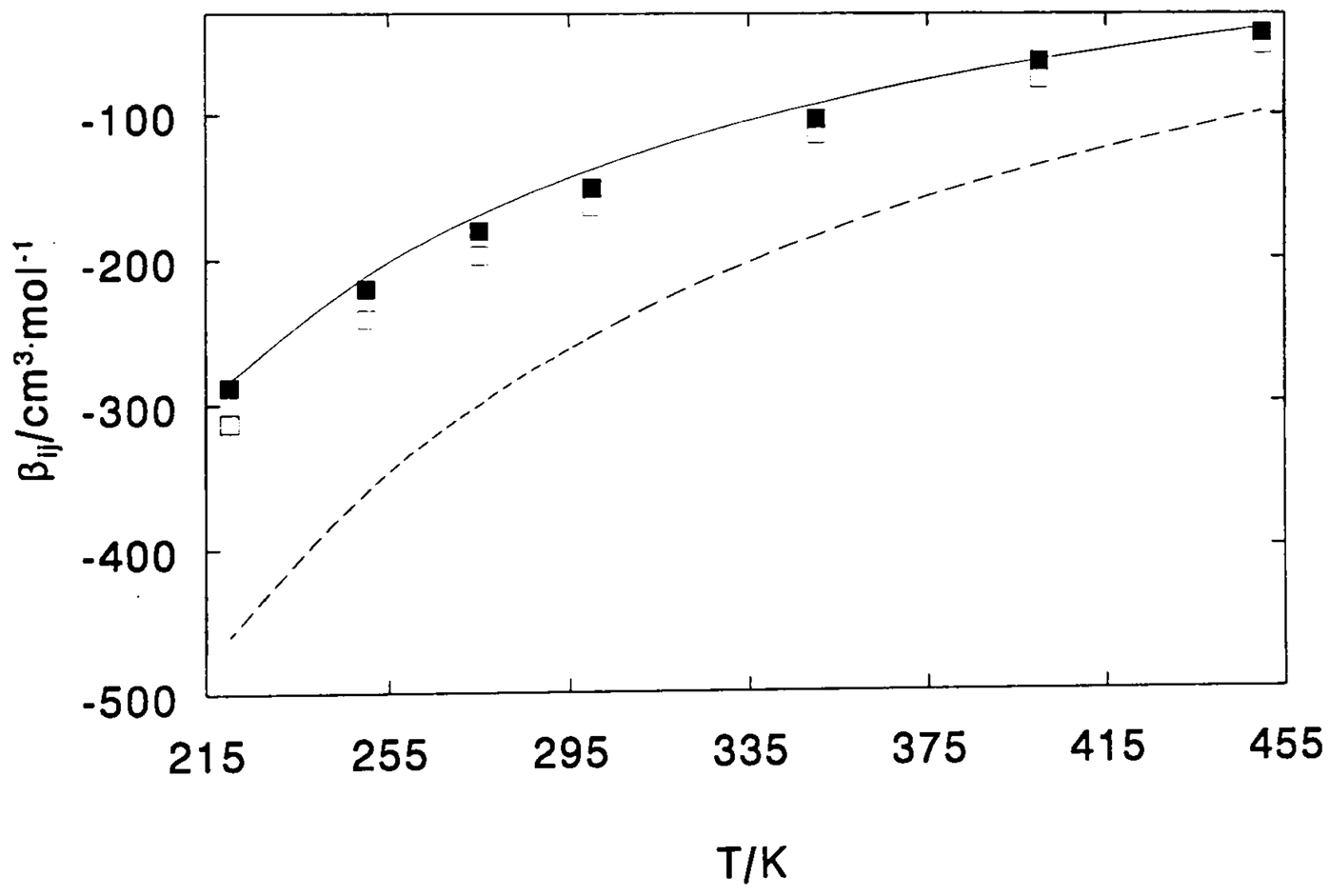


Figure 6.20 Second acoustic virial coefficients of the mixture β_{mix} and interaction second acoustic virial coefficient β_{12} of the system carbon dioxide + ethane. Curves represent the pure-component second acoustic virial coefficients calculated from a site-site intermolecular potential model: (—), carbon dioxide; (---), ethane. □, β_{mix}; ■, β_{12}.

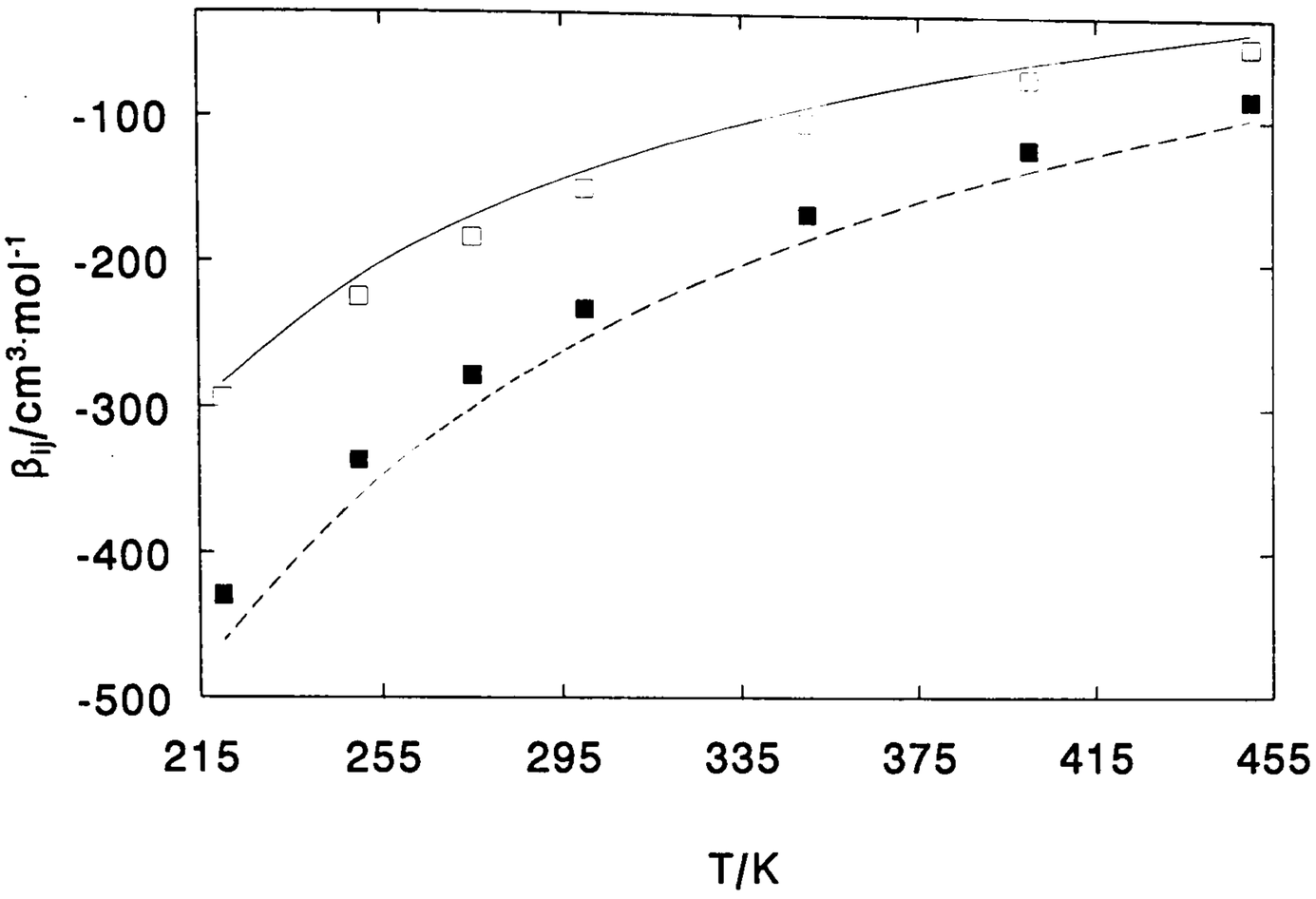


Figure 6.21 Second pseudo-acoustic virial coefficients β_{jj} of the system carbon dioxide + ethane. Curves represent the pure-component second acoustic virial coefficients calculated from a site-site intermolecular potential model: (—), carbon dioxide; (---), ethane. □, β_{11}; ■, β_{22}.

References.

1. Estrada-Alexanders, A.F.; Trusler, J.P.M.; *J.Chem.Thermodynamics*, **25**, 1075 (1995).

2. Letterberg, H.M.; *Cryogenics*, **22**, 653 (1982).

3. Younglove, B.A.; Hanley, H.J.M.; *J. Phys. Chem. Ref. Data*, **15**, 1323 (1986).

4. Lee, B.I.; Kesler, M.G.; *AIChE Journal*, **21**, 510 (1975).

5. Trusler, J.P.M.; Zarari, M.; *J. Chem. Thermodynamics*, **24**, 973 (1992).

6. Moldover, M.R.; Mehl, J.B.; Greenspand, M.; *J. Acoust. Soc. Am.* , **79**, 253 (1986).

7. Ewing, M.B.; Goodwin, A.R.H.; *J. Chem. Thermodynamics*, **24**, 531 (1992).

8. Ewing, M.B.; Owusu, A.A.; Trusler, J.P.M.; *Physica A*, **156**, 899 (1989).

9. Thoen, J; Vangeel, E.; van Dael, W.; *Physica*, **52**, 205 (1971).

10. Goring, G.E.; *J. Chem. Phys.*, **54**, 4514 (1971).

11. Rusby, R.L.; *J.Chem.Thermodynamics*, **23**, 1153 (1991).

12. Moldover, M.R.; Trusler, J.P.M.; Edwards, T.J.; Mehl, J.B.; Davis, R.S.; *J. Res. NBS.*, **93**, 85 (1988).

13. Ewing, M.B.; Goodwin, A.R.H.; McGlashan, M.L.; Trusler, J.P.M.; *J. Chem. Thermodynamics*, **20**, 243 (1988).

14. Esper, G.; Lemming, W.; Beckermann, W.; Kohler, F., *Fluid Phase Equilibria*, **105**, 173 (1995).

15. Aziz, R.A.; Slaman, M.J.; *Mol. Phys.*, **58**, 679 (1986).

16. Ewing, M.B.; Trusler, J.P.M.; *Physica A*, **184**, 415 (1992).

17. Gilger, R.; Kleinrahm, R.; Wagner, W.; *J.Chem.Thermodynamics*, **26**, 383 (1994).

18. Younglove, B.A.; Ely, J.F.; *J. Phys. Chem. Ref. Data*, **16**, 577 (1987).

19. Private communication.

20. Boyes, R.; PhD Thesis, University of London (1992).

21. Holmes, R.; Jones, G.R.; Pusat, N.; *J. Chem. Phys.*, **41**, 2512 (1964).

22. Chao, J.; Wilhoit, R.C.; Zwolinski, B.J.; *J. Phys. Chem. Ref. Data*, **2**, 427 (1973).

23. Vesovic, V.; Wakeham, W.A.; Olchowy, G.A.; Sengers, J.V.; Watson, J.T.R.; Millat, J.; *J. Phys. Chem. Ref. Data*, **19**, 763 (1990).

24. Woolley, H.W.; *J.Research Nat. Bur. Stand.*, **52**, 289 (1954).

25. Brown, T.S.; Kidnay, A.J.; Sloan, E.D.; *Fluid Phase Equilibria*, **40**, 169 (1988).

26. Wei, M.S.-W.; Brown, T.S.; Kidnay, A.J.; Sloan, E.D.; *J. Chem. Eng. Data*, **40**, 726 (1995).

27. Vesovic, V.; Wakeham, W.A.; *Int. J. Thermophys.*, **10**, 125 (1989). Vesovic, V.; Wakeham, W.A.; *High Temp.-High Press.*, **23**, 179 (1991).

28. Di Pippo, R.; Dorfman, J.R.; Kestin, J.; Khalifa, H.E.; Mason, E.A.; *Physica A*, **86**, 205 (1977). Mason, E.A.; Khalifa, H.E.; Kestin, J.; Di Pippo, R.; Dorfman, J.R.; *Physica A*, **91**, 377 (1978).

29. Herzfeld, K.F.; Litovitz, T.A.; *Absorption and Dispersion of Ultrasonic Waves*, 1959, Academic Press: London.

30. Kohler, M.; *Z.Physik*, **127**, 40 (1949).

31. Trusler, J.P.M.; *Physical Acoustic and Metrology of Fluids*, 1991, Adam Hilger: Bristol.

32. Robjohns, H.L.; Dunlop, P.J.; *Ber. Bunsenges. Phys. Chem.* **88**, 1239 (1984).

33. Trusler, J.P.M.; Wakeham, W.A.; Zarari, M.; *Int. J. Thermophys.*, **17**, 35 (1996).

Chapter 7. Analysis of data.

7.1 Introduction.

In this chapter, a detailed discussion of both the thermodynamics properties and the model intermolecular potential functions derived from the experimental results is presented. Comparisons between the results derived from the speed of sound and those measured directly are carried out for Z and the heat capacities for two gases: argon and ethane. Extensive tables of the thermodynamics properties derived for those systems are appended. Intermolecular potential models were obtained from second acoustic virial coefficients for the cases of ethane and carbon dioxide. These potentials were then utilised to **subtract** the pure-component contributions to the second acoustic virial coefficient of the binary mixture studied in this work. After that, interaction second acoustic virial coefficients were determined from which an intermolecular potential model was obtained for the unlike interactions between ethane and carbon dioxide. Comparisons between experimental ordinary second virial coefficient and those predicted by the intermolecular potential are made for each system.

7.2 Thermodynamic properties derived from the speed of sound.

Here, the results obtained from a numerical integration of the equations that link the speed of sound and the thermodynamic properties are discussed. The algorithm employed for the calculations has been described in detail in chapter 3.

Interpolations of the speed of sound were carried out as described in §3.3.3. The equation of state used to obtain the reduced densities ω, needed to calculated the intermediate function F in the interpolation routine, was that proposed by Stewart *et al.*[1]

7.2.1 Argon.

As mentioned briefly in §3.3.2, a first trial of integration the pVT surface was performed in the supercritical region with the simplest treatment for the initial conditions: i.e. with only two initial isotherms and equation (3.3.5) with $N = 2$. The

necessary data were obtained from the recent and highly accurate pVT measurements of Gilgen *et al.*[2]

These workers reported density measurements along isotherms placed at both supercritical and subcritical temperatures with pressures up to 12 MPa. Several of the isotherms are close to the critical temperature, those at $T_1 = 153$ K and $T_2 = 155$ K were selected and therefore T_0 was set to 154 K. Compression factors at these two temperatures Z_j ($j = 1, 2$) were fitted to a fourth-degree polynomial in density which accommodated all the data within ± 9 ppm up to densities of nearly 7.0 mol·dm^{-3}. Furthermore, the constant term of each polynomial was restricted to be unity to ensure that $\lim_{\rho_n \to 0} Z = 1$. Then, the values of α_j^k in equation (3.3.16) became $|\alpha_j^k| = 0.5$ for $j = 1, 2$ and $k = 1, 2$. Thus, this treatment is corrected to $O(\Delta T^3)$ in $(\partial Z/\partial T)_{\rho_n}$ since T_0 is the average temperature of T_1 and T_2.

The integration was then performed at both supercritical and subcritical temperatures. For the former, the maximum density reached in the integration was 6.8 mol·dm^{-3} while for the latter, it was that corresponding to 74 per cent of the estimated saturation density ($\phi \leq 0.74$). For $T \geq 350$ K, the isochore at 6.8 mol·dm^{-3} exceeded 19 MPa, the maximum pressure at which u was measured, hence the isotherms at 400 K and at 450 K were completed by extrapolation from a density of roughly 5.5 mol·dm^{-3} and 4.9 mol·dm^{-3}, respectively, up to the maximum density. The rational approximation of the type given by equation (3.3.15) was used for this purpose. For the isotherm at 400 K, the rational approximation was selected to pass from the four greatest densities, while for the isotherm at 450 K, the extrapolation range was greater and six points were preferred. This led to rational polynomial extrapolation of quadratic and cubic degree, respectively. The roots of the polynomial Q_{2n} were obtained and, although they were real values, they were found to lie outside of the working density range of Q_{2n}. Unfortunately, there were no available data, of the required accuracy, to compare with at those pressures and it has therefore been difficult to estimate the accuracy of the extrapolated results.

In both regions, the integration took place along fifty evenly spaced paths: they were isochores for $T \geq 150$ K and lines parallel to the saturation curve for $T < 150$ K. A temperature increment $\Delta T = +0.5$ K was used to carry out the integration along

isochores in most of the supercritical region, while a second short integration along the same set of isochores but with a $\Delta T = -0.1$ K was performed to extend the results downwards in temperature to 150 K. The derived values of Z and Z' at this temperature were used as the initial conditions for the integration in the sub-critical region. There, the integration paths were calculated by means of [3]

$$\mathrm{f}(T) = \rho_n^{\sigma}(T)/\rho_n^{\mathrm{c}} = 1 + 0.797(1 - T/T^{\mathrm{c}}) - 1.76(1 - T/T^{\mathrm{c}})^{0.326}. \qquad (7.2.1)$$

Equation (7.2.1) is just a correlation for the saturated vapour densities of simple fluids based on the principle of the corresponding states but it is accurate enough for the present purpose.

At 150 K equation (6.3.5) gave, for a density of 6.8 mol·dm^{-3}, a rounded value of $\phi = 0.74$. A three-point interpolation formula was used to adjust the values of Z and $(\partial Z/\partial T)_{\rho_n}$ from the extended isochores on to the corresponding fifty evenly-spaced lines at constant ϕ. Equation (3.2.20) was employed to change the direction of the partial derivative $(\partial Z/\partial T)_{\rho_n}$ into the new partial derivative $(\partial Z/\partial T)_{\phi}$. With these initial conditions, the integration was carried in the subcritical domain. In order to maintain the accuracy of the method, it was necessary to reduce the temperature increment from -0.1 K to -0.01 K (see §3.4.1).

In figure 1, interposed values of Z, $C_{V,\mathrm{m}}$ and $C_{p,\mathrm{m}}$, are shown calculated by means of both algorithms on the 150 K isotherm. It is evident that the calculation of these three quantities match properly there and thus no discontinuity was introduced.

As mentioned in §3.3.2, the accuracy of the method relies upon accurate initial conditions and these have been established from experimental information. For argon, the heat capacities are smaller than those of a polyatomic gas and this made the problem of establishing with sufficient accuracy the initial values of $(\partial Z/\partial T)_{\rho_n}$ more acute. Although the data reported by Gilgen *et al.* have outstanding accuracy and precision, they were not sufficient to obtain $(\partial Z/\partial T)_{\rho_n}$ unambiguously. This was discovered after a preliminary integration. There, derived values of Z deviated systematically with respect to the values determined by direct pVT measurements.

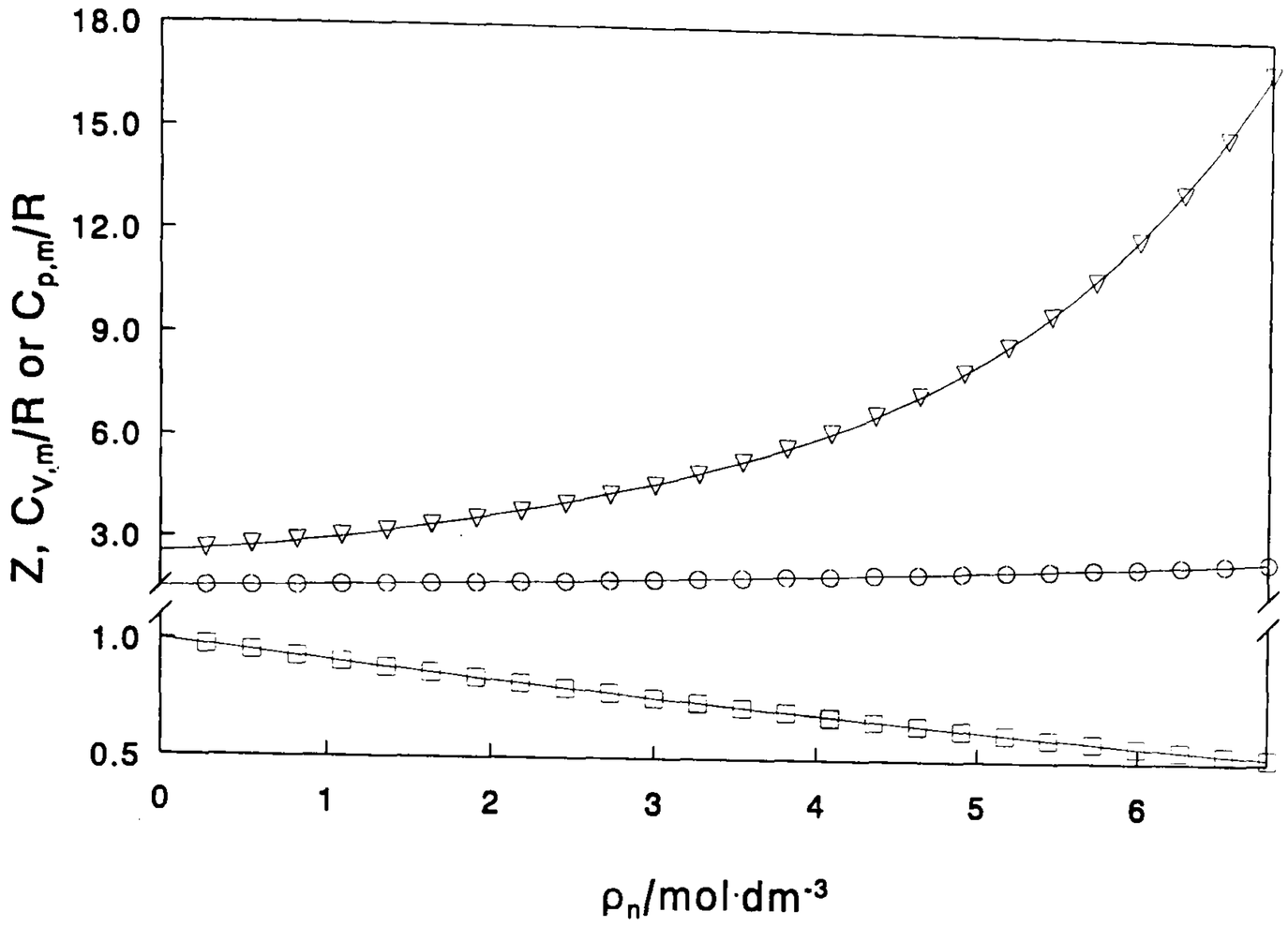


Figure 7.1 Thermodynamic properties of argon at 150 K from two different algorithms. Solid curves are calculated from integration along lines at constant ϕ and symbols are calculated from integration along isochores. □, Z; ○, $C_{V,m}/R$; ▽, $C_{p,m}/R$.

This systematic deviation showed a maximum disagreement of about $-4\cdot10^{-4}\cdot Z$ at T = 250 K and $\rho_n \approx 6.6$ mol·dm^{-3} which tended to decline at higher temperatures towards values within the $\pm\ 2\cdot10^{-4}\cdot Z$ claimed uncertainty of Gilgen's data; this trend is expected from a small error in Z'_0.[4] In addition, it was noticed that the derived compression factors at T_1 and T_2 did not quite agree with the polynomials that represented Z_1 and Z_2 (the fractional deviations were as much as -107 ppm and -94 ppm respectively for $\rho_n \sim 6.0$ mol·dm^{-3}) unless the correction to Z_0, suggested in §3.3.2, was applied. When the correction to Z_0 based on $(\partial^2 Z/\partial T^2)_{\rho_n}$ was applied, only tiny deviations amounting at most to ± 5 ppm were obtained and this level of difference is certainly insignificant.

In the case of Z'_0 the order of magnitude of the truncation error involved in (3.3.10b) was estimated to reach about $1.9\cdot10^{-4}\cdot Z'_0$ at the greatest density. On the other hand, the experimental uncertainty propagated from equation (3.3.10.b) was about $15\cdot10^{-4}\cdot Z'_0$ if it is assumed that systematic errors in Z cancel out in the calculation of

Z'_0 and hence that the actual uncertainty corresponds to the imprecision of Z_1 and Z_2. In view of this relatively large experimental uncertainties, it was legitimate to modify the estimated Z'_0 by a factor $(1 + K)$ where K is a small parameter. The value of was adjusted by trial until agreement with experimental data on a third isothem, $T = 250$ K, was obtained. The value $6.8 \cdot 10^{-4}$ was obtained in this way and this remains **consistent** with the experimental data at T_1 and T_2.

Figures 2, 3 and 4, show a comparison of the derived compression factors with those determined from the experimental data of Gilgen *et al.*[2] The greatest deviations in the region covered by both the integration and the experimental results (up to densities of 6.8 $mol \cdot dm^{-3}$ for $T \geq 150$ K and 74 per cent of the saturation density for $T < 150$ K) were no worse than ± 0.023 per cent. The root-mean-square deviation of 311 points was of only 0.0086 per cent.

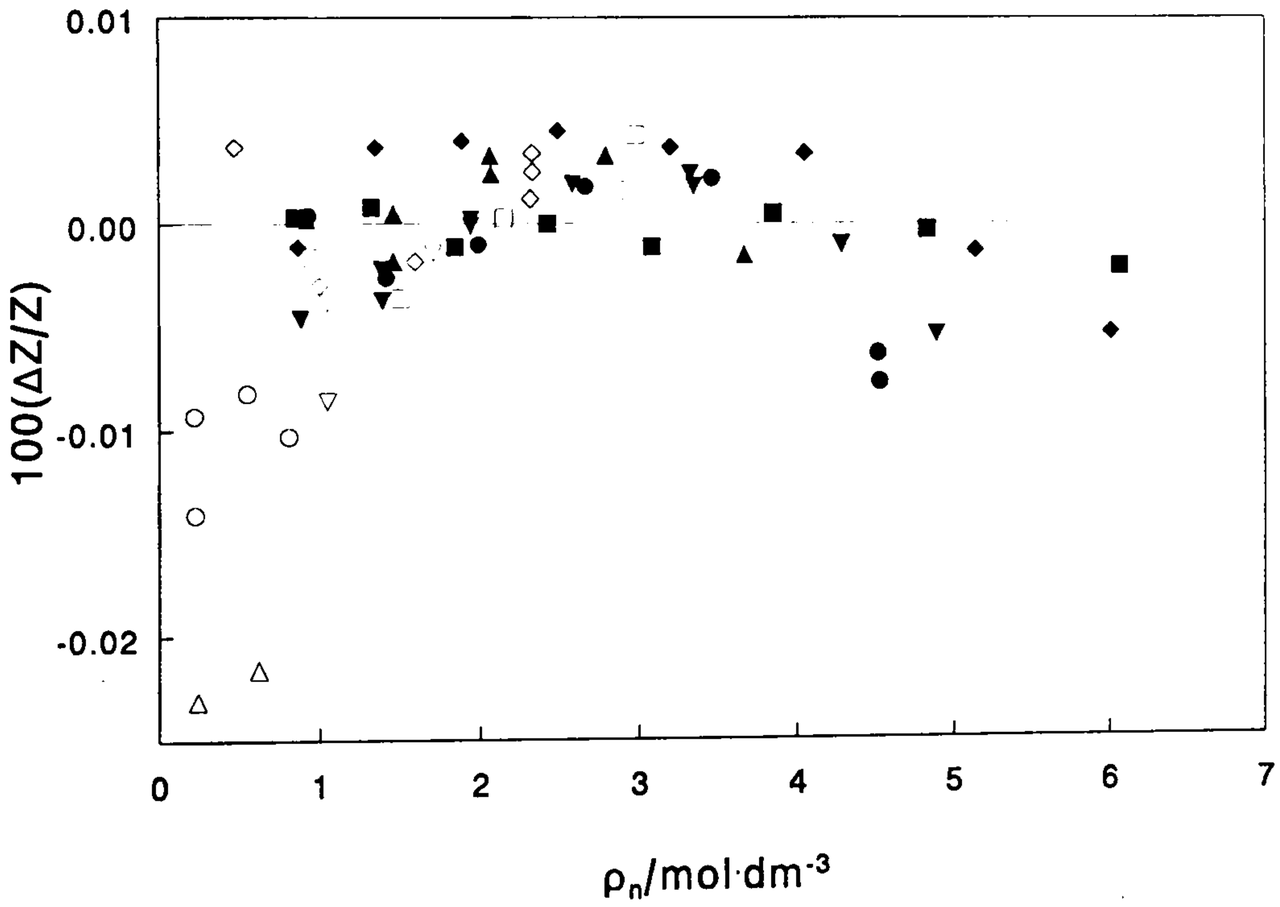


Figure 7.2 Fractional deviations $\Delta Z/Z$ of the compression factors Z of argon reported by Gilgen *et al.*[2] from the present results for temperatures between 110 K and 153 K. ■, 153 K; ◆, 150.7 K; ▼, 148 K; ●, 146 K; ▲, 143 K; ⎯, 140 K; ◇, 135 K; ▽, 130 K; ○, 120 K; △, 110 K.

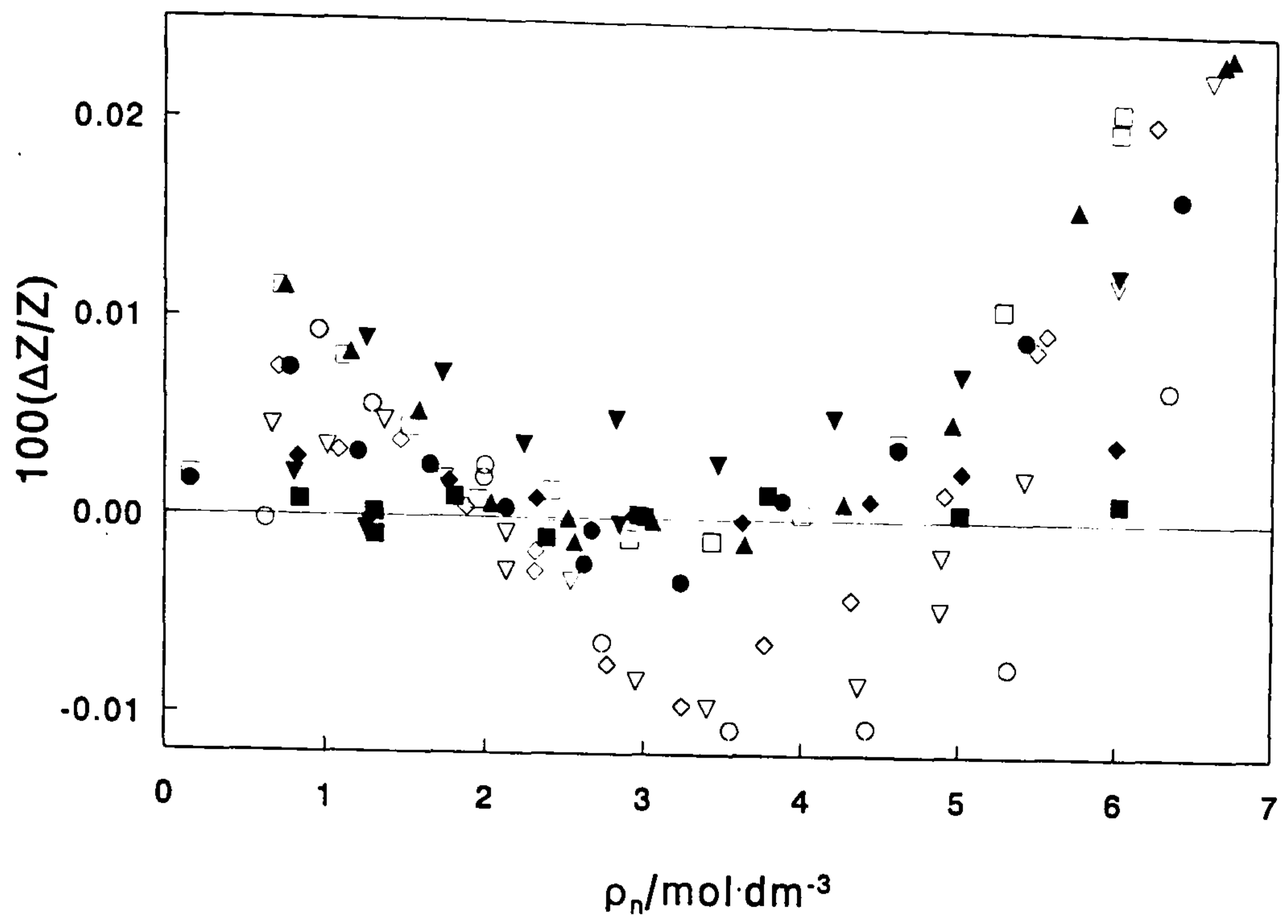


Figure 7.3 Fractional deviations $\Delta Z/Z$ of the compression factors Z of argon reported by Gilgen *et al.*[2] from the present results for temperatures between 154 K and 200 K. ■, 155 K; ◆, 157 K; ▼, 160 K; ●, 165 K; ▲, 170 K; □, 175 K; ◇, 180 K; ▽, 190 K; ○, 200 K.

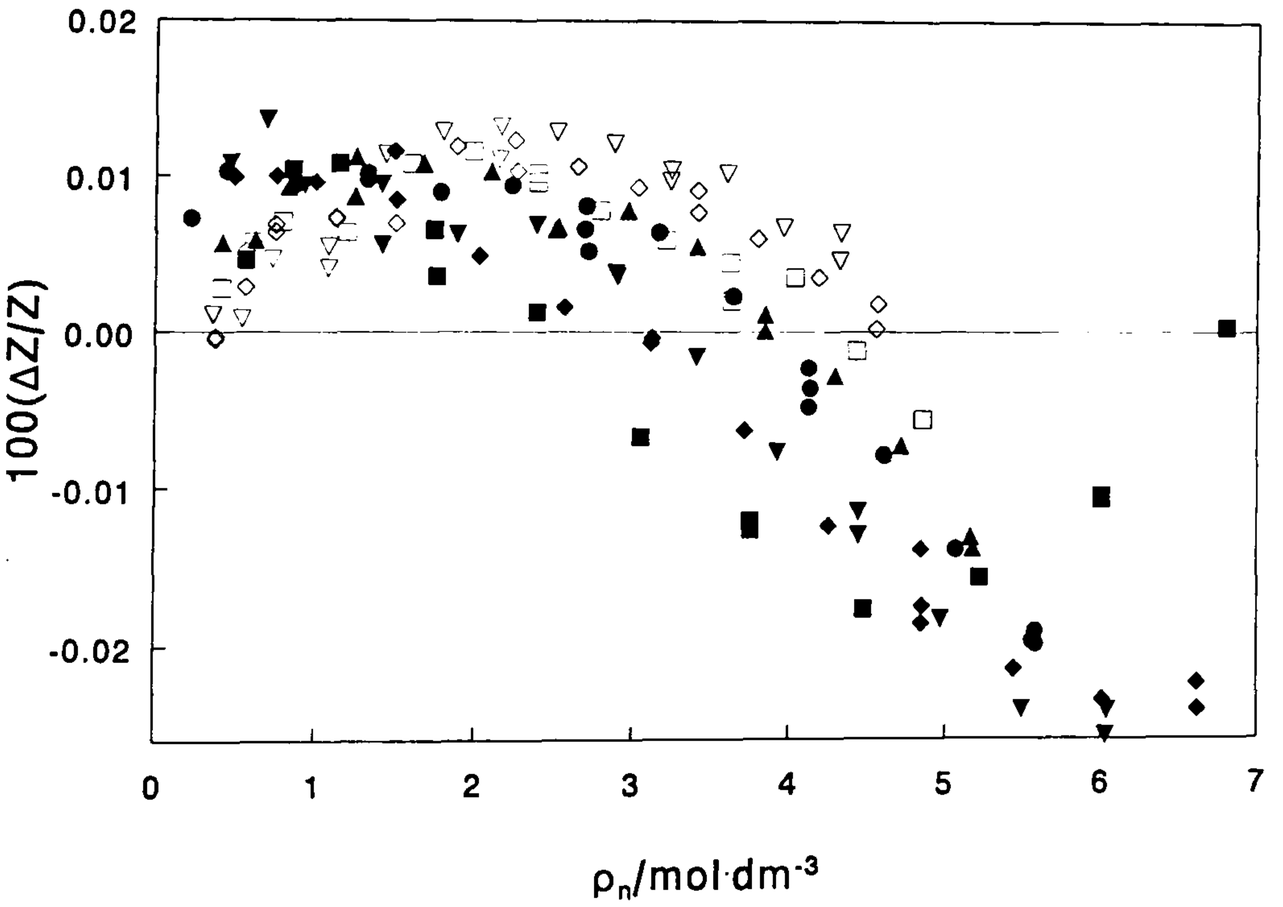


Figure 7.4 Fractional deviations $\Delta Z/Z$ of the compression factors Z of argon reported by Gilgen *et al.*[2] from the present results for temperatures between 220 K and 340 K. ■, 220 K; ◆, 250 K; ▼, 265 K; ●, 280 K; ▲, 295 K; □, 310 K; ◇, 325 K; ▽, 340 K;

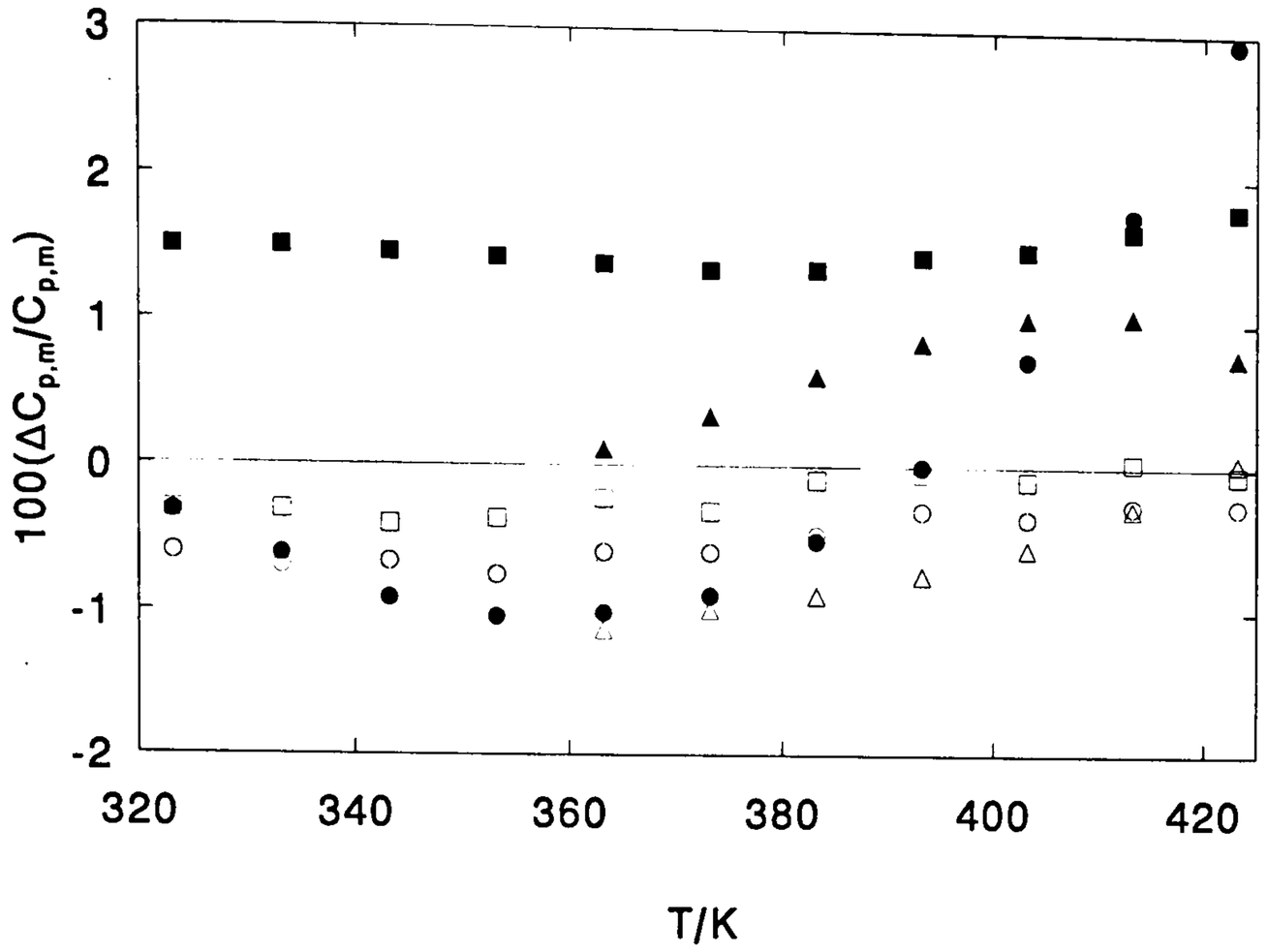


Figure 7.5 Fractional deviations $\Delta C_{p,\mathrm{m}}/\ C_{p,\mathrm{m}}$ of the heat capacities at constant pressure $C_{p,\mathrm{m}}$ reported by Baba *et al.* and from reference [8] along three isobars. Filled and open symbols are respectively from Baba *et al.* and reference [8]. ■, 5.0 MPa; ●, 9.9 MPa; ▲, 20.7 MPa; □ , 5.0 MPa; ○, 9.9 MPa; △ , 20.7 MPa.

The heat capacities were also determined in the above range with an estimated uncertainty of 0.1 per cent. The 'filter' routine applied to the heat capacities (a fourth-degree polynomial in density) was used for the integration along isochores but was not needed for the integration below 150 K where smooth values of $C_{V,\mathrm{m}}$ were always obtained. A comparison with recent determinations of $C_{p,\mathrm{m}}$,[4] is shown in figure 5. This comparison is not very informative because the likely errors in the experimental $C_{p,\mathrm{m}}$ are at least one order of magnitude larger than the estimated uncertainty of those derived here; nevertheless the agreement is satisfactory.

Finally, the derived properties, Z, $C_{V,\mathrm{m}}$ and $C_{p,\mathrm{m}}$, for gaseous argon are reported in table A.1 (see the appendix at the end of this chapter). The table has been designed in such way that values at intermediate T and ρ_n can be obtained by a simple quadratic interpolation in both T and ρ_n without significant loss of accuracy.

7.2.2 Ethane.

Thermodynamic properties of gaseous ethane were derived from the speed of sound data by a numerical integration of the equations (3.2.12) and (3.2.15) in a similar way as for argon. An equation of state due to Stewart *et al.*[1] was used to derived the reduced densities that were involved the interpolation routine and the coefficients were obtained from reference [6].

Once again, the speed of sound was measured at pressures up to that corresponding to half the critical density ($\rho_n^c = 6.875$ mol·dm^{-3}) for temperatures ($T \geq 300.65$ K) near and above the critical ($T^c = 305.33$ K). Below 300.65 K, the measurements on each isotherm extended up to a pressure corresponding to 80 per cent of the saturated vapour density.

The pVT data reported by Douslin and Harrison[7] was used to set up the initial conditions for the integration. The isotherm at 300.65 K was selected as the initial temperature T_0 for the integration because it is close to the critical temperature and corresponded to the average temperature of two isotherm reported by Douslin and Harrison, namely $T_1 = 298.15$ K and $T_2 = 303.15$ K. With this choice, both integrations in the subcritical and supercritical regions could be performed without changing the initial conditions. As in the case of argon, each Z_j ($j = 1, 2$) was obtained from fourth-degree as polynomials in ρ_n (with the constant term taken equal to unity) fitted to the pVT data. In this way, Z_j was represented up to densities of 3.5 mol·dm^{-3} with a precision better than ± 70 ppm for Z_1 and ± 50 ppm for Z_2. Although this precision is well within the claimed accuracy of these data (0.03 per cent of Z), it is evident that these data were not as precise as in the case of argon.

For $T \geq T_0$ (mostly the supercritical region), the integration was performed along isochores covering the density range up to 3.3 mol·dm^{-3}, slightly below half the critical density, with a temperature step of +0.5 K. This density range was covered by most of the isotherms but the isotherm at 415 K reached a density of only 3.19 mol·dm^{-3} and an extrapolation was required. This short extrapolation should not require a rational approximation and therefore a straightforward polynomial extrapolation was performed.

The density of the saturated vapour $\rho_n{}^{\sigma}$ required to calculate f(T) and hence ϕ, was obtained from the correlation given in the review of thermodynamic properties of ethane by Tester,[8] expressed in terms of the saturation pressure p^{σ} and the temperature T,

$$(\rho_n^{\sigma})^{-1} = M[(C_0 RT/p^{\sigma}) - C_1/(T/100\mathrm{K})^{m} - C_2 (p^{\sigma})^2 /(T/100\mathrm{K})^{n}]. \qquad (7.3.1)$$

In equation (7.3.1) the coefficients are $C_0 = 0.98041\times10^{-2}\,\mathrm{mol\cdot kg^{-1}}$, $C_1 = 0.089\ \mathrm{m^3\cdot kg^{-1}}$ and $C_2 = 2.9026\times10^{-6}\,\mathrm{m^2\cdot s^{-2}}$, while the exponents are $m = 2.4$ and $n = 9.0$. This equation was supplemented with the following correlation of the saturation pressure:[8]

$$\begin{aligned}\log_{10}(p^{\sigma}/\mathrm{kPa}) = 6.26141 - (780.24\mathrm{K}/T) - 10.2996\times10^{-5}(T/\mathrm{K}) \\ + 69.824\times10^{-12}[(T/\mathrm{K}) - 241.3]^{4.62}.\end{aligned} \qquad (7.3.2)$$

The densities of the saturated vapour are then reproduced with an accuracy of one per cent in the temperature range of 170 K to 305 K.

The integration in the subcritical region took place along fifty lines of constant ϕ; the maximum fraction of the saturated vapour density corresponded to a value of $\phi = 0.8$. The temperature increment in this case was set to -0.01 K. Initial conditions were also set at T_0 and care was taken to change the direction of the derivative of the compression factor with respect to temperature from that at constant ρ_n to that at constant ϕ.

All calculations the were performed in a similar manner to the case of argon except for two details. Firstly, no correction was applied to Z'_0. In part, this was because the data used was not sufficiently accurate to justify any further attempt to enhance the agreement. Secondly, it was found, from a preliminary analysis, that the filter applied to heat capacities had to be used at both the supercritical and subcritical temperatures. The filter routine for the heat capacity was applied to $C_{\phi,\mathrm{m}}$ directly by means of a fourth-degree polynomial in ϕ. It must be noticed that for ethane the integration in the subcritical region extended over a temperature range of 80 K, twice that for argon and therefore it is plausible to assume that errors in the heat capacities will develop and eventually be noticeable, especially as the appearance of ripples in

$C_{V,m}$ was observed only below 235 K. In any case the maximum likely change introduced in Z by this filter routine was $8 \cdot 10^{-5} \cdot Z$, at the greatest density at $T = 220$ K.

The derived Z, $C_{V,m}$ and $C_{p,m}$ in the range of 220 K to 450 K and densities up to 80 per cent of the saturated vapour density, for $T < 300.65$ K, or up to 3.3 mol·dm^{-3} for $T \geq 300.65$ K are given in table A.2. The temperature and density spacing have been **chosen** in such a way that values of the derived thermodynamic properties at intermediate temperatures and densities can be obtained from quadratic interpolation of the values reported there without loss of accuracy.

Although a large amount of pVT data for ethane have been reported, only few of these sources have an accuracy comparable to that achieved by the numerical integration of the speed of sound. The results of the integration are compared with data reported by Douslin and Harrison[7] and by Mansoorian *et al.*[9] and the differences are plotted in figures 6 and 7. Firstly, it was noticed that the smoothed Z_j used as the initial conditions were reproduced by the integration to better than $\pm 10^{-5} \cdot Z_j$; thus, the deviations showed in figure 6 corresponded to the actual scatter of those data. Secondly, from a total of 122 points considered only four of deviated more than 0.06 per cent. This compares very favourably with the data reported by Douslin and Harrison since the uncertainty of their data varied from 0.02 to 0.3 per cent. The RMS deviation of the 122 points was just 0.022 per cent. Last, but not least, good agreement with the data reported by Mansoorian *et al.*, which has a claimed uncertainty of 0.033 per cent, can be seen in figure 7. All these data were within ±0.04 per cent, although the measurements spanned the more modest density range up to densities $\rho_n \leq 1.5$ mol·dm^{-3}. Moreover, it should be noticed that initial conditions were taken from a different source and therefore, this level of agreement should be considered very good.

Heat capacities were also compared with data reported elsewhere.[10] As in the case of argon, this comparison is not very meaningful since the uncertainty in measured heat capacities is typically 2 per cent. In figure 8, the differences between direct determinations of $C_{V,m}$[10] and those derived from speed of sound are shown. The deviations lie in the interval from −1.2 to +0.6 per cent, with a root-mean-square deviation of just 0.16 per cent.

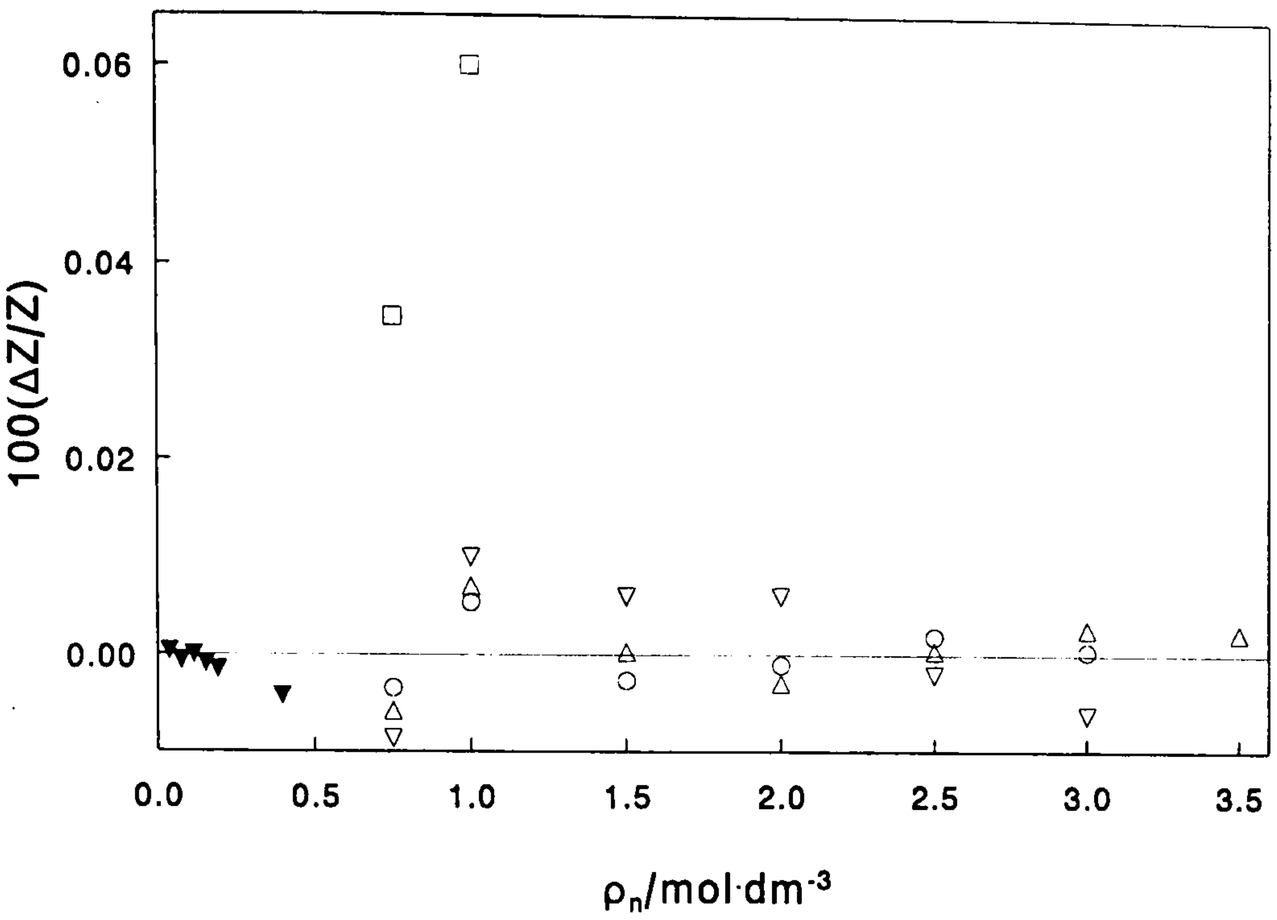


Figure 7.6 Fractional deviations $\Delta Z/Z$ of the compression factors Z of ethane reported by Douslin and Harrison[7] (open symbols) and by Mansoorian *et al.*[9] (filled symbols) from the present results for temperatures between 273.15 K and 323.15 K. □, 273.15 K; ○, 298.15 K; △, 303.15 K; ▽, 323.15 K.

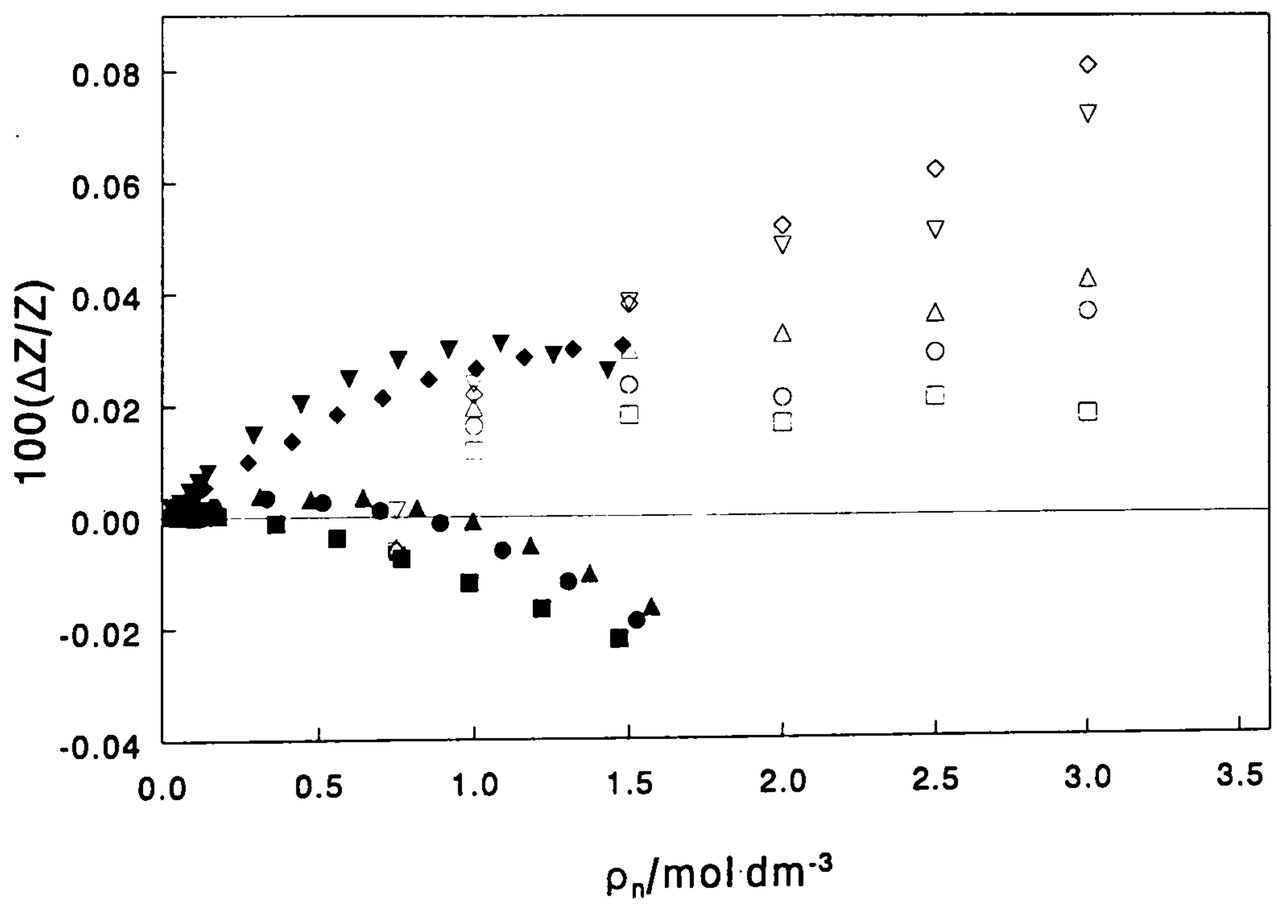


Figure 7.7 Fractional deviations $\Delta Z/Z$ of the compression factors Z of ethane reported by Douslin and Harrison[7] (open symbols) and by Mansoorian *et al.*[9] (filled symbols) from the present results for temperatures between 348.15 K and 448.15 K. □, 348.15 K; ○, 373.15 K; △, 398.15 K; ▽, 423.15 K ; ◇, 448.15 K.

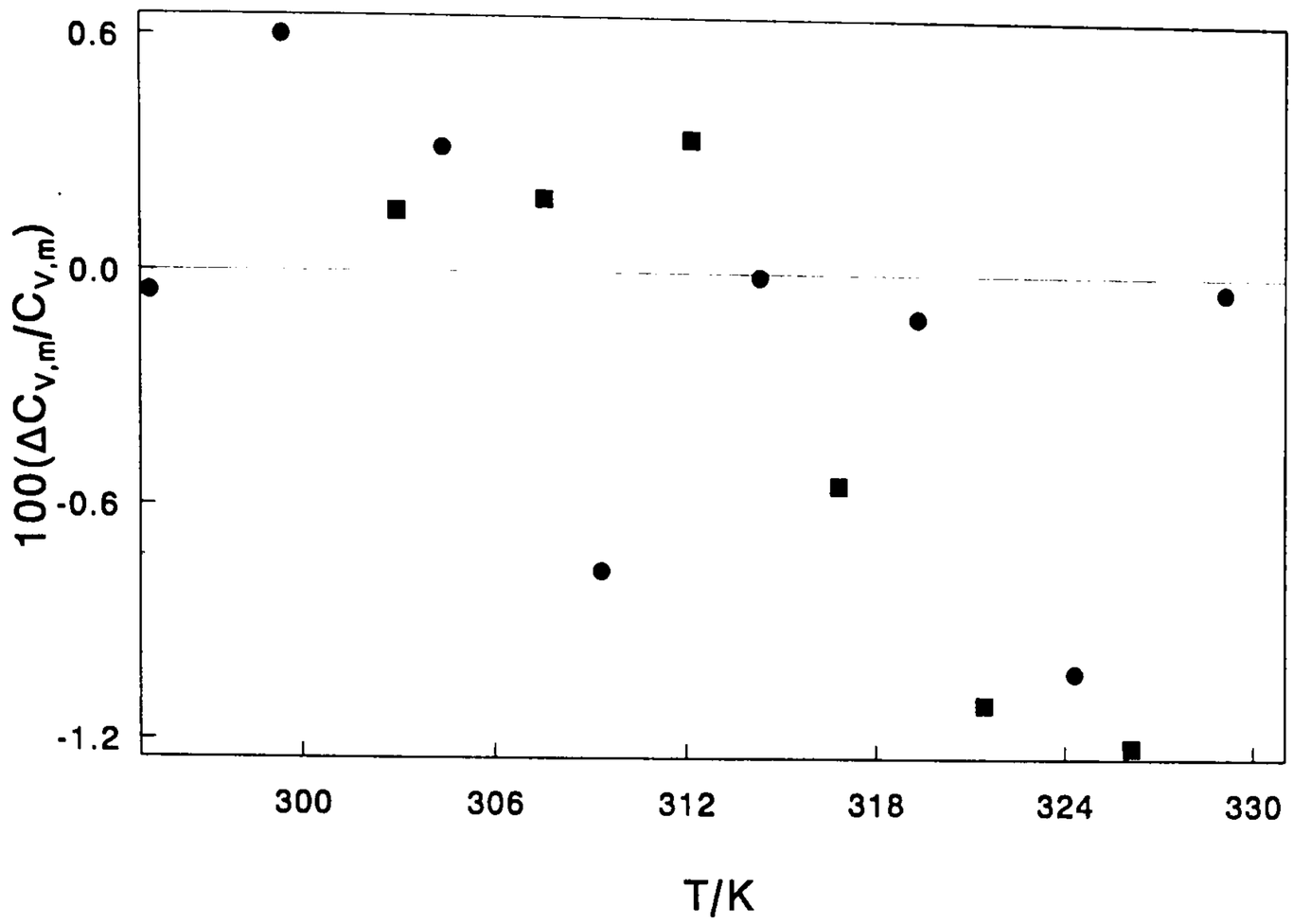


Figure 7.8 Fractional deviations $\Delta C_{V,m}/C_{V,m}$ of the heat capacities at constant volume $C_{V,m}$ of ethane reported by Roder[10] along two isochores. ■, ρ_n = 1.58 mol·dm^{-3}; ●, ρ_n = 3.27 mol·dm^{-3}.

The possibility of using initial conditions taken from a smooth equation of state rather than from experimental isotherms was investigated. The recent equation of state for ethane proposed by Friend and Ely[11] was considered with the objective of finding out if better agreement with the *pVT* data would be obtained with initial conditions from that source. However, it was found that almost no change occurred with initial conditions estimated in that way.

7.3 Intermolecular potential model.

The intermolecular potential proposed in this work for ethane, carbon dioxide and the mixture ethane plus carbon dioxide was a site-site model in which the site-site potential was represented by a Maitland-Smith function as described in chapter four. For all these systems, the procedure to fit the values of second acoustic virial coefficients was the same and all the calculations were carried out in the following way.

7.3.1 Numerical calculations.

According to equation (4.4.9), the calculation of β_a from the intermolecular potential requires an angle average. This was evaluated by Gauss-Legendre quadrature over the angles θ_1, θ_2 and $\varphi_{12} = (\varphi_2 - \varphi_1)$ and the number of points used for this quadrature was varied from four up to eight; the final choice was 6. Preliminary results showed that acoustic virial coefficients may differ, in the worst case by 0.1 $cm^3 \cdot mol^{-1}$, when the average was carried out using four and eight points, but differences between results with 6 and 8-point formulae were negligible (always less than 0.01 $cm^3 \cdot mol^{-1}$). The symmetry of the systems (all composed of symmetric linear molecules) allows one to reduce the ranges of integration for θ_1 and θ_2 to [0, π/2] and for φ_{12} to [0, π]. The semi-infinite integration over r was performed in five panels jointed at $r/\sigma = 0.5$, 1, 3 and 15, where σ is the separation at which the potential is zero. The first and the last panels were integrated over analytically while the central three panels were integrated over numerically using an adaptive Simpson's rule algorithm which successively doubled the number of quadrature points until an accuracy of 0.001 $cm^3 \cdot mol^{-1}$ was achieved.

The non-linear fitting of the intermolecular potential parameters to the experimental β_a was carried out by minimising the statistical function χ^2 given by equation (4.4.10). The standard deviation $\sigma(\beta_a)$ assigning to each second acoustic virial coefficient was

$$\sigma(\beta_a) = [(\Delta\beta_a)^2 + (\Delta_\beta)^2]^{1/2}. \qquad (7.4.1)$$

Here, $\Delta\beta_a$ is the reported uncertainty of β_a for each system (tables 6.5, 6.8 and 6.13) and Δ_β was a constant term set to 0.1 $cm^3 \cdot mol^{-1}$ for the pure components and to 0.5 $cm^3 \cdot mol^{-1}$ for interaction acoustic virial coefficients chosen to represent other (non-random) sources of uncertainty.

7.3.2 Ethane.

Strictly speaking, for ethane this approach should require 8 sites per molecule (one for each atom) but it was assumed that two sites would be sufficient to describe the interactions between molecules. This assumption reduced dramatically the number of

interactions between sites but still preserved to some extent the anisotropy of the function.

Besides the four parameters of the Maitland-Smith potential (namely ε, σ, m and γ), the effect of different separations between sites was also investigated. The analysis started with the sites coincident and proceeded by allowing then to separate along the carbon-carbon axis, until they reached the carbon nuclei. Here, the distance between carbon nuclei was taken as the carbon-carbon bond distance $l_b = 0.1534$ nm. In this way, it was expected that any effect that the anisotropy of the molecule had could be observed. After a few attempts at fitting all four parameters to β_a, for a fixed site-site separation, it was decided to look for the minimum of the reduce χ^2 in a slightly different manner. It was recognised that there is insufficient information available to fit both m and γ. The parameter γ was therefore constrained to have a constant value through the fitting procedure. Once a minimum value of the reduced χ^2 was obtained with both γ and the site-site separation fixed, the value of γ was varied and a new minimum of the reduced χ^2 was determined. After varying γ in a range from zero to nearly 20 (or less if m became comparable to γ) the distance between the sites was incremented and the whole procedure was repeated. Values of the reduced χ^2 obtained in that way are plotted in figure 9. Two remarks are appropriate here. Firstly, when $\gamma = 0$, the MS potential is identical with the well-known Lennard-Jones (n, 6) potential. All Lennard-Jones potential fits gave values of the repulsive exponent between 22 and 42; values rather larger than the traditional (12, 6) potential. Secondly, and in close connection with the above, it was noted that as the separation between sites increased the parameter m decreased from a value of about 40 to about 17 for values of γ in the range from 8 to 12. From figure 9, we can see that the variation of χ^2 gave no definitive solution and it was therefore necessary to constrain γ in a totally arbitrary way. The final choice was $\gamma = 10$.

Heat capacities required to calculate β_a from equation (4.4.9) were taken from the unsmoothed experimental values reported in table 6.5. All calculations required for the non-linear fitting were carried out in the way described in section 7.3.1.

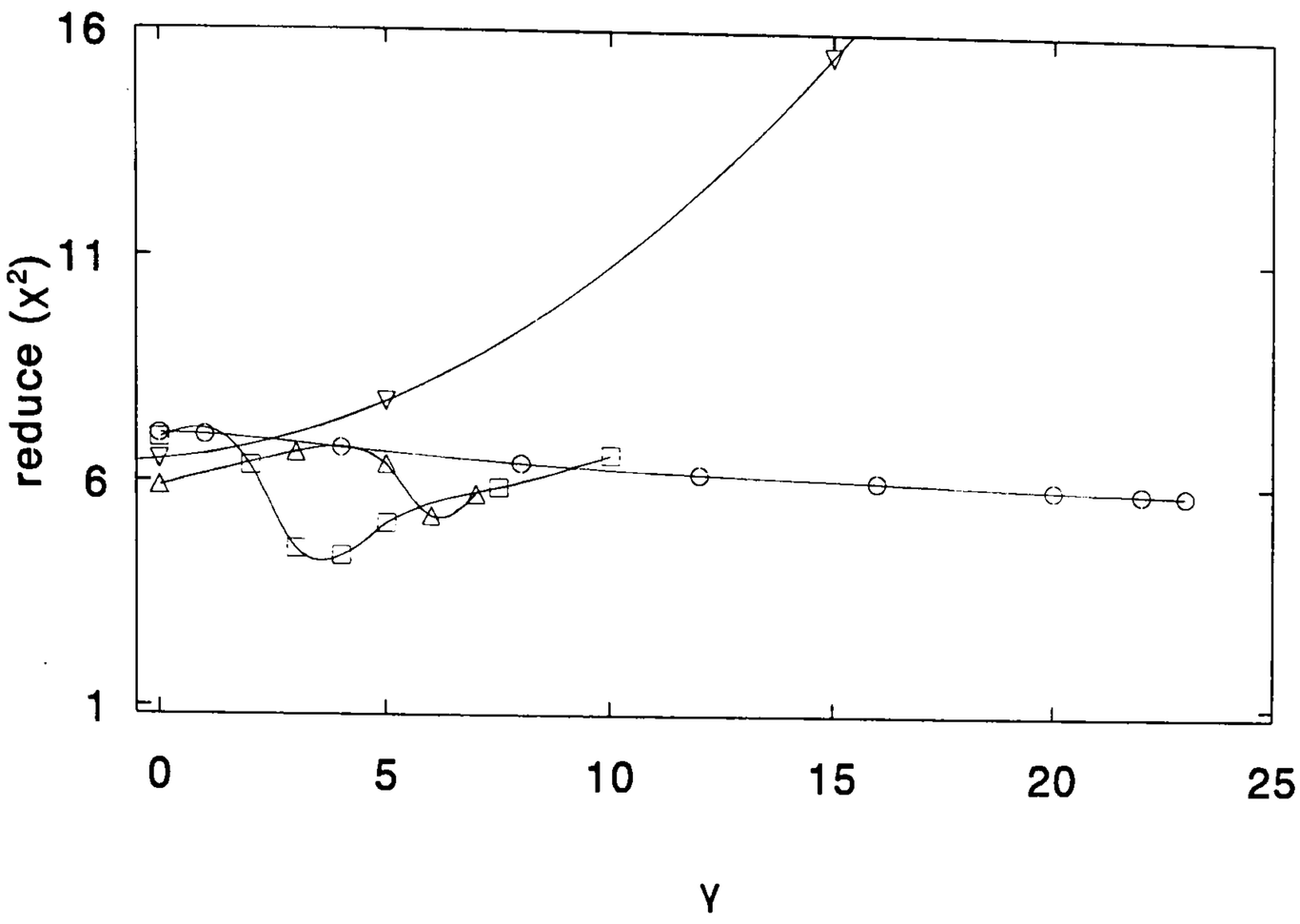


Figure 7.9 Resulting reduce χ^2 of the fittings procedure of the parameters of the intermolecular potential as a function of the parameter γ when all experimental second acoustic virial coefficients of ethane were included in the fitting. Curves are graphical interpolations for different site-site separations l_{ss} expressed in terms of the carbon-carbon bond distance l_b = 0.1534 nm. (l_{ss}/l_b): □, 0.25; ○, 0.5; ▽, 0.75; △, 1.0.

When the fitting procedure included all the available β_a, the minimum value of the reduced χ^2 was never less than 5.3 and differences between the experimental β_a and those calculated from the intermolecular potential showed a systematic trend. Changes in the heat capacities used did not explain this pattern; for instance, when heat capacities were calculated by equation (6.4.2), the maximum change of the calculated acoustic virial coefficient was $-0.12\ cm^3 \cdot mol^{-1}$ at 250 K leaving the systematic deviation unchanged. Inclusion of quantum corrections, although having an effect on values of the set of parameters finally determined, did not alter the systematic trend observed earlier. A better solution was obtained by omitting the value of β_a at 220 K. This exclusion had a dramatic effect upon the reduced χ^2 which was decreased to just above unity and, at the same time, destroyed the systematic deviation observed. Unfortunately, but not surprisingly, the deviation of β_a at 220 K was then increased to $2.2\ cm^3 \cdot mol^{-1}$, while the remaining β_a were reproduced within

$\pm 0.4\ cm^3 \cdot mol^{-1}$. Whether the calculation included the first quantum corrections or not, made no difference to the pattern of deviations. Furthermore, incorporating the second quantum correction corresponding to the translational modes changed the acoustic virial coefficients by only about $0.025\ cm^3 \cdot mol^{-1}$ in the worst case (at 220 K).

In table 1 the set of potential parameters determined in fits including and excluding the first quantum corrections are reported. In both cases, the calculations were constrained to have $\gamma = 10$. Values for the reduced mass and the moment of inertia are also given in table 1 together with the statistical information on the fit.

Finally, the second ordinary virial coefficients B calculated from the intermolecular potential were compared with values derived from pVT data. Accurate second virial coefficients of ethane have been reported by Douslin and Harrison[7] and by Mansoorian *et al.*[9] Data reported by the former cover the temperature range from 273 K up to 623 K, while for the latter cover only the interval between 323 K to 473 K. The deviations are found to be mostly negative and to some extent systematic but not worse than $-1.2\ cm^3 \cdot mol^{-1}$ as can be seen in figure 10.

Table 7.1 Parameters of intermolecular potential model obtained from fitting of second acoustic coefficient of ethane. $\mu = 2.4965 \cdot 10^{-26}$ kg, $I = 2.9373 \cdot 10^{-46}\ kg \cdot m^{-2}$, $l_{ss} = 0.1534$ nm.

parameter	quantum corrections	
	0	1
$(\sigma/\text{nm}) \cdot 10^3$:	364.01 ± 0.80	363.37 ± 0.33
(ε/k)/K:	612.90 ± 5.02	624.97 ± 2.09
γ:	10.0	10.0
m:	17.55 ± 0.18	18.06 ± 0.08
$\sigma_\beta/cm^3 \cdot mol^{-1}$:	0.162	0.144
reduce χ^2:	1.48	1.18

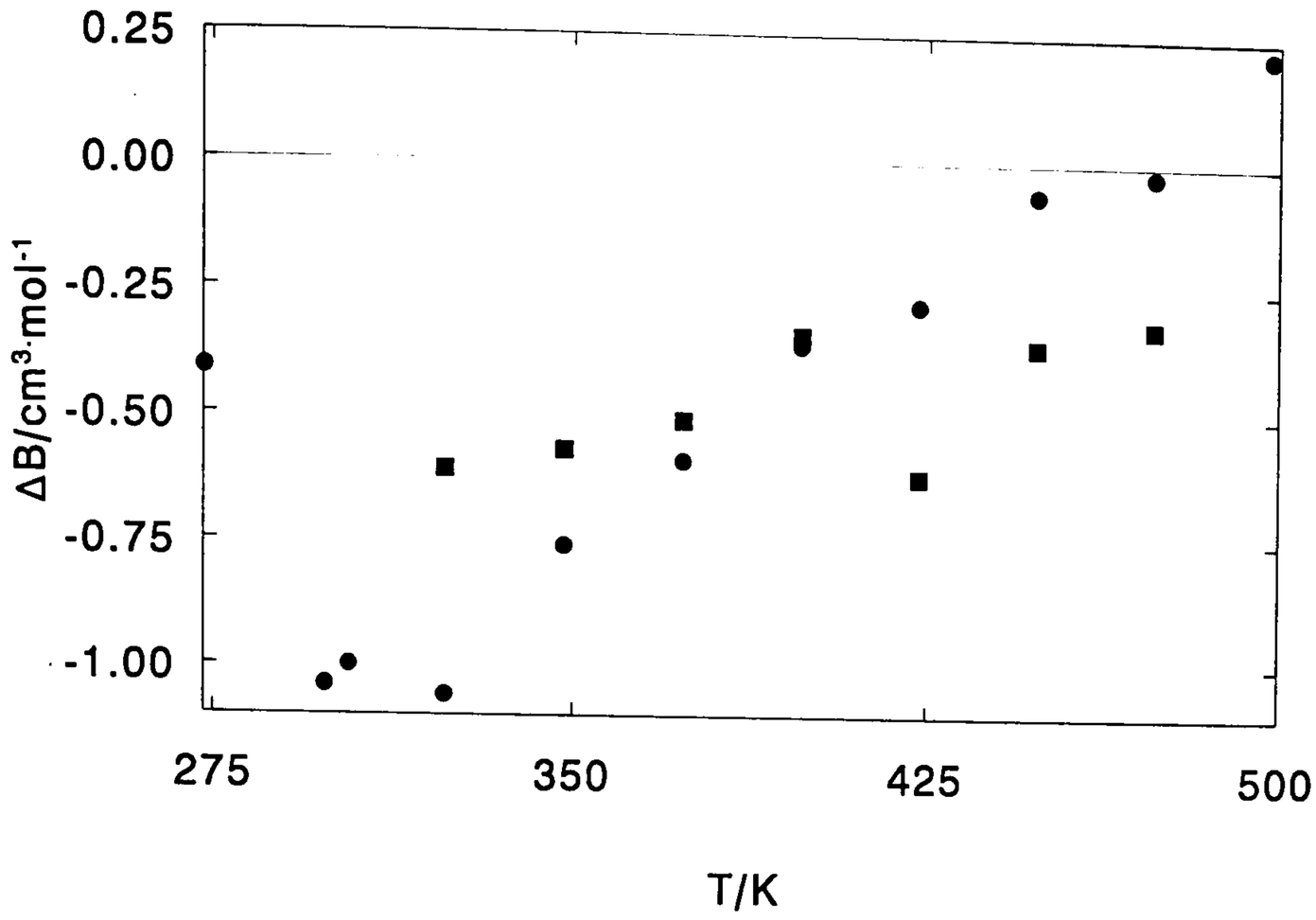


Figure 7.10 Deviations ΔB of the second virial coefficient B of ethane reported by Douslin and Harrison[7] and by Mansoorian[10] from those calculated from the MS intermolecular potential model adjusted by means of second acoustic virial coefficients. Calculations were carried out with the set of parameters given in table 7.1 that includes the first quantum correction. ●, reference [7]; ■, reference [10].

7.3.3 Carbon Dioxide.

The intermolecular potential model used for carbon dioxide was the same as that employed for the case of ethane: a site-site intermolecular potential. Once again, the potential describing the interactions between sites was of the Maitland-Smith type and the problem was simplified by placing only two interaction sites on the molecule instead of the usual choice of placing one site per atom. Although three sites are not too difficult to handle, especially with the non-linear fitting procedure available, more parameters must be fitted for a heteroatomic molecule. Strictly, at least eight parameters would need to be fitted for carbon dioxide if the molecule were described with three sites. Since, there were at most seven data points available, this case could not be solved and some approximations had to be made. It was assumed that the interaction between molecules could be described with only two sites per molecule

and, although this is a crude approximation, it at least retains some molecular anisotropy. All computations needed for the non-linear fitting (evaluation of integrals and angle averages) were carried out in the same way as described in section 7.3.1

Second acoustic virial coefficients given in table 6.8 were employed for the fitting procedure. Heat capacities required for the fitting were obtained from equation (6.5.2) rather than from those determined experimentally. Furthermore the uncertainty assigned to second acoustic virial coefficient was calculated according to (7.4.1) with the same value of Δ_β.

As in the case of ethane, the sensitivity of the goodness of the fit to changes of the site-site separation l_{ss} along the internuclear axis of the molecule was tested. This may be interesting for this model since, with the approximation of representing three atoms with only two interaction sites, it is not obvious where each site should be placed. Thus, the sites were placed symmetrically about the central carbon but the separation was varied from zero up to a maximum in which each site was placed over an oxygen nucleus. This distance is twice the distance of the carbon-oxygen bond $l_b = 0.1166$ nm. Figure 11 summarises the behaviour of the reduced χ^2 as function of l_{ss}, for the special case of a Lennard-Jones (n, 6) potential ($\gamma = 0$). It was evident that the best fit was obtained for the maximum distance between sites ($l_{ss} = 2l_b$) and simultaneously, the repulsive exponent m decreased drastically from values above 200 to more common figures of the order of 20. However, even though the reduce χ^2 was monotonically decreasing with increasing l_{ss}, its values were rather large for this sort of fit, being of the order of 20. This implies that the model does not fit the data within their estimated uncertainty.

Finally the second acoustic virial coefficients were fitted with Maitland-Smith potential sites place on each oxygen atom and with only three free parameters, namely ε, σ and m, while the parameter γ was kept fixed for each fit. Values of γ were allowed within the interval from zero to fifteen in steps of 2.5, but in this mapping along the γ axis, no minimum in the reduced χ^2 was observed. Inclusion of the first quantum corrections also provided no improvement.

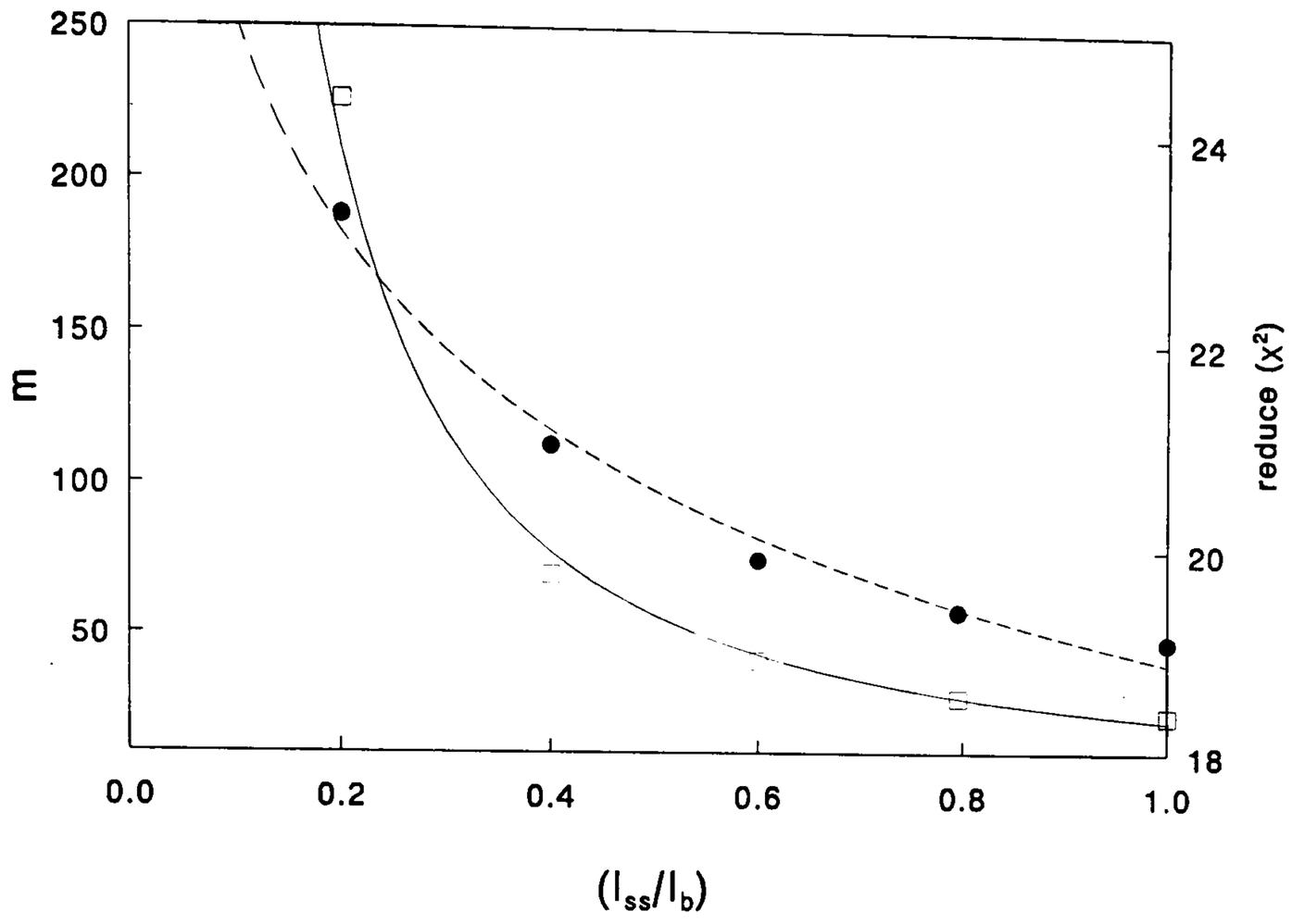


Figure 7.11 Resulting reduce χ^2 and parameter m from the fitting of a Lennard-Jones intermolecular potential as a function of the site-site separation l_{ss} when all experimental second acoustic virial coefficients of carbon dioxide were included. The separation l_{ss} is measured in terms of the carbon-carbon bond distance l_b = 0.22 nm (considered just as twice of the bond distance oxygen-carbon). ●, reduce χ^2; □, m.

Although exclusion of the point at $T = 220$ K from the fit had the effect of decreasing the reduce χ^2 from about 18 to about 7, this is not a very substantial reduction and, as only seven points were available, it was considered that there were no grounds for exclusion of any point from the fit.

The final values of the parameters that fitted second acoustic virial coefficients are given in table 2. There both cases are reported: those with and without the inclusion of the first quantum correction. Statistical information concerning both fits and the reduce mass μ and moment of inertia I required for the calculations of the first quantum correction are also listed there.

Finally, the values of ordinary second virial coefficients B predicted by this potential were compared with values derived from pVT data by Duschek *et al.*[12] and by Holste *et al.*[13].

Table 7.2 Parameters of intermolecular potential model obtained from fitting of second acoustic coefficient of carbon dioxide. $\mu = 3.6537 \cdot 10^{-26}$ kg, $I = 7.2236 \cdot 10^{-46}$ kg·m^{-2}, $l_{ss} = 0.22$ nm.

parameter	quantum corrections	
	0	1
$(\sigma/\text{nm}) \cdot 10^3$:	283.24 ± 1.0	282.07 ± 1.1
(ε/k)/K:	932.79 ± 12.0	964.42 ± 14.0
γ:	10.0	10.0
m:	19.47 ± 0.39	20.57 ± 0.47
σ_β/cm^3·mol^{-1}:	0.594	0.585
reduce χ^2:	18.3	17.7

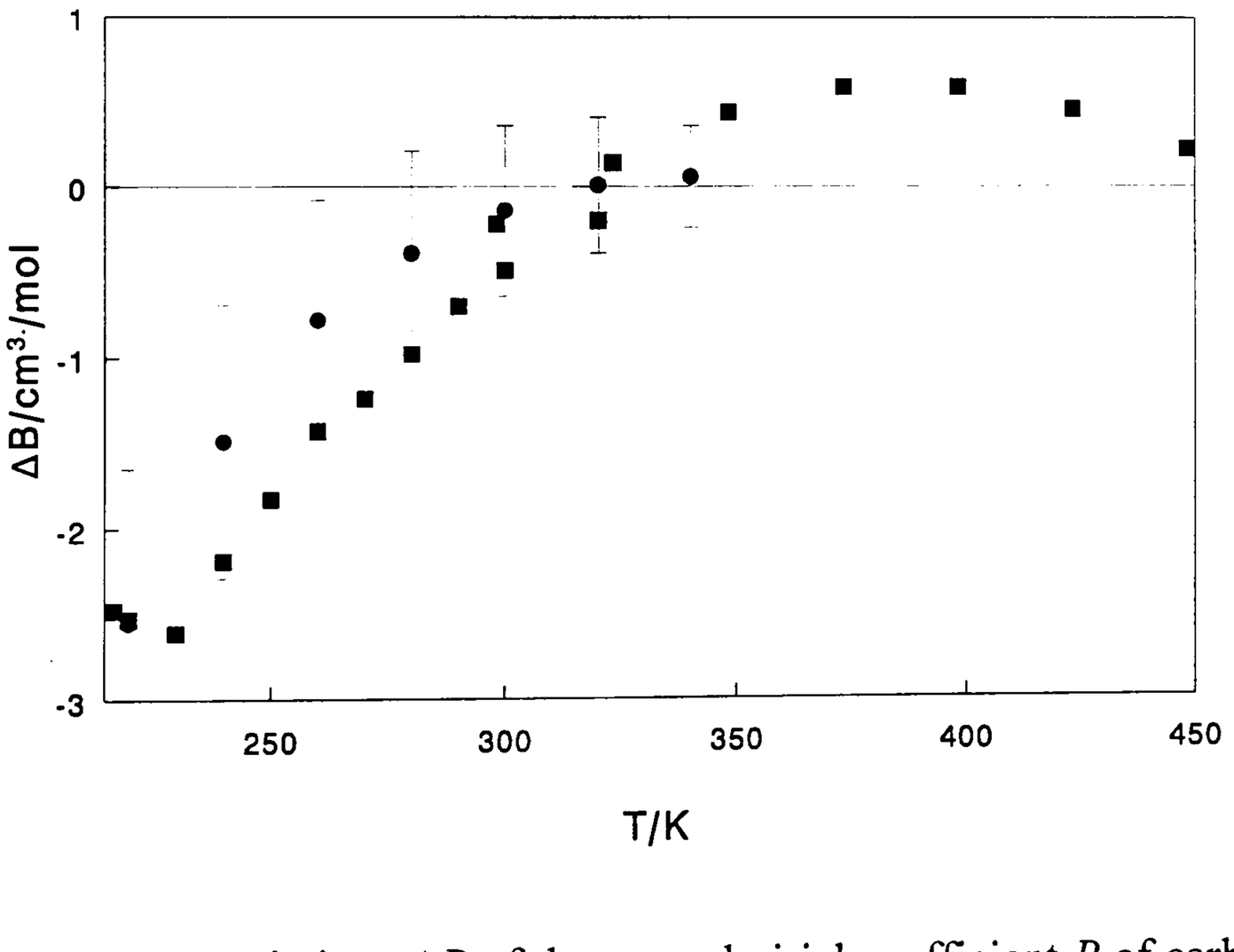


Figure 7.12 Deviations ΔB of the second virial coefficient B of carbon dioxide reported by Duschek *et al.*[12] and by Holste *et al.*[10] from those calculated from the MS intermolecular potential model adjusted by means of second acoustic virial coefficients. Calculations were carried out with the set of parameters given in table 7.2 that includes the first quantum correction. ●, reference [12]; ■, reference [13].

This comparison is shown in figure 12; only Duschek *et al.* gave estimated uncertainties while, for the results of Holste *et al.* no clear specification of uncertainties was given.

It is evident that ΔB shows a systematic deviation with the maximum disagreement at low temperatures where the empirical potential has already failed in representing properly second acoustic virial coefficients. Despite this, satisfactory agreement has been achieved with this method since the maximum disagreement was only about 2.7 $cm^3 \cdot mol^{-1}$ and, for $T \geq 275$ K, all deviations were within ± 1.0 $cm^3 \cdot mol^{-1}$.

7.3.4 Mixture of ethane and carbon dioxide.

Once interaction acoustic virial coefficients β_{12} were derived, it was a simple matter to fit them to an intermolecular pair potential and then to predict ordinary interaction second virial coefficient B_{12} for this system. Values of β_{12} and $C_{p,m}^{pg}$ reported in table 6.13 were used for the non-linear fitting of the potential. In this case, Δ_β was chosen to be 0.5 $cm^3 \cdot mol^{-1}$ for each coefficient β_{12}; a value slightly larger than for the pure components.

The intermolecular potential utilised was again of the site-site type with Maitland-Smith interaction functions. The sites were placed in the same position as those selected for each of the pure components. All the calculation were performed in the same way as those for a pure substance and, furthermore, the parameter γ was restricted to be 10.

A first try, including all temperatures, produced a poor fit with a reduce χ^2 of around 33 and β_{12} at 400 K deviated from the fit by nearly 5.5 $cm^3 \cdot mol^{-1}$. With this indication, another fit was carried out excluding the datum at $T = 400$ K. This time a much better fit was obtained with a reduce χ^2 of just above 5. Once again, all calculations were performed with the inclusion of the first **quantum** correction and a similar fit was obtained. In both cases, with and without inclusion of first quantum correction, β_{12} at 400 K deviated from the fit by a similar amount: 6.41 $cm^3 \cdot mol^{-1}$ for the former and 6.43 $cm^3 \cdot mol^{-1}$ for the latter.

Table 7.3 Parameters of intermolecular potential model obtained from fitting of the interaction second acoustic coefficient of the mixture ethane plus carbon dioxide. $\mu = 2.966 \cdot 10^{-26}$ kg, $I_1 = 7.2236 \cdot 10^{-46}$ kg·m^{-2}, $I_2 = 2.9373 \cdot 10^{-46}$ kg·m^{-2}, $2l_1 = 0.22$ nm, $2l_2 = 0.1534$ nm.

parameter	quantum corrections	
	0	1
$(\sigma/\text{nm}) \cdot 10^3$:	330.85 ± 6.3	329.78 ± 5.3
(ε/k)/K:	604.0 ± 41	619.0 ± 36
γ:	10.0	10.0
m:	15.2 ± 1.2	15.7 ± 1.1
σ_β/cm^3·mol^{-1}:	1.28	1.28
reduce χ^2:	5.12	5.13

The parameters that fit interaction second acoustic virial coefficients are given in table 3 for both cases (with and without inclusion of the first **quantum** correction). Statistical information on the fits is included there also, together with the reduced mass and the moments of inertia used in the calculation of the quantum corrections. Figure 13 shows the deviations of the experimental interaction virial coefficients from those calculated from the intermolecular potential. The agreement is satisfactory bearing in mind the relatively large composition variations.

The parameters σ_{12} and ε_{12} for the mixture were compared with classical mixing rules: the arithmetic mean for the collision diameter and the geometric mean for the energies. For the collision diameter σ_{12} it was found that an arithmetic mean of the pure components predicted a **slightly** shorter diameter than the fit required. This difference is just 2.2 per cent. For the energy parameter, the value predicted by the geometric-mean rule is larger than the actual value obtained during the fit by about 25 per cent. A similar result is obtained when a harmonic-mean rule is applied: ε_{12} predicted by this rule was 23 per cent above the value obtained by the fit.

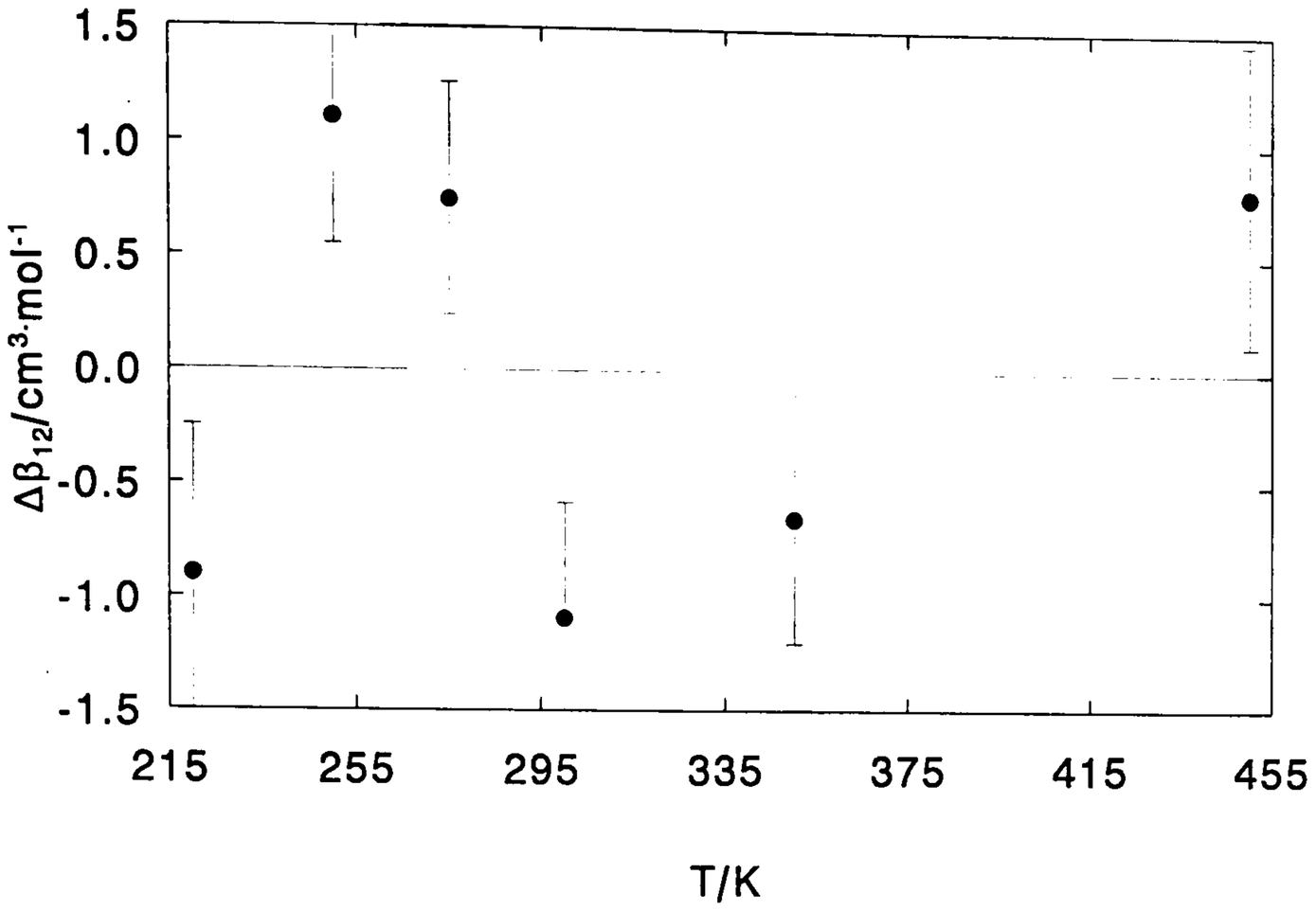


Figure 7.13 Deviation $\Delta\beta_{12}$ of the interaction second acoustic virial coefficient β_{12} from those calculated from the final fit of the site-site intermolecular potential model. Calculations were carried out with the set of parameters given in table 7.3 that includes the first quantum correction.

Finally, ordinary interaction second virial coefficient B_{12} were calculated from the derived intermolecular potential. Several sets of values of B_{12} have been reported from a variety of experimental techniques, ranging from classical pVT methods to refraction index measurements.[14-17] The comparison is shown in figure 14 for sixteen temperatures. Except for one datum from reference [16], which has a positive deviation, the rest of the data lie somewhat below the present results. Deviations as large as 4.5 cm^3·mol^{-1} can be observed in figure 14, but in most cases they were within ± 3.0 cm^3·mol^{-1}. This can be considered as a good agreement since the potential model reproduced the experimental β_{12} only within ± 1.0 cm^3·mol^{-1} (excluding the datum at $T = 400$ K) which reflected the problems observed with variations of composition.

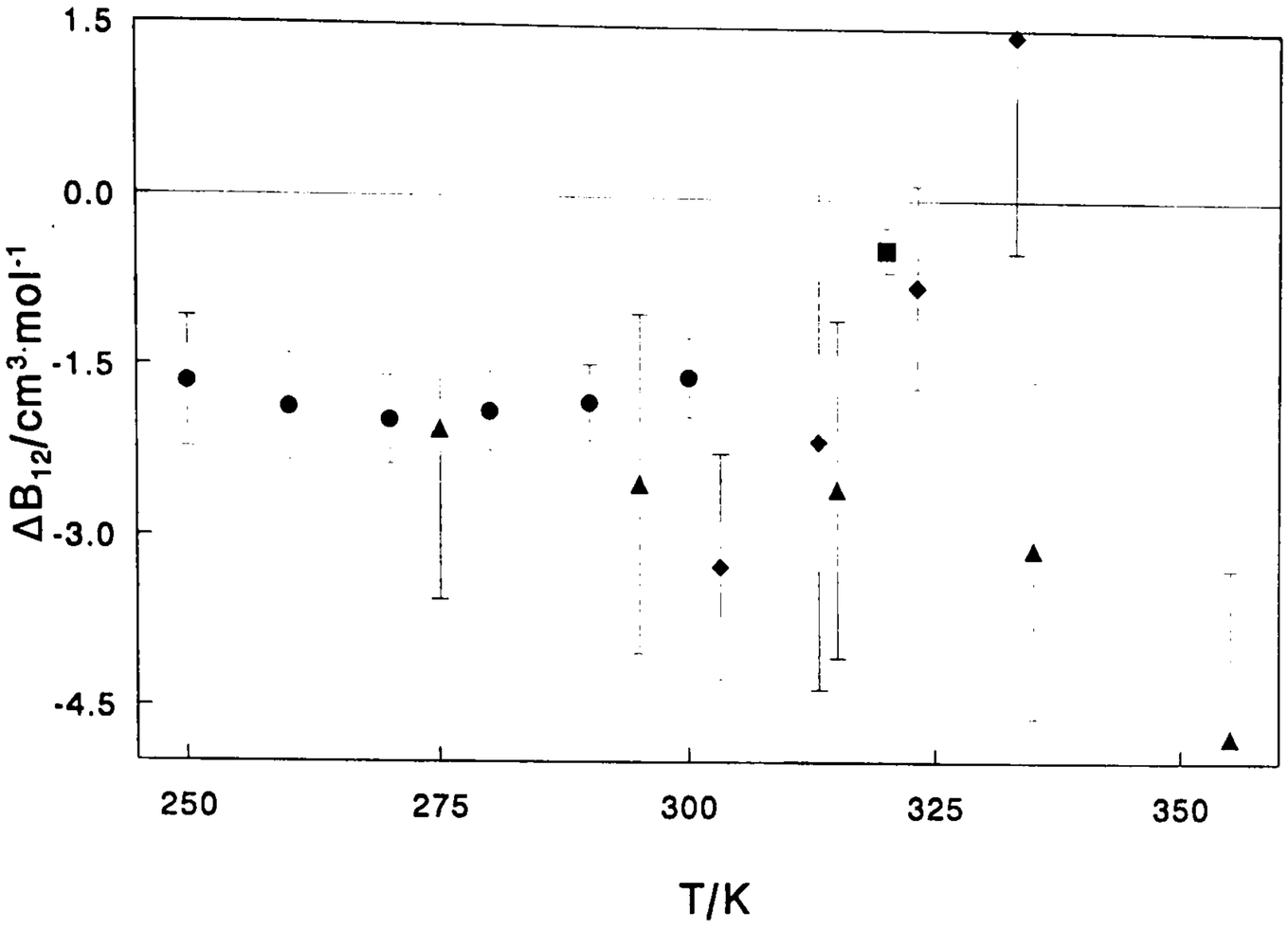


Figure 7.14 Deviations ΔB_{12} of the interaction second virial coefficient B_{12} of the system carbon dioxide and ethane reported in the literature from those calculated from the MS intermolecular potential model adjusted by means of second acoustic virial coefficients. Calculations were carried out with the set of parameters given in table 7.3 that includes the first quantum correction. ■, reference [14]; ●, reference [15]; ◆, reference [16]; ▲, reference [17].

References.

1. Stewart, R.B.; Jacobson, R.T.; Becker, J.H.; Center for applied Thermo. Studies Report N0. 81-3, University of Idaho (1981). Younglove, B.A.; *J. Phys. Chem. Ref. Data Suppl.*, **11** (1982).

2. Gilgen, R.; Kleinrahm, R.; Wagner, W.; *J.Chem.Thermodynamics*, **26**, 383 (1994).

3. McGlashan, M.L., *Chemical Thermodynamics*, 1979, London: Academic Press.

4. Estrada-Alexanders, A.F.; Trusler, J.P.M.; Zarari, M.; *Int. J. Thermophys.*, **16**, 663 (1995).

5. Baba, M.; Dordain, L.; Coxam, J-Y.; Grolier, J-P.E.; *Indian J. Technol.*, **30**, 553 (1992). Angus, S.; Amstrong, B.; *International Thermodynamic Table of the Fluid state-1, Argon*, 1972, London: Butterworths.

6. Younglove, B.A.; Ely, J.F.; *J. Phys. Chem. Ref. Data*, **16**, 577 (1987).

7. Douslin,D.R.; Harrison,R.H.; *J.Chem.Thermodynamics*, **5**, 491 (1973).

8. Tester, H.E.; *Thermodynamic Functions of Gases, Vol. 3*, ed. Din, F.; 1961, London: Butterworths.

9. Mansoorian, H.; Hall, K.R.; Holste, J.C.; Eubank, P.T.; *J.Chem.Thermodynamics*, **13**, 1001 (1981).

10. Roder, H.M.; *J.Research Nat. Bur. Stand.*, **80A**, 739 (1976).

11. Friend, D.G.; Ely, J.F.; *J. Phys. Chem. Ref. Data*, **20**, 275 (1991).

12. Duschek, W.; Kleinrahm, R.; Wagner, W.; *J.Chem.Thermodynamics*, **22**, 827 (1990).

13. Holste, J.C.; Hall, K.R.; Eubank, P.T.; Esper, G.; Watson, M.Q.; Warowny, W.; Bailey, D.C.; Young, J.G.; Bellomy, M.T.; *J.Chem.Thermodynamics*, **19**, 1233 (1987).

14. Weber, L.A.; *Int. J. Thermophys.*, **13**, 1011 (1992).

15. Holste, J.C.; Young, J.G.; Eubank, P.T.; Hall, K.R.; *AIChE Journal*, **28**, 807 (1982).

16. McElroy, P.J.; Dowd, M.K.; Battino, R.; *J.Chem.Thermodynamics*, **22**, 505 (1990).

17. Jaeschke, M.; *Int. J. Thermophys.*, **81**, 81 (1987).

Appendix.

Tables of thermodynamic properties of argon and ethane derived from the speed of sound in the temperature range and densities at which speeds of sound were available. The spacing in temperature and density of both tables were estimated to reproduce Z at intermediate temperatures and densities by means of a simple three-point interpolation formula in either variable without significant lost of accuracy.

In all calculations, the value of $R = 8.31451$ J·mol^{-1}·K^{-1} has been consistently used. All Z, $C_{V,\mathrm{m}}$ and $C_{p,\mathrm{m}}$ are given with more significant figures than that justified by the claimed uncertainties associated with each property (0.025 per cent on Z and 0.2 per cent on either heat capacity), in order to maintain negligible the truncation errors that can arise during the interpolations.

Table A1 Compression factor Z, heat capacities $C_{V,m}$ and $C_{p,m}$ of argon in a temperature range from 110 K to 450 K and densities up to 6.8 mol·dm^{-3}.

ρ_n/mol·dm^{-3}	Z	$C_{V,m}/R$	$C_{p,m}/R$	ρ_n/mol·dm^{-3}	Z	$C_{V,m}/R$	$C_{p,m}/R$
			T = 110.0 K				
0.025	0.996159	1.5060	2.5202	0.350	0.946419	1.5906	2.8178
0.050	0.992320	1.5120	2.5407	0.375	0.942603	1.5978	2.8439
0.075	0.988482	1.5181	2.5617	0.400	0.938789	1.6047	2.8698
0.100	0.984649	1.5242	2.5827	0.425	0.934980	1.6116	2.8958
0.125	0.980818	1.5303	2.6042	0.450	0.931174	1.6185	2.9223
0.150	0.976989	1.5367	2.6262	0.475	0.927371	1.6258	2.9499
0.175	0.973159	1.5433	2.6490	0.500	0.923570	1.6335	2.9786
0.200	0.969329	1.5500	2.6722	0.525	0.919768	1.6413	3.0080
0.225	0.965504	1.5566	2.6955	0.550	0.915966	1.6492	3.0380
0.250	0.961683	1.5631	2.7186	0.575	0.912165	1.6571	3.0682
0.275	0.957866	1.5696	2.7422	0.600	0.908365	1.6650	3.0990
0.300	0.954051	1.5763	2.7665	0.625	0.904566	1.6732	3.1307
0.325	0.950236	1.5834	2.7918				
			T = 115.0 K				
0.034	0.995187	1.5068	2.5247	0.476	0.933050	1.6092	2.9026
0.068	0.990378	1.5139	2.5501	0.510	0.928302	1.6176	2.9358
0.102	0.985575	1.5212	2.5762	0.544	0.923560	1.6257	2.9694
0.136	0.980778	1.5283	2.6024	0.578	0.918822	1.6342	3.0041
0.170	0.975984	1.5355	2.6292	0.612	0.914088	1.6433	3.0404
0.204	0.971195	1.5430	2.6569	0.646	0.909356	1.6528	3.0781
0.238	0.966411	1.5510	2.6855	0.680	0.904627	1.6625	3.1166
0.272	0.961632	1.5590	2.7145	0.714	0.899901	1.6720	3.1556
0.306	0.956859	1.5670	2.7439	0.748	0.895179	1.6814	3.1951
0.340	0.952091	1.5749	2.7739	0.782	0.890461	1.6911	3.2359
0.374	0.947325	1.5830	2.8047	0.816	0.885747	1.7014	3.2783
0.408	0.942563	1.5916	2.8367	0.850	0.881035	1.7121	3.3223
0.442	0.937804	1.6004	2.8695				

Table A1 -continued.

ρ_n/mol·dm^{-3}	Z	$C_{V,m}/R$	$C_{p,m}/R$	ρ_n/mol·dm^{-3}	Z	$C_{V,m}/R$	$C_{p,m}/R$
			T = 120.0 K				
0.044	0.994242	1.5082	2.5298	0.616	0.920190	1.6256	2.9873
0.088	0.988493	1.5165	2.5602	0.660	0.914554	1.6355	3.0290
0.132	0.982754	1.5250	2.5913	0.704	0.908926	1.6457	3.0722
0.176	0.977023	1.5336	2.6232	0.748	0.903304	1.6562	3.1166
0.220	0.971301	1.5422	2.6558	0.792	0.897690	1.6668	3.1623
0.264	0.965588	1.5510	2.6891	0.836	0.892083	1.6775	3.2092
0.308	0.959884	1.5598	2.7231	0.880	0.886483	1.6883	3.2573
0.352	0.954189	1.5688	2.7580	0.924	0.880891	1.6993	3.3067
0.396	0.948502	1.5779	2.7939	0.968	0.875307	1.7105	3.3577
0.440	0.942823	1.5872	2.8307	1.012	0.869730	1.7220	3.4105
0.484	0.937151	1.5966	2.8685	1.056	0.864159	1.7338	3.4650
0.528	0.931488	1.6062	2.9072	1.100	0.858595	1.7457	3.5212
0.572	0.925835	1.6158	2.9467				
			T = 125.0 K				
0.057	0.993085	1.5096	2.5356	0.798	0.904588	1.6460	3.0981
0.114	0.986186	1.5192	2.5721	0.855	0.897885	1.6578	3.1513
0.171	0.979303	1.5290	2.6095	0.912	0.891196	1.6699	3.2064
0.228	0.972435	1.5390	2.6480	0.969	0.884520	1.6823	3.2633
0.285	0.965582	1.5491	2.6876	1.026	0.877858	1.6947	3.3220
0.342	0.958744	1.5593	2.7281	1.083	0.871211	1.7073	3.3825
0.399	0.951922	1.5695	2.7698	1.140	0.864577	1.7201	3.4452
0.456	0.945115	1.5799	2.8126	1.197	0.857957	1.7332	3.5103
0.513	0.938322	1.5905	2.8568	1.254	0.851351	1.7467	3.5779
0.570	0.931545	1.6014	2.9024	1.311	0.844757	1.7605	3.6481
0.627	0.924783	1.6123	2.9491	1.368	0.838177	1.7746	3.7209
0.684	0.918036	1.6234	2.9973	1.425	0.831610	1.7889	3.7965
0.741	0.911305	1.6345	3.0468				
			T = 130.0 K				
0.073	0.991769	1.5109	2.5421	1.022	0.887082	1.6687	3.2327

Table A1 -continued.

ρ_n/mol·dm^{-3}	Z	$C_{V,\mathrm{m}}/R$	$C_{p,\mathrm{m}}/R$	ρ_n/mol·dm^{-3}	Z	$C_{V,\mathrm{m}}/R$	$C_{p,\mathrm{m}}/R$
0.146	0.983564	1.5220	2.5855	1.095	0.879204	1.6825	3.3002
0.219	0.975385	1.5332	2.6302	1.168	0.871350	1.6965	3.3703
0.292	0.967231	1.5445	2.6764	1.241	0.863521	1.7108	3.4432
0.365	0.959103	1.5561	2.7240	1.314	0.855716	1.7253	3.5191
0.438	0.950999	1.5678	2.7732	1.387	0.847935	1.7403	3.5982
0.511	0.942921	1.5797	2.8240	1.460	0.840178	1.7555	3.6807
0.584	0.934869	1.5918	2.8765	1.533	0.832445	1.7711	3.7667
0.657	0.926841	1.6041	2.9307	1.606	0.824736	1.7871	3.8566
0.730	0.918840	1.6165	2.9868	1.679	0.817051	1.8035	3.9506
0.803	0.910863	1.6292	3.0449	1.752	0.809391	1.8203	4.0490
0.876	0.902912	1.6421	3.1052	1.825	0.801753	1.8376	4.1524
0.949	0.894985	1.6553	3.1677				
			$T = 135.0$ K				
0.094	0.990128	1.5127	2.5505	1.316	0.865605	1.6974	3.4150
0.188	0.980298	1.5255	2.6028	1.410	0.856318	1.7137	3.5033
0.282	0.970510	1.5385	2.6569	1.504	0.847074	1.7303	3.5956
0.376	0.960763	1.5517	2.7131	1.598	0.837871	1.7472	3.6924
0.470	0.951059	1.5652	2.7713	1.692	0.828711	1.7646	3.7941
0.564	0.941396	1.5788	2.8319	1.786	0.819592	1.7825	3.9009
0.658	0.931776	1.5927	2.8948	1.880	0.810515	1.8008	4.0133
0.752	0.922197	1.6069	2.9601	1.974	0.801479	1.8196	4.1318
0.846	0.912661	1.6212	3.0281	2.068	0.792485	1.8390	4.2569
0.940	0.903166	1.6358	3.0989	2.162	0.783533	1.8590	4.3890
1.034	0.893713	1.6506	3.1728	2.256	0.774621	1.8796	4.5287
1.128	0.884302	1.6659	3.2500	2.350	0.765752	1.9008	4.6765
1.222	0.874933	1.6815	3.3307				
			$T = 140.0$ K				
0.123	0.987945	1.5151	2.5618	1.722	0.837675	1.7367	3.6855
0.246	0.975960	1.5303	2.6263	1.845	0.826618	1.7565	3.8071
0.369	0.964046	1.5458	2.6935	1.968	0.815633	1.7769	3.9358

Table A1 -continued.

ρ_n/mol·dm^{-3}	Z	$C_{V,m}/R$	$C_{p,m}/R$	ρ_n/mol·dm^{-3}	Z	$C_{V,m}/R$	$C_{p,m}/R$
0.492	0.952202	1.5616	2.7637	2.091	0.804722	1.7977	4.0724
0.615	0.940428	1.5776	2.8372	2.214	0.793884	1.8192	4.2174
0.738	0.928726	1.5939	2.9140	2.337	0.783119	1.8413	4.3715
0.861	0.917094	1.6105	2.9944	2.460	0.772428	1.8641	4.5357
0.984	0.905534	1.6273	3.0787	2.583	0.761811	1.8876	4.7107
1.107	0.894045	1.6445	3.1672	2.706	0.751268	1.9118	4.8977
1.230	0.882627	1.6621	3.2603	2.829	0.740800	1.9368	5.0977
1.353	0.871281	1.6801	3.3583	2.952	0.730407	1.9626	5.3123
1.476	0.860007	1.6985	3.4615	3.075	0.720089	1.9893	5.5427
1.599	0.848805	1.7173	3.5704				
			T = 145.0 K				
0.167	0.984704	1.5186	2.5789	2.338	0.797537	1.7977	4.1549
0.334	0.969533	1.5374	2.6620	2.505	0.784065	1.8234	4.3414
0.501	0.954489	1.5566	2.7496	2.672	0.770728	1.8498	4.5423
0.668	0.939571	1.5762	2.8422	2.839	0.757529	1.8771	4.7588
0.835	0.924781	1.5962	2.9401	3.006	0.744467	1.9052	4.9926
1.002	0.910120	1.6165	3.0437	3.173	0.731544	1.9342	5.2457
1.169	0.895587	1.6373	3.1537	3.340	0.718760	1.9642	5.5203
1.336	0.881184	1.6584	3.2704	3.507	0.706116	1.9952	5.8191
1.503	0.866912	1.6801	3.3947	3.674	0.693613	2.0275	6.1450
1.670	0.852771	1.7024	3.5271	3.841	0.681251	2.0609	6.5012
1.837	0.838763	1.7253	3.6684	4.008	0.669032	2.0957	6.8919
2.004	0.824887	1.7487	3.8195	4.175	0.656957	2.1319	7.3215
2.171	0.811145	1.7729	3.9813				
			T = 147.5 K				
0.202	0.982109	1.5216	2.5929	2.828	0.766489	1.8496	4.6011
0.404	0.964398	1.5435	2.6915	3.030	0.751258	1.8803	4.8568
0.606	0.946869	1.5658	2.7964	3.232	0.736228	1.9120	5.1358
0.808	0.929524	1.5885	2.9081	3.434	0.721401	1.9448	5.4411
1.010	0.912364	1.6116	3.0275	3.636	0.706776	1.9787	5.7758

Table A1 -continued.

ρ_n/mol·dm^{-3}	Z	$C_{V,m}/R$	$C_{p,m}/R$	ρ_n/mol·dm^{-3}	Z	$C_{V,m}/R$	$C_{p,m}/R$
1.212	0.895391	1.6353	3.1551	3.838	0.692357	2.0137	6.1439
1.414	0.878605	1.6596	3.2919	4.040	0.678144	2.0501	6.5499
1.616	0.862009	1.6845	3.4388	4.242	0.664139	2.0878	6.9991
1.818	0.845604	1.7100	3.5969	4.444	0.650343	2.1271	7.4977
2.020	0.829391	1.7363	3.7672	4.646	0.636757	2.1679	8.0529
2.222	0.813371	1.7633	3.9513	4.848	0.623383	2.2104	8.6736
2.424	0.797547	1.7912	4.1504	5.050	0.610221	2.2547	9.3704
2.626	0.781919	1.8199	4.3664				
			$T = 150.0$ K				
0.272	0.976716	1.5276	2.6220	3.808	0.704737	1.9702	5.8014
0.544	0.953754	1.5558	2.7541	4.080	0.686300	2.0134	6.2769
0.816	0.931119	1.5848	2.8973	4.352	0.668234	2.0583	6.8134
1.088	0.908815	1.6145	3.0532	4.624	0.650541	2.1052	7.4210
1.360	0.886845	1.6451	3.2233	4.896	0.633224	2.1540	8.1122
1.632	0.865212	1.6766	3.4093	5.168	0.616286	2.2050	8.9016
1.904	0.843922	1.7091	3.6133	5.440	0.599731	2.2582	9.8075
2.176	0.822976	1.7426	3.8377	5.712	0.583559	2.3138	10.8522
2.448	0.802379	1.7772	4.0852	5.984	0.567775	2.3719	12.0633
2.720	0.782134	1.8131	4.3590	6.256	0.552380	2.4326	13.4752
2.992	0.762244	1.8502	4.6628	6.528	0.537377	2.4962	15.1312
3.264	0.742712	1.8887	5.0009	6.800	0.522767	2.5626	17.0859
3.536	0.723543	1.9286	5.3785				
			$T = 150.7$ K				
0.272	0.976924	1.5273	2.6210	3.808	0.707516	1.9604	5.7298
0.544	0.954169	1.5552	2.7518	4.080	0.689265	2.0022	6.1879
0.816	0.931739	1.5838	2.8935	4.352	0.671383	2.0456	6.7028
1.088	0.909638	1.6130	3.0474	4.624	0.653873	2.0906	7.2834
1.360	0.887870	1.6431	3.2151	4.896	0.636736	2.1375	7.9404
1.632	0.866438	1.6740	3.3983	5.168	0.619976	2.1861	8.6867
1.904	0.845347	1.7058	3.5988	5.440	0.603595	2.2367	9.5377

Table A1 -continued.

ρ_n/mol·dm^{-3}	Z	$C_{V,m}/R$	$C_{p,m}/R$	ρ_n/mol·dm^{-3}	Z	$C_{V,m}/R$	$C_{p,m}/R$
2.176	0.824599	1.7386	3.8191	5.712	0.587596	2.2893	10.5121
2.448	0.804199	1.7725	4.0616	5.984	0.571980	2.3439	11.6326
2.720	0.784149	1.8075	4.3293	6.256	0.556750	2.4008	12.9268
2.992	0.764452	1.8438	4.6256	6.528	0.541908	2.4599	14.4288
3.264	0.745112	1.8813	4.9546	6.800	0.527457	2.5214	16.1804
3.536	0.726133	1.9201	5.3208				
			T = 152.5 K				
0.272	0.977448	1.5266	2.6184	3.808	0.714489	1.9369	5.5594
0.544	0.955212	1.5536	2.7459	4.080	0.696704	1.9755	5.9777
0.816	0.933298	1.5811	2.8837	4.352	0.679282	2.0152	6.4435
1.088	0.911709	1.6092	3.0328	4.624	0.662226	2.0562	6.9634
1.360	0.890449	1.6380	3.1948	4.896	0.645537	2.0985	7.5449
1.632	0.869521	1.6675	3.3710	5.168	0.629218	2.1420	8.1972
1.904	0.848930	1.6978	3.5633	5.440	0.613271	2.1867	8.9304
2.176	0.828679	1.7289	3.7736	5.712	0.597697	2.2328	9.7568
2.448	0.808771	1.7610	4.0040	5.984	0.582499	2.2801	10.6904
2.720	0.789210	1.7941	4.2570	6.256	0.567677	2.3287	11.7476
2.992	0.769998	1.8281	4.5356	6.528	0.553234	2.3786	12.9472
3.264	0.751138	1.8633	4.8429	6.800	0.539170	2.4297	14.3113
3.536	0.732634	1.8995	5.1828				
			T = 155.0 K				
0.272	0.978149	1.5255	2.6148	3.808	0.723785	1.9078	5.3507
0.544	0.956609	1.5513	2.7380	4.080	0.706616	1.9426	5.7230
0.816	0.935384	1.5775	2.8706	4.352	0.689803	1.9781	6.1330
1.088	0.914479	1.6041	3.0137	4.624	0.673346	2.0145	6.5851
1.360	0.893898	1.6313	3.1683	4.896	0.657248	2.0516	7.0843
1.632	0.873643	1.6591	3.3357	5.168	0.641510	2.0895	7.6360
1.904	0.853720	1.6875	3.5175	5.440	0.626133	2.1280	8.2466
2.176	0.834131	1.7166	3.7152	5.712	0.611119	2.1672	8.9227
2.448	0.814879	1.7465	3.9306	5.984	0.596467	2.2069	9.6722

Table A1 -continued.

ρ_n/mol·dm^{-3}	Z	$C_{V,m}/R$	$C_{p,m}/R$	ρ_n/mol·dm^{-3}	Z	$C_{V,m}/R$	$C_{p,m}/R$
2.720	0.795968	1.7771	4.1657	6.256	0.582179	2.2472	10.5032
2.992	0.777401	1.8085	4.4225	6.528	0.568256	2.2879	11.4247
3.264	0.759179	1.8408	4.7038	6.800	0.554697	2.3289	12.4464
3.536	0.741306	1.8739	5.0121				
			T = 157.5 K				
0.272	0.978822	1.5245	2.6114	3.808	0.732662	1.8821	5.1688
0.544	0.957948	1.5491	2.7306	4.080	0.716079	1.9137	5.5034
0.816	0.937384	1.5741	2.8584	4.352	0.699842	1.9458	5.8684
1.088	0.917134	1.5994	2.9957	4.624	0.683954	1.9784	6.2668
1.360	0.897202	1.6252	3.1436	4.896	0.668414	2.0115	6.7020
1.632	0.877592	1.6514	3.3032	5.168	0.653226	2.0449	7.1774
1.904	0.858306	1.6781	3.4755	5.440	0.638388	2.0787	7.6968
2.176	0.839349	1.7054	3.6620	5.712	0.623901	2.1128	8.2643
2.448	0.820724	1.7333	3.8641	5.984	0.609766	2.1470	8.8840
2.720	0.802433	1.7618	4.0833	6.256	0.595982	2.1814	9.5604
2.992	0.784479	1.7910	4.3214	6.528	0.582549	2.2157	10.2979
3.264	0.766864	1.8207	4.5802	6.800	0.569467	2.2498	11.1008
3.536	0.749591	1.8511	4.8620				
			T = 160.0 K				
0.272	0.979467	1.5235	2.6081	3.808	0.741154	1.8592	5.0088
0.544	0.959233	1.5471	2.7235	4.080	0.725127	1.8881	5.3119
0.816	0.939303	1.5709	2.8469	4.352	0.709439	1.9173	5.6399
1.088	0.919681	1.5951	2.9790	4.624	0.694091	1.9468	5.9949
1.360	0.900371	1.6195	3.1207	4.896	0.679083	1.9766	6.3791
1.632	0.881377	1.6444	3.2730	5.168	0.664416	2.0066	6.7948
1.904	0.862702	1.6696	3.4368	5.440	0.650090	2.0367	7.2442
2.176	0.844350	1.6953	3.6132	5.712	0.636105	2.0668	7.7299
2.448	0.826323	1.7215	3.8034	5.984	0.622461	2.0969	8.2541
2.720	0.808624	1.7481	4.0087	6.256	0.609156	2.1268	8.8191
2.992	0.791255	1.7752	4.2303	6.528	0.596190	2.1565	9.4272

Table A1 -continued.

ρ_n/mol·dm^{-3}	Z	$C_{V,m}/R$	$C_{p,m}/R$	ρ_n/mol·dm^{-3}	Z	$C_{V,m}/R$	$C_{p,m}/R$
3.264	0.774220	1.8027	4.4698	6.800	0.583562	2.1857	10.0803
3.536	0.757518	1.8308	4.7287				
			T = 175.0 K				
0.680	0.957629	1.5469	2.7389	4.080	0.772229	1.7802	4.5328
1.360	0.916963	1.5935	3.0108	4.760	0.740648	1.8263	5.0451
2.040	0.878054	1.6401	3.3211	5.440	0.710914	1.8712	5.6159
2.720	0.840944	1.6869	3.6748	6.120	0.683011	1.9144	6.2443
3.400	0.805663	1.7336	4.0772	6.800	0.656908	1.9550	6.9264
			T = 190.0 K				
0.680	0.964383	1.5383	2.7053	4.080	0.809956	1.7167	4.0896
1.360	0.930295	1.5757	2.9327	4.760	0.783978	1.7494	4.4415
2.040	0.897778	1.6123	3.1839	5.440	0.759653	1.7806	4.8154
2.720	0.866868	1.6481	3.4601	6.120	0.736970	1.8103	5.2075
3.400	0.837589	1.6829	3.7621	6.800	0.715910	1.8380	5.6132
			T = 205.0 K				
0.680	0.969927	1.5320	2.6795	4.080	0.840989	1.6755	3.8034
1.360	0.941243	1.5630	2.8744	4.760	0.819648	1.7005	4.0674
2.040	0.913982	1.5929	3.0848	5.440	0.799820	1.7241	4.3394
2.720	0.888171	1.6217	3.3104	6.120	0.781506	1.7464	4.6161
3.400	0.863834	1.6492	3.5504	6.800	0.764704	1.7672	4.8941
			T = 220.0 K				
0.680	0.974557	1.5274	2.6593	4.080	0.867012	1.6472	3.6035
1.360	0.950393	1.5537	2.8295	4.760	0.849594	1.6674	3.8130
2.040	0.927532	1.5789	3.0100	5.440	0.833581	1.6863	4.0245
2.720	0.906001	1.6029	3.2001	6.120	0.818989	1.7040	4.2352
3.400	0.885820	1.6257	3.3985	6.800	0.805829	1.7205	4.4424
			T = 235.0 K				
0.680	0.978479	1.5238	2.6429	4.080	0.889164	1.6267	3.4559
1.360	0.958148	1.5466	2.7937	4.760	0.875114	1.6438	3.6289
2.040	0.939029	1.5683	2.9515	5.440	0.862388	1.6597	3.8010

Table A1 -continued.

ρ_n/mol·dm^{-3}	Z	$C_{V,m}/R$	$C_{p,m}/R$	ρ_n/mol·dm^{-3}	Z	$C_{V,m}/R$	$C_{p,m}/R$
2.720	0.921144	1.5890	3.1155	6.120	0.851010	1.6745	3.9699
3.400	0.904515	1.6084	3.2841	6.800	0.841001	1.6882	4.1336
			T = 250.0 K				
0.680	0.981840	1.5209	2.6294	4.080	0.908249	1.6113	3.3424
1.360	0.964801	1.5410	2.7645	4.760	0.897128	1.6262	3.4894
2.040	0.948901	1.5601	2.9045	5.440	0.887265	1.6401	3.6340
2.720	0.934161	1.5782	3.0484	6.120	0.878693	1.6530	3.7745
3.400	0.920602	1.5953	3.1948	6.800	0.871439	1.6649	3.9093
			T = 265.0 K				
0.680	0.984751	1.5186	2.6181	4.080	0.924857	1.5994	3.2523
1.360	0.970567	1.5365	2.7403	4.760	0.916305	1.6128	3.3799
2.040	0.957465	1.5536	2.8660	5.440	0.908961	1.6253	3.5045
2.720	0.945463	1.5698	2.9940	6.120	0.902860	1.6368	3.6246
3.400	0.934586	1.5851	3.1232	6.800	0.898038	1.6476	3.7391
			T = 280.0 K				
0.680	0.987294	1.5167	2.6085	4.080	0.939432	1.5900	3.1792
1.360	0.975609	1.5329	2.7200	4.760	0.933152	1.6023	3.2918
2.040	0.964959	1.5484	2.8338	5.440	0.928040	1.6137	3.4011
2.720	0.955364	1.5631	2.9490	6.120	0.924133	1.6243	3.5059
3.400	0.946846	1.5770	3.0645	6.800	0.921471	1.6342	3.6053
			T = 295.0 K				
0.680	0.989534	1.5152	2.6002	4.080	0.952318	1.5824	3.1185
1.360	0.980051	1.5299	2.7027	4.760	0.948061	1.5938	3.2192
2.040	0.971567	1.5441	2.8066	5.440	0.944938	1.6044	3.3165
2.720	0.964101	1.5576	2.9112	6.120	0.942991	1.6143	3.4095
3.400	0.957675	1.5703	3.0155	6.800	0.942260	1.6236	3.4974
			T = 310.0 K				
0.680	0.991520	1.5140	2.5931	4.080	0.963784	1.5761	3.0673
1.360	0.983993	1.5275	2.6878	4.760	0.961337	1.5868	3.1584
2.040	0.977434	1.5405	2.7833	5.440	0.959999	1.5968	3.2461

Table A1 -continued.

ρ_n/mol·dm^{-3}	Z	$C_{V,m}/R$	$C_{p,m}/R$	ρ_n/mol·dm^{-3}	Z	$C_{V,m}/R$	$C_{p,m}/R$
2.720	0.971862	1.5530	2.8789	6.120	0.959810	1.6063	3.3296
3.400	0.967303	1.5649	2.9739	6.800	0.960815	1.6151	3.4084
			T = 325.0 K				
0.680	0.993292	1.5129	2.5869	4.080	0.974044	1.5709	3.0236
1.360	0.987511	1.5254	2.6748	4.760	0.973225	1.5810	3.1066
2.040	0.982673	1.5375	2.7631	5.440	0.973495	1.5906	3.1864
2.720	0.978799	1.5491	2.8511	6.120	0.974893	1.5996	3.2623
3.400	0.975912	1.5603	2.9382	6.800	0.977466	1.6082	3.3338
			T = 340.0 K				
0.680	0.994882	1.5120	2.5814	4.080	0.983271	1.5665	2.9859
1.360	0.990668	1.5237	2.6634	4.760	0.983924	1.5761	3.0621
2.040	0.987377	1.5350	2.7454	5.440	0.985648	1.5853	3.1352
2.720	0.985030	1.5459	2.8270	6.120	0.988484	1.5941	3.2048
3.400	0.983651	1.5564	2.9073	6.800	0.992479	1.6025	3.2703
			T = 355.0 K				
0.680	0.996315	1.5112	2.5765	4.080	0.991609	1.5627	2.9530
1.360	0.993516	1.5222	2.6533	4.760	0.993596	1.5720	3.0234
2.040	0.991622	1.5328	2.7299	5.440	0.996639	1.5809	3.0909
2.720	0.990655	1.5432	2.8057	6.120	1.000783	1.5895	3.1549
3.400	0.990640	1.5531	2.8803	6.800	1.006071	1.5977	3.2153
			T = 370.0 K				
0.680	0.997613	1.5105	2.5722	4.080	0.999173	1.5595	2.9241
1.360	0.996096	1.5209	2.6443	4.760	1.002374	1.5684	2.9894
2.040	0.995469	1.5310	2.7161	5.440	1.006620	1.5771	3.0520
2.720	0.995754	1.5408	2.7870	6.120	1.011954	1.5854	3.1114
3.400	0.996978	1.5503	2.8564	6.800	1.018422	1.5936	3.1674
			T = 385.0 K				
0.680	0.998793	1.5099	2.5682	4.080	1.006063	1.5567	2.8985
1.360	0.998442	1.5197	2.6363	4.760	1.010372	1.5654	2.9594
2.040	0.998968	1.5294	2.7038	5.440	1.015716	1.5738	3.0177

Table A1 -continued.

ρ_n/mol·dm^{-3}	Z	$C_{V,m}/R$	$C_{p,m}/R$	ρ_n/mol·dm^{-3}	Z	$C_{V,m}/R$	$C_{p,m}/R$
2.720	1.000394	1.5387	2.7702	6.120	1.022137	1.5819	3.0730
3.400	1.002748	1.5479	2.8353	6.800	1.029683	1.5900	3.1251
			T = 400.0 K				
0.680	0.999870	1.5094	2.5647	4.080	1.012358	1.5543	2.8756
1.360	1.000585	1.5188	2.6290	4.760	1.017683	1.5627	2.9327
2.040	1.002164	1.5279	2.6927	5.440	1.024032	1.5709	2.9872
2.720	1.004633	1.5369	2.7552	6.120	1.031451	1.5789	3.0389
3.400	1.008020	1.5457	2.8163	6.800	1.039983	1.5867	3.0876
			T = 415.0 K				
0.680	1.000857	1.5090	2.5615	4.080	1.018130	1.5522	2.8551
1.360	1.002547	1.5179	2.6225	4.760	1.024386	1.5604	2.9087
2.040	1.005091	1.5267	2.6826	5.440	1.031660	1.5683	2.9600
2.720	1.008516	1.5353	2.7417	6.120	1.039994	1.5762	3.0085
3.400	1.012852	1.5438	2.7993	6.800	1.049433	1.5838	3.0542
			T = 430.0 K				
0.680	1.001764	1.5087	2.5586	4.080	1.023436	1.5503	2.8365
1.360	1.004350	1.5172	2.6166	4.760	1.030551	1.5583	2.8871
2.040	1.007781	1.5256	2.6736	5.440	1.038676	1.5661	2.9355
2.720	1.012086	1.5339	2.7294	6.120	1.047854	1.5737	2.9812
3.400	1.017293	1.5422	2.7838	6.800	1.058129	1.5811	3.0242
			T = 450.0 K				
0.680	1.002863	1.5083	2.5552	4.080	1.029874	1.5480	2.8143
1.360	1.006536	1.5164	2.6095	4.760	1.038031	1.5558	2.8614
2.040	1.011044	1.5243	2.6627	5.440	1.047192	1.5635	2.9064
2.720	1.016415	1.5323	2.7147	6.120	1.057398	1.5709	2.9489
3.400	1.022681	1.5401	2.7653	6.800	1.068692	1.5779	2.9889

Table A2 Compression factor Z, heat capacities $C_{V,m}$ and $C_{p,m}$ of ethane in a temperature range from 220 K to 450 K and densities up to 3.3 mol·dm^{-3}.

ρ_n/mol·dm^{-3}	Z	$C_{V,m}/R$	$C_{p,m}/R$	ρ_n/mol·dm^{-3}	Z	$C_{V,m}/R$	$C_{p,m}/R$
			$T = 220.0$ K				
0.009	0.996894	4.3096	5.3227	0.126	0.956779	4.4194	5.6175
0.018	0.993792	4.3184	5.3447	0.135	0.953708	4.4278	5.6416
0.027	0.990693	4.3271	5.3668	0.144	0.950639	4.4362	5.6660
0.036	0.987597	4.3357	5.3889	0.153	0.947570	4.4447	5.6907
0.045	0.984504	4.3443	5.4110	0.162	0.944503	4.4532	5.7157
0.054	0.981414	4.3527	5.4333	0.171	0.941437	4.4617	5.7410
0.063	0.978327	4.3611	5.4557	0.180	0.938372	4.4703	5.7667
0.072	0.975243	4.3695	5.4782	0.189	0.935308	4.4790	5.7928
0.081	0.972160	4.3778	5.5009	0.198	0.932245	4.4877	5.8192
0.090	0.969080	4.3861	5.5238	0.207	0.929182	4.4965	5.8460
0.099	0.966002	4.3945	5.5469	0.216	0.926121	4.5053	5.8732
0.108	0.962926	4.4028	5.5702	0.225	0.923060	4.5143	5.9008
0.117	0.959852	4.4111	5.5937				
			$T = 235.0$ K				
0.016	0.995186	4.4837	5.5038	0.224	0.933161	4.6349	5.9566
0.032	0.990379	4.4959	5.5364	0.240	0.928426	4.6467	5.9957
0.048	0.985578	4.5079	5.5691	0.256	0.923696	4.6585	6.0356
0.064	0.980785	4.5197	5.6021	0.272	0.918970	4.6706	6.0764
0.080	0.975997	4.5314	5.6353	0.288	0.914248	4.6827	6.1181
0.096	0.971216	4.5430	5.6689	0.304	0.909530	4.6950	6.1607
0.112	0.966440	4.5544	5.7029	0.320	0.904817	4.7074	6.2043
0.128	0.961671	4.5659	5.7374	0.336	0.900107	4.7200	6.2490
0.144	0.956906	4.5773	5.7724	0.352	0.895402	4.7327	6.2947
0.160	0.952147	4.5887	5.8079	0.368	0.890700	4.7456	6.3414
0.176	0.947393	4.6001	5.8440	0.384	0.886002	4.7586	6.3893
0.192	0.942644	4.6117	5.8808	0.400	0.881308	4.7717	6.4383
0.208	0.937900	4.6232	5.9184				

Table A2 -continued.

ρ_n/mol·dm^{-3}	Z	$C_{V,m}/R$	$C_{p,m}/R$	ρ_n/mol·dm^{-3}	Z	$C_{V,m}/R$	$C_{p,m}/R$
			$T = 250.0$ K				
0.025	0.993375	4.6688	5.6962	0.350	0.908445	4.8553	6.3251
0.050	0.986764	4.6837	5.7393	0.375	0.902002	4.8701	6.3824
0.075	0.980166	4.6984	5.7830	0.400	0.895572	4.8851	6.4415
0.100	0.973581	4.7129	5.8273	0.425	0.889154	4.9004	6.5024
0.125	0.967009	4.7272	5.8723	0.450	0.882749	4.9158	6.5652
0.150	0.960450	4.7413	5.9181	0.475	0.876356	4.9315	6.6301
0.175	0.953904	4.7554	5.9648	0.500	0.869976	4.9475	6.6970
0.200	0.947371	4.7695	6.0125	0.525	0.863608	4.9637	6.7662
0.225	0.940851	4.7836	6.0614	0.550	0.857253	4.9801	6.8377
0.250	0.934345	4.7977	6.1114	0.575	0.850909	4.9969	6.9117
0.275	0.927851	4.8119	6.1627	0.600	0.844578	5.0138	6.9882
0.300	0.921369	4.8262	6.2153	0.625	0.838259	5.0310	7.0674
0.325	0.914901	4.8407	6.2694				
			$T = 260.0$ K				
0.033	0.991929	4.7986	5.8321	0.462	0.889049	5.0124	6.6151
0.066	0.983880	4.8155	5.8836	0.495	0.881296	5.0295	6.6895
0.099	0.975853	4.8322	5.9362	0.528	0.873567	5.0470	6.7667
0.132	0.967848	4.8487	5.9899	0.561	0.865862	5.0647	6.8469
0.165	0.959866	4.8650	6.0447	0.594	0.858179	5.0828	6.9302
0.198	0.951905	4.8812	6.1010	0.627	0.850521	5.1012	7.0168
0.231	0.943968	4.8973	6.1587	0.660	0.842885	5.1199	7.1070
0.264	0.936053	4.9134	6.2180	0.693	0.835273	5.1390	7.2010
0.297	0.928161	4.9296	6.2790	0.726	0.827684	5.1586	7.2989
0.330	0.920292	4.9459	6.3419	0.759	0.820118	5.1785	7.4012
0.363	0.912446	4.9622	6.4068	0.792	0.812575	5.1988	7.5079
0.396	0.904624	4.9787	6.4739	0.825	0.805055	5.2195	7.6195
0.429	0.896825	4.9954	6.5433				
			$T = 270.0$ K				
0.044	0.990040	4.9338	5.9753	0.616	0.864186	5.1838	6.9814

Table A2 -continued.

ρ_n/mol·dm^{-3}	Z	$C_{V,m}/R$	$C_{p,m}/R$	ρ_n/mol·dm^{-3}	Z	$C_{V,m}/R$	$C_{p,m}/R$
0.088	0.980118	4.9532	6.0381	0.660	0.854798	5.2042	7.0824
0.132	0.970234	4.9724	6.1027	0.704	0.845453	5.2250	7.1881
0.176	0.960389	4.9915	6.1692	0.748	0.836152	5.2462	7.2990
0.220	0.950583	5.0104	6.2378	0.792	0.826893	5.2678	7.4153
0.264	0.940818	5.0293	6.3087	0.836	0.817677	5.2900	7.5377
0.308	0.931093	5.0482	6.3820	0.880	0.808505	5.3127	7.6664
0.352	0.921409	5.0671	6.4579	0.924	0.799376	5.3361	7.8021
0.396	0.911767	5.0861	6.5367	0.968	0.790289	5.3600	7.9454
0.440	0.902166	5.1052	6.6185	1.012	0.781246	5.3846	8.0968
0.484	0.892608	5.1245	6.7037	1.056	0.772245	5.4099	8.2571
0.528	0.883091	5.1440	6.7923	1.100	0.763286	5.4360	8.4270
0.572	0.873617	5.1637	6.8848				
			$T = 280.0$ K				
0.059	0.987609	5.0739	6.1261	0.826	0.833079	5.3723	7.4597
0.118	0.975286	5.0966	6.2039	0.885	0.821723	5.3970	7.6031
0.177	0.963032	5.1191	6.2847	0.944	0.810446	5.4223	7.7551
0.236	0.950848	5.1416	6.3689	1.003	0.799248	5.4483	7.9166
0.295	0.938736	5.1641	6.4565	1.062	0.788129	5.4750	8.0884
0.354	0.926696	5.1866	6.5480	1.121	0.777089	5.5025	8.2716
0.413	0.914730	5.2091	6.6436	1.180	0.766127	5.5308	8.4673
0.472	0.902837	5.2317	6.7436	1.239	0.755245	5.5602	8.6768
0.531	0.891019	5.2545	6.8485	1.298	0.744441	5.5906	8.9017
0.590	0.879278	5.2775	6.9585	1.357	0.733716	5.6222	9.1436
0.649	0.867612	5.3007	7.0741	1.416	0.723069	5.6551	9.4044
0.708	0.856023	5.3241	7.1958	1.475	0.712500	5.6893	9.6865
0.767	0.844512	5.3480	7.3241				
			$T = 290.0$ K				
0.078	0.984772	5.2183	6.2833	1.092	0.798246	5.5741	8.0619
0.156	0.969663	5.2447	6.3793	1.170	0.784824	5.6040	8.2683
0.234	0.954676	5.2712	6.4802	1.248	0.771538	5.6346	8.4901

Table A2 -continued.

ρ_n/mol·dm^{-3}	Z	$C_{V,m}/R$	$C_{p,m}/R$	ρ_n/mol·dm^{-3}	Z	$C_{V,m}/R$	$C_{p,m}/R$
0.312	0.939811	5.2978	6.5865	1.326	0.758389	5.6662	8.7291
0.390	0.925070	5.3245	6.6986	1.404	0.745379	5.6988	8.9874
0.468	0.910456	5.3513	6.8169	1.482	0.732506	5.7326	9.2670
0.546	0.895970	5.3782	6.9418	1.560	0.719771	5.7677	9.5709
0.624	0.881613	5.4053	7.0740	1.638	0.707174	5.8044	9.9019
0.702	0.867386	5.4326	7.2141	1.716	0.694715	5.8427	10.2637
0.780	0.853290	5.4601	7.3628	1.794	0.682395	5.8830	10.6606
0.858	0.839328	5.4880	7.5210	1.872	0.670212	5.9253	11.0974
0.936	0.825499	5.5162	7.6895	1.950	0.658167	5.9700	11.5802
1.014	0.811805	5.5448	7.8694				
			$T = 295.0$ K				
0.091	0.982862	5.2924	6.3663	1.274	0.775594	5.6891	8.4894
0.182	0.965887	5.3215	6.4750	1.365	0.760903	5.7226	8.7484
0.273	0.949076	5.3509	6.5903	1.456	0.746397	5.7571	9.0295
0.364	0.932432	5.3804	6.7126	1.547	0.732077	5.7928	9.3354
0.455	0.915958	5.4102	6.8425	1.638	0.717943	5.8297	9.6693
0.546	0.899654	5.4401	6.9806	1.729	0.703995	5.8682	10.0348
0.637	0.883524	5.4701	7.1275	1.820	0.690234	5.9084	10.4364
0.728	0.867568	5.5004	7.2842	1.911	0.676660	5.9506	10.8791
0.819	0.851789	5.5309	7.4514	2.002	0.663274	5.9950	11.3691
0.910	0.836189	5.5616	7.6303	2.093	0.650073	6.0420	11.9136
1.001	0.820767	5.5927	7.8221	2.184	0.637060	6.0918	12.5213
1.092	0.805527	5.6243	8.0281	2.275	0.624233	6.1447	13.2027
1.183	0.790469	5.6564	8.2499				
			$T = 300.0$ K				
0.108	0.980377	5.3683	6.4538	1.512	0.747034	5.8210	9.0878
0.216	0.960981	5.4012	6.5799	1.620	0.730836	5.8596	9.4306
0.324	0.941818	5.4346	6.7150	1.728	0.714895	5.8995	9.8073
0.432	0.922888	5.4682	6.8596	1.836	0.699213	5.9408	10.2224
0.540	0.904196	5.5022	7.0145	1.944	0.683790	5.9840	10.6817

Table A2 -continued.

ρ_n/mol·dm^{-3}	Z	$C_{V,m}/R$	$C_{p,m}/R$	ρ_n/mol·dm^{-3}	Z	$C_{V,m}/R$	$C_{p,m}/R$
0.648	0.885744	5.5363	7.1806	2.052	0.668627	6.0291	11.1915
0.756	0.867534	5.5706	7.3592	2.160	0.653724	6.0767	11.7600
0.864	0.849570	5.6052	7.5513	2.268	0.639081	6.1270	12.3961
0.972	0.831852	5.6400	7.7584	2.376	0.624698	6.1805	13.1114
1.080	0.814383	5.6751	7.9823	2.484	0.610576	6.2374	13.9197
1.188	0.797166	5.7107	8.2248	2.592	0.596714	6.2983	14.8381
1.296	0.780201	5.7467	8.4881	2.700	0.583111	6.3636	15.8871
1.404	0.763490	5.7835	8.7748				
			$T = 305.0$ K				
0.132	0.976861	5.4329	6.5353	1.848	0.708357	6.0187	10.0683
0.264	0.954062	5.4689	6.6845	1.980	0.690291	6.0718	10.5712
0.396	0.931607	5.5073	6.8479	2.112	0.672604	6.1265	11.1325
0.528	0.909501	5.5476	7.0266	2.244	0.655297	6.1830	11.7618
0.660	0.887747	5.5896	7.2218	2.376	0.638371	6.2417	12.4700
0.792	0.866350	5.6331	7.4348	2.508	0.621826	6.3029	13.2705
0.924	0.845312	5.6778	7.6673	2.640	0.605662	6.3671	14.1797
1.056	0.824637	5.7237	7.9213	2.772	0.589880	6.4346	15.2173
1.188	0.804328	5.7705	8.1994	2.904	0.574477	6.5062	16.4077
1.320	0.784388	5.8182	8.5042	3.036	0.559456	6.5822	17.7809
1.452	0.764818	5.8668	8.8392	3.168	0.544813	6.6633	19.3745
1.584	0.745622	5.9164	9.2083	3.300	0.530549	6.7502	21.2364
1.716	0.726801	5.9670	9.6162				
			$T = 310.0$ K				
0.132	0.977640	5.5054	6.6048	1.848	0.718679	6.0501	9.8655
0.264	0.955617	5.5398	6.7485	1.980	0.701283	6.0977	10.3073
0.396	0.933933	5.5761	6.9050	2.112	0.684257	6.1460	10.7940
0.528	0.912592	5.6141	7.0753	2.244	0.667599	6.1953	11.3312
0.660	0.891598	5.6536	7.2603	2.376	0.651312	6.2456	11.9257
0.792	0.870954	5.6943	7.4612	2.508	0.635396	6.2971	12.5852
0.924	0.850661	5.7361	7.6794	2.640	0.619850	6.3500	13.3185

Table A2 -continued.

ρ_n/mol·dm^{-3}	Z	$C_{V,m}/R$	$C_{p,m}/R$	ρ_n/mol·dm^{-3}	Z	$C_{V,m}/R$	$C_{p,m}/R$
1.056	0.830724	5.7788	7.9166	2.772	0.604675	6.4045	14.1356
1.188	0.811144	5.8223	8.1746	2.904	0.589870	6.4609	15.0482
1.320	0.791924	5.8666	8.4557	3.036	0.575435	6.5195	16.0697
1.452	0.773066	5.9115	8.7621	3.168	0.561370	6.5805	17.2151
1.584	0.754571	5.9571	9.0970	3.300	0.547675	6.6443	18.5021
1.716	0.736442	6.0033	9.4635				
			$T = 315.0$ K				
0.132	0.978386	5.5787	6.6753	1.848	0.728503	6.0888	9.7033
0.264	0.957104	5.6116	6.8139	1.980	0.711742	6.1320	10.0965
0.396	0.936156	5.6462	6.9641	2.112	0.695339	6.1756	10.5249
0.528	0.915546	5.6822	7.1267	2.244	0.679294	6.2196	10.9923
0.660	0.895276	5.7194	7.3026	2.376	0.663608	6.2639	11.5027
0.792	0.875348	5.7578	7.4928	2.508	0.648280	6.3086	12.0607
0.924	0.855765	5.7970	7.6983	2.640	0.633311	6.3538	12.6714
1.056	0.836530	5.8371	7.9206	2.772	0.618700	6.3996	13.3400
1.188	0.817643	5.8778	8.1612	2.904	0.604447	6.4461	14.0724
1.320	0.799108	5.9191	8.4215	3.036	0.590552	6.4933	14.8748
1.452	0.780925	5.9609	8.7037	3.168	0.577015	6.5414	15.7537
1.584	0.763095	6.0032	9.0097	3.300	0.563834	6.5906	16.7158
1.716	0.745621	6.0458	9.3421				
			$T = 320.0$ K				
0.330	0.948364	5.7009	6.9516	1.980	0.721713	6.1721	9.9258
0.660	0.898791	5.7870	7.3483	2.310	0.682835	6.2718	10.9387
0.990	0.851315	5.8788	7.8254	2.640	0.646124	6.3713	12.1685
1.320	0.805963	5.9746	8.3990	2.970	0.611575	6.4704	13.6601
1.650	0.762758	6.0727	9.0903	3.300	0.579176	6.5693	15.4580
			$T = 330.0$ K				
0.330	0.951698	5.8483	7.0841	1.980	0.740334	6.2629	9.6723
0.660	0.905378	5.9259	7.4481	2.310	0.704173	6.3479	10.4893
0.990	0.861067	6.0073	7.8769	2.640	0.670042	6.4305	11.4424

Table A2 -continued.

ρ_n/mol·dm^{-3}	Z	$C_{V,m}/R$	$C_{p,m}/R$	ρ_n/mol·dm^{-3}	Z	$C_{V,m}/R$	$C_{p,m}/R$
1.320	0.818782	6.0914	8.3815	2.970	0.637926	6.5094	12.5455
1.650	0.778537	6.1770	8.9750	3.300	0.607801	6.5832	13.8061
			T = 340.0 K				
0.330	0.954769	5.9976	7.2201	1.980	0.757401	6.3637	9.5036
0.660	0.911436	6.0679	7.5559	2.310	0.723729	6.4374	10.1822
0.990	0.870023	6.1402	7.9443	2.640	0.691971	6.5090	10.9519
1.320	0.830543	6.2141	8.3928	2.970	0.662103	6.5769	11.8161
1.650	0.793003	6.2889	8.9098	3.300	0.634098	6.6398	12.7722
			T = 350.0 K				
0.330	0.957606	6.1492	7.3598	1.980	0.773116	6.4748	9.3988
0.660	0.917027	6.2136	7.6717	2.310	0.741738	6.5388	9.9739
0.990	0.878282	6.2786	8.0264	2.640	0.712174	6.6009	10.6123
1.320	0.841381	6.3442	8.4292	2.970	0.684400	6.6602	11.3129
1.650	0.806327	6.4097	8.8851	3.300	0.658387	6.7157	12.0706
			T = 370.0 K				
0.330	0.962675	6.4557	7.6455	1.980	0.801143	6.7236	9.3249
0.660	0.927012	6.5118	7.9194	2.310	0.773863	6.7722	9.7588
0.990	0.893024	6.5669	8.2225	2.640	0.748236	6.8187	10.2240
1.320	0.860716	6.6207	8.5569	2.970	0.724239	6.8629	10.7171
1.650	0.830091	6.6730	8.9242	3.300	0.701852	6.9045	11.2319
			T = 390.0 K				
0.330	0.967067	6.7621	7.9346	1.980	0.825460	6.9902	9.3615
0.660	0.935663	6.8116	8.1780	2.310	0.801757	7.0294	9.7072
0.990	0.905798	6.8593	8.4422	2.640	0.779578	7.0660	10.0689
1.320	0.877475	6.9050	8.7277	2.970	0.758908	7.1001	10.4427
1.650	0.850697	6.9487	9.0344	3.300	0.739731	7.1313	10.8230
			T = 410.0 K				
0.330	0.970904	7.0681	8.2257	1.980	0.846793	7.2690	9.4671
0.660	0.943226	7.1134	8.4456	2.310	0.826259	7.3020	9.7534
0.990	0.916972	7.1560	8.6800	2.640	0.807147	7.3327	10.0477

Table A2 -continued.

ρ_n/mol·dm^{-3}	Z	$C_{V,m}/R$	$C_{p,m}/R$	ρ_n/mol·dm^{-3}	Z	$C_{V,m}/R$	$C_{p,m}/R$
1.320	0.892148	7.1960	8.9289	2.970	0.789448	7.3611	10.3469
1.650	0.868755	7.2337	9.1917	3.300	0.773156	7.3868	10.6465
			$T = 430.0$ K				
0.330	0.974278	7.3711	8.5157	1.980	0.865674	7.5564	9.6190
0.660	0.949885	7.4139	8.7170	2.310	0.847971	7.5855	9.8629
0.990	0.926825	7.4537	8.9286	2.640	0.831611	7.6123	10.1102
1.320	0.905101	7.4906	9.1502	2.970	0.816591	7.6369	10.3583
1.650	0.884717	7.5248	9.3808	3.300	0.802912	7.6593	10.6039
			$T = 450.0$ K				
0.330	0.977260	7.6678	8.8012	1.980	0.882496	7.8423	9.7947
0.660	0.955781	7.7059	8.9838	2.310	0.867346	7.8703	10.0087
0.990	0.935563	7.7430	9.1760	2.640	0.853473	7.8956	10.2231
1.320	0.916608	7.7783	9.3763	2.970	0.840881	7.9184	10.4356
1.650	0.898918	7.8115	9.5832	3.300	0.829580	7.9390	10.6433

Chapter 8. Conclusions

Highly accurate speed-of-sound measurements on several gases have been made during this work. These were performed by means of a spherical resonator which gave outstanding precision and usually achieved uncertainties better than 0.004 per cent for pure fluids in the absence of relaxation phenomena. The uncertainty increased in cases where the frequency range of the measurements overlapped the dispersion curve.

One of the achievements of this work was to obtain speed-of-sound data by the spherical-resonator technique in a pressure range far larger than that achieved previously. Formerly, acoustic measurements in gases using acoustic resonators were restricted to low or intermediate pressures. So far, only for a few systems (three of them reported in this work: argon, ethane and carbon dioxide) have speeds of sound been measured with an acoustic resonator at pressures above 10 MPa and only in this work have measurements been made with that technique at temperatures above 400 K. The present limitation to pressures below 20 MPa was entirely due to the restriction imposed by the available pressure transducers, otherwise, the current resonator could have been operated at pressures up to 30 MPa.

A severe sound absorption (such as that observed in carbon dioxide at pressures below 600 kPa) can easily diminish the amplitude of radial modes so much that the usual procedure for measuring the speed of sound becomes impossible. Under those conditions, a viable alternative investigated in this work is to measure the resonance frequency of the non-radial mode (1, 1) which, being lower in frequency, is less affected than any radial mode. Based on the experience acquired during the measurements on carbon dioxide, it can be said that speed-of-sound data may be derived from the non-radial mode (1, 1) with an accuracy similar to that obtained from radial modes (though occasionally a more conservative uncertainty of up to 100 ppm would be appropriate).

It was also noted that ethane has an extraordinary 'catalytic' effect on the vibrational dexcitation of carbon dioxide molecules, and therefore greatly reduces absorption of sound in the mixture (ethane + carbon dioxide) as compared to that observed in pure carbon dioxide. However, in the mixture other difficulties were

found; in contrast with previous experience, comparatively large variations ($\pm 3 \cdot 10^{-3}$ mole fraction) of composition took place between different fillings even though all the samples were obtained from the same source. This behaviour is still not well understood.

The study of the excess half-widths of the radial modes can provided valuable information about vibrational relaxation times and thereby permit the estimation of dispersion corrections.

Thus, one main conclusion is that measurements of the speed of sound in gases can be performed in a wide pressure and temperature range with an outstandingly small uncertainty (ranging from 20 ppm to 40 ppm in most cases). The existing acoustic model has been sufficient to describe accurately all acoustic phenomena observed in this work.

These experimental factors favour the use of the speed of sound for determining thermodynamic properties, especially the pVT surface and the heat capacities at constant volume and at constant pressure. The method applied here to obtain thermodynamic properties has proved to give results as good as or better than those obtained from the most accurate direct experimental techniques: in all cases better than 0.025 per cent in the compression factor and better than 0.2 per cent in the isochoric heat capacity.

The uncertainty of the pVT data derived from the speed of sound was controlled mainly by initial conditions which may not always be known with sufficient accuracy. A finite difference approach was employed to set up those initial conditions from two closely-spaced pVT isotherms. The treatment resulted in both initial conditions being correct to $O(\Delta T^3)$, where ΔT was the spacing between the two isotherms. It seems that for polyatomic gases this treatment is appropriate while for monatomic gases the initial conditions, especially that concerning the first derivative of the compression factor, must be set up correct to $O(\Delta T^4)$ at least. A correction for the leading term neglected in the truncated expansion of the first derivative of the compression factor was obtained for argon with the introduction of a term proportional to the first derivative itself. The coefficient of this term was determined by comparison with a third pVT isotherm. For ethane, this additional term was

unnecessary. These observations are supported further by the study of error propagation and it is possible to conclude that effects of errors in the initial conditions are less severe for a polyatomic gas than they are for a monatomic gas.

Moreover, it has been shown that the *pVT* surface for the whole gas phase can be derived from speed of sound measurements when a single set of initial conditions are available as long as they are given along an isotherm near to T^c. The algorithm applied in this work, permitted determinations of the thermodynamic properties in the supercritical region by means of a integration along isochores while the subcritical region was obtained by selecting an integration path that followed lines parallel to the saturation curve.

Compression factors have been obtained in this work at densities up to half the critical but, in principle, the method may be extended to greater densities (but still inside the single-phase region).

Although, the results reported are quite encouraging there is room for improvement. One feature that can be improved is the way in which the heat capacities are freed of likely errors introduced by ripples in the interpolation of the speed of sound. The method of obtaining smooth values for the heat capacities may introduce a systematic error which is not easy to detect since the accuracy of direct determinations of heat capacities is still not comparable with the accuracy claimed here.

A second conclusion is that an equation of state, as accurate as the most precise conventional equations of states, but in numerical form, may be obtained from the speed of sound with the addition of only a few pieces of extra information. Consistency between all thermodynamic properties is ensured automatically.

Finally, the other aspect that has been investigated in this work concerns the use of the speed of sound to determine virial coefficients. This provided a means of determining simple but useful model intermolecular potentials. The semi-empirical approach followed in this work was able to produce models that contained most of the relevant physical features. The anisotropy of the linear or pseudo-linear molecules studied here has been represented to some extent by the utilisation of a site-site

potential model (but with only two sites per molecule) with the Maitland-Smith radial potential model to describe each site-site interaction.

However, it seemed that the final model has been oversimplified because, for both pure substances studied, the agreement between experimental second virial coefficients and those predicted by the model was not very good, particularly at low temperatures. This could be due to the exclusion of the quadrupolar interaction since for both system a permanent quadrupolar moment exists. There is numerical evidence that inclusion of a quadrupolar-quadrupolar interaction may produce second virial coefficients more negative at low temperature than those calculated without this interaction. Unfortunately, the inclusion of this interaction has to be modified to some extent since it tends to diverge as the molecules approach each other closely. This would lead to a more complicated model of the intermolecular potential.

Regarding the interaction second virial coefficient, the agreement with directly measured values achieved with this semi-empirical procedure seems to be at first glance less satisfactory but this may not be in fact the case. First at all, interaction virial coefficients obtained from pVT data are susceptible to quite larger experimental uncertainties. Second, the source data for the determination of the intermolecular potential model was not always as precise as, under normal conditions, one would expect. Factors that prevented for the determination of highly-accurate second acoustic virial coefficients were dispersion of sound (for pure carbon dioxide) and variations of composition (for the mixture).

Thus, considering the simplicity of the approach used, the predictions provided by site-site model are satisfactory.

There are several possibilities for continuation of the present line of research that deserve to be investigated with the main aim of obtaining accurate thermodynamic properties from speed-of-sound measurements.

First at all, the extension of the numerical integration to cover the liquid phase seems to be the obvious next step. For this purpose, the present algorithm must be adapted to the appropriate choice of the integration path (such that the numerical procedure remains stable), and bearing in mind that for the compress gas phase the uncertainty of the speed of sound did not affect significantly the derived compression

factors, it may be possible to tolerate the usually larger uncertainty with which the speed of sound is measured in liquids. However, it would be preferable to make further developments of the methods used to measure the speed of sound in liquids in order to achieve an accuracy in the determinations comparable to that obtained in gases by means of acoustic resonators. In any case, an extensive programme of measurements of speed of sound in a large numbers of liquids may be required to supply the data needed to perform the numerical integration. Boundary conditions for the speed of sound at the saturation curve may be necessary to match both solutions in a thermodynamically consistent manner and thereby to generate the whole *pVT* surface.

However, it is clear that difficulties may rise near to the critical point, where some thermodynamic properties diverge and therefore it is certain that any numerical procedure based on the assumption that the thermodynamic functions are analytical will fail. Moreover, severe practical difficulties are found when the speed of sound is measured near to the critical point with the unavoidable result that the accuracy of the speed-of-sound measurements near to the critical point is no longer better than any other thermodynamic property measured by conventional methods.

A further extension of this approach to the case of binary mixtures seems also possible if one considers only mixtures with fixed composition as pseudo-pure fluids but a generalisation in which the composition appears explicitly as an independent variable during the integration does not seem to be straightforward.

Finally, the possibility of fitting useful and realistic potential models to the speed of sound is not only restricted to the method presented in this thesis. Several different approaches can be exploited, starting with the utilisation of more acoustic virial coefficients than just the second. Another alternative is to fit the potential model directly to the speed of sound surface, making use (for example) of an integral equation theory to relate the properties to the potential.